

# SUSPENDED GRAPHENE MEMBRANES FOR ELECTROSTATICALLY ACTUATED RESONATORS

MANVIKA SINGH

Master of Science Thesis



# SUSPENDED GRAPHENE MEMBRANES FOR ELECTROSTATICALLY ACTUATED RESONATORS

MASTER OF SCIENCE THESIS

For the degree of Master of Science in Electrical Engineering  
at Delft University of Technology

BY

MANVIKA SINGH

BORN ON THE 15<sup>TH</sup> OF FEBRUARY 1993 IN JABALPUR, INDIA

29<sup>TH</sup> November, 2017

Delft University of Technology  
Faculty of Electrical Engineering, Mathematics and Computer Sciences  
Laboratory of Electronic Components, Technology and Materials (ECTM)  
Else Kooi Laboratory

Approved by

Responsible Professor

Prof.dr.ir. P.M. Sarro

Faculty of Electrical Engineering, Mathematics and Computer Science

Delft University of Technology

Supervisors

Dr. ir. S. Vollebregt

Assistant professor

Faculty of Electrical Engineering, Mathematics and Computer Science

Delft University of Technology

Robin Dolleman

PhD Candidate

Faculty of Applied Sciences

Kavli Institute of Nanoscience

Delft University of Technology

Third reader and Committee member

Prof.dr. Peter Steeneken

Dept. of Precision and Microsystems Engineering and Kavli Institute of Nanoscience

Delft University of Technology



"I have never understood why some people are lucky enough to be born with the chance that I had, to have this path in life and why across the world, there is a woman just like me. With the same abilities and the same desires, same work ethic and love for her family, who would most likely make better films and better speeches. Only she sits in a refugee camp, and she has no voice. She worries about what her children will eat, how to keep them safe, and if they'll ever be allowed to return home. I don't know why this is my life and that's hers. I don't understand that but I will do as my mother asked, and I will do the best I can with this life, to be of use."  
-Angelina Jolie

# ABSTRACT

As we are moving towards nano level devices, there is a greater need to miniaturize resonators. With miniaturization, we can achieve a higher resonant frequency and reduce power consumption. Since graphene has the highest stiffness of all known materials and various other exceptional mechanical properties, graphene based resonators are of interest. Most of the graphene resonators in the past have been measured using optical setup. In order to get rid of this large and bulky setup, we aim to integrate it with an actuation electrode. The main goal of this thesis is to fabricate an electrostatically actuated graphene resonator.

We start with the design of the actuator in chapter 3. For the graphene membrane to work as a resonator, it needs to be suspended. Chapter 4 details the procedure to fabricate suspended graphene membranes. Various samples of different shapes, sizes and gap sizes have been analyzed using different experiments. Some samples are found to be collapsed. Whereas the other samples show corrugations and wave like structure. We observe clear differences between the SEM and AFM images of the collapsed and likely suspended samples.

This is followed by the fabrication of graphene resonator with a buried electrode. Chapter 5 presents all the failed attempts to fabricate suspended graphene membrane on a buried electrode before realizing the suspended graphenes membrane on p doped polysilicon and niobium electrode.

Then chapter 6 presents the measurements done on the graphene samples to find out the resonant frequency of the graphene resonator. We found that the fundamental mode being detected is because of gold and not graphene. To find the resonant frequency of the graphene membrane, experiments such as DC tuning and nonlinearity were performed on the samples. We found a high frequency peak becoming much more non linear at high oscillation amplitudes than low frequency peak. We suspect it to be graphene but we donot observe spring hardening in graphene membranes which would have been a stronger proof of detecting graphene motion.

In chapter 7 the cause of the collapse of membranes is analyzed. Using stress measurements and observations from various samples, some hypothesis have been proposed for the collapsing graphene membranes. We also observed bubble like structures on graphene samples which formed suspended membranes after release. We found the cause of collapse of membranes but the exact mechanism of suspension is still unknown. The EDX analysis on the bubbles show that the bubble area has significant amount of more oxygen than the other area of graphene. In order to achieve good performance by the graphene resonator, it should be completely suspended. Hence, it is crucial to understand the process of suspension of graphene in more detail.

# Acknowledgments

I would like to thank Prof. Dr. Lina Sarro, for her valuable suggestions. Both her suggestions of changing one parameter in each wafer to analyze the cause and usage of polysilicon instead of molybdenum helped my thesis take new direction. When my membranes collapsed for the first time she had asked me " Do you like solving puzzles?? Think it as a puzzle." From then until now I am trying to solve the pieces of this puzzle. At this stage, I feel happy that I was able to solve the puzzle to some extent.

I would like to thank Sten for guiding me in fabrication and evaluating my report. I am thankful to Prof. Dr. Peter Steeneken for taking part in my thesis defence committee. I would like to thank Robin for explaining me the exciting physics concepts, which were quite new to me, and the measurements.

I am thankful to Marcel Bus, Violeta, Hans Goosen, Filiberto and Mario for helping me with some experiments. I am also thankful to all my fellow EKL lab members and colleagues with whom I spent this past one year.

Finally, I would like to thank my parents who always encourage and motivate me.

Manvika Singh  
Delft, November 2017

# Contents

## Abstract

## Acknowledgements

<b>1</b>	<b>Introduction</b>	<b>1</b>
1.1	Miniaturization of resonators	1
1.2	Graphene	3
1.3	Graphene growth	4
1.4	Suspended graphene membranes	7
1.5	Problem statement and research objectives	7
1.6	Thesis outline	8
1.7	Summary	9
<b>2</b>	<b>Graphene Resonators</b>	<b>10</b>
2.1	Resonant Frequency	10
2.1.1	Tension and Bending stiffness	11
2.1.2	Effect Of Temperature	12
2.1.3	Non Linearity	13
2.2	Actuation of mechanical motion of a resonator	14
2.2.1	Magnetic actuation	14
2.2.2	Electrostatic actuation	15
2.2.3	Electrothermal actuation	16
2.2.4	Comparison of actuation principles	16
2.2.5	Squeeze Film effect	17
2.3	Summary	18
<b>3</b>	<b>Design of the device</b>	<b>19</b>
3.1	Design of the graphene resonator	19
3.2	Design of the electrostatically actuated graphene resonator	22
3.3	Design of other structures	26
3.3.1	Magnetic Actuators	26
3.3.2	Wheatstone Bridge	26
3.3.3	Gold Graphene Resonator	27
3.4	Summary	29
<b>4</b>	<b>Fabrication of suspended graphene membranes</b>	<b>30</b>
4.1	Fabrication procedure	30
4.1.1	Initial fabrication steps and Thermal Oxidation	32
4.1.2	Molybdenum deposition	33
4.1.3	Etching of Molybdenum	34
4.1.4	Graphene growth	37

4.1.5	Gold contacts	38
4.1.6	Release of the membrane	38
4.2	Fabricated batches of wafer	41
4.3	Issues Faced While Fabrication	42
4.4	Analysis of of the fabricated samples	43
4.4.1	Structure of the suspended graphene membrane	43
4.4.2	Graphene membrane under the microscope	44
4.4.3	Analysis of graphene membranes using AFM and SEM	45
4.5	Summary	49
<b>5</b>	<b>Fabrication of the actuator</b>	<b>51</b>
5.1	Fabrication procedure for buried molybdenum electrodes	51
5.1.1	Fabrication procedure 1	51
5.1.2	Patterning and etching of buried molybdenum metal	54
5.1.3	Sheet resistance of buried molybdenum metal	56
5.1.4	Fabrication procedure 2	58
5.1.5	Fabrication procedure 3	60
5.2	Fabrication of suspended graphene membranes with different types of electrodes	62
5.2.1	Polysilicon	63
5.2.2	Niobium and titanium nitride + titanium	65
5.3	Summary	68
<b>6</b>	<b>Measurements</b>	<b>69</b>
6.1	Dynamical characterization	69
6.1.1	Resonant frequency measurements using laser interferometry setup	69
6.1.2	Gold resonance	71
6.1.3	Electrostatic actuation	74
6.1.4	Non linearity in grahene membranes	77
6.1.5	Optical measurements on graphene samples with localized electrode	79
6.1.6	Discussion	82
6.2	Electrical measurements	83
6.2.1	I-V measurements	83
6.2.2	Resistance measurements	86
6.3	Summary	86
<b>7</b>	<b>Analysis of cause of collapse of graphene membranes</b>	<b>87</b>
7.1	Cause Analysis	87
7.2	Important Observations	91
7.3	Graphene Bubbles	95
7.4	Stress measurements	97
7.5	Possible explanations for collapsing graphene membranes	99
7.5.1	Oxide thickness	99
7.5.2	Molybdenum etching recipe	100
7.6	Analysis	101
7.7	Cause analysis: types of oxide	103
7.8	Case study	104
7.9	Summary	105
<b>8</b>	<b>Conclusion</b>	<b>106</b>
.1	APPENDIX A	124



# Chapter 1

## Introduction

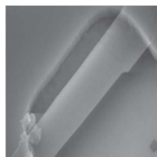


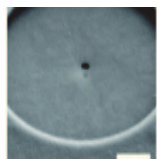
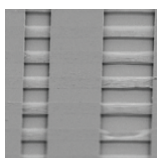
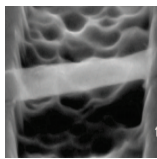
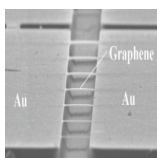

### 1.1 Miniaturization of resonators

A resonator is a device which will naturally resonate with greater amplitude at some frequencies as compared to other frequencies. These frequencies at which it will naturally oscillate with greater amplitude are called resonant frequencies. A resonator could be used for various applications such as signal generators, various types of sensors (mass, force, biological, chemical etc.), oscillators, filters, various RF applications etc. This thesis focuses on mechanical resonators. A prototypical nanoelectromechanical resonator is a nanoscale beam clamped on one or both ends that vibrates in response to an applied external force [1, 2]. Mechanical structures such as beams, strings, plates and membranes are used as vibrating parts. Research on MEMS (microelectromechanical systems) has been going on for decades. Scaling down the resonators to micro level helped the industries to make small micro sized devices for various consumer applications. The increasing need to further scale down the size of mechanical devices and transistors for various applications paved the way for nanoresonators.

We are going from MEMS to NEMS (nanoelectromechanical systems) leading to fabrication of various nanoresonators. Miniaturization of resonators helps to attain higher sensitivity, lower power consumption, higher resonance frequency along with lesser requirement of space [1, 3]. NEMS have applications in various areas, such as mass [4], force [5] and position [6] sensing, which can be explored. Two important parameters of any resonator are its resonance frequency and quality factor. The sensitivity of a NEMS resonator is defined by its resonant frequency. The resonant frequency of a nanoresonator depends on various factors such as its material properties, shape, stress, surface topography, external factors such as pressure, temperature and the environmental factors in which the measurement takes place such as vacuum or air [3]. These factors can cause a shift in the resonant frequency of the nanoresonators. This shift can be compensated with the tunability of the resonant frequency in the nanoresonators [3]. Hence, nanoresonators with a tunable gap have the potential for various applications.

In the past prototypical nanoresonators made of Si, SiO<sub>2</sub>, SiN and SiC have been studied [2]. The limit of a resonator would be one atom thick. A single layer of atom should be very stiff, strong and robust so that it can be used as a resonator. Single layer graphene's Young modulus (1TPa) is much higher than that of silicon (165 GPa). Infact graphene has the highest stiffness of all known materials. This means that graphene based resonator can give higher frequencies as compared to silicon based materials. These properties make graphene suitable as a nanoelectromechanical resonator. Thus, single layer graphene (one atom thick) and few layer graphene are of interest.

Table 1.1: List of graphene resonators fabricated in the past. Taken from [3, 7]

	Resonator structure	Device Picture	Excitation and detection method	Fabrication	Resonant Frequency (MHz)	Quality Factor
1	Doubly clamped single layer graphene resonator[8]		optical actuation and detection	mechanically exfoliated graphene	70.5	78
2	Fully clamped square resonators [9]		optical actuation and detection	mechanically exfoliated graphene	66	25
3	Doubly clamped single layer graphene resonator [10]		electrostatic actuation and motion-modulated conductance detection	mechanically exfoliated graphene	33 at 77K	10,000 at 77K
4	Fully clamped circular drum resonators [11]		optical actuation and detection	chemically reduced Graphene oxide	10 to 110	1500 to 4000
5	Doubly clamped single layer graphene resonators [12]		optical actuation and detection, electrical actuation and detection	transferred CVD graphene	5 to 75	250
6	Doubly clamped few layer graphene [13]		electrostatic actuation and detection with frequency modulation by AFM	mechanically exfoliated graphene	18 to 85	64
7	Doubly clamped graphene resonators [14]		optical actuation and detection	epitaxial graphene on silicon carbide substrate	3 to 100	50 to 400
8	Doubly clamped single layer graphene resonators [15]		electrostatic actuation and electrical frequency mix down	transferred exfoliated graphene	30 to 130	100

In the past, various graphene resonators have been fabricated using mechanical exfoliation methods, as shown in table 1.1, but when it comes to the industry compatible wafer scale fabrication of graphene resonators, not much results are available.

Transduction of the mechanical motion of these NEMS devices to electrical signal, as shown in figure 1.1, is of utmost importance so that it can be used in electronic devices in future and not merely remain a prototype to be studied at the research level. However, scaling of resonators brings various challenges in transduction of mechanical motion. Data on the transduction of the wafer scale graphene resonator is even more scarce. Moreover, integrating the graphene resonators with sensing and actuating principles, from a fabrication point of view, still remains very challenging. This thesis is an attempt to fill this gap in research and explore the possibilities of fabricating a graphene resonator with an integrated actuation electrode using a wafer scale transfer free approach.



Figure 1.1: *Transduction mechanism in a nanoresonator. Adapted from [2]*

To fabricate a resonator, one of the basic and essential requirements is that the material that is being used as a resonator should be suspended and be able to resonate freely. There are various methods using which suspended graphene membranes can be fabricated. To fabricate suspended graphene membranes, it is essential to understand the graphene growth mechanism too. First, we discuss what is graphene and its various important properties, along with state of the art on graphene growth on metals. Then various methods to produce suspended graphene membranes have been presented followed by the research objectives.

## 1.2 Graphene

Graphene, discovered in 2004, is a two dimensional material which consists of layers of carbon atoms arranged as six-membered rings [16]. It is the parent of all graphitic forms such as carbon nanotube and buckminsterfullerene as shown in figure 1.2. It is a crystalline allotrope of carbon [16]. Each carbon atom is connect to three other carbon atoms in the x-y plane and the in plane bonds are  $sp_2$  hybridized. It has attracted a lot of attention due to its unique structure, properties and potential for applications [17–19].

Graphene has various unique and important properties such as its tunable band gap, high elasticity, quantum hall effect at room temperature and ambipolar electric field effect [16]. Some of its other interesting properties are its velocity saturation of  $3 \times 10^7 \text{ cm/s}$  and carrier mobility of upto  $200,000 \text{ cm}^2/\text{Vs}$  [20]. Its exceptional electronic properties can be denoted to its linear dispersion relation near the six corners of first Brillouin zone [20]. Graphene is a single layer (SL) material. Even bilayer graphene (BG) and few layer graphene (FG) are of equal interest. In few layer graphene the number of layers are less than or equal to 10 [16].

Some of its exceptional mechanical properties are its highest young's modulus ( $\sim 1 \text{ TPa}$ ) of all known materials [21–23], a breaking strain of nearly 25 % [24] lowest mass density and bending rigidity of all impermeable membranes [25] and large surface area. When scaling down to nano level, most of the materials become mechanically unstable. However single

layer graphene is strong and stiff and is one atom thick making it an ideal candidate to be used as a nanoresonator. Graphene's exceptional mechanical properties have led the way for it to be used for mechanical applications, such as membranes separating disparate environments [26, 27], switches [28] etc. Other advantages of graphene include its high thermal conductivity [29]. It shows a high electron mobility which leads to a high electrical conductivity [30]. Single layer graphene and bilayer graphene were first obtained by micro-mechanical cleavage [16]. Various physical techniques and microscopes have been used to characterize graphene such as scanning tunneling microscopy, transmission electron microscopy, atomic force microscopy, Raman spectroscopy and X-ray diffraction [16]. A lot of research and study has been presented in recent years which has helped to understand the properties of graphene better [22, 31–37].

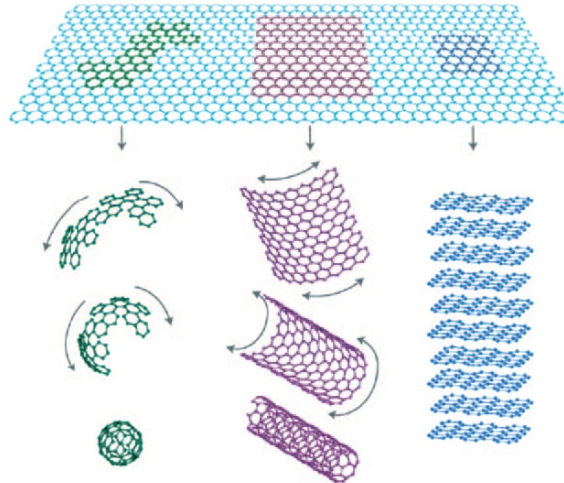


Figure 1.2: Graphene : parent of all graphitic forms Taken from [38]

One of the major applications of graphene is in the field of mechanical resonators as shown in table 1.1. Among mechanical resonators, pressure sensors are the most important application. Pressure sensors are present in most of the mobile sets and are the most widespread membrane based mechanical sensors. Conventional pressure sensors use membranes which are hundreds of nanometers thick [25]. Using graphene as a membrane in these sensors would allow for a higher responsivity and lesser requirement of space [25]. Various graphene pressure sensors have been proposed in the past [39–43]. Most of the conventional graphene based pressure sensors use pressure difference based sensing methods and so require an impermeable reference cavity. However, graphene sealed cavities were shown to have leak time constants of many hours [9]. At this stage, they are not known to be stable for a period of many years. Hence, it would be interesting to develop pressure sensors which do not require an impermeable reference cavity. Squeeze film pressure sensors are one of these sensors. Graphene based squeeze film pressure sensors have been reported in the past [25]. Other applications of graphene are in the field of gas sensors [44, 45], as cantilevers [46, 47] etc.

### 1.3 Graphene growth

Graphene can be synthesized in various ways such as mechanical exfoliation, reduction of graphene oxide, unzipping of carbon nanotubes, graphitization of silicon carbide, organic synthesis etc. However, these methods cannot be used for large scale production of graphene. The most efficient way to fabricate graphene based structures on a large scale is chemical vapour deposition (CVD). It is essential to understand this process in detail so that its growth

parameters (temperature, pressure, flow rate, catalyst) can be controlled and the desired layer thickness and crystallinity can be achieved for graphene. This can pave the way for getting the highest quality of graphene at large scale with lowest possible cost. In past graphene has been grown on metals such as nickel [48–50], copper [51–53], platinum [54], palladium [55], cobalt [56], molybdenum [57–59] etc.

Multilayer graphene growth mechanism on metal is quite unique. In a typical film growth, as shown in figure 1.3(a), the growth of the film takes place by the usual on the top mechanism. In this mechanism the adatoms nucleate on top of the previous layer. The new graphene layer can grow from below the previous layer as shown in figure 1.3(b). This is possible because of the bond strength differences between the carbon adatoms bonded to graphene as compared to the carbon adatoms on the metal surface [60]. The weakly bonded carbon adatoms to the graphene try to go to the metal interface if there is an existing pathway from the surface to the substrate. Then the carbon concentration keeps increasing at the metal-graphene interface until saturation is achieved. Once saturation is reached, new graphene layer is nucleated. This type of growth mechanism is called underlayer nucleation and growth mechanism and it occurs in those parts where carbon concentration is low. Areas where carbon concentration is high and there are increasing number of graphene layers, graphene growth can take place using the on the top mechanism [60].

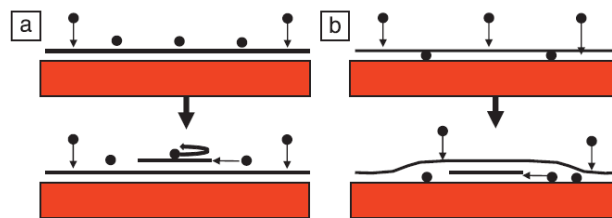


**Figure 1.3:** a) Typical growth mechanism of films other than graphene. b) Underlayer mechanism of graphene growth on metals. Taken from [60]

Chemical vapour deposition of graphene consists of four main steps [59]

1. Precursor gas is adsorbed and is decomposed with the help of a catalyst into carbon species.
2. Bulk diffusion of the carbon species into the metal and surface diffusion of carbon on the surface of metal
3. The dissolved carbon species are segregated onto the surface of the metal.
4. Surface nucleation and graphene growth

The use of the metal substrate on which graphene grows becomes very important since it is involved in all the four mentioned steps above. By choosing the correct metal and suppressing or enhancing one or more of the four main steps described above, the desired property of graphene such as layer thickness can be achieved. If graphene is grown on metals such as nickel, all the four steps mentioned above are involved. Since nickel has high carbon solubility, graphene grows on it with dissolution and segregation process [50]. It has been reported that in order to suppress the formation of multilayer graphene on nickel, factors such as cooling rate is important [50]. Getting uniform graphene on nickel still remains a challenge.

Graphene growth can take place via another route. In this route, after adsorption and decomposition of precursor gas, directly surface nucleation and graphene growth takes place

on the surface of graphene. This is more of a surface phenomena and this happens when the bulk diffusion and segregation processes are negligible in chemical vapor deposition process. This growth process takes place for metals such as copper whose carbon solubility is very low and so after the adsorption and decomposition of precursor gas on the surface, the graphene growth takes place. Hence, formation of graphene on copper is self limited and it is difficult to grow multilayer graphene on copper [59]. These two routes have been described in figure 1.4.

Both the routes described above coexist in nearly all the chemical vapour deposition of graphene. However, which of these routes will dominate, depends on the properties of the metal being used.

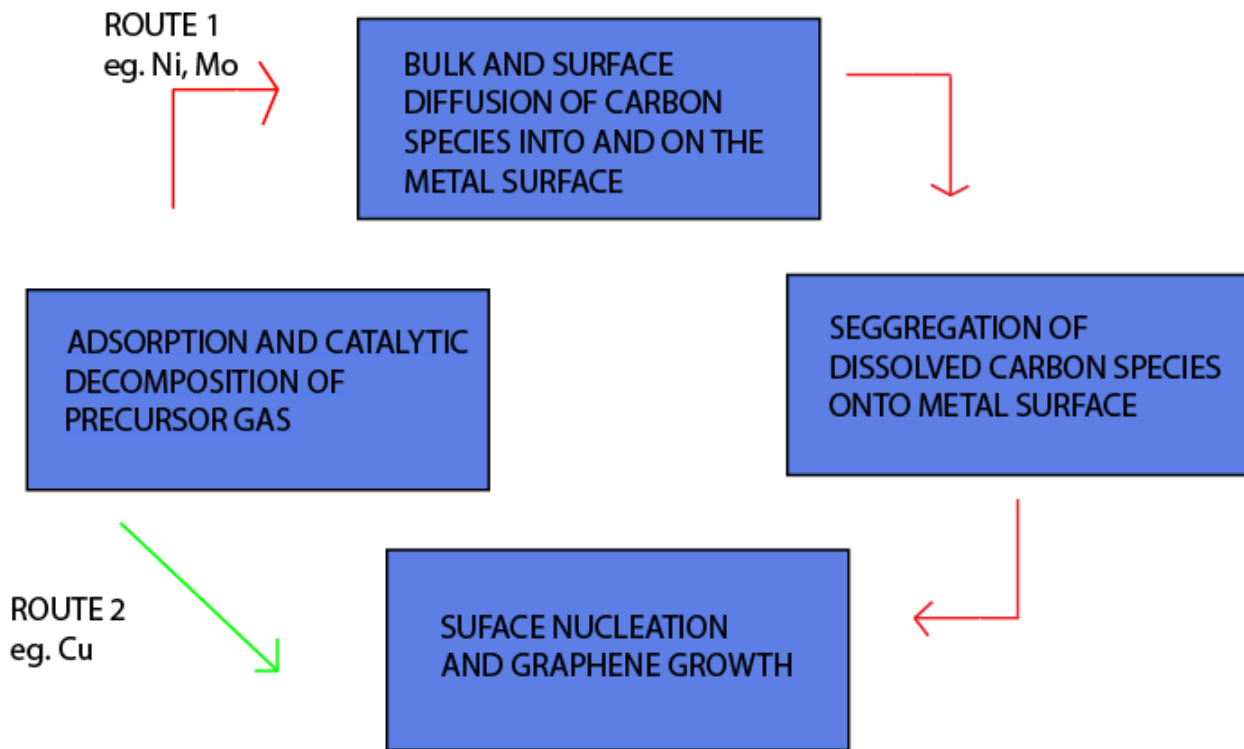


Figure 1.4: CVD of graphene on substrates via two different routes

In order to control the thickness of graphene and to get the required uniformity of graphene, the choice of metal becomes essential. Another metal that has been used to grow graphene is molybdenum. Graphene has been grown on molybdenum foils (100  $\mu\text{m}$ ) thick. Even though molybdenum has low carbon solubility like copper, graphene growth process on molybdenum foils takes place by dissolution and segregation process [58] and not by surface adsorption phenomena. The growth mechanism for copper metal cannot be applied in the case of molybdenum as copper has a poor affinity to carbon [61] because of which graphene is formed only on the surface of copper metal and there is no carbide phase detected in copper [62].

Molybdenum provides various advantages which makes it an ideal metal for graphene growth. Some of these are its high melting temperature of 2623  $^{\circ}\text{C}$  and a smooth surface for graphene growth [63]. The XRD pattern of the molybdenum foil shows a molybdenum carbide peak after graphene growth on the molybdenum foil [57, 58]. This shows the diffusion of carbon atoms into the metal molybdenum [58]. If more carbon is precipitated

on the metal molybdenum surface, it becomes difficult for remaining carbon to precipitate on the surface of molybdenum foil. This leads to a thin and uniform growth of graphene and hence, better quality of graphene is achieved. Also, when graphene is grown at a higher temperature, more carbon precipitates on the metal surface and better quality of graphene layer is achieved [57].

However, most of the above mentioned substrates, which are used to grow graphene, are thick foils. For miniaturization and industry compatibility, replacing them with sputtered metal thin films would be a good option. In the past, graphene was grown on 50 nm molybdenum thin films [63]. In [64] graphene growth on thin molybdenum films ranging from 30 nm to 90 nm with the best 2D/G ratio was reported for 60 nm molybdenum. In [65], transfer free wafer scale fabrication of graphene sensors was reported. Graphene was grown on molybdenum via CVD and then this molybdenum was etched by using phosphoric acid. This type of process allowed pre patterning of molybdenum to any required shape or size which eliminated the need for further processing after graphene growth. This thesis focuses on the use of molybdenum as graphene growth substrate because of the various advantages discussed above.

## 1.4 Suspended graphene membranes

Many suspended graphene membranes have been fabricated in the past [8, 13, 15, 25, 32, 66–72]. However, most of these were made using exfoliated graphene and were not fabricated using wafer scale transfer free process. One of the methods used is by suspending the mechanically exfoliated graphene across trenches that have been patterned photolithographically on the oxide.

For wafer scale fabrication, a transfer free approach is beneficial. Such a fabrication process has been described in [73] to fabricate suspended graphene membranes. Advantage of this fabrication process is that molybdenum (Mo) layer is used both as a catalyst for the chemical vapor deposition (CVD) of multi-layer graphene and as a sacrificial layer at the end of the process [73]. This procedure involves growth of 90 nm (average) thermal oxide on p type silicon wafer, followed by growth of metal molybdenum. Molybdenum is patterned which is used as a catalyst to grow graphene. After graphene growth, manual coating, exposure and manual development are done to pattern graphene. Then gold contacts are deposited and molybdenum is etched away using peroxide. Hence, it is this molybdenum that defines the gap size. To avoid stiction problems, critical point drying is done. This method has been used to fabricate the suspended part of graphene membrane because of its transfer free, wafer scale approach and the various advantages it offers because of the use of molybdenum as both, a catalyst and a sacrificial layer. This fabrication approach will be described in more detail in chapter 4.

## 1.5 Problem statement and research objectives

As described in the earlier sections, graphene has exceptional mechanical and electrical properties which makes it suitable as a nanoresonator. However, most of the research in the past used exfoliated graphene which needed to be transferred. This type of graphene production is not industry compatible. Hence, new alternatives have to be looked into the area of fabricating graphene resonators using a scalable and industry compatible process flow. Moreover, in order to use these graphene resonators as electronic equipments, transduction of the mechanical motion to electrical signal becomes important. Most of the graphene

resonators have been actuated by optical setup in the past. This optical setup is large, bulky and impractical for real world applications. Suitable actuation techniques have to be integrated with these graphene resonators, as shown in figure 1.5, at a wafer scale level, which is quite challenging. This thesis attempts to fill this gap in research and presents an innovative way to fabricate suspended graphene membranes on a buried electrode.

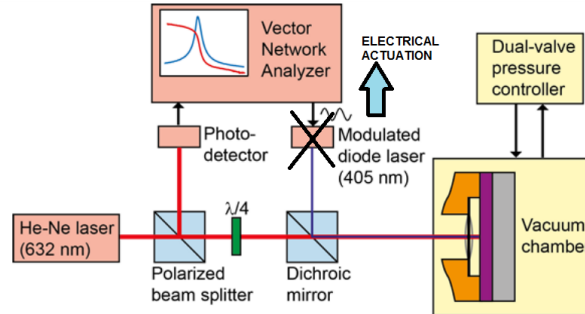


Figure 1.5: Actuation and detection of a graphene resonator. Adapted from [73]

The main objective of this thesis is to fabricate a graphene resonator with a buried electrode. For graphene membranes to be used as a resonator, it should be suspended. Hence, one of the other goals of this project is to study the factors affecting the suspension of the graphene membrane. During research, the following questions are to be answered:

1. What are the different possible shapes and sizes of graphene membrane that can be suspended using wafer scale transfer free approach?
2. What are the different actuating methods which could be used in place of the optical setup to actuate the graphene resonator?
3. How to fabricate an electrostatically actuated graphene resonator?
4. How can technology parameters affect suspension of graphene?

To approach these tasks, a mask design has been created. The mask design has different shapes and sizes of graphene membrane to see which dimensions could be suspended. The analysis and results of the fabricated graphene membranes is described in chapter 4. The mask design also includes structures which use different actuation mechanisms to actuate graphene resonator. These have been described in chapter 3. Various different parameters such as gap sizes, thickness of oxide and different buried metals have been taken into account during fabrication of the electrostatically actuated graphene resonators. The fabrication process of an electrostatically actuated graphene resonator is presented in chapter 6. To use graphene membranes as a resonator, it needs to be fully suspended and so it was necessary to understand the technology factors that affected the suspension of membrane. An, in depth analysis on the suspension of graphene membrane has been done in chapter 7.

## 1.6 Thesis outline

Chapter 1 included the background information and examined state of the art in the field of graphene resonators. It talked about the importance using graphene as a resonator and described the direction of thesis.



Chapter 2 describes the concepts and details related to graphene resonators that would be utilized in analyzing the graphene devices in subsequent chapters. It describes the effects of various parameters on the resonant frequency of a graphene resonator. It also gives an introduction to the various actuation mechanisms of a resonator.

In continuation to the actuation mechanisms described in previous chapter, chapter 3 embodies the design of the graphene resonator and the actuator. The design concepts and parameters taken have been elaborated. Finally the masks layouts have been presented.

Chapter 4 includes fabrication details of suspended graphene membranes along with analysis of the fabricated graphene membranes.

Chapter 5 describes the fabrication process flow of a suspended graphene membrane on a buried electrode. It also incorporates the detailed analysis of the failed attempts before arriving to the final solution.

Chapter 6 describes the setup, experiments and the measurements performed on the graphene resonators.

In chapter 7, the cause of collapse of graphene membranes has been analyzed in detail. This chapter also sheds light on the process of suspension of graphene membrane.

Chapter 8 concludes the thesis work and presents direction for future work.

## 1.7 Summary

This chapter presented the importance of miniaturization of resonators and the benefits of using graphene as a nanoresonator. Graphene and its exceptional mechanical properties have been described. Then, the various substrates that could be used to grow graphene have been presented followed by the various fabrication methods used to suspend graphene. Out of these, the transfer free, wafer scale approach of growing graphene on molybdenum seems most promising and has been integrated with the fabrication process flow of the device being fabricated in this project. Before going to the design of the device, the next chapter describes various factors affecting the resonant frequency of a graphene resonator and the actuation mechanisms of a resonator.

# Chapter 2

## Graphene Resonators

This chapter gives an introduction and background to the various aspects of resonators and then relates them to graphene resonators in particular. These aspects related to graphene resonators have been referred to and used in the subsequent chapters.

### 2.1 Resonant Frequency

At eigenfrequency of mechanical structures such as beams, plates, membranes and strings, the total energy in the system is passed back and forth between kinetic energy of the vibration and potential energy stored in the vibrational deformation of the structure [74]. However, this is an ideal situation. In real world mechanical structures, the total energy in the system does not pass between kinetic energy and potential energy. During each vibration, some energy is lost from this total energy due to various reasons . Hence, a real mechanical structure would vibrate only till the entire energy that was given to the system is lost. It vibrates for a finite amount of time [74]. A mechanical resonator has a suspended part that resonates and anchors to support it. Figure 2.1 show structures of two different types of mechanical resonators, a beam and a cantilever.

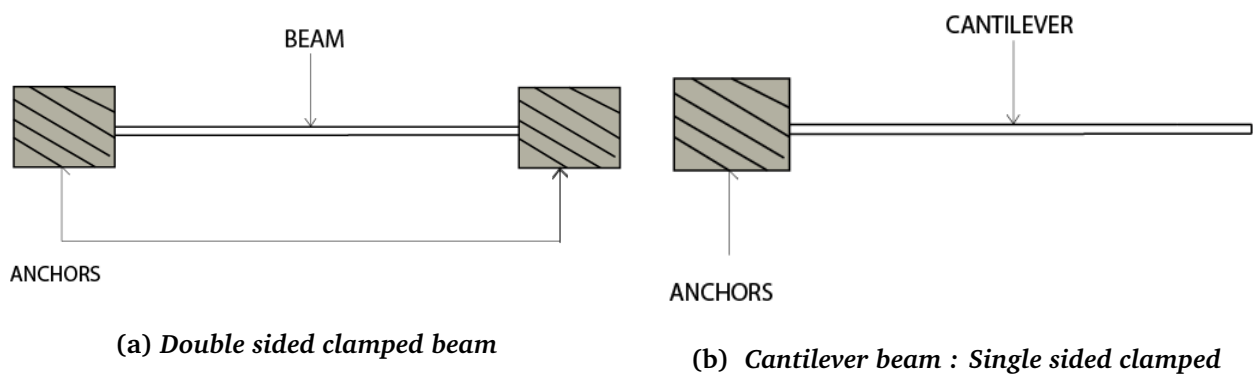


Figure 2.1: Different types of mechanical resonators

The resonant frequency of a mechanical resonator is determined by its geometry, dimensions, material properties of the material used and residual stress. The resonant frequency of a clamped-clamped beam ( $f_{cc}$ ), circular disk ( $f_{cd}$ ) and cantilever beam ( $f_{cb}$ ) is given by equation 2.1, 2.2 and 2.3 respectively [75, 76]. Here, in the equations,  $E$  is the young's modulus,  $\rho$  is the density,  $L$  is the length of the beam,  $D$  is the diameter of the disk and  $h$  is the thickness of the beam.

$$f_{cc} = 1.03\left(\frac{h}{L^2}\right)\left(\sqrt{\frac{E}{\rho}}\right) \quad (2.1)$$

$$f_{cd} = 1.65\left(\frac{h}{D^2}\right)\left(\sqrt{\frac{E}{\rho}}\right) \quad (2.2)$$

$$f_{cb} = 0.162\left(\frac{h}{L^2}\right)\left(\sqrt{\frac{E}{\rho}}\right) \quad (2.3)$$

For the graphene resonators, subsequent sections will discuss the impact of various factors on the resonant frequency.

### 2.1.1 Tension and Bending stiffness

The resonant frequency of a clamped beam which has tension and bending stiffness is given by equation 2.4 [77]. Here E is the young's modulus, t is the thickness of the beam,  $\rho$  is the density of the resonator material, L is the length of the beam, T is the tension and m is the mass of the beam.

$$f = 1.03\sqrt{\frac{Et^2}{\rho L^4} + \frac{T}{3.4mL}} \quad (2.4)$$

Tension and bending stiffness, both play an important role in determining resonant frequency of a vibrating structure. A plate is bending rigidity dominated whereas a membrane is tension dominated. A membrane has no out of plane stiffness and so it can be bent easily . On the other hand, a plate has no in plane stiffness and so it cannot bear any horizontal load. A shell has both in plane and out of plane stiffness. Few layer graphene membranes behave more like a shell since they have both tension and bending rigidity playing a role in determining their resonant frequency. In order to make the analysis simple, it is important to determine if one of these terms (tension or bending stiffness) is dominant so that the other term can be neglected.

In the past , it has been found that graphene resonators made of exfoliated graphene is in tension and this tension is process dependent. The value of this tensile strain is found to be in the range  $10^{-5}$  to  $10^{-4}$ . Various researchers have used different experimental techniques. According to Bunch [8], the tension in the graphene resonators arise due to the fabrication process which causes a strain of  $2 \times 10^{-5}$ . In his work, he states that it is during mechanical exfoliation that the friction between graphite and oxide surface stretches the graphene membrane across the trench [8]. In [15] , the graphene resonator is considered as a membrane with zero bending stiffness and the strain reported is in the  $10^{-4}$  range. This strain decreases to  $10^{-5}$  after annealing process to remove adsorbates. Frank [66] reported a tension of 300nN in suspended graphene sheets of different thicknesses which were not single layer using force microscopy. Lee [21] determined the pre-strain in the range from mid  $10^{-5}$  to mid  $10^{-4}$  using force microscopy. However, all the above mentioned results are for mechanically exfoliated graphene membranes. According to our knowdege, no results have been reported for tension measurements of CVD grown graphene in literature so far.

Figure 2.2, shows a plot of resonant frequency versus strain for clamped graphene beams of two different lengths ( $1\mu\text{m}$  and  $10\mu\text{m}$ ). It shows the range of strain values for which the resonant frequency is dominated by bending force and tension. The strain values reported from the literature [8, 15, 21] are also marked in this figure . From the figure 2.2, it can be seen that for shorter clamped graphene beams, the tension starts to dominate the resonant frequency at a higher strain values as compared to longer clamped graphene beams [30].

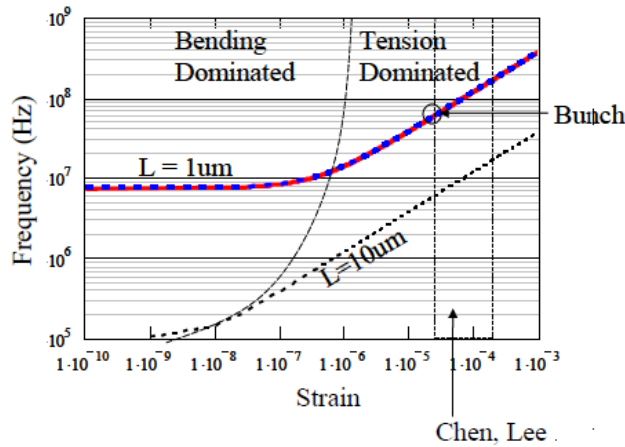


Figure 2.2: Deflection of rectangular, square and circular shaped graphene sheets vs number of layers of graphene sheets. Taken from [78]

Bending rigidity is an important parameter that is needed to predict the linearity of graphene resonator and also describe the formation of ripples on graphene [79]. In the past, this parameter has been estimated from AFM measurements [80] and by electrostatically actuating pre buckled graphene membranes [81]. However, since graphene membrane is tension dominated, most of the times its bending rigidity can be ignored.

### 2.1.2 Effect Of Temperature

It is important to study the temperature effects on resonant frequency of a graphene resonator. It has been seen that the resonant frequency of the suspended graphene electromechanical resonator increases as it is cooled from room temperature [69], as shown in figure 2.3. This change in the frequency with temperature is attributed to the expansion/contraction of gold electrodes, the suspended graphene membrane and the substrate.

In the past, a lot of research has been done to extract the thermal expansion of monolayer graphene. The thermal expansion coefficient of graphene is reported to be negative at low temperatures due to the presence of the flexural modes (out of plane modes). [69, 82–89]

This means that graphene would expand on cooling to these temperatures whereas a material with positive expansion of coefficient would contract. However, unlike other materials, many properties in graphene change with the way it is grown and the various parameters such as temperature, amount of gas used, rate of cooling etc., used during its growth.

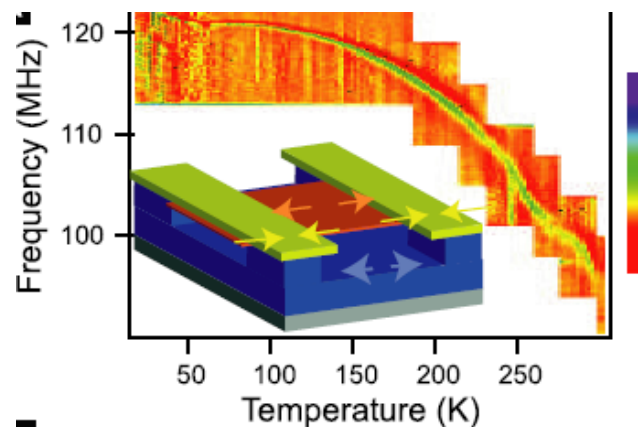


Figure 2.3: Plot of resonant frequency vs temperature for DC gate voltage of 15V. The arrows indicate the external strain in suspended membranes. Taken from [69]

### 2.1.3 Non Linearity

It is important to understand effects of nonlinear damping a on nanoscale resonators such as graphene since this can have an impact on its performance and motion (amplitude and velocity).

Equation for a harmonic oscillator is given by equation 2.5[90, 91]. Derivation of equation this equation can be found in [90]

$$m \frac{d^2x}{dt^2} = -kx - \gamma \frac{dx}{dt} - \alpha x^3 - \eta x^2 dx/dt + F_{\text{drive}} \cos(2\pi ft) \quad (2.5)$$

At large amplitude of vibration, an additional term  $\alpha x^3$ , where  $\alpha$  is the duffing parameter (nonlinear spring constant), enters the equation of motion of a resonator. This makes the restoring force nonlinear. Two effects which bring about  $\alpha$  [7] are:

1. Tension in the membrane, that stretches it, gives positive contribution to  $\alpha$ . This positive  $\alpha$  leads to increase in frequency with higher driving powers.
2. Nonlinear terms in the capacitive electrostatic force give negative contribution to  $\alpha$  which leads to decreasing frequency .

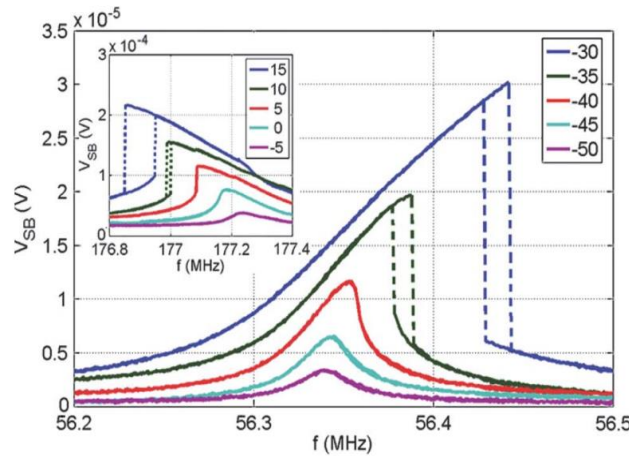


**Figure 2.4: Duffing nonlinear behaviour of doubly clamped graphene resonator, positive nonlinear spring constant and negative(inset) nonlinear spring constant. Taken from [92]**

Both the above mentioned non linearities have been shown in graphene resonators in the past [92], shown in figure 2.4. The other nonlinearity occurs due to the term  $\eta x^2 dx/dt$ , where  $\eta$  is called the non linear damping coefficient. Non linear damping leads to widening of resonance linewidth, when  $\alpha$  is small or close to zero. This means that the quality factor reduces due to non linear damping. So, in order to achieve high quality factor, non linear damping has to be reduced. The highest quality factor for a graphene resonator (100,000), till date, has been achieved by Eichler et al.[93].

The amplitude of the resonator at the start of the non linearity is denoted by  $\alpha_c$ .  $\alpha_c$  is very useful as it determines the dynamic range of a resonator. Equation 2.6 [94] shows the relation between  $\alpha_c$ , quality factor(Q) and strain( $\epsilon$ ). This relation shows that the dynamic range of the resonator will increase with increasing strain values but decrease with increasing quality factor. Hence, in order to understand the performance of graphene resonators, it is important to know the relation between Q and  $\epsilon$

$$|\alpha_c| = 0.98 \sqrt{\frac{\epsilon}{Q}} \quad (2.6)$$

Another important point to be noted is that all the above experiments were performed at low temperatures which helps to reduce thermal noise. But in this work, the experiments will be performed at room temperature which makes it more challenging.

## 2.2 Actuation of mechanical motion of a resonator

Continuous actuation and detection of a resonator is essential to monitor its resonant frequency continuously. The transduction of mechanical motion of a resonator to electrical signal and vice versa is quintessential for detection and actuation respectively. In the past graphene resonators have been actuated electrically [8] and optically [8, 25]. The resonant frequency of the graphene resonator has been detected optically [8, 25]. Some of the commonly used techniques to actuate [74, 95] the mechanical motion of a resonator are given below:

- Magnetic actuation
- Electrostatic actuation
- Thermal actuation
- Piezoelectric actuation
- Piezoresistive actuation
- Optic actuation

The following sections will discuss the three important actuation methods namely electrothermal, electrostatic and magnetic actuation, using which the design of the device has taken place in the next chapter.

### 2.2.1 Magnetic actuation

This technique of actuation is based on the use of Lorentz force that acts on a current carrying conductor placed in a uniform magnetic field and allows for actuation of frequencies upto GHz range [96]. The Lorentz force acting on an electric charge with charge  $q$  moving with velocity vector  $v$  in a uniform magnetic field  $B$  is given by equation 2.7 [74].

$$F = qv \times B \quad (2.7)$$

The electric current running in a wire of length  $L$  is given in equation 2.8. Here,  $n$  represents the total number of charges [74].

$$I = \frac{nqv}{L} \quad (2.8)$$

Using equation 2.7 and 2.8, we can get the total magnetic force (equation 2.9) [74] acting on a wire of length  $L$  which is carrying current  $I$  and is placed in a uniform magnetic field  $B$ . This Lorentz force can actuate a doubly clamped beam as shown in figure 2.5.

$$F = IL \times B \quad (2.9)$$

If an AC current is passed through the conductor, then the current is a function of frequency and so the Lorentz force generated by keeping such a conductor in a magnetic field, is also a function of frequency. However, the problem with using magnetic actuation is that it requires very strong magnetic fields for which superconducting coils have to be used. It becomes difficult to integrate these superconducting coils with the device since there are only some materials such as Nb<sub>3</sub>Sn, Nb-Ti, V<sub>3</sub>Ga [97] that can be used as superconducting coils.

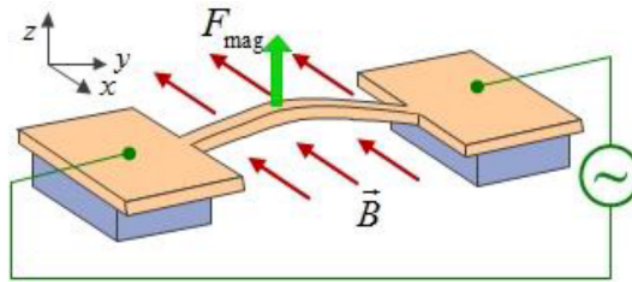


Figure 2.5: Magnetic actuation of a doubly clamped resonator. Taken from [3]

### 2.2.2 Electrostatic actuation

Electrostatic actuation and detection technique is commonly used in accelerometers, pressure sensors, mirror arrays, gyroscopes and smaller nanomechanical resonators. It is a commonly used technique since it requires low power consumption and is easy to integrate. Figure 2.6 shows a model of an electrostatic actuator. The movable suspended electrode is generally grounded and the fixed electrode is electrically biased to the same potential as the substrate. It is because the movable electrode is grounded and the nature of Coulomb force, electrostatic force is always attractive in this case. This attractive force is given by equation 2.10. Here,  $A$  is the area of the electrode,  $V$  is the potential difference applied between the plates,  $\epsilon$  is the permittivity of the dielectric medium,  $g$  is the gap between the capacitor plates and  $x$  is the distance moved by the plate. When voltage is applied between the two plates, the electrostatic attractive force moves the movable electrode towards it to increase the capacitance. This deflection takes place until an equilibrium is attained between the restoring force and electrostatic force.

$$F = \frac{1}{2} \epsilon V^2 \frac{A}{(g-x)^2} \quad (2.10)$$

Electrostatic actuation is simple and so widely used but it has some issues attached to it. Some of the issues associated with electrostatic force are the pull in effect and that the electrostatic force is non linear.

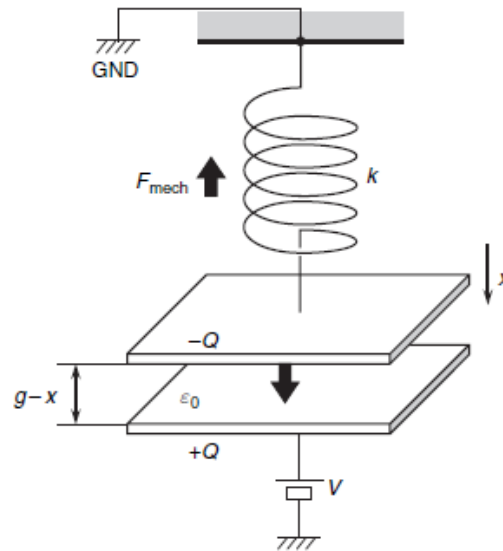


Figure 2.6: *Electrostatic actuator model with a mechanical force*

### 2.2.3 Electrothermal actuation

In electrothermal actuation, current is passed through the conductor which can be placed on top of the surface to be actuated or the current can be passing through the surface itself if the surface is a conductor. This current heats up the conductor and mechanically strains it, thereby actuating it. When current is passed through a bimetal (two metals which have different thermal expansion coefficients), due to joule heating, the metals are heated but deform differently because of the different thermal expansion coefficients. This creates an out of plane deflection and has been shown in figure 2.7. Unlike electrostatic actuation, electrothermal actuation does not require high actuation voltages. However, the issue with electrothermal actuation is that it leads to high power dissipation. Also, it has a much slower response.

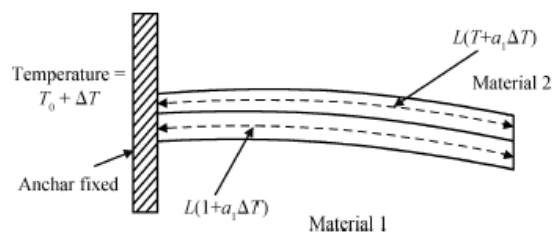


Figure 1. Bimetal film structure.

Figure 2.7: *Strain in bimetal structure due to difference in thermal expansion of coefficients of the two different materials. Taken from [98]*

### 2.2.4 Comparison of actuation principles

Table 2.1 compares the three actuation mechanisms described above.



**Table 2.1: Comparison of different actuation methods. Taken from [3, 95]**

Actuation technique	Required voltages	Required current values	Required Power values	Fabrication process
Electrothermal	Low	High	High	Simple
Electrostatic	High	Low	Low	Medium
Magnetic	Low	Medium	Medium	Complex

Although electrothermal actuation is much simpler than the other two actuation principles as far as fabrication and the simplicity of the method is concerned but it has various other issues. Since high values of current are required to electrothermally actuate a device, lot of heat is generated which leads to cooling problems in the device [95]. For electronic devices, heating due to large values of current can be a major concern. As far as magnetic actuation is concerned, the fabrication of superconductor coils needed in it becomes very complex. In comparison to the other two actuation mechanisms, electrostatic actuation seems to be a better option. Neither it is very complex as far as the fabrication is concerned nor does it require large current values. Hence, finally this method is chosen to actuate the graphene resonator.

The next section presents squeeze film effect seen in graphene resonators which changes its resonant frequency and makes it a potential use as a pressure sensor.

### 2.2.5 Squeeze Film effect

Squeeze film pressure sensors work on the principle of compressing the gas in the cavity which is at ambient pressure. When this compression takes place at high frequency, the gas is not able to move out of its place because of viscous forces [99]. It is because of this compression of gas, there is an added stiffness component, as shown in equation 2.11, which is a function of pressure. The resonator's resonance frequency  $f_r$  changes according to equation (1) [25] for isothermal compression.

$$f_r^2 = f_0^2 + \frac{p_{amb}}{4\pi^2 g \rho h} \quad (2.11)$$

Here,  $f_0$  is the resonance frequency at vacuum,  $g$  is the gap size between the membrane and the substrate that lies below the membrane and  $\rho h$  is the mass per unit square. In these graphene based squeeze film pressure sensors, an open venting channel (see figure 2.8) maintains the average pressure inside the cavity equal to ambient pressure [25]. It is because of this open venting channel that there is no need of an impermeable reference cavity.

As shown in figure 2.8, a plate moving normally to the surface squeezes the air between itself and the substrate, which in turn causes lateral flow of air. The viscous flow of air changes the pressure in the gap between the plate and the substrate. The force due to the pressure acts against the motion of the moving plate. In this way, the air behaves like a damper. This process is known as the squeeze film damping [100]. Squeeze film damping is dominant for structures where the thickness of the air gap is much smaller than the lateral dimensions of the structures.

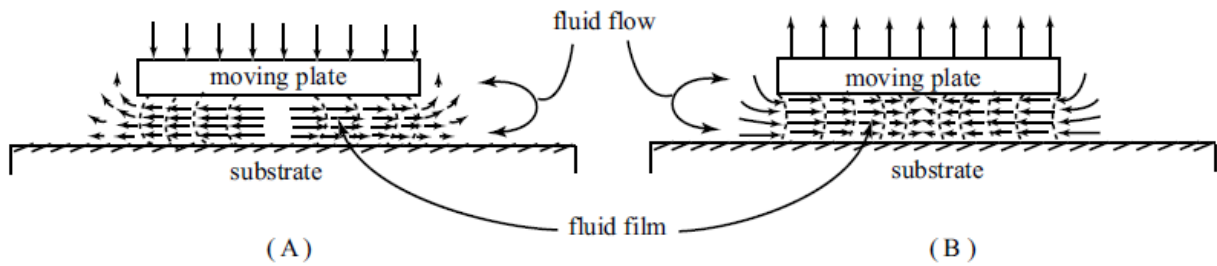


**Figure 2.8:** *Diagram of squeeze film flow. A) Downward normal motion B) Upward normal motion. Taken from [101]*

Griffin [102] and Blech [103], in their work, have presented calculations models that are only applicable to oscillations with small amplitude. Their work shows that at low frequencies, the damping effect of air film dominates whereas at higher frequencies, the spring effect is dominant. At a high frequency, the number of oscillations of the membrane are so high that there is not enough time for the air film beneath it to move and so it is squeezed which is called as the squeeze film effect. Squeeze film effect in graphene membranes has been shown in [25].

## 2.3 Summary

This chapter discussed the various factors that affect the resonant frequency of a graphene resonator. Also, the various actuation mechanisms were discussed. Due to simplicity in fabrication of an electrostatic actuator and no heating issues, electrostatic actuation is chosen to drive the graphene resonator in this work. The design of the this electrostatic actuator will be discussed in the next chapter.

# Chapter 3

## Design of the device

To fabricate devices, both design and technology factors have to be taken into account. Sometimes a trade-off has to be made between the design and the technology factors. Hence, it is important to discuss both these factors together. This chapter explains both the design and technology factors taken into account for the graphene devices and the actuator. The technology factors will also be elaborated in chapter 4 and 5. This chapter will elaborate on the electrostatic actuation of graphene membranes. It also discusses the designing of various other structures on the mask. Finally the masks layout of the structures fabricated are given.

### 3.1 Design of the graphene resonator

This section gives a schematic representation of different types of graphene resonators that were fabricated and the mask designs which were used to fabricate them. To fabricate these devices, two layers in the mask are used. In the mask design, red colour denotes the molybdenum layer which is used to grow graphene and yellow denotes the gold layer. The main aim of making different shapes and sizes for the graphene membrane was to study which one of them could be suspended. It is also to see if shape and size have any influence on suspension.

As described in the previous chapters, a resonator should have a suspended part and anchors to support it. Our graphene resonators have three regions, the suspended graphene membrane, the overlap region between graphene and gold and the only gold region. Hence, the graphene resonator, in our case, is a coupled structure with suspended gold and suspended graphene part. This is because when molybdenum is removed underneath the graphene membrane for suspension of the membrane, the molybdenum underneath the overlap region of gold and graphene is also removed and therefore that part of gold is also suspended. This step will be explained in the next chapter in detail. One of the commonly used shapes for a membrane is the rectangular shape. Two basic structures used as rectangular shaped graphene resonators are shown in figure 3.1. These two basic structures, namely bar shape structures and Hbar structures were drawn with all possible combinations of lengths and widths ranging from 1 to 10  $\mu\text{m}$ . The graphene membrane has been shown as flat in these 3D representation but in the real case it is not flat, as will be described in the coming chapters. Also, for the actual device, the transition from gold to graphene would not be so steep as shown in the schematic. The Hbar structure has a bigger overlap region with gold as compared to the bar shaped structure. This was done so that the graphene has more mechanical support from the anchors and it becomes easy for it to be suspended. The length of the overlap region is 4  $\mu\text{m}$  and the width of the overlap region is equal to the width of the suspended graphene membrane for the bar shaped structures, and it is equal to the width of the suspended graphene + 8  $\mu\text{m}$  for the Hbar structures

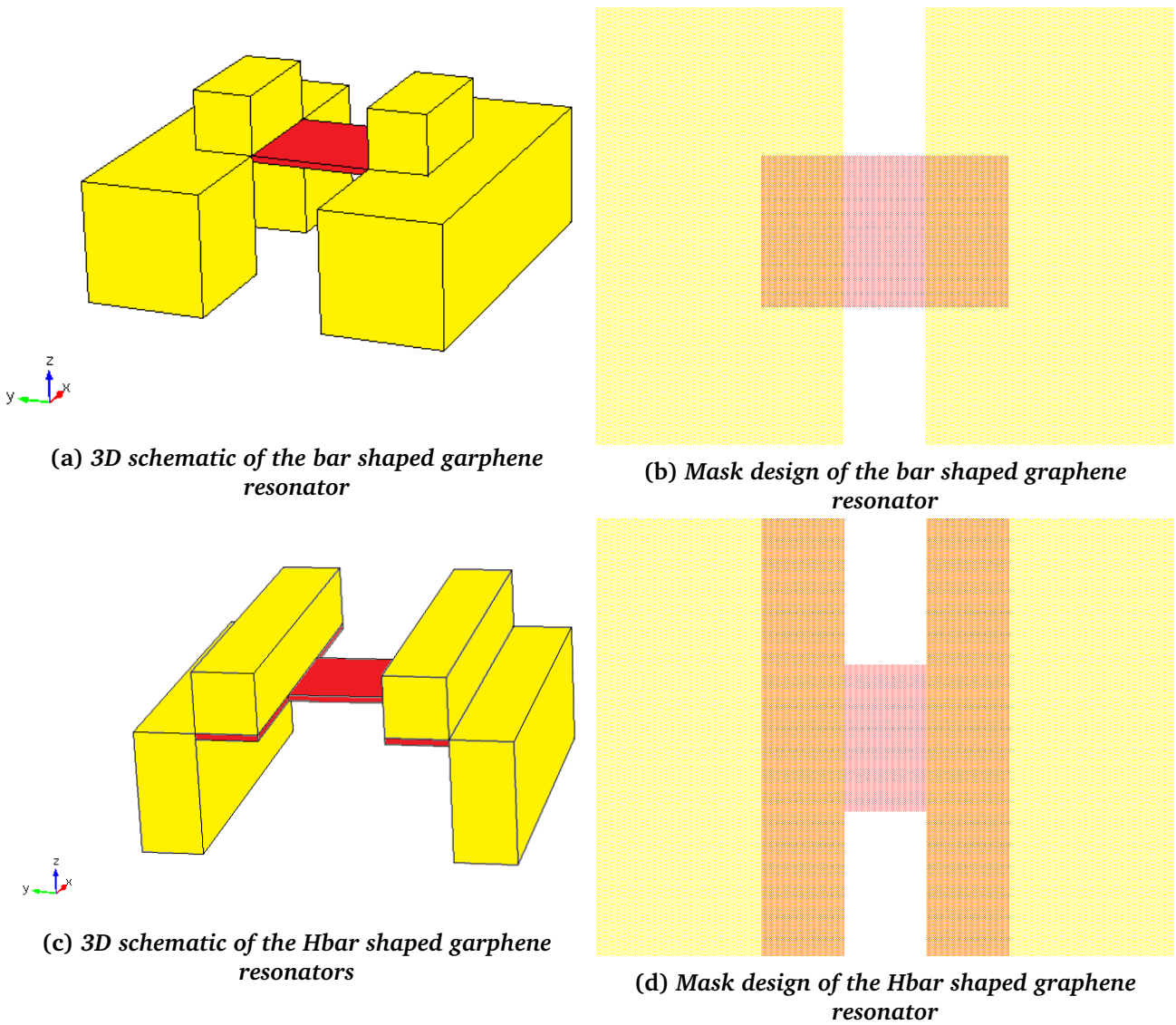


**Figure 3.1:** 3D representation of the graphene resonators along with their mask designs. Red: Suspended graphene membrane. Yellow: Gold metal

The technology factor that plays an important role in fabrication of a graphene resonator is its gap size, see figure 3.2. Since graphene is grown on molybdenum and then this molybdenum is etched away for it to become suspended, this gap size is determined by the thickness of the molybdenum. This fabrication step will be described in the next chapter. In the past, graphene membranes were shown to be suspended on 100 nm and 200 nm gap size [73]. For very small gap sizes, we cannot predict if graphene would be suspended or not since suspended graphene has height variations. We expect these variations to be larger for the multilayer graphene used in our case and if the gap size is very small, the membrane could already be touching the substrate. However, a smaller gap size would help in miniaturization and would allow this resonator to be used for various applications such as a squeeze film pressure sensor. The smaller the gap size, the better the squeeze film effect. Hence, an ideal gap size for our case will be in the order of nanometers on which the complete graphene membrane is suspended. Gap sizes ranging from 25 nm to 200 nm have been used for the fabrication of graphene resonators.

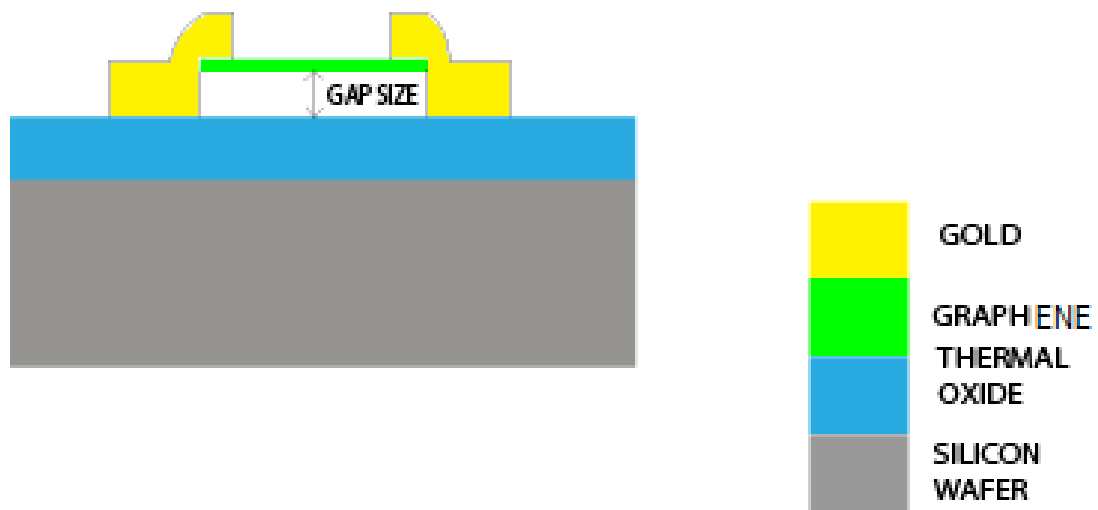


Figure 3.2: Cross sectional view of a graphene resonator

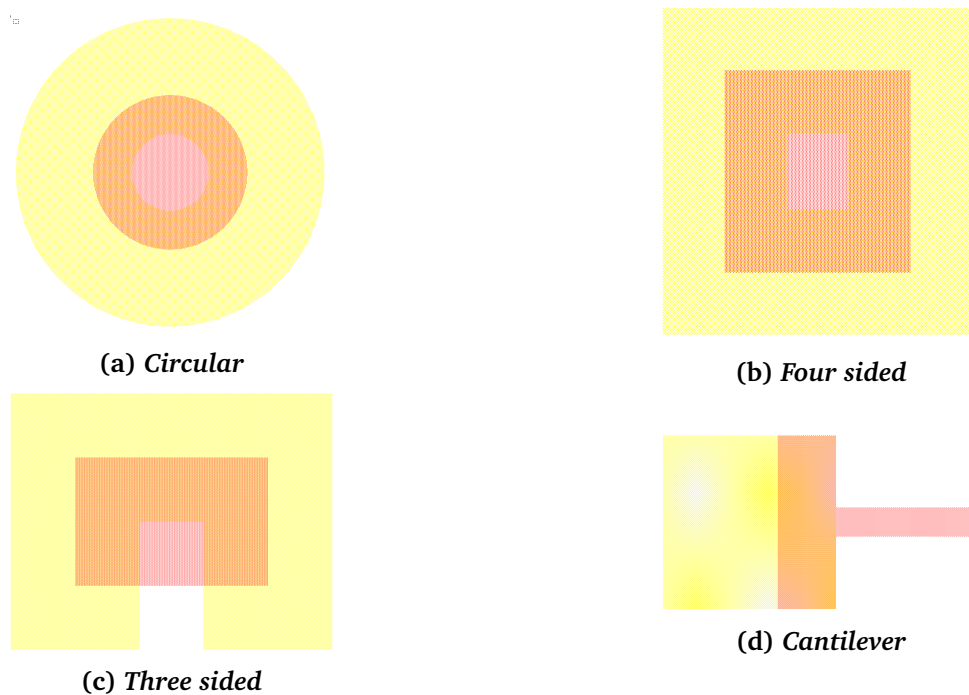


Figure 3.3: Other graphene resonators. Red: Suspended graphene Yellow: Gold metal

Some other geometries such as circular graphene resonators are shown in figure 3.3a were also included with the radius of the suspended graphene membrane ranging from  $1 \mu\text{m}$  to  $10 \mu\text{m}$ . Clamping conditions play a pivotal role in determining the resonant frequency of the

resonator. Therefore, graphene resonators clamped from all four sides, clamped from three sides and graphene cantilevers clamped from one end were also designed. Figure 3.3 shows their mask layouts.

### 3.2 Design of the electrostatically actuated graphene resonator

In order to actuate the above discussed graphene resonator electrostatically, the graphene resonator has to be integrated with a buried electrode metal. In electrostatic actuation, two electrodes are required out of which one acts as an actuated element. In our case, a buried metal layer is used as one of the static element and the graphene membrane as the second actuated element as shown in figure 3.4. An AC signal between the electrodes sets up an electrostatic force that drives the device into motion. This actuation electrode is separated from the graphene resonator with a dielectric, which in our case is the PECVD oxide. To fabricate the electrostatic devices, four layers are required in the mask. These are the buried metal (denoted by blue colour), molybdenum (for growth of graphene, denoted by red colour), contact openings (denoted by black colour) and gold (denoted by yellow colour). The complete mask design of the electrostatic actuator is given in figure 3.5

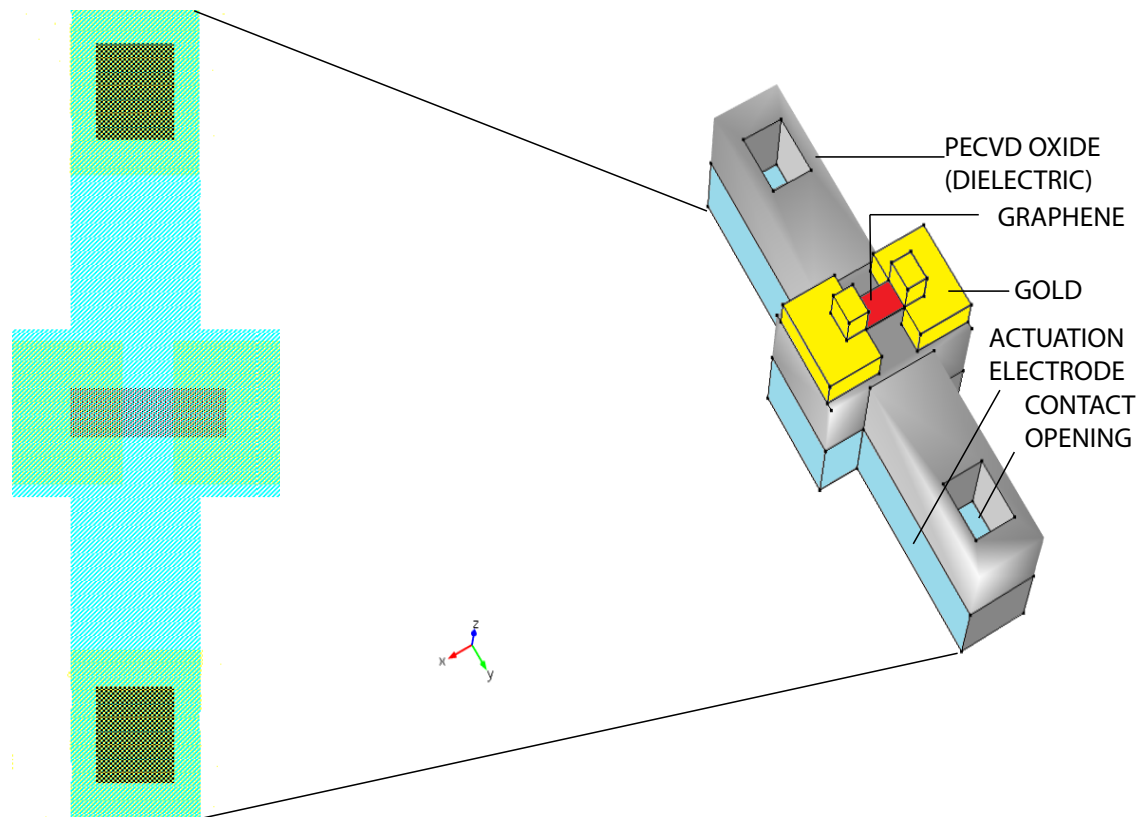


**Figure 3.4:** Mask design and 3D schematic representation of the graphene electrostatic capacitor. The gold bond pads on the contact opening have not been shown in the 3D schematic model

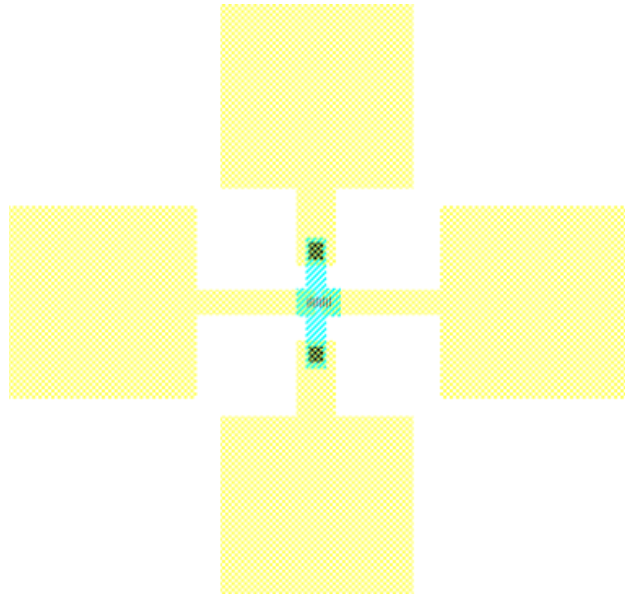


**Figure 3.5: Complete mask design of an electrostatically actuated graphene resonator with gold bond pads. Blue: actuation electrode, Red: graphene membrane, Black: contact openings, Yellow: gold metal**

The important factors to be considered while designing the electrostatic actuator are given as follows

1. The area of the electrodes

The area of the bottom electrode should be minimized in order to avoid the parasitic capacitances. As can be seen from figure 3.6, a larger electrode area will give additional capacitances as parasitic capacitance will exist between the buried metal and gold. These parasitic capacitances can pose problems such as block low frequency signals and it can add to the main capacitance value to give unnecessarily large output capacitances. However, this electrode area cannot be made very small as it will give step coverage problems during fabrication of the actuator. The oxide on top of the actuation electrode decreases slowly at its edges. If the electrode is made very small, the graphene membrane on top of the oxide would follow the morphology of the oxide and would not be flat anymore. Hence, a trade off has to be made between reducing the parasitic capacitances and getting a good step coverage for the buried metal. Therefore, the area of the actuation electrode was made bigger than the graphene resonator with each side of the resonator extended by  $4 \mu\text{m}$  from the graphene resonator.

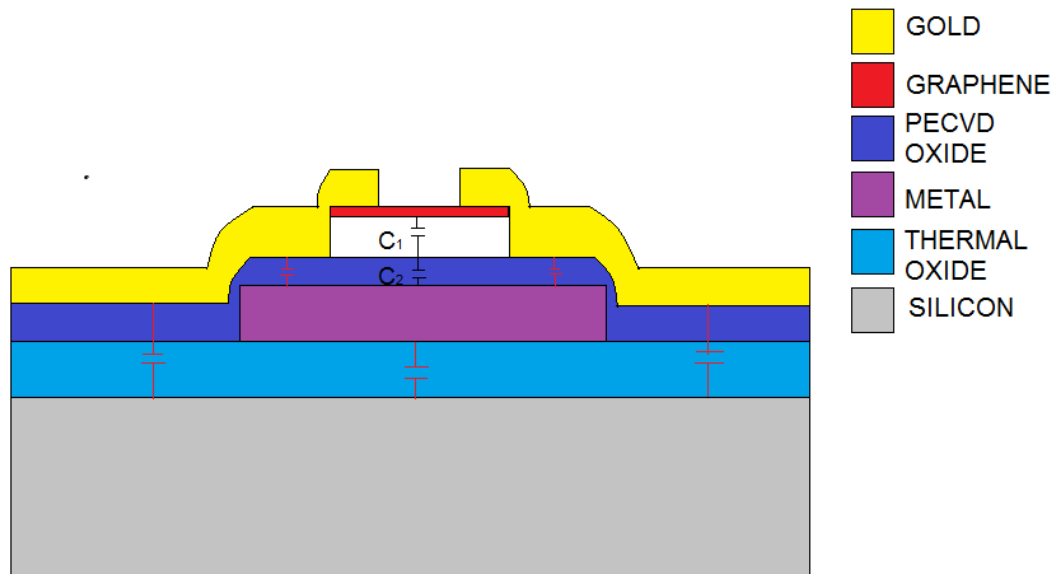


**Figure 3.6:** Cross sectional view (Horizontal cross section of the figure 3.5) of an electrostatically actuated graphene resonator. Red coloured capacitances are the stray capacitances

## 2. Thickness of the dielectric (PECVD oxide)

The thickness of the dielectric has a major influence on the the capacitance of the device. Using thinner oxide will give rise to larger capacitance values. A larger capacitance value would mean a smaller potential would be required to actuate the device. However, a thinner PECVD oxide such as lower than 100nm will have quality issues because of pinholes and leakage. Hence a medium thickness of oxide should be chosen. The thickness of this dielectric is taken in the range of 100nm to 300nm.

## 3. Thickness of thermal oxide

Thermal oxide is grown everywhere on the bare silicon wafer and the buried metal is deposited on this thermal oxide . A parasitic capacitance exists between the buried electrode and the silicon (see figure 3.6). The thickness of the thermal oxide should be increased if the effect of this parasitic capacitance has to be reduced. In the past graphene membranes are shown to be suspended on 90 nm thermal oxide [73]. Choosing a oxide thicker than 90 nm may cause some processing problems such as issues in suspension of graphene. Again a trade- off has to be made between reducing the parasitic capacitance and keeping a thinner oxide. The influence of thickness of the oxide on suspension is discussed in chapter 7

## 4. Gap size

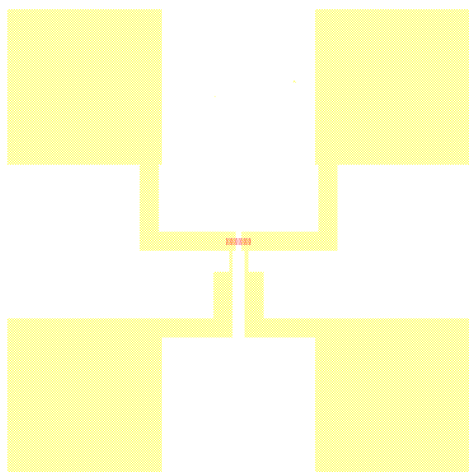
The effects of the gap size on the graphene resonator have been discussed in the previous section. This gap size of the graphene resonator affects the total capacitance of the actuator since it is in series with the capacitance of the dielectric (see figure 3.6). Various combinations of the gap size and the dielectric size can be considered for fabricating the graphene electrostatic actuator.



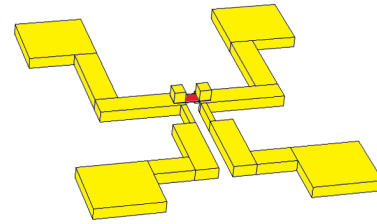
### 5. Choice of metal to be used as buried electrode

The choice of the metal is also very crucial in designing the actuator. Each metal has a different residual stress that can affect suspension of the graphene membrane. This selection of metal will be elaborated in chapter 5.

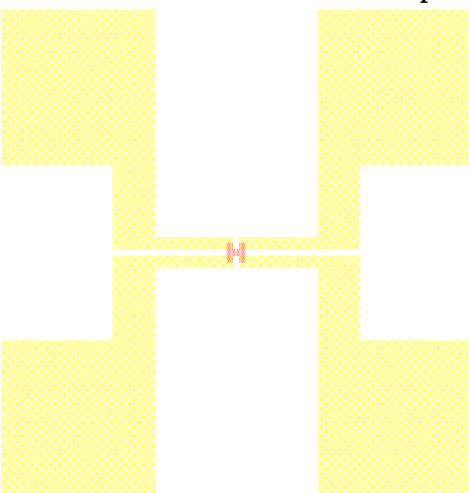
The other structures that can be used as electrostatically actuated graphene resonators, the bar shaped and Hbar shaped graphene resonators with bond pads are given in figure 3.7. Here the static electrode is the back gate silicon and the moving electrode is the suspended graphene and gold. The problem with having silicon as the back gate is that it gives a very high parasitic capacitance because silicon has a much larger area. Hence the earlier discussed design of an electrostatic actuator with localized metal electrode is much better since it gives less parasitic capacitances as compared to the structures given in figure 3.7. Structure given in, figures 3.7 (a) and (b), have also been used to measure contact resistances in chapter 6. These structures can also be used for electrothermal actuation of graphene resonators.



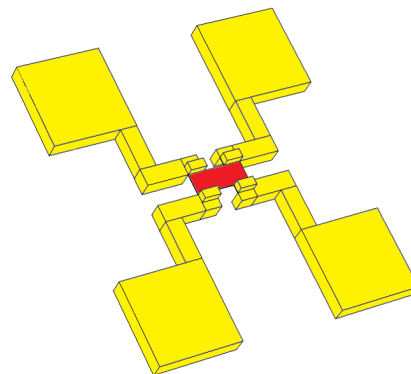
(a) Mask design of the bar shaped graphene resonator with bond pads



(b) 3D representation of the bar shaped graphene resonator with bond pads



(c) Mask design of the Hbar shaped graphene resonator with bond pads



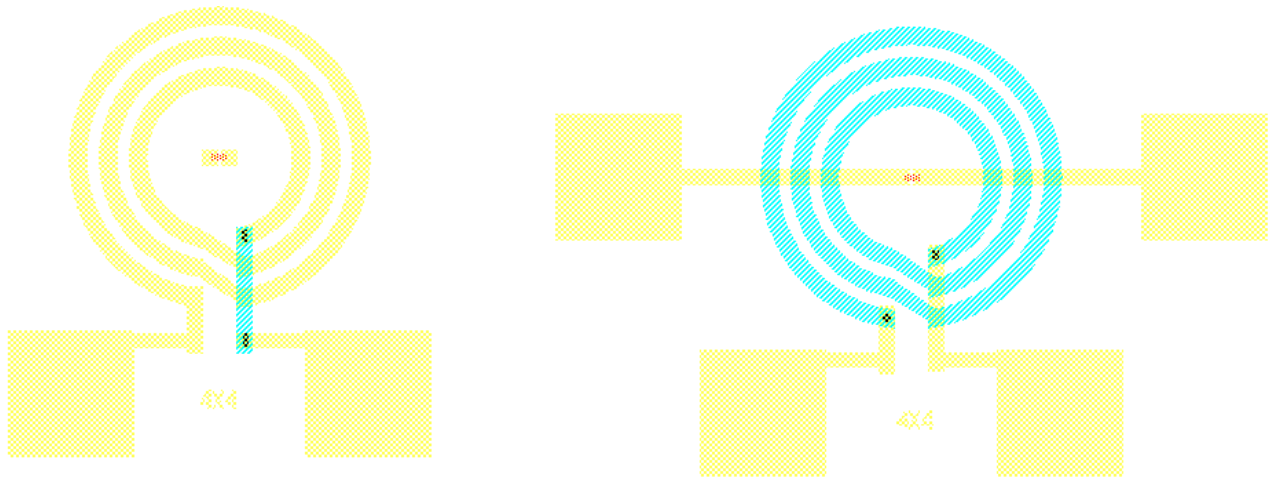
(d) 3D representation of the Hbar shaped graphene resonator with bond pads

Figure 3.7: Other structures which can be used as electrostatic actuators

### 3.3 Design of other structures

This section will present some new ideas for the graphene resonators that were incorporated in the mask design.

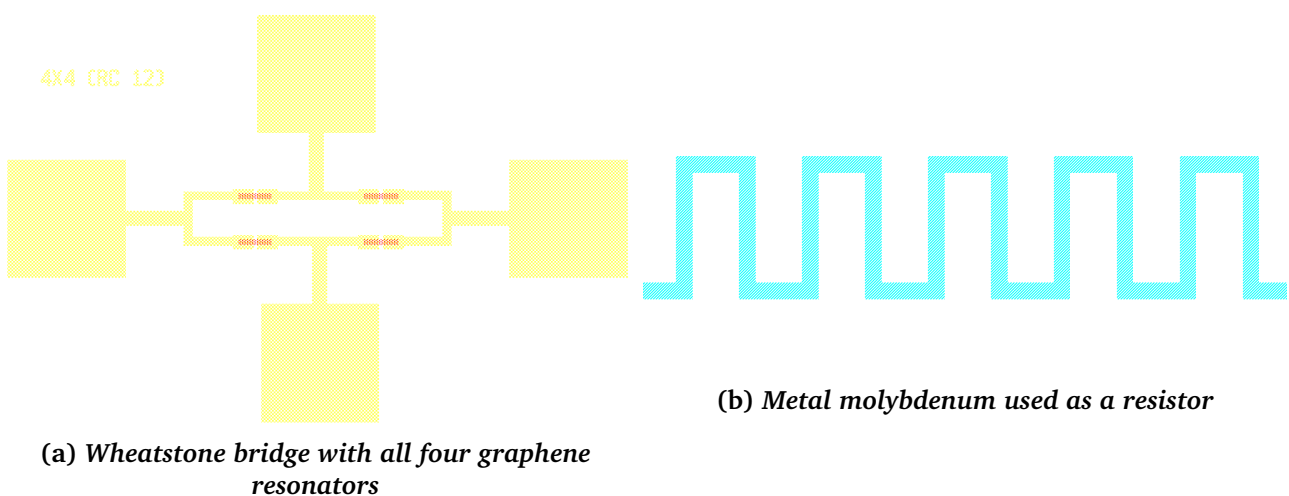
#### 3.3.1 Magnetic Actuators



**Figure 3.8:** The mask design of a magnetically actuated rectangular graphene membrane. Yellow: gold, Red: graphene, Blue: buried metal

Two different ways, the graphene resonators can be actuated magnetically. One of them is an AC current passing through the graphene membrane which is positioned into an external static magnetic field. Hence, a Lorentz force acts on the graphene membrane, thereby actuating it. The other one uses an alternating field from spiral coils (made of gold or another metal) (see figure 3.8) to drive the ferromagnetic nanoparticles which can be deposited on the graphene membrane which can actuate the membrane [104].

#### 3.3.2 Wheatstone Bridge



(a) Wheatstone bridge with all four graphene resonators

(b) Metal molybdenum used as a resistor

**Figure 3.9:** Mask design for Wheatstone bridge configuration. Yellow: gold, Red: graphene, Blue: buried metal

A Wheatstone bridge configuration can be fabricated from the graphene resonators [39]. These configurations were designed using two different approaches. One of them is shown in figure 3.9a. In this configuration four graphene resonators are connected in a Wheatstone bridge configuration. One of the resonators can be actuated using a laser light which changes its resistance and hence the output voltage. The second approach uses the graphene resonator as one of the resistors and the other three resistors are made of molybdenum metal. Each box of molybdenum of length and width  $1\mu\text{m}$  are connected together to form a twisted tube shaped molybdenum metal resistor as shown in figure 3.9b. The molybdenum metal is designed in a way such that its resistance becomes equal to the resistance of suspended graphene membrane. However, the problem with it is that it will work only if during fabrication, the buried metal used is molybdenum. Some other metal will only work if its sheet resistance is equal to that of molybdenum. Calculations for this are given below.

The relation of sheet resistance ( $R_s$ ) and the number of squares (N) with resistance is given in equation 3.1. For graphene membrane the sheet resistance is  $900\ \Omega/\text{square}$  and for one square, the resistance value becomes  $900\ \Omega$ . For molybdenum, the sheet resistance value is calculated using equation 3.2 and the calculation is shown in equation 3.3. In equation 3.2  $\rho$  is the resistivity of molybdenum and  $t$  is the thickness of molybdenum. For molybdenum metal, the corners give  $0.56\ \Omega/\text{square}$  sheet resistance. So, using equation 3.1, the resistance value is calculated for molybdenum in equation 3.4 for 802 squares of molybdenum and 159 corner squares of molybdenum. Equation 3.5 shows that the calculated resistance value of graphene membrane and molybdenum are almost equal.

$$R = R_s \times N \quad (3.1)$$

$$R_s = \frac{\rho}{t} \quad (3.2)$$

$$10.1\mu\Omega\text{cm}/100\text{nm} = 1.01\Omega/\text{square} \quad (3.3)$$

$$R = 1.01 \times [802 + 0.56 \times 159] = 899.9504\Omega \quad (3.4)$$

$$900\Omega \approx 899.9504\Omega \quad (3.5)$$

### 3.3.3 Gold Graphene Resonator

In this device, given in figure 3.10, the gold is suspended with the help of graphene. Gold is on top of graphene and when graphene is suspended, the gold should also suspend on top of graphene. There is also a buried metal electrode which can be used as the actuation electrode.

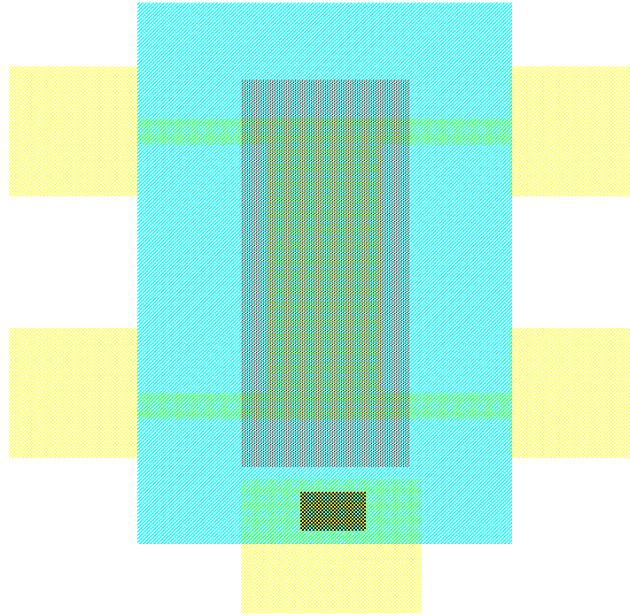


**Figure 3.10:** Mask design of a gold graphene resonator. Yellow: Gold metal Red: Graphene, Blue: Buried metal molybdenum

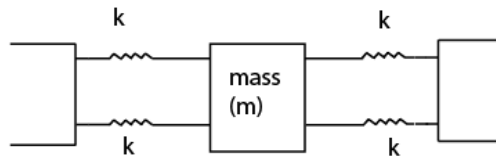


**Figure 3.11:** Equivalent mechanical diagram of the gold graphene resonator

The stiffness of a single cantilever is given by equation 3.6, where  $E$  is the young's modulus of gold,  $W$  is the width of the gold spring,  $t$  is the thickness of the gold spring and  $L$  is the length of the gold spring.. Since, we have four springs attached to the mass, the spring constant in our case will be  $4k$ . The mass of the gold resonator can be calculated from equation 3.7, where  $\rho$  is the density of gold,  $A$  is the area of the gold mass and  $t$  is the thickness of gold mass which is the same as the thickness of the gold spring. Equation 3.8 gives the resonant frequency for gold graphene resonator. Using equations 3.6 and 3.7 in equation 3.8, we get equation 3.9.

$$k = \frac{EWt^3}{4L^3} \quad (3.6)$$

$$m = \rho At \quad (3.7)$$

$$f = \frac{1}{2\pi} \sqrt{\frac{4k}{m}} \quad (3.8)$$

$$f = \frac{1}{2\pi} \sqrt{\frac{EWt^2}{\rho AL^3}} \quad (3.9)$$

Using  $f=100\text{kHz}$ ,  $E=79\text{GPa}$ ,  $\rho=19320\text{ kg/m}^3$ ,  $t=100\text{nm}$ , equation 3.10 is obtained. Now, values of  $A$ ,  $L$  and  $W$  can be optimized for the design of the resonator.

$$\frac{AL^3}{W} = 1.0357 \times 10^{-19} \quad (3.10)$$

### 3.4 Summary

This chapter discussed the parameters taken into account while designing the suspended part of graphene and the electrostatically actuated graphene membrane. Most of the factors required trade offs between two desirable outcomes. Hence, instead of choosing one value for the parameter, a range of values are considered for most of the parameters. After discussing the fabrication of the device, it will become clearer as to which value is best suited for each parameter. So, a lot of the designing parameters of the device can be optimized further depending on the fabrication results. This chapter also included designing of other structures which will be used for doing measurements and analyzing some of the properties of graphene resonators. Next chapter will discuss fabrication of these suspended graphene membranes. The fabrication of the electrostatically actuated graphene resonator will be discussed in chapter 5.

# Chapter 4

## Fabrication of suspended graphene membranes

As described in the earlier chapters, the most important part of a resonator is the suspended part, which is required for it to resonate. Hence, for graphene membranes to be used as a resonator, it should be suspended. Moreover, this fabrication procedure should be undertaken using a wafer scale, transfer free approach, so that it is industry compatible. This chapter describes in detail the entire process flow undertaken to fabricate wafer scale, transfer free suspended graphene membranes. This fabrication procedure is similar to the one used in [73]. It is integrated with other steps to fabricate the electrostatically actuated graphene resonator, which will be described in chapter 5.

### 4.1 Fabrication procedure

Figure 4.1, describes the steps performed to fabricate suspended graphene membranes. First, on a bare silicon wafer (step a), thermal silicon dioxide is grown (step b). Metal molybdenum (Mo) is then deposited on this thermal oxide layer (step c). This is followed by patterning and etching of the molybdenum layer (step d). Mo is not etched in places where graphene growth has to take place. However, etching of molybdenum never stops immediately when entire molybdenum layer is etched. It also etches some oxide layer underneath the molybdenum. Hence, the oxide layer under the etched molybdenum is thinner than the oxide layer under the remaining molybdenum. After removal of the resist in NMP (N-methylpyrrolidone), graphene is grown on the patterned molybdenum (step e). Wafers are coated with photoresist, patterned and this is followed by gold deposition using e-beam evaporation. Then lift off is done using NMP. Gold remains in areas where photoresist is not there. The remaining gold works as contacts/anchors of the suspended graphene membranes (step f). After this, catalyst molybdenum, underneath graphene, is etched away using peroxide. Critical point drying is performed to avoid collapse of membranes after removal of the underneath Mo layer. This leads to suspension of the graphene membranes (step g). The following sections will elaborate on each of the above mentioned steps performed during fabrication.

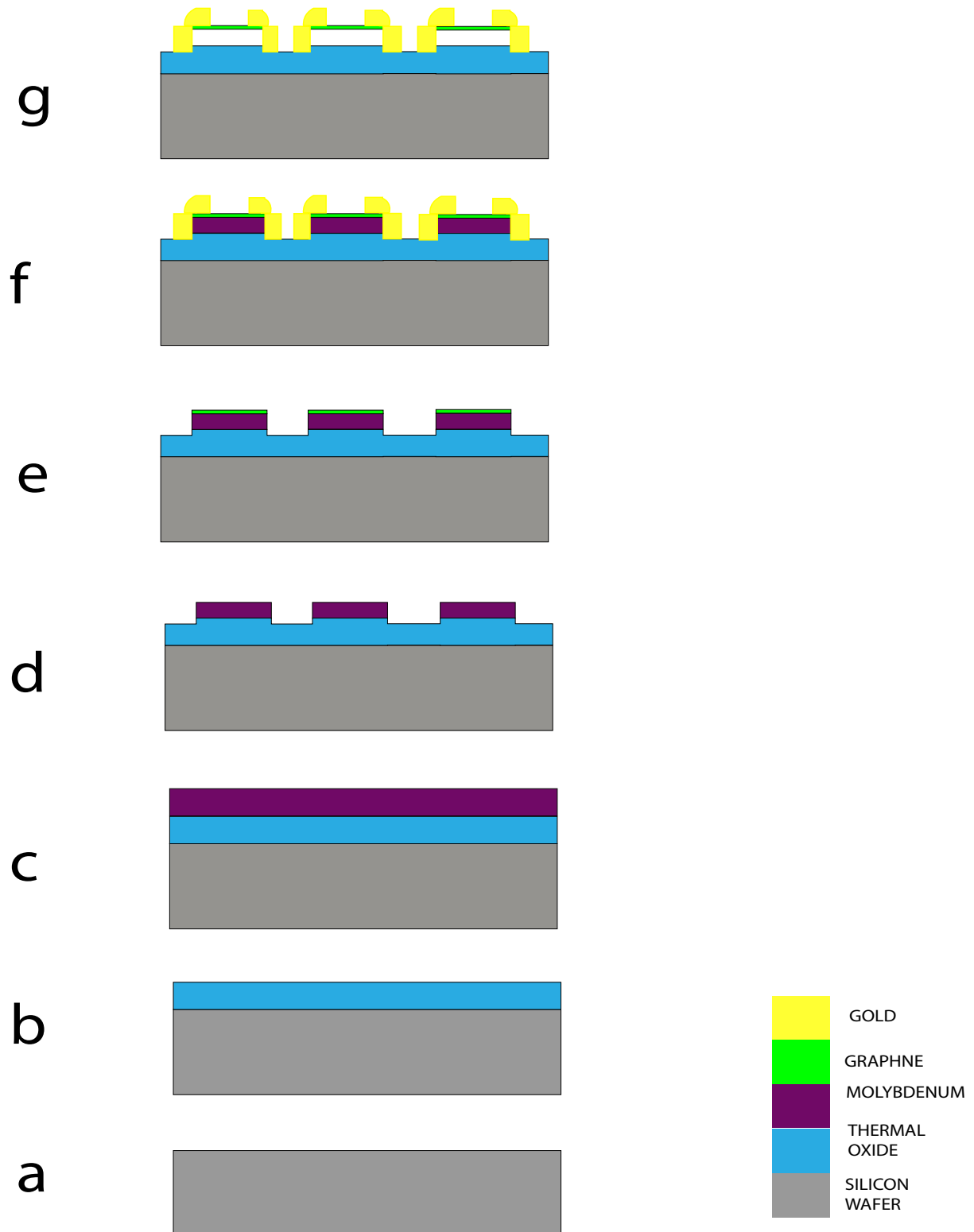


Figure 4.1: Fabrication process flow for suspended graphene membranes

### 4.1.1 Initial fabrication steps and Thermal Oxidation

The fabrication procedure starts with making alignment markers. This step is important as these alignment markers are needed in the subsequent steps by the waferstepper (machine that is used to expose mask on the wafer) to align the mask with the wafer. To make these alignment markers, first the wafer is coated with zero layer and then exposed with a COMURK mask and developed. After development, these alignment markers are etched inside the silicon and then the photoresist is removed from the remaining parts of the wafer using O<sub>2</sub> plasma stripping (tepla). As shown in figure 4.2, tepla has a magnetron which is excited by radiofrequency energy. The gas (O<sub>2</sub>) that is introduced into the chamber is ionized into a reactive plasma because of this magnetic energy [105]. This plasma then helps to strip off the photoresist by attacking it physically and chemically.

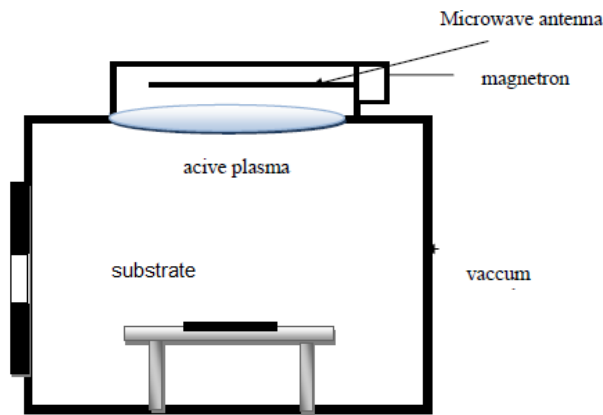
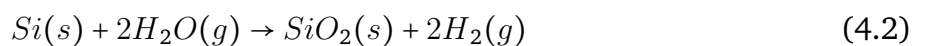


Figure 4.2: TEPLA: the photoresist stripper. Taken from [105]

After photoresist removal and cleaning, thermal oxidation of silicon is done to grow oxide layer on silicon. In this process, silicon is also consumed. Since, we would require to go to high temperatures such as 950 ° celsius for graphene growth, an oxide layer is needed as it helps to prevent diffusion of metals into the silicon layer at higher temperature. Equations 4.1 and 4.2 show the reactions that take place for dry and wet oxidation [106], respectively. Wet oxide has a higher growth rate than dry oxide but the quality of dry oxide is better. Table 4.1 shows the application of different thicknesses of oxide in CMOS technology. For our process, we chose to grow 1000 nm of wet oxide on the first batch of wafers as it is grown much faster. This thickness was used to see if it is possible to suspend graphene membranes on such a thick oxide. This would then be helpful in using the same thickness for the electrostatic devices as for them a thicker oxide would lead to less parasitic capacitance. On the second batch of wafers 90 nm of dry oxide was grown which is the standard thickness of oxide used in [73]. The choice of type and thickness of oxide will become important in suspension of device which would be discussed in detail in the chapter 7.





**Table 4.1: Silicon Dioxide: Thickness and Uses. Taken from [106]**

Thickness(nm)	Application
6-10	Tunneling gates
15-50	Gate oxides, capacitor dielectrics
20-50	LOCOS (local oxidation of silicon) pad oxide
200-500	Hard masks, surface passivation
300-1000	Field oxides

### 4.1.2 Molybdenum deposition

Thin film of molybdenum is deposited using DC magnetron sputtering process in the sigma machine. This is a type of physical vapor deposition process. Figure 4.3 shows the process of DC magnetron sputtering of molybdenum. There is a target molybdenum present in deposition chamber. The magnetic energy from the rotating magnetic field on top of the target densifies the plasma. A DC power is applied to the target to ignite the plasma. This makes the ionized argon atoms to accelerate towards the the target molybdenum. These atoms hit the target plate and knock out molybdenum atoms from the plate which are in vapour phase. These vapours are then deposited onto the substrate forming a thin layer of molybdenum. Using this method, a uniform layer of molybdenum is obtained on the substarte. There are 3 steps in physical vapour deposition. Vapourization of the target material due to plasma, transportation of these vapours to the substarte and then finally condensation of these vapours onto the substrate as thin film. 100 nm and 200 nm thick molybdenum is deposited using this procedure. The recipes used for 100 nm molybdenum deposition is described in table 4.2.

**Table 4.2: Molybdenum 100 nm recipe**

Parameter	Value
Process Pressure	8 mTorr
Target Power	1 kW
Process Time	53.5 s
Gas Flow	150 sccm

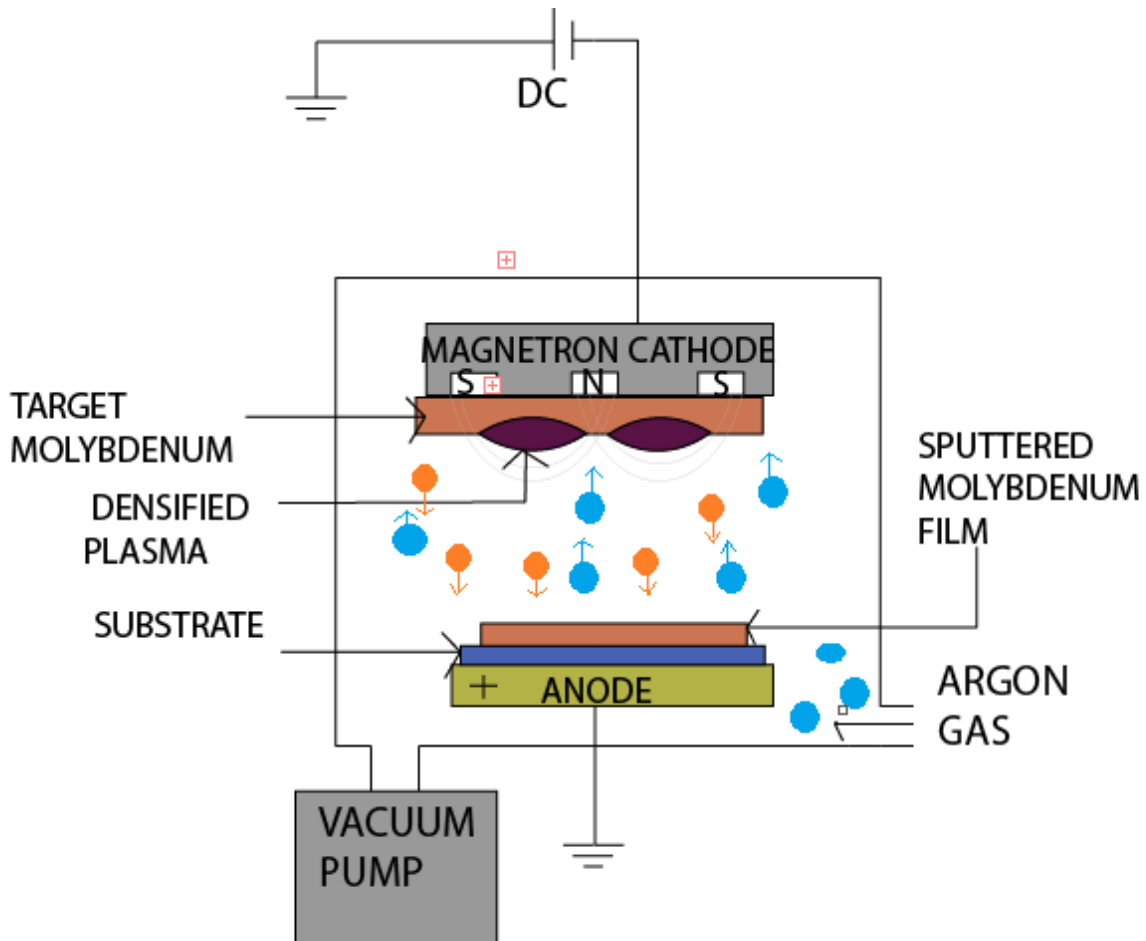


Figure 4.3: DC magnetron sputtering of molybdenum. Adapted from [107]

### 4.1.3 Etching of Molybdenum

For all the automatic coating and development processes, an EVG120 is used as shown in figure 4.4. Depending on the photoresist used, the exposed parts of a wafer become soluble or insoluble. The soluble parts are removed using a developer. For the molybdenum layer, photoresist in all the areas where molybdenum needs to be etched, becomes soluble and is removed by the developer.

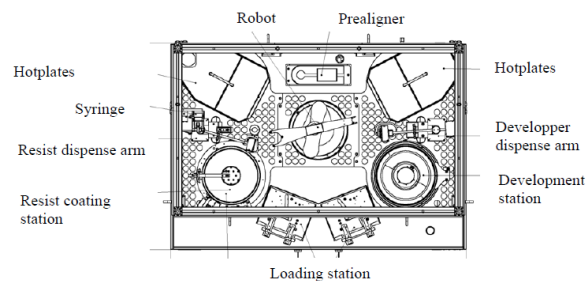


Figure 4.4: Automatic coater and developer: EVG 120. Taken from [108]

Exposure energy and focus values are critical in determining the size of structure. As we have various different sizes starting from  $1 \mu\text{m}$  to  $10 \mu\text{m}$  of devices on our mask, it is important to give the correct exposure and focus values, so that we get the correct dimensions on the wafer. Exposure energy and focus values are important parameters that affect the size of the structures on a wafer. An overexposure can lead to thinner lines and bigger holes.

On the other hand, underexposure can give wider lines and smaller holes. Incorrect focus can lead to unexposed areas on the mask and can also affect the slope of the device. It is important to optimize these parameters, in order to get the correct dimensions. For the bigger structures, it is less of a problem. This is because if a  $10\ \mu\text{m}$  width is exposed as  $10.5\ \mu\text{m}$  width on the wafer, the percentage change in the width is only 5%. However, for a  $1\ \mu\text{m}$  width exposed as  $1.5\ \mu\text{m}$  width, the percentage change is 50%. Hence, it is important to optimize the smallest dimensions. For this, an E-F (energy-focus) matrix exposure is performed on the wafer, as shown in figure 4.5. With this exposure each die on the wafer is exposed with increasing energy on the positive x axis and decreasing energy in the negative x axis direction. The focus is decreased by a step value in the positive y direction and increased by a step value in the negative y direction. The structures used to optimize the dimensions are linewidth structures as shown in figure 4.5.

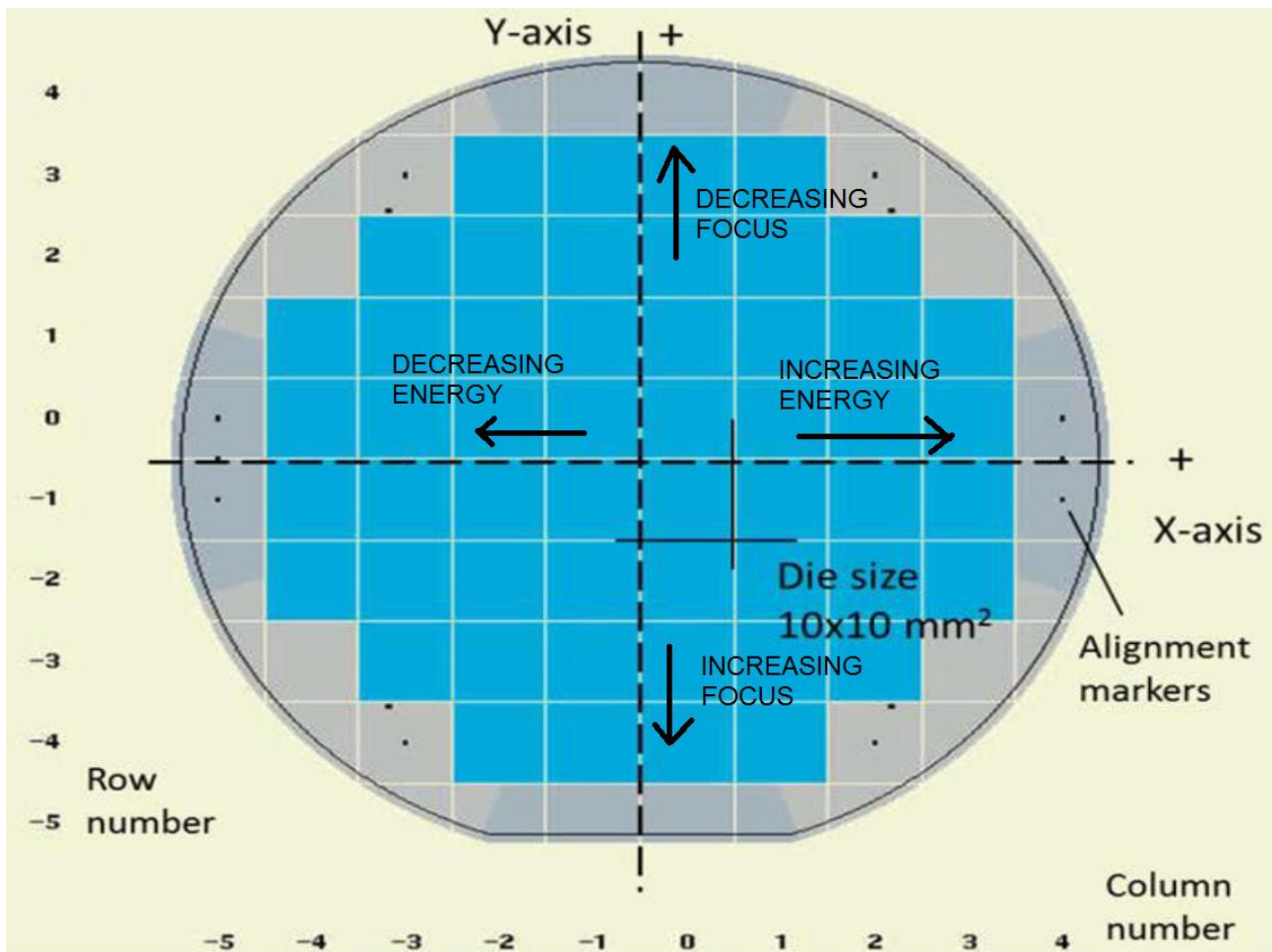


Figure 4.5: EF exposure on the dies of the wafer

The exposure energy and focus values, optimized for  $2.1\ \mu\text{m}$ ,  $2.5\ \mu\text{m}$  and  $3\ \mu\text{m}$  thick photoresist on molybdenum layer and oxide layer are given in table 4.3. The values have been optimized for oxide layer on top of the Mo also, since for electrostatic structures, this oxide layer acts as a light scattering layer on molybdenum that is used to pattern molybdenum which will be described in chapter 5. The linewidth structures (see figure 4.6) are used to measure the width of the line for each die. The results for  $2.1\ \mu\text{m}$  photoresist are shown in figure 4.7.

Table 4.3: Optimized exposure energy and focus values for different thickness values of photoresist

	Thickness of photoresist	Patterned material	Energy value (units)	Focus value
1	2.1 $\mu\text{m}$	Mo	240	-1
2	2.5 $\mu\text{m}$	Mo	270	-0.5
3	3.1 $\mu\text{m}$	Mo	360	0
4	2.5 $\mu\text{m}$	200 nm oxide on Mo	250	-0.5

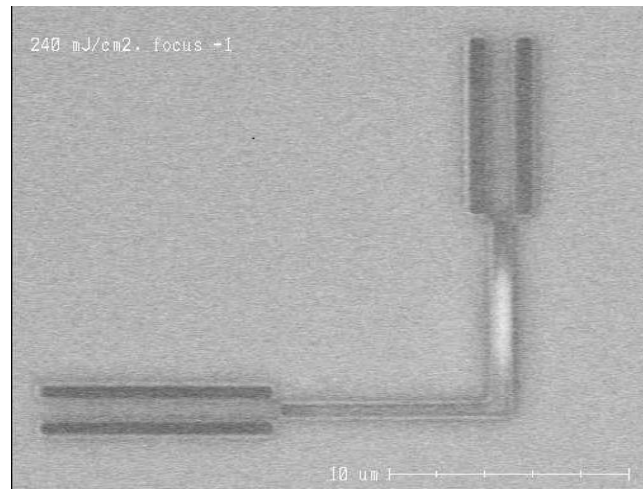
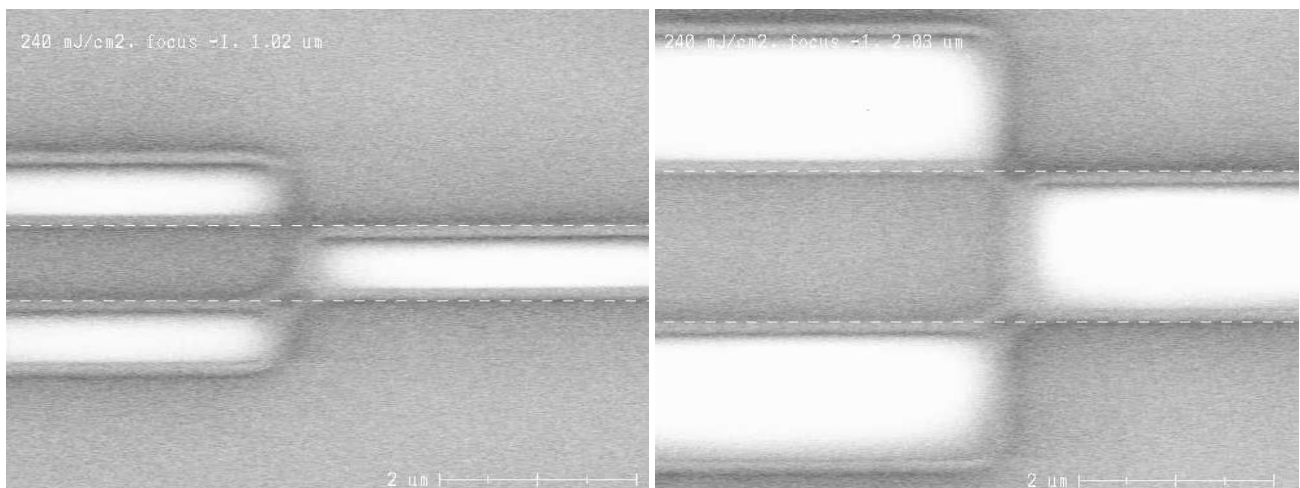


Figure 4.6: Line width structures



(a) E-F results for 1  $\mu\text{m}$  line

(b) E-F results for 2  $\mu\text{m}$  line

Figure 4.7: E-F measurement results for 2.1  $\mu\text{m}$  line

Etching in the semiconductor process means removing unmasked or unprotected parts from the surface of the element being etched. There are two major kinds of etching, namely, wet and dry etching. When a material is removed by the means of chemicals and liquids then it is called wet etching. In dry etching, gases and plasma are used to etch away the material. Wet etching is generally faster than dry etching. However, dry etching is better in defining

small feature sizes as it is anisotropic. This is in contrast with wet etching which is mostly isotropic. Hence, we use dry etching for the removal of molybdenum.

To etch away molybdenum, Omega machine is used which works on the principle of ICP (Inductive Coupled Plasma) as shown in figure 4.8. A RF generator excites the coil that is placed around the chamber which ionizes the gas in the chamber in a reactive plasma which is accelerated to the wafer by a bias power. The material to be etched is attacked by the plasma physically and chemically. Two different recipes were used to etch molybdenum. For the first batch of wafers, Motest2 was used and for the second batch of wafers Mo50 was used. The first recipe was used since it etches the metal much faster as compared to the second recipe. The time in these recipes can be altered according to thickness of molybdenum being used. The difference between these two recipes will be elaborated in chapter 7.

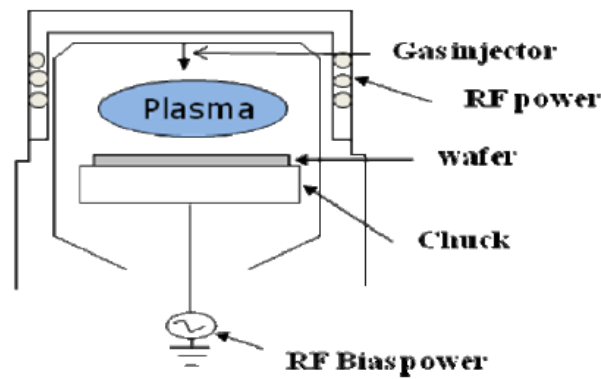


Figure 4.8: Inductive Coupled Plasma Etching. Taken from [109]

Once the etching is done, the photoresist, which is protecting the molybdenum in all the areas where graphene growth has to take place, is removed using NMP. NMP dissolves the photoresist without affecting molybdenum. For graphene growth, oxidized molybdenum is not favourable. Tepla is not used to strip off the photoresist as it may lead to oxidation of molybdenum which can cause a hindrance in the next step that is graphene growth.

#### 4.1.4 Graphene growth

The AIXTRON Black magic machine or CVD reactor is used for the growth of graphene on molybdenum substrate. It has a top and bottom heater, as shown in the figure 4.9, to maintain uniform temperature distribution within the chamber. The wafer is mounted on the stage present inside the chamber. A thermocouple is attached to the top heater and the surface of the stage that measures their temperature respectively. The showerhead in front of the top heater is where the gases enter into the chamber. Initially argon is let into the chamber to push out the oxygen and air molecules from the chamber. Then, 1000 sccm of hydrogen gas is let into the chamber and the chamber is heated to 950 °C. Hydrogen reduces molybdenum oxide to metallic molybdenum. This is necessary since metallic molybdenum catalyst is required for graphene growth. Once the chamber is heated to 950 °C, 960 sccm of argon is let into the chamber and the hydrogen flow is reduced to 40 sccm. The amount of hydrogen gas is reduced so that there is no etching of graphene. After that, 25 sccm methane flows into the chamber through the showerhead for 5 minutes during which graphene growth occurs. The heat energy from the top heater and the catalyst helps to break the hydrogen bond in methane. Surface diffusion and bulk diffusion of these unbonded carbon atoms from the methane gas, in the molybdenum, help in the formation of graphene. A pressure of 25 mbar is maintained inside the chamber during graphene growth using a pressure controller.

For the first batch of wafers the graphene growth was done at 915 °C for 40 minutes. For the second batch, 950 °C for 5 minutes was used.

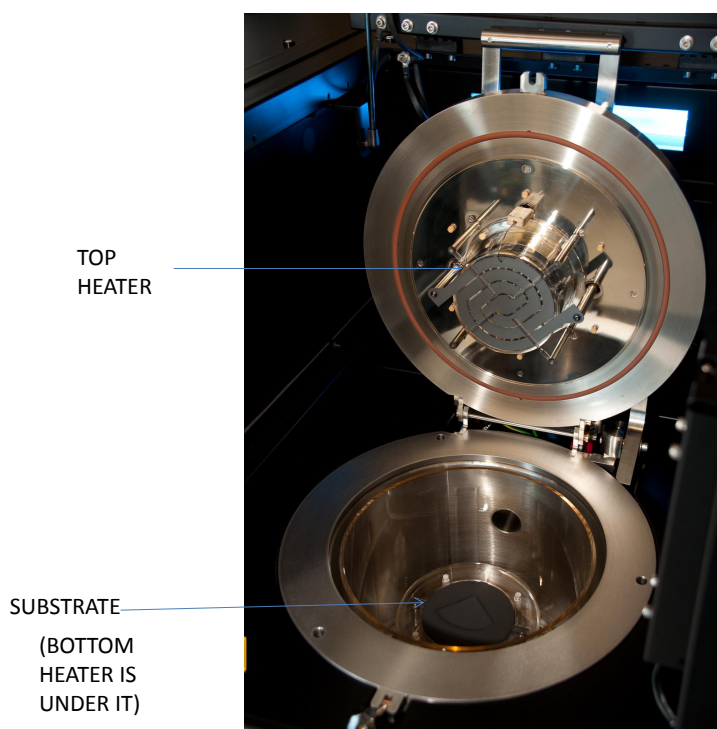


Figure 4.9: *Blackmagic machine used to grow graphene*

#### 4.1.5 Gold contacts

The backside of the wafers become contaminated with copper particles from black magic machine after graphene growth and so it cannot be used for further processing using other clean equipments since it poses a danger of contaminating these machines. Hence, a layer of titanium nitride is deposited on the backside of the wafer. Titanium nitride layer acts as a barrier layer for copper particles.

Then the wafers are coated, exposed and developed for gold deposition. A positive resist gives positive slope sidewalls. If this photoresist is used, then gold will be deposited even on the sidewall structures. This would make it difficult to perform lift off as NMP will not be able to enter by the sidewalls. Hence, a negative photoresist is used as it gives negative slope of the sidewalls and makes it easier for NMP to get into via the sidewalls and remove the photoresist during lift off. For the first batch of wafers automatic coating and development is done whereas for the second batch of wafers manual coating and development is done as in [73]. Gold is deposited on the entire wafer using e beam evaporation. Then lift off is performed using NMP in ultrasonic bath. All the places, where photoresist is present, gold is removed with the photoresist.

#### 4.1.6 Release of the membrane

Now, the fabrication is done on a die level. A die is cut out from the wafer. For the release of the membrane, the following procedure is followed. The die is placed in peroxide for 5 minutes. Peroxide etches the molybdenum under the graphene membrane and does not etch any other material on the die. It can penetrate through the pin holes in the graphene membrane also, to etch away the molybdenum. It was observed that this time is enough for the entire molybdenum to be etched away. Then the die is rinsed in DI water for 5 minutes.

This is done to remove any peroxide left on the die. Once the etching is done, the die is kept in isopropyl alcohol or isopropanol (IPA) for 5 minutes. After that it is switched to another beaker of IPA where sample transfer to another holder takes place. This is done because the holder is going to be placed in CPD ( Critical Point Drying) tool after this. The die is then placed in ultra pure IPA to ensure that no water content is left in the die. This procedure has been shown in figure 4.10.

CPD is a procedure commonly used for drying specimens that can collapse due to air drying. Water has a very high surface tension to air. Hence, if water is dried in air, the surface of the membranes on which water is present, will face high surface tension and can easily collapse. For this purpose , a liquid (carbon dioxide in our case) is dried at critical temperature and pressure (31.1 ° C and 1072 P.S.I ). At critical temperature and pressure, there is no difference between the liquid and gaseous phase of the substance and hence, the transition of the liquid to the gaseous phase happens smoothly. Since the critical temperature and critical pressure of carbon dioxide is in a convenient range, liquified carbon dioxide is used to dry the specimens. It is called as the transition fluid. However, the issue is that carbon dioxide is not miscible in water. So, something has to be used that is miscible in water as well as in carbon dioxide. For this purpose, isopropyl alcohol (IPA) is used. Carbon dioxide is miscible in IPA. So, IPA in this case acts as an intermediate fluid.

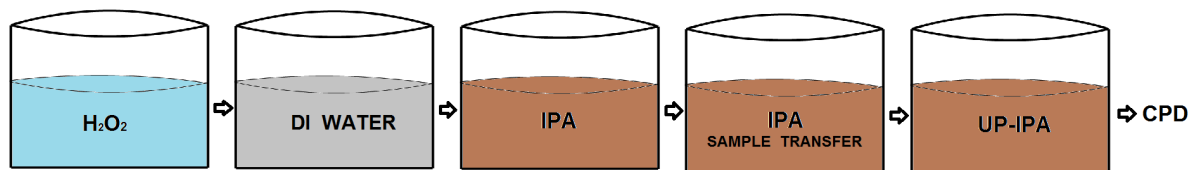


Figure 4.10: Steps undertaken for the release of the membrane

Another way, suspended graphene membranes could be fabricated is by etching some part of oxide using BHF under the graphene membrane area, as shown in figure 4.11. For this etching, another layer on mask is needed which will help etching of the oxide from under the graphene membrane in the middle area. Then photoresist is removed using warm acetone. Finally molybdenum is removed from under the graphene membrane, using peroxide. This way of fabrication is useful for suspending long beams that are useful for pirani sensor applications. For pirani sensors, the gold contacts should be further away from the graphene membrane.

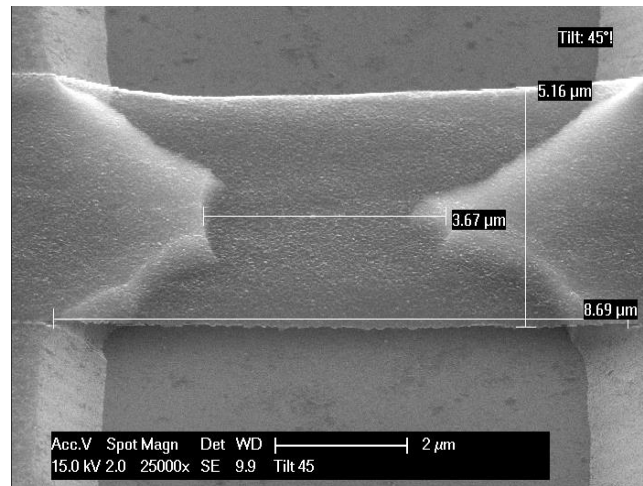
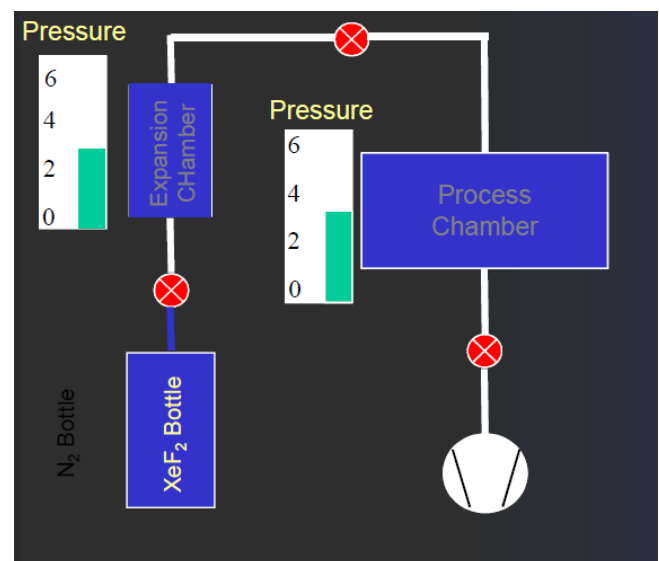


Figure 4.11: Suspended graphene membrane for pirani sensor application

The other method used for etching molybdenum in the last step for the release of the membrane is by dry etching using xenon difluoride. In Xactix,  $\text{XeF}_2$  is used to isotropically etch silicon, germanium and molybdenum. It is a dry process and so there is no stiction issues between the substrate and the released part. Also it is very selective to silicon, germanium and molybdenum. The etchant is in the vapour phase. For our case it was used to etch molybdenum under graphene. Xactix (figure 4.12a) was used in pulsed mode [110] (figure 4.12b).  $\text{XeF}_2$  is diluted in  $\text{N}_2$  in a 1:1 ratio, the pressure of the expansion chamber was set to 6 Torr. However, as shown in figure 4.13, molybdenum was not etched completely using this etching method. The blackish areas are graphene with molybdenum etched from underneath. The light grey areas are where molybdenum is left under the graphene membrane.



(a) Xactix equipment



(b) Pulsed flow process in Xactix

Figure 4.12: Xactix Equipment. Taken from [110]



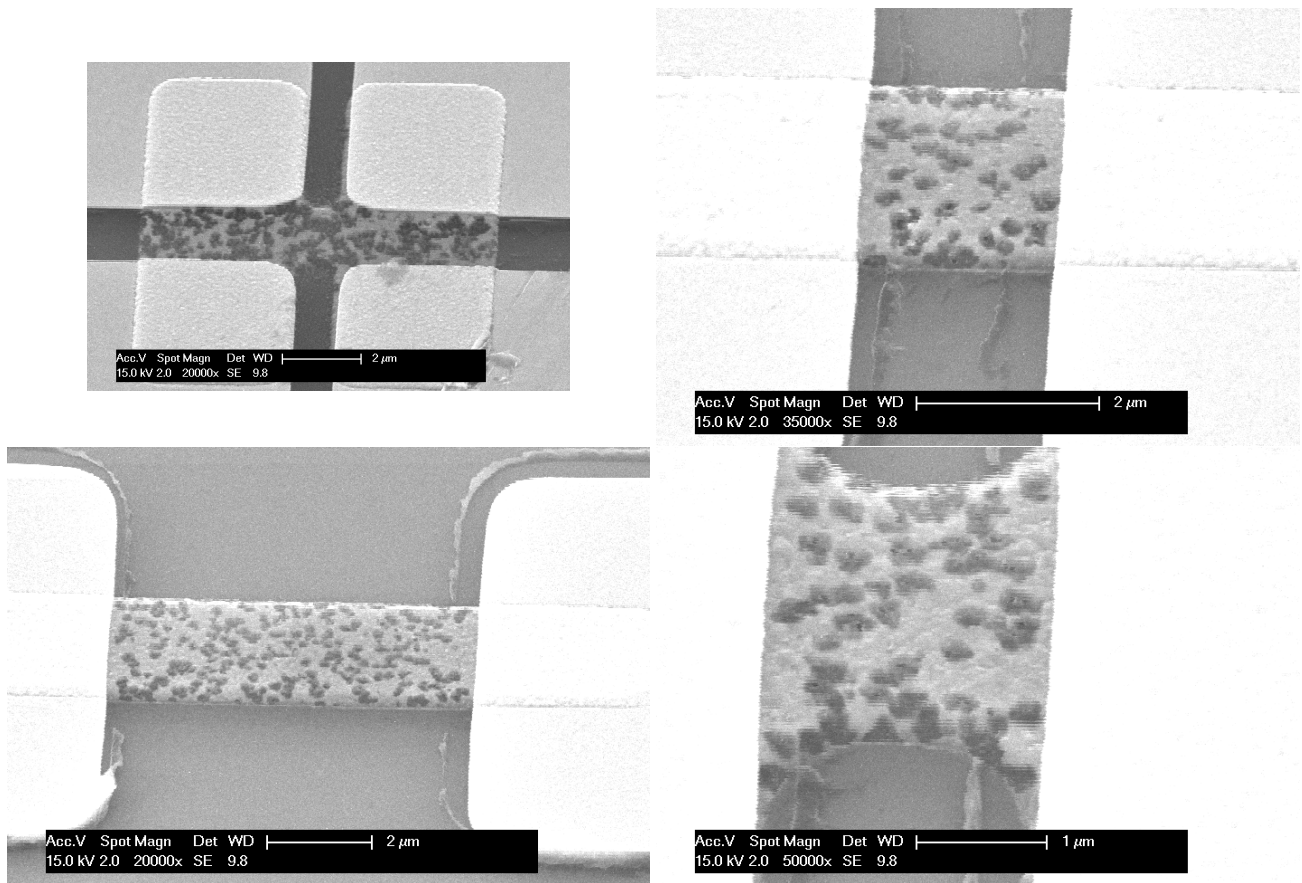


Figure 4.13: SEM images of the device etched in Xactix

## 4.2 Fabricated batches of wafer

Table 4.4 and 4.5 display the results obtained for the first and second fabricated batch of wafers. The first batch of wafers, which were fabricated using some different parameters, were found to be collapsed as shown in figure 4.14. However, the second batch of wafers which were fabricated using the same process parameters as in [73], were found to be suspended as can be seen in figure 4.15. This clearly indicated that suspension of graphene is dependent on process parameters. This aspect will be analyzed in detail in the chapter 7.

Table 4.4: Fabrication Results (First Batch)

Wafer	Structures	Molybdenum thickness (gap size)	Suspended
1	Electrothermal	25nm	×
2	Electrothermal	50nm	×
3	Electrothermal	100nm	×
4	Electrothermal	200nm	×

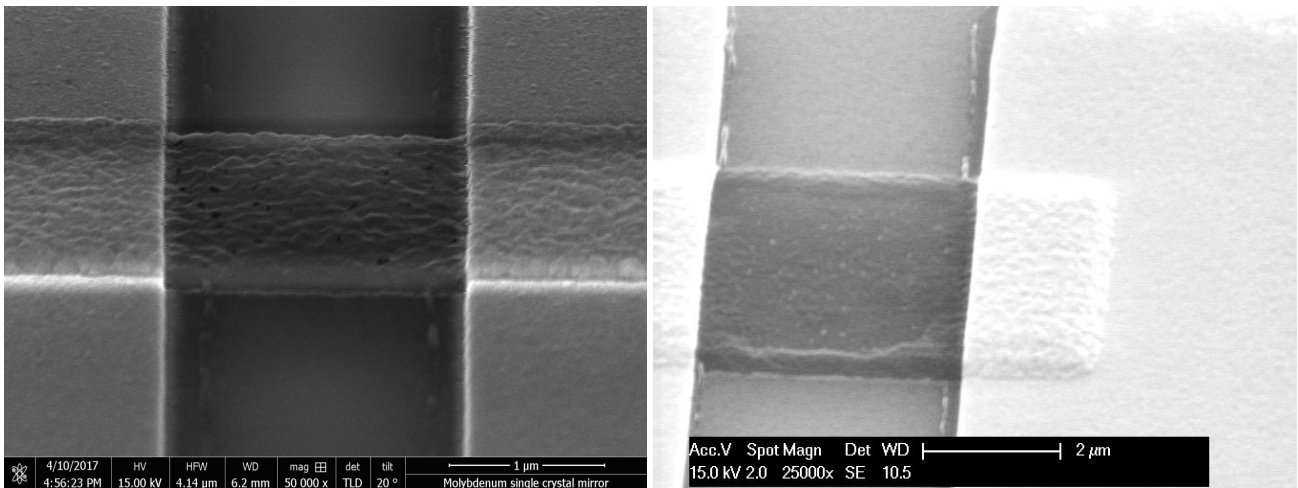


Figure 4.14: SEM images of the collapsed graphene membranes

Table 4.5: Fabrication Results (Second Batch)

Wafer	Structures	Molybdenum thickness (gap size)	Suspended
1	Electrothermal	100nm	✓
2	Electrothermal	200nm	✓

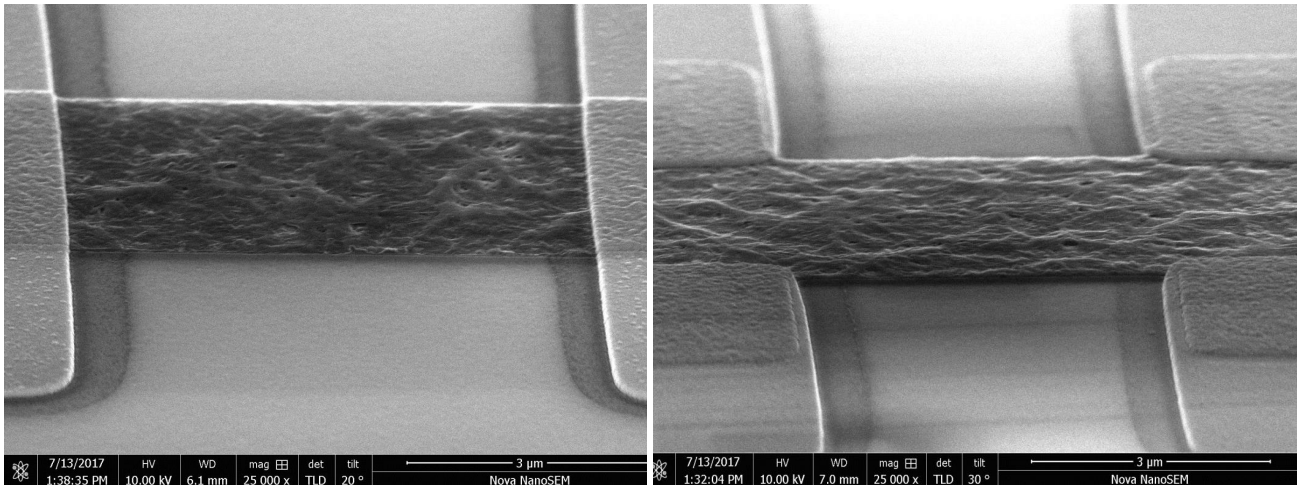


Figure 4.15: SEM images of the suspended graphene membranes

### 4.3 Issues Faced While Fabrication

One of the critical steps in this fabrication cycle is etching of molybdenum. This etching should remove molybdenum completely from the unmasked regions without removing the photoresist completely. This means that the recipe should be selective. This is because if the photoresist is removed completely, molybdenum under the photoresist would also start reducing and then the obtained device would not be of correct thickness. Moreover, the etching rate of molybdenum is not stable. The etching rates of molybdenum, in Omega, were ranging between 0.4 nm/s and 0.7 nm/s.

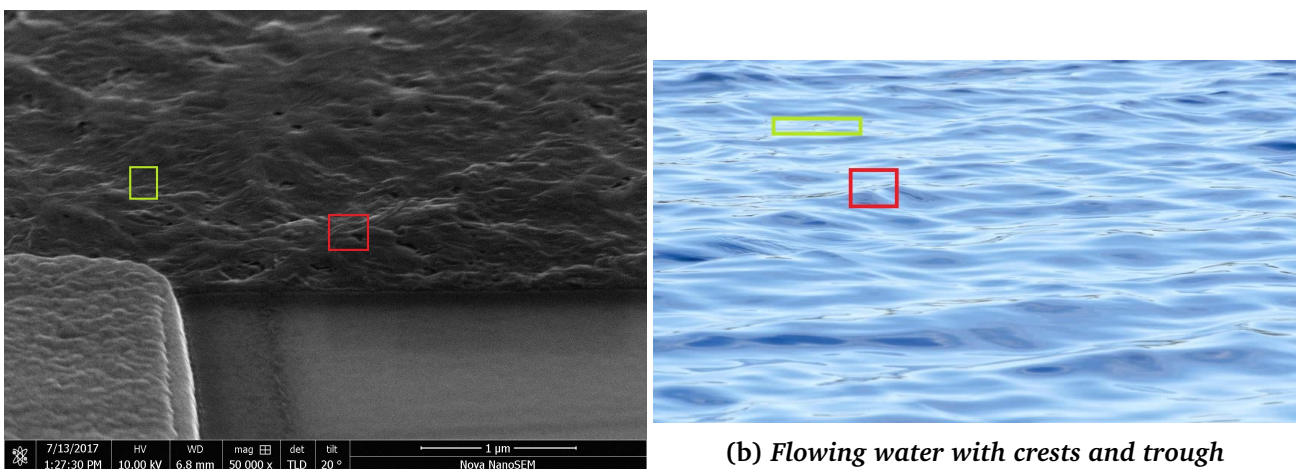
The other critical issue was to get the correct size for  $1\ \mu\text{m}$  linewidth also. This is smallest used dimension in the mask design. When a mask is exposed, depending on the photoresist being used, the dimensions of the structures may change. Since, an analysis had to be done to find out membrane of which dimensions are suspended, it was crucial to get the correct dimensions. This was difficult and some optimization had to be done for this. Hence, an E-F matrix exposure was used.

Another issue faced was regarding suspension of membrane. Since removal of molybdenum and release of the graphene membrane is the last step in the fabrication cycle, the entire fabrication cycle had to be completed to find out if the graphene membrane was suspended or not. Later, some clues were found out before molybdenum etching, to see if the graphene membrane is suspended or not. This will be described in chapter 7.

## 4.4 Analysis of of the fabricated samples

### 4.4.1 Structure of the suspended graphene membrane

It has been shown in the past that 2D membranes can exist in 3D but with strong height fluctuations and the membrane is crumpled [111]. Ripples have been observed in freely hanging graphene [79, 112]. Research has shown that suspended monolayer graphene membranes have roughness in its third dimension. This roughening gives it extraordinary electrical, mechanical and optical properties [112]. In comparison to the unsuspended graphene membranes, our few layer suspended graphene membranes show much more height variations, roughness and wave like structure. It is corrugated and has ripples. The structure of the suspended membrane is a combination of various peaks and valleys just like crests and troughs on the surface of flowing water, as shown in figure 4.16.

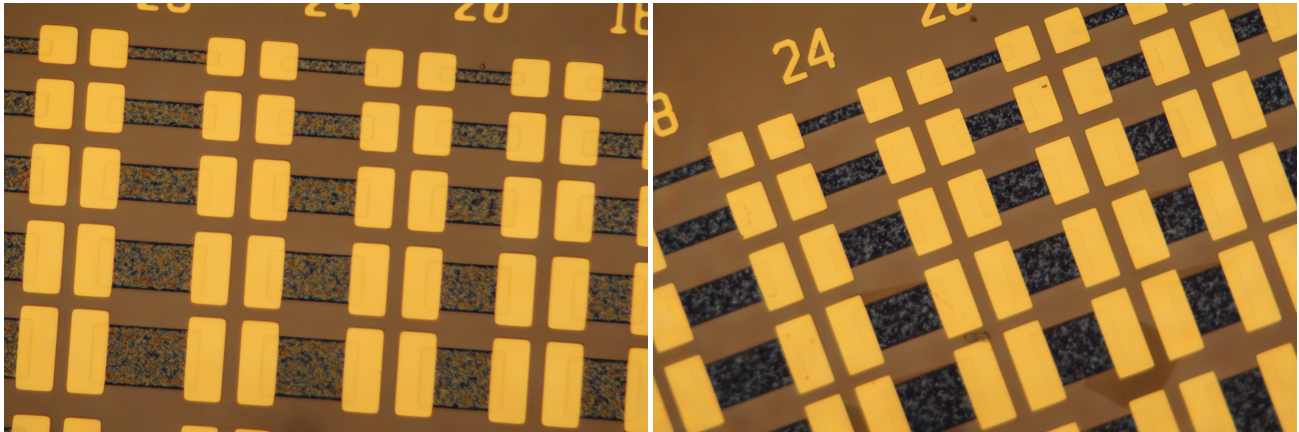


(a) Suspended graphene membrane

(b) Flowing water with crests and trough

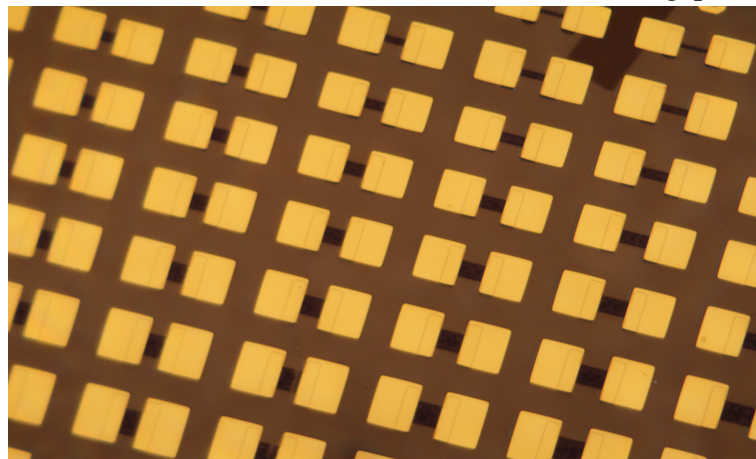
Figure 4.16: Structure of suspended garphene membrane. Red square denotes the crests and the green square denotes the trough

### 4.4.2 Graphene membrane under the microscope



(a) Suspended graphene membrane with 200nm gap size

(b) Suspended graphene membranes with 100nm gap size

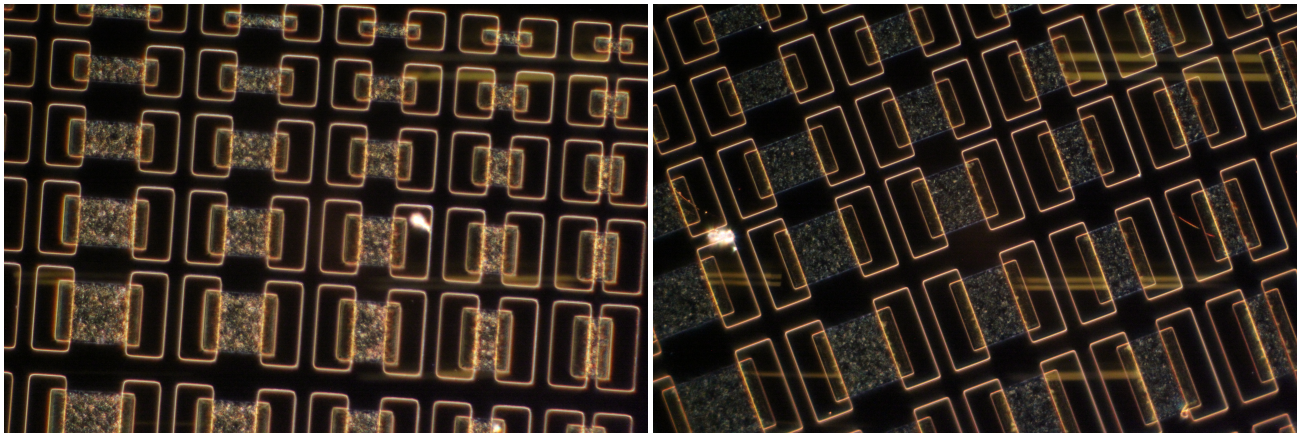


(c) Collapsed graphene membrane

Figure 4.17: Microscope images of different types of graphene membranes

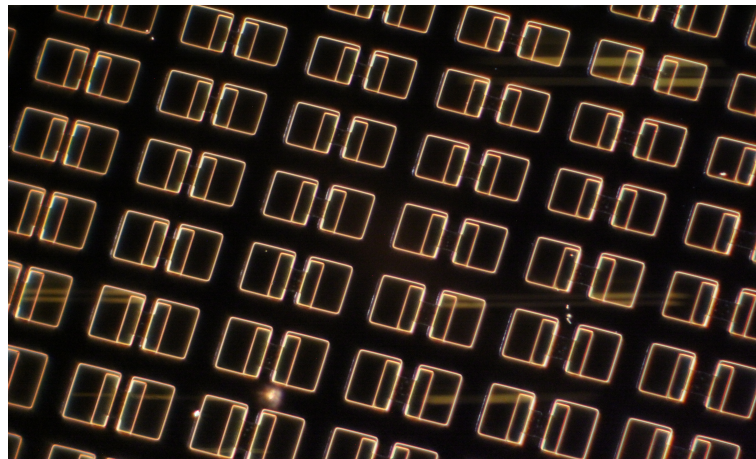
Researchers have shown that graphene is best detected under the microscope if it is on silicon dioxide thickness of 90 nm [113]. Graphene, itself is semi transparent and not visible under the microscope. However, when it is on top of layers such as silicon oxide and silicon, due to interference of light and contrast, it becomes visible. Under the microscope, suspended graphene membranes look very different from collapsed membranes. This means that using different thickness of layers beneath the graphene membrane can have a significant impact on the colour of the graphene membrane.

As can be seen in figure 4.17 , the 100nm gap size suspended graphene membrane has a bluish colour. Parts of it look dark blue in colour and the other parts have light blue colour. Since, suspended graphene membrane is corrugated and has peaks and valleys, that is why a difference in shades of colour is seen across the surface of suspended graphene membranes. On the other hand, parts of 200 nm gap size suspended graphene membrane, show light blue colour whereas the other parts show orange colour. This is again because the graphene membrane is not flat. Some parts of it are high and the other parts are low. The collapsed graphene membrane is plane and does not have significant height variations. So, it does not show different colours



(a) Suspended graphene membrane with 200nm gap size

(b) Suspended graphene membranes with 100nm gap size



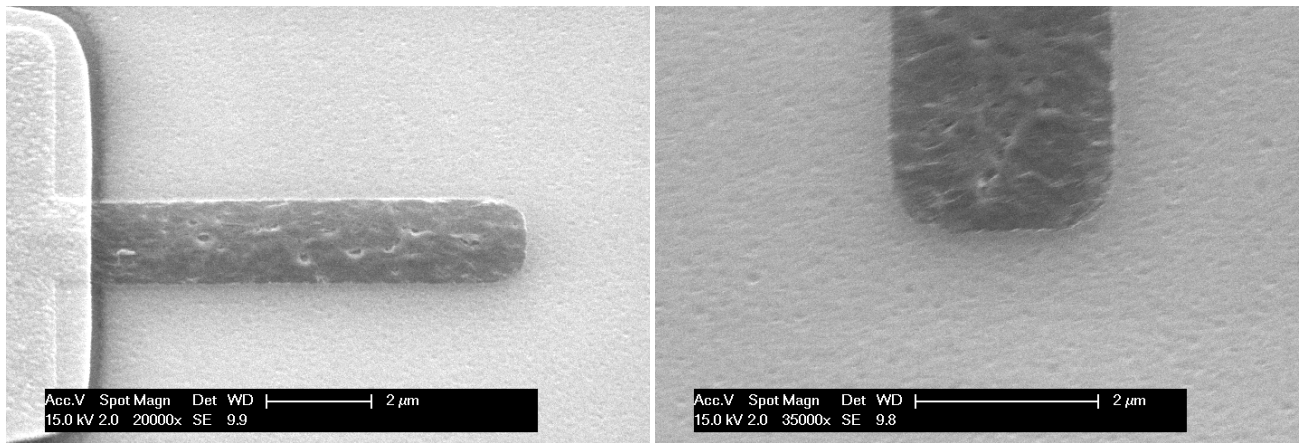
(c) Collapsed graphene membrane

**Figure 4.18:** Dark field images taken on different samples of graphene membrane

The three samples were also observed under the microscope in dark field. Dark field microscopy is useful for observing structures which are transparent or have similar refractive indices as the surroundings. In dark field microscopy, the specimen is seen against a dark background. In this type of microscopy, only the scattered light is allowed to hit the sample. Hence light hits the sample at different angles, gets reflected, refracted and diffracted. As shown in figure 4.18, clear differences are visible for the 100 nm, 200 nm and collapsed sample viewed in dark field microscopy. All the three samples were viewed under the same settings. Suspended graphene membrane is rough and has peaks and valleys, so it is able to reflect light at different angles thereby making itself more visible. Graphene sample suspended on a 200 nm gap size is much more visible than the 100 nm sample, again suggesting that the graphene membrane with 200 nm gap size is rougher and suspended in more parts of the membrane. The membrane in figure 4.18(c), is not at all visible again confirming that it is collapsed.

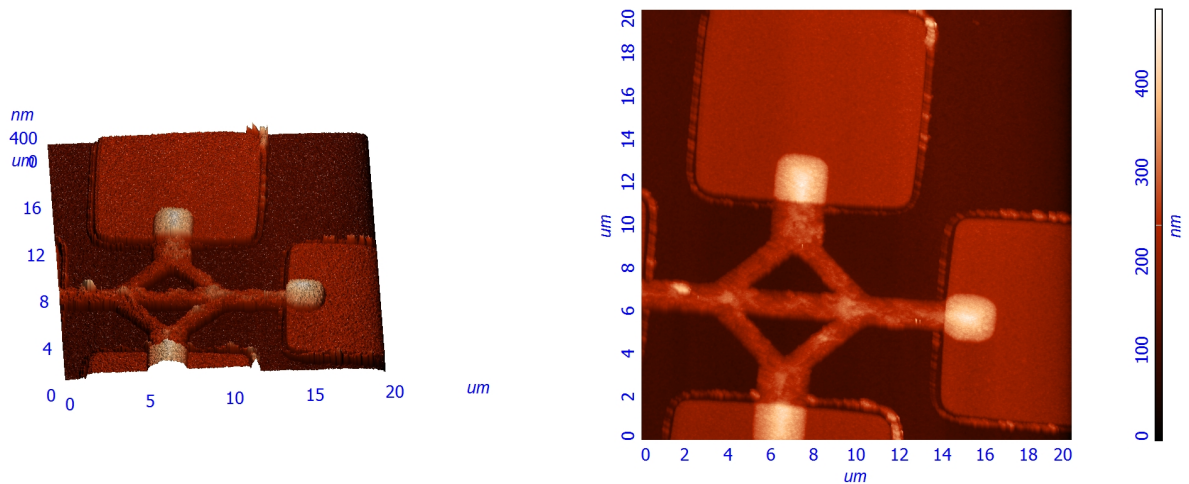
#### 4.4.3 Analysis of graphene membranes using AFM and SEM

This section presents analysis of the graphene membranes using SEM and AFM images. It includes the analysis of the various graphene samples using various roughness parameters. Figure 4.19 shows that even structures such as cantilever (supported only from one side) and stress structures seem suspended for the 200nm gap size.



(a) SEM of cantilever

(b) Zoomed in SEM image of cantilever



(c) 3D AFM image of stress structure

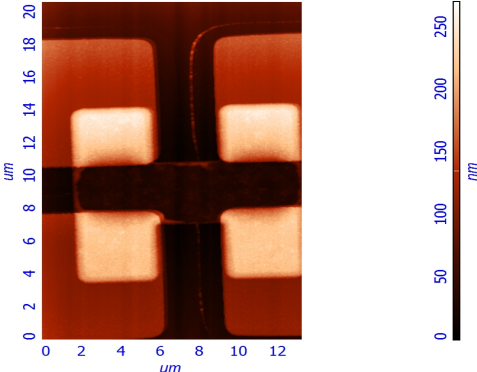
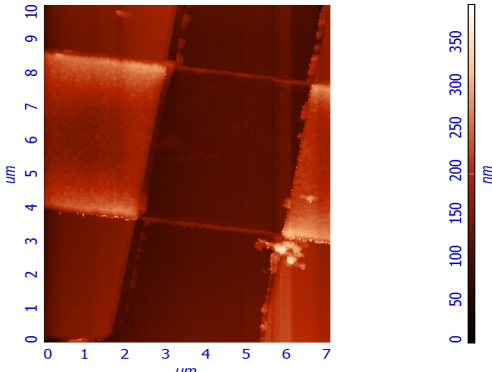
(d) AFM image of stress structure

Figure 4.19: SEM and AFM Images of 200 nm gap size samples

Tables 4.6, 4.7 and 4.8 give a comparison among the collapsed graphene samples, the 200 nm gap size suspended membrane and 100 nm suspended garphene membrane using roughness parameters. The surface profile parameters that have been used to quantify roughness have been described below [114]:

1. Average Roughness ( $R_a$ ) : This parameter gives the deviation in height from the mean height of the profile.
2. RMS roughness ( $R_{rms}$ ) : This parameter gives the standard deviation of the height.

Table 4.6: AFM images of collapsed graphene samples

	AFM Image	Size and Structure	R <sub>avg</sub> (nm)	R <sub>rms</sub> (nm)
1		5µm × 5µm HBar shape with four bond pads	3.79	4.86
2		4µm × 4µm Bar shape	4.17	5.45

The tables clearly show that collapsed graphene samples give very low roughness values. For the 100 nm and 200 nm sample the roughness values are almost similar. Also, from the AFM images and SEM images analysis of the structures, structures with 200nm gap size seem to be suspended in more parts than 100 nm gap size. For greater sizes of graphene membranes, less areas seem to be suspended as compared to small size membranes. Structure does not seem to influence the suspension of the graphene membranes.

Table 4.7: AFM images of 200 nm gap size graphene samples

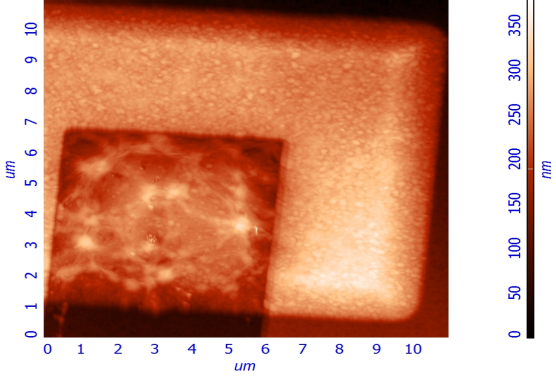
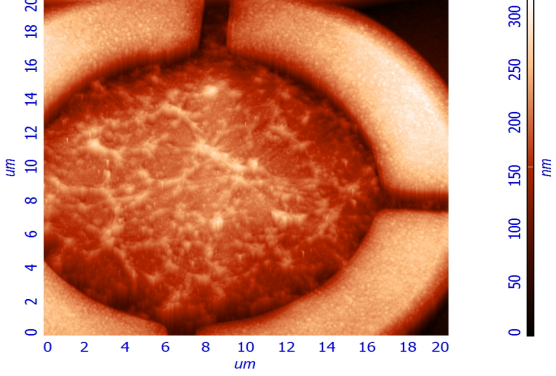
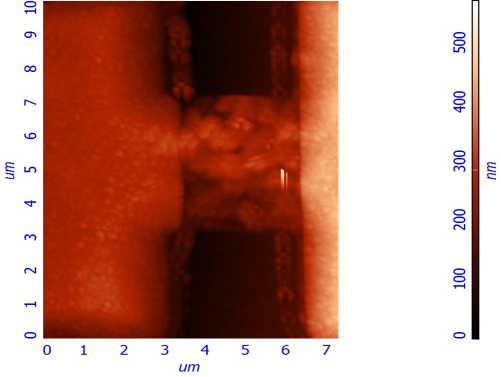
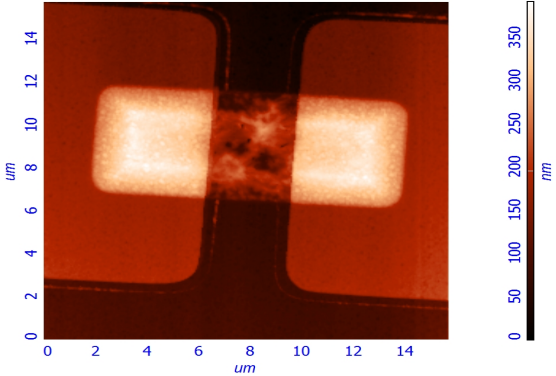
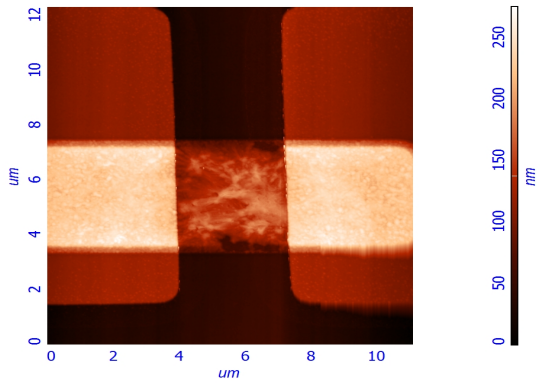
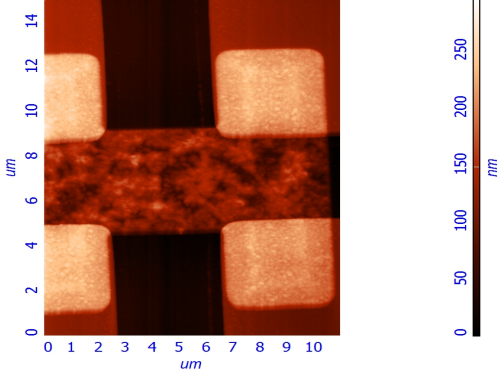
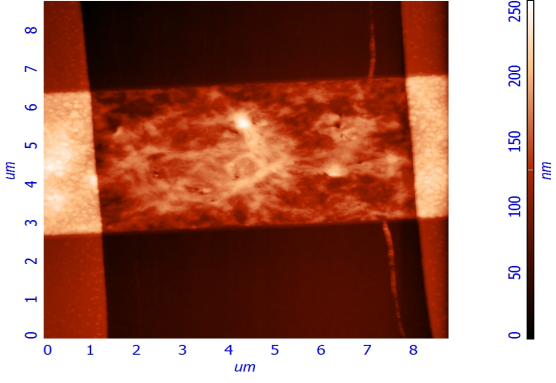
	AFM Image	Size and Structure	$R_{avg}$ (nm)	$R_{rms}$ (nm)
1		$7\mu m \times 7\mu m$ Three sided	24.85	31.81
2		radius = $10\mu m$ circle	19.65	24.34
3		$4\mu m \times 4\mu m$ Bar shape	24.38	30.45
4		$4\mu m \times 4\mu m$ HBar shape	36.32	44.30



Table 4.8: AFM images of 100 nm gap size graphene samples

	AFM Image	Size and Structure	R <sub>avg</sub> (nm)	R <sub>rms</sub> (nm)
1		4 μm × 4 μm Bar shape	18.86	23.22
2		5 μm × 5 μm HBar shape with four bond pads	21.57	27.79
3		10 μm × 7 μm Bar shape	42.30	51.76

## 4.5 Summary

This chapter explained the fabrication steps of making suspended graphene membranes and also analyzed the suspended membranes. As discussed in this chapter, following a fabrication process flow which had some different parameters from [73] led to collapse of graphene membranes. However, following exactly the same fabrication process as in [73] led to suspension of graphene membranes. This indicates that even a slight change in process parameters can affect suspension of graphene. 200 nm gap sizes structures seem to be suspended for a greater region than 100 nm gap size structures. For very large area membranes, less area of graphene membrane is suspended. The inspection under the microscope, the AFM image analysis, roughness parameter analysis and the SEM images of the graphene

samples show clear differences between different graphene samples. This shows that our graphene samples are indeed suspended. But whether they are suspended in parts or entirely cannot be inferred from these results alone. Also why some graphene membranes are collapsed and what is the cause of this collapse cannot be answered from the results obtained till this chapter. This analysis will be presented in chapter 7. Before that, next chapter will discuss the fabrication process flow of the graphene actuator.

# Chapter 5

## Fabrication of the actuator

This chapter explains the fabrication steps undertaken to make an electrostatically actuated graphene resonator (See figure 3.6). It incorporates the details of the various attempts made to integrate the graphene resonator with an actuation electrode and the problems faced during each fabrication cycle along with the lessons learnt. These are incorporated into a new fabrication flow each time. Finally, it presents the fabrication process using which the successful graphene actuator was made. This chapter also incorporates the analysis of the fabricated samples.

### 5.1 Fabrication procedure for buried molybdenum electrodes

The choice of metal is very crucial in fabricating the electrostatically actuated devices. Since molybdenum gave good results as catalyst metal for growing graphene and has a high melting temperature of 2623 ° C (which is needed as for graphene growth we go to temperature as high as 950 ° C , the fabrication process flow of integrating the actuation electrode with the graphene resonator was made initially keeping molybdenum as the choice for buried metal. The following subsection will describe the first fabrication procedure followed to fabricate the graphene actuator.

#### 5.1.1 Fabrication procedure 1

The fabrication procedure started with making alignment markers and then growing thermal oxide on bare silicon wafer, as shown in step (a) in figure 5.1. Figure 5.1 shows a vertical crosssection of the actuator device shown in figure 3.5 in chapter 3. This batch of wafers was fabricated with the first batch of graphene resonators wafers and so it uses the same process parameters used for fabricating graphene resonators in chapter 4. A thick 1000 nm wet thermal oxide is grown on the wafers (step b) to minimize the parasitic capacitances between the silicon wafer and the buried metal as explained in chapter 3, section 3.2. Wet oxides grow much faster than dry oxides and so wet oxidation is used to grow a thicker oxide. Then molybdenum layer (100 nm thick) is deposited on thermal oxide wafer (step c) using DC magnetron sputtering that has been explained in chapter 4, section 4.3. This buried molybdenum metal is patterned and etched in Omega (inductive coupled plasma etcher) using Motest2 recipe (step d). The composite gases involved in this recipe have been explained in chapter 7.

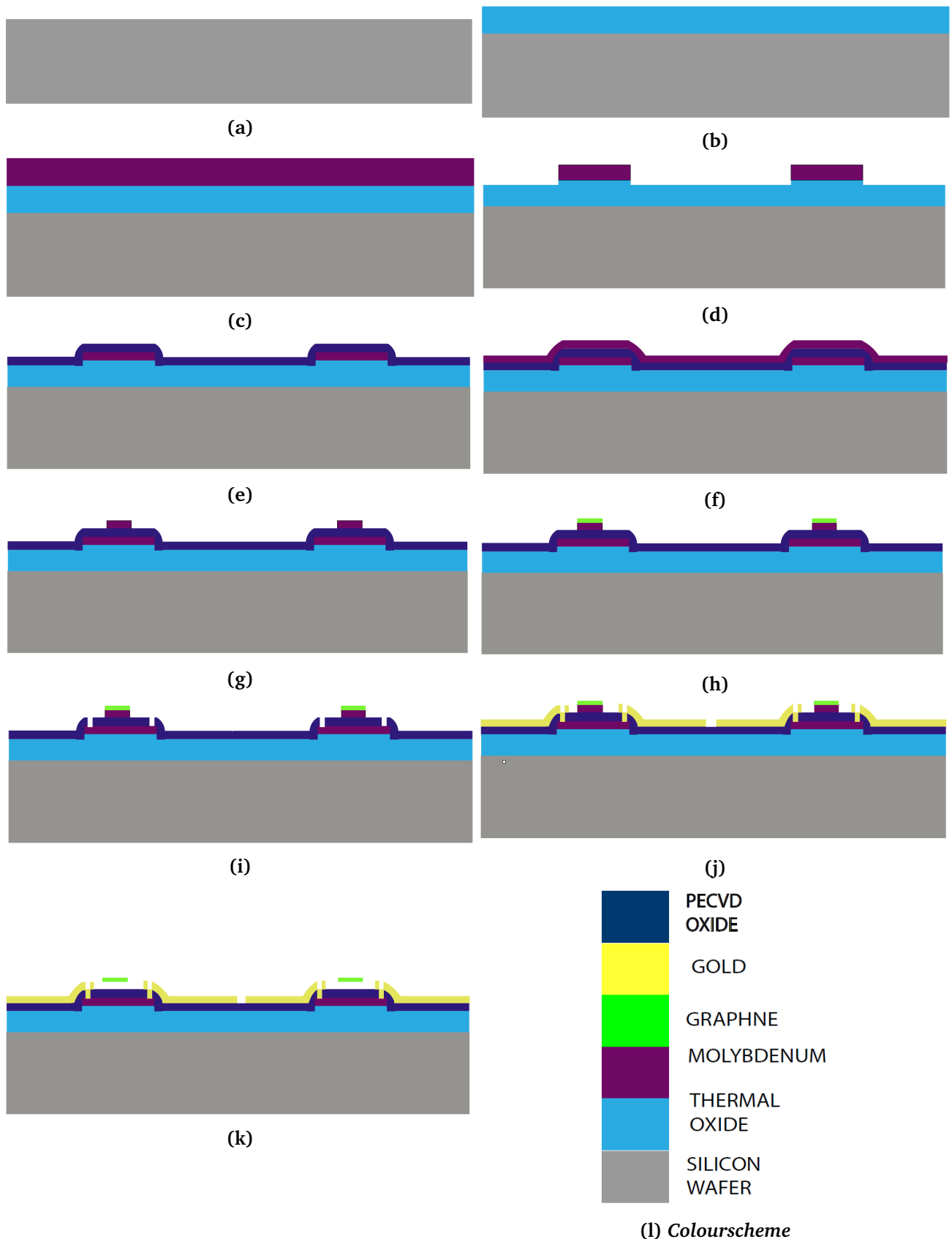


Figure 5.1: Fabrication Process flow of electrostatically actuated graphene resonator (vertical cross section of figure 3.5 in chapter 3)

The actuation electrode needs to be separated from the graphene resonator with a dielectric since it needs to work as an electrostatic actuator. For this we use PECVD oxide deposited at 400° C (step e). Around 100nm thick oxide is deposited on the buried metal molybdenum,

using plasma enhanced chemical vapour deposition process. The reaction that occurs inside the chamber during the process is shown by equation 5.1. Here, silane reacts with nitrogen dioxide to form silicon dioxide at 400° C. The reaction chamber is shown in figure 5.2. The PECVD reactor chamber is a parallel plate capacitor. The top electrode has a showerhead through which all the gases come in. RF generator generates an alternating electric field ( a high frequency generator (13.56MHz) and a low frequency generator(100-350kHz)), that creates an electric discharge between the two electrodes. A plasma is created and the species react among themselves to get deposited on the wafer on the substrate . Mixing of these two frequencies control the ion bombardment on the film deposited and its stress. The recipe used for this process is given in table 5.2

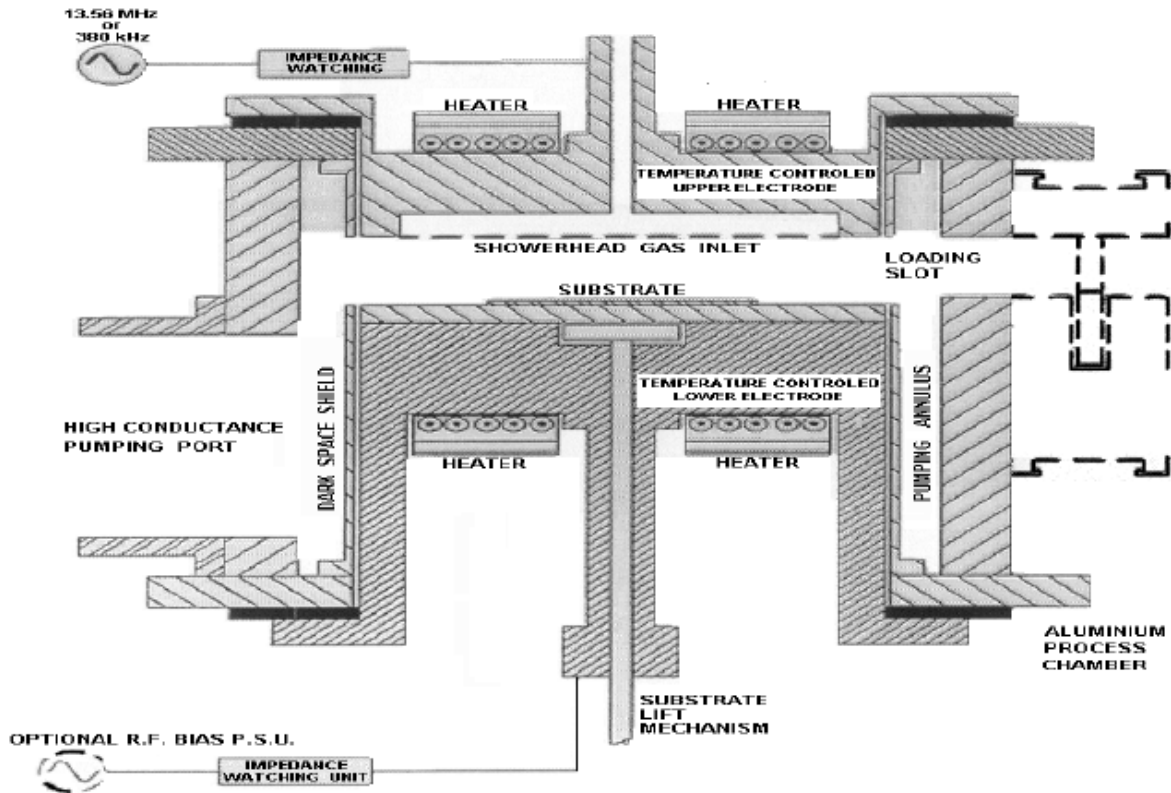
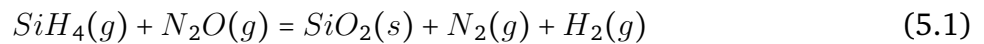


Figure 5.2: PECVD reactor chamber. Taken from [115]



After the deposition of PECVD oxide, the catalyst molybdenum is deposited, step f in figure 5.1 using dc magnetron sputtering process. This is followed by patterning and etching of the catalyst metal molybdenum (step g). Then graphene is grown at 950 ° celsius (step h) using the same recipe explained in chapter 4. Then contact openings are defined using positive photoresist and dark field mask. The oxide in this contact opening is etched away using BHF(1:7) (step i). This is done so that the gold bond pads can be connected to the buried metal molybdenum. After this step , when the samples were observed under microscope, oxide was found to be underetched and peeling off near the contact area openings, as can be seen from figures 5.3a and 5.3b. The gold contacts are deposited using e beam evaporation combined with lift off (step j) and this is followed by etching away of the catalyst molybdenum by peroxide and critical point drying (step k) as explained in chapter 4. The underetching of oxide resulted in the buried molybdenum getting attacked after peroxide etching , as can be seen from figure 5.3c.

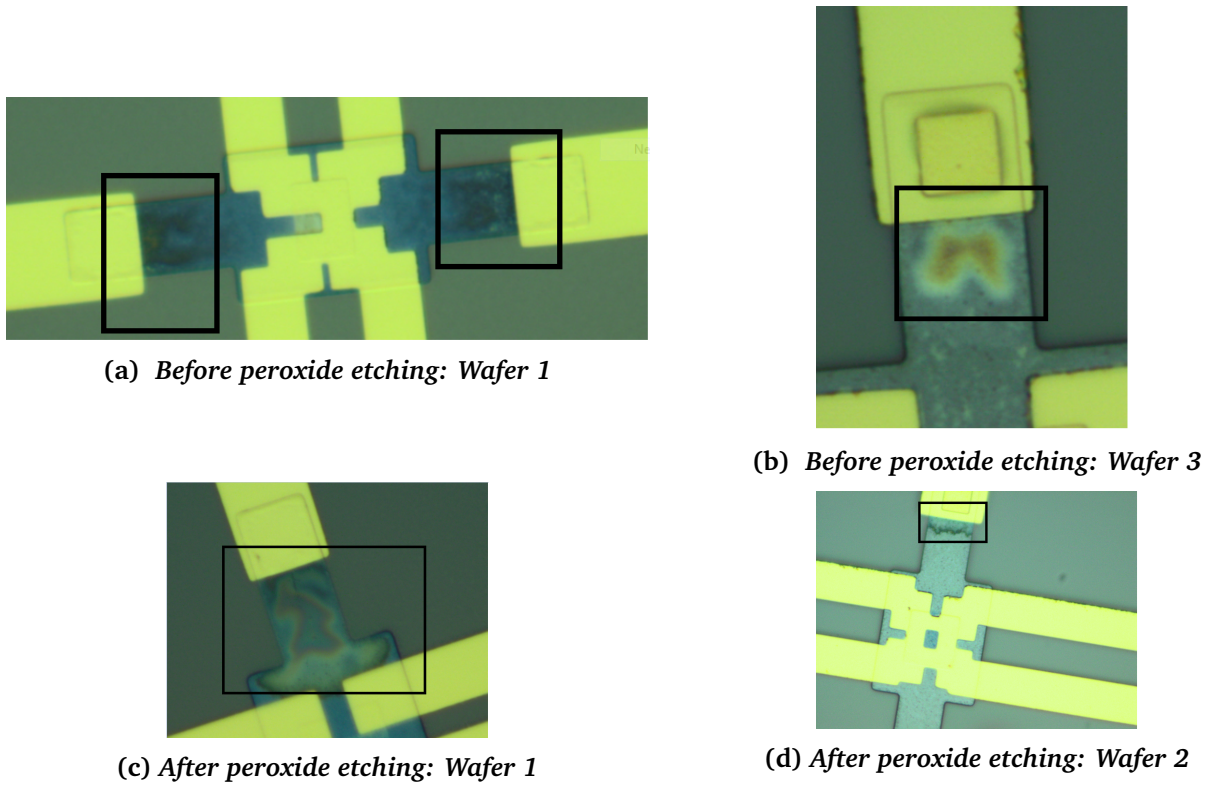


Figure 5.3: Microscope images of the electrostatic devices fabricated using fabrication procedure 1

The wafers fabricated along with the results obtained are presented in table 5.1. None of the samples were suspended. This batch was fabricated with first batch of wafers in chapter 4 and so no process parameter was changed. The issue of suspension will be dealt in later sections. During fabrication of these samples, we encountered issues during wet etching of contact opening which has been resolved in the coming subsection.

Table 5.1: Fabrication procedure 1 parameters and results

Wafer	Thermal Oxide	Buried Molybdenum	PECVD TEOS	Catalyst Molybdenum	Suspended
1	1000nm	100nm	100nm	25nm	×
2	1000nm	100nm	100nm	50nm	×
3	1000nm	100nm	100nm	100nm	×
4	1000nm	100nm	100nm	200nm	×

### 5.1.2 Patterning and etching of buried molybdenum metal

During fabrication of the first batch of wafers, wet etching of oxide using BHF(1:7) to form contact openings led to underetching and peeling off of oxide. This happens due to poor adhesion between molybdenum and PECVD oxide. After photoresist is removed from the molybdenum surface using NMP, there are some organic remains of the photoresist that still remain on the surface of molybdenum. Molybdenum cannot be cleaned in  $\text{HNO}_3$  since it gets etched by  $\text{HNO}_3$ . So, PECVD oxide is directly deposited on this patterned layer of molybdenum with photoresist residues on it. This leads to very poor adhesion between the molybdenum structures and the oxide. When oxide is etched in the contact openings using

BHF, underetching of the oxide leads to breaking away of the oxide due to this poor adhesion between oxide and molybdenum.

A solution to this is found by using PECVD TEOS as hard mask to pattern molybdenum. PECVD TEOS is used because it is denser than PECVD oxide. TEOS (tetraethyl orthosilicate) is a colourless liquid that reacts with oxygen to give silicon dioxide. It is deposited at 350 °C. The reaction chamber that is used to deposit PECVD TEOS oxide is described in figure 5.2. The recipe used for depositing PECVD oxide is given in table 5.2. As can be seen from figure 5.4, first PECVD TEOS is deposited on molybdenum, followed by patterning and etching of this layer using reactive ion etching (shown in figure 5.5). Then the molybdenum layer is etched using inductive coupled echer. The molybdenum structures remain protected by PECVD TEOS oxide layer on top of them. This oxide is etched away using BHF. This way, any photoresist remaining on the PECVD TEOS oxide would go away with it. After this when PECVD TEOS is deposited on the molybdenum structures to be used as dielectric, the adhesion between them is found to be very good.

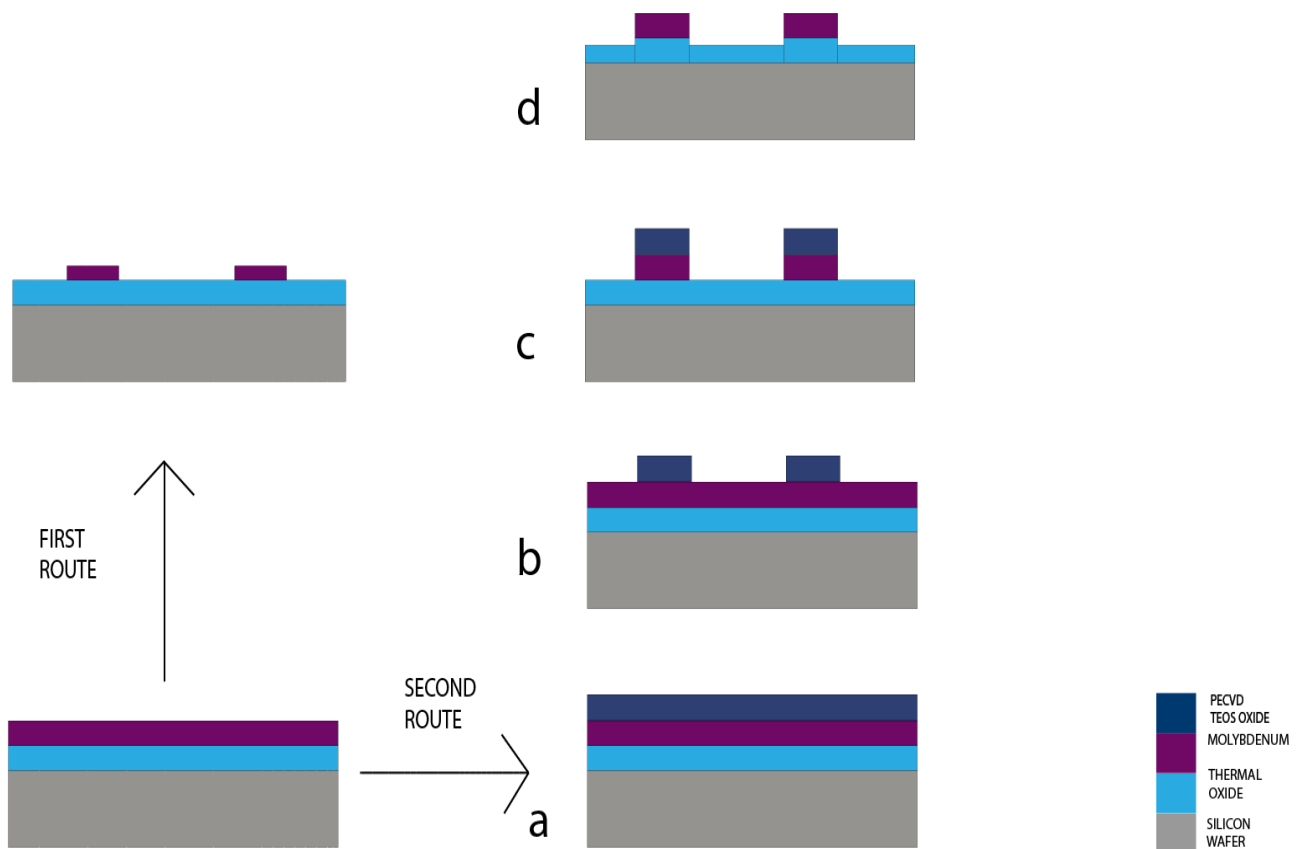


Figure 5.4: Two routes to pattern buried molybdenum

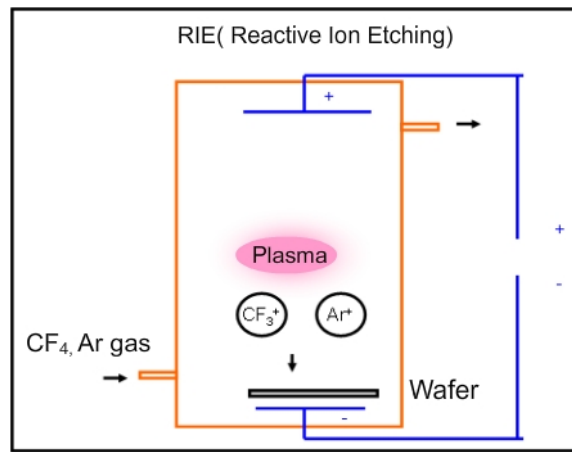


Figure 5.5: Schematic representation of a reactive ion etcher. [116]

Table 5.2: Recipes:PECVD and PECVD Oxide

	HF Power	LF Power	Pressure	Temperature	Time (per station)
PECVD Oxide(100nm)	1kW	0kW	2.2 Torr	400 °celsius	1.4s
PECVD TEOS(100nm)	0.5 kW	0.5kW	2.2 Torr	350 °celsius	3.3s

Wafer 5, was fabricated using the second route shown in figure 5.4 and the adhesion of the oxide to the metal molybdenum was found to be good. There was no underetching or undercut visible after wet etching with BHF, as can be seen in figure 5.6c. Wafer 5 was also optimized for getting the correct sheet resistance which has been explained in the next subsection.

### 5.1.3 Sheet resistance of buried molybdenum metal

Chapter 3, section 3.3.2 presents the design of Wheatstone bridge configuration of a graphene membrane. The resistivity value of molybdenum is considered to be  $10.1 \mu\Omega cm$  for all the calculations. From this value, the sheet resistance comes out to be  $1.01 \Omega/square$  for 100nm thick molybdenum. This value was taken from old laboratory records. However, when measured, 100nm thick molybdenum gave a higher sheet resistance value. Infact for every batch of wafers, the sheet resistance value fluctuated even for the same thickness of molybdenum. This constant change in sheet resistance value of a metal is intriguing. Equation 5.2 gives the relation between sheet resistance  $R_s$ , resistivity  $\rho$  and thickness  $t$ , of a material.

$$R_s = \frac{\rho}{t} \quad (5.2)$$

Past research shows resistivity of molybdenum sputtered by D.C magnetron sputtering changing with argon pressure in the chamber [117] and with the deposition power used[118]. It has been shown that molybdenum thin film sputtered at high argon pressures have more porous structures and higher resistivity. This happens because there are more multi gas phase collisions and so the energy of the sputtered atoms is reduced at high pressure. Even



the angle at which the sputtered atoms hit the substrate becomes more slanting [117]. At decreasing pressure there is less scattering of sputtered molybdenum species and so the layer formed is more dense and has a lower resistivity [117]. Two molybdenum samples deposited on soda lime glass at different deposition powers have shown different resistivity values. The sample deposited at higher DC power (200W) showed lower resistivity value and higher average surface roughness as compared to the sample with molybdenum deposited at lower DC power [118]. A higher deposition power leads to larger amount of sputtered molybdenum species at the surface which gives a higher surface roughness [118]. For the deposition at lower power, there is a decrease in the number of molybdenum species arriving at the substrate which leads to a porous structure [118]. The lower resistivity in film deposited at higher DC power is attributed to a higher density and lower defects in the layer formed [118]. In our case also a change in the argon pressure and DC power has been seen for sputtered molybdenum films of same thickness, especially for wafers sputtered with molybdenum on different days. Some of these are given in table 5.3. These two factors could be playing role in changing the resistivity and so the sheet resistance of the molybdenum film. The changes we see in the sheet resistance values are in the order of 1 % to 3%.

**Table 5.3: DC Power and Argon Pressure values for wafers fabricated at different times**

Thickness	Argon Pressure(mTorr)	DC Power(kW)
100nm	8.32	0.960
100nm	8.28	0.933
100nm	8.42	0.970

In our case, since the sheet resistance of 100 nm of molybdenum was not what we expected, the thickness of the metal had to be varied to get sheet resistance value of  $1.01 \Omega / \text{square}$  according to equation 5.2. First, sheet resistance of a test wafer with 100nm molybdenum was measured and then the thickness was calculated to get the correct sheet resistance for wafer 5. The thickness of the molybdenum calculated came out to be 166.3nm. Since wafer 5 was sputtered with 166.3nm molybdenum just after the test wafer, the sheet resistance value of the wafer did not fluctuate much and was quite close to  $1.01 \Omega / \text{square}$ .

The parameters used for wafer 5 are given in table 5.4. Wafer 5 was optimized for correct sheet resistance and also showed no issues during wet etching of oxide for contact openings. However, after release, as can be seen from figures 5.6a and 5.6d, the buried molybdenum was attacked from the edges. The issue arises because of using oxide hard mask which creates a step difference. When PECVD TEOS oxide on top of molybdenum is etched in BHF, BHF also attacks the thermal oxide on the wafer. This creates a step difference between the thermal oxide underneath molybdenum and the thermal oxide on the remaining part of the wafer (see step d of figure 5.4). Even after using a thick oxide of 300 nm, molybdenum was attacked from the edges. This could be due to thinning of the PECVD oxide at the edges which happens because of a step difference created in thermal oxide by using PECVD TEOS oxide as hard mask.

**Table 5.4: Wafer 5 Parameters**

Wafer	Thermal Oxide	Buried Molybdenum	PECVD TEOS	Catalyst Molybdenum	Suspended
5	1000nm	166.30 nm	300nm	100nm	×

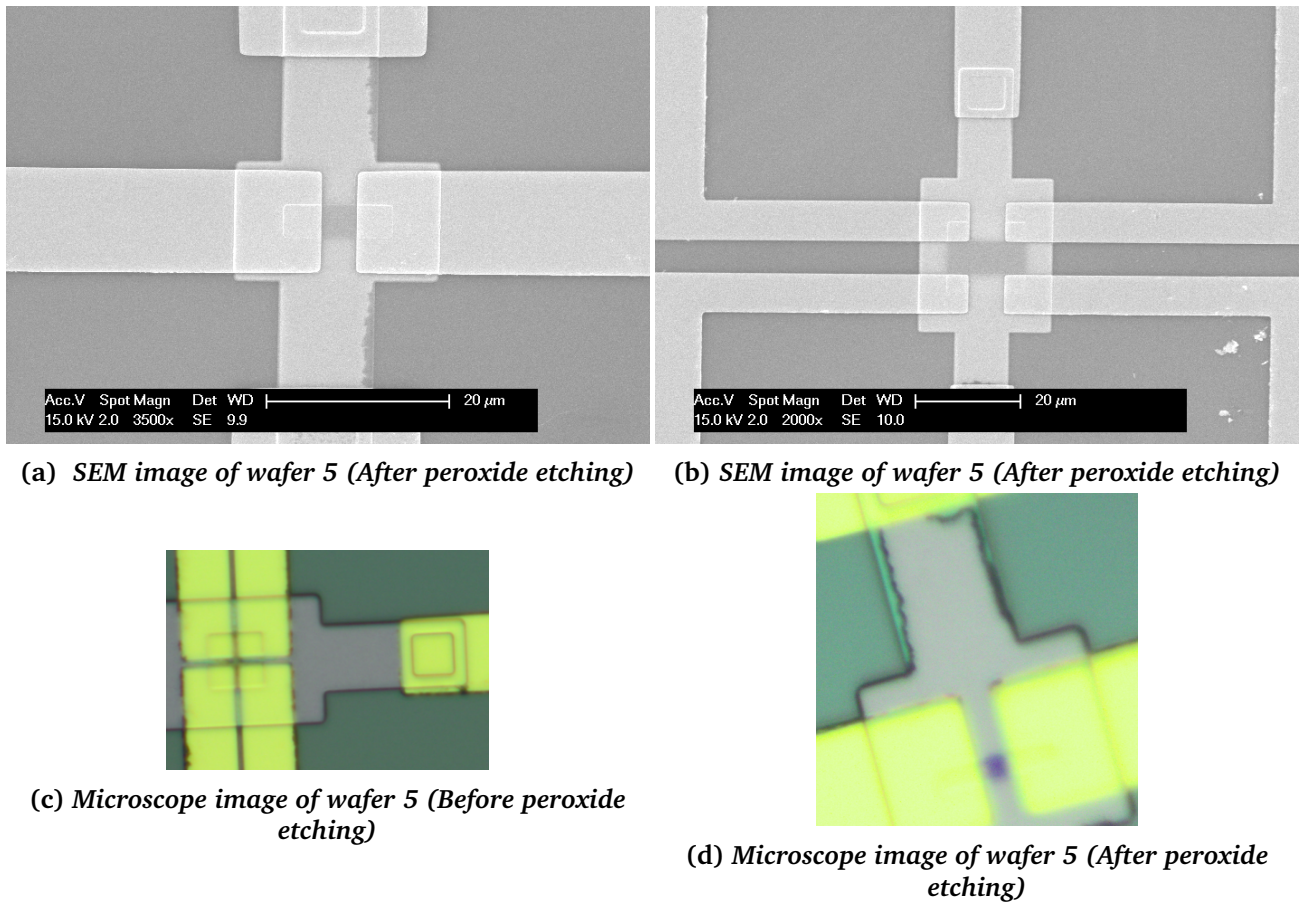


Figure 5.6: SEM and microscope images of wafer 5

The wafer in this case were also not suspended. A graphene actuator has two more layers (the electrode and the dielectric layers) in addition to the layers of the graphene resonator. It is difficult to say how the addition of the buried metal layer and the dielectric layer would affect the suspension of graphene. Hence, a batch of wafers was fabricated, described in the coming subsection, to test suspension of graphene on these four layers.

#### 5.1.4 Fabrication procedure 2

This batch of wafers was fabricated after the cause of collapsing membranes was investigated (See chapter 7. Hence, the two factors which were causing the collapse of the membranes in the earlier batches were eliminated for this batch of wafers. One of the factors, the Motest2 etching recipe was replaced by Mo50 etching recipe. Also, the thickness of thermal oxide was reduced. The idea was to minimize the total thickness of the device and keep the overall thickness of the composite layers as thin as possible and so four wafers were fabricated which are given in table 5.5 with the thicknesses of the layers used during processing . The rest of the process used for the fabrication of this batch is similar to one described for wafer 5.

Table 5.5: Fabrication Procedure 2 Parameters

Wafer	Thermal Oxide	Buried Molybdenum	PECVD TEOS	Catalyst Molybdenum
6	90nm	150nm	120nm	100nm
7	50nm	25nm	120nm	25nm
8	50nm	50nm	120nm	50nm
9	90nm	50nm	120nm	50nm

Before peroxide etching, the devices were inspected under the microscope and they were showing no peeling off or delamination as can be seen from figure 5.7.



Figure 5.7: Microscope images of the devices fabricated : fabrication procedure 2

These devices when released , showed abnormal structures and so whether the graphene membranes are suspended or not could not be examined properly. SEM and AFM images of the devices inspected after release have been shown in figures 5.8 and 5.10. It can be clearly seen from the images that the buried molybdenum metal has been attacked during peroxide etching. The following factors could be responsible for attacking of the buried metal electrode

1. Step Height: As explained the previous sections, using a hard mask leads to a step difference and subsequently thinning of oxide at the edges. This makes it easier for peroxide to attack the metal from the edges.
2. Molybdenum etching: When unmasked molybdenum on PECVD oxide is etched , the oxide beneath it is also partly etched. For these four devices fabricated, the PECVD oxide used is 120 nm thick. However, after etching of the molybdenum the oxide becomes thinner. Thin PECVD layer is more sensitive to pin holes. So, it could be possible that while etching the catalyst molybdenum using peroxide in the final step, the peroxide is able to reach the buried molybdenum via the thin defective PECVD TEOS layer.

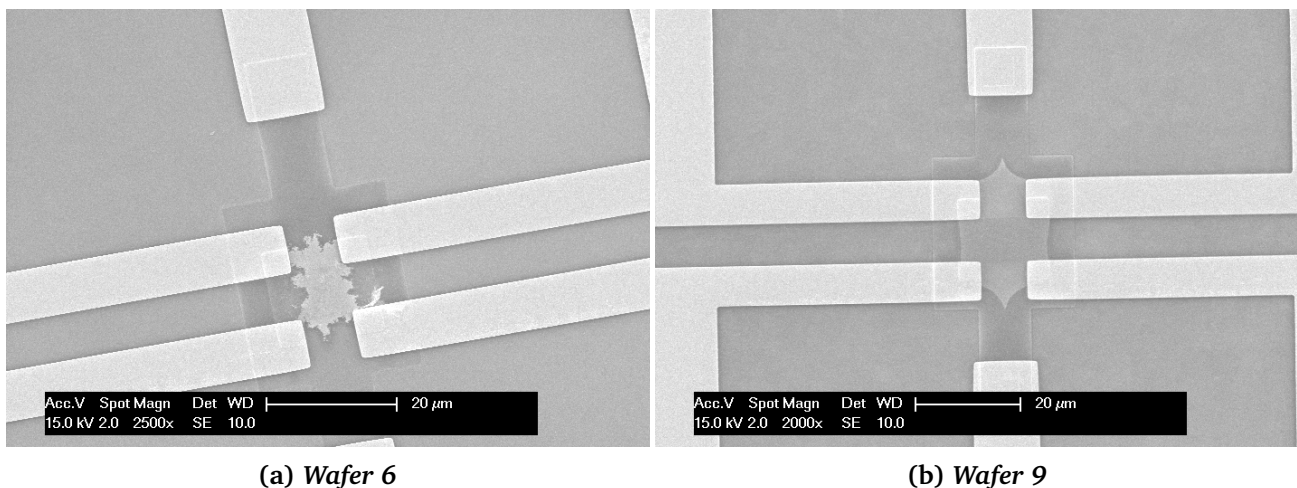


Figure 5.8: SEM images of the devices fabricated : fabrication procedure 2

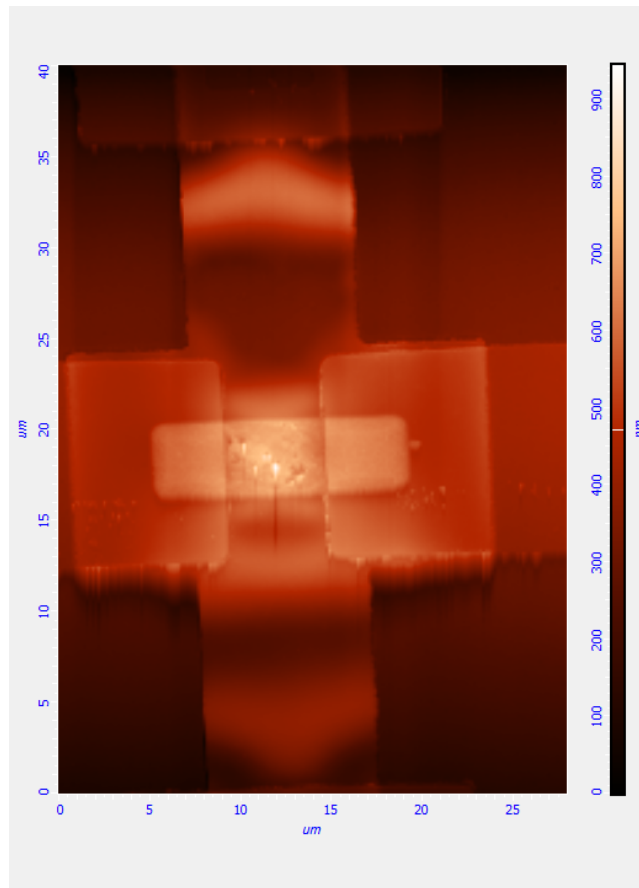


Figure 5.10: AFM images of the devices fabricated on wafer 6

We tried to overcome these problems by fabricating another batch of wafers which has been described in the coming subsection.

### 5.1.5 Fabrication procedure 3

In order to circumvent the issues faced during fabrication of the previous batch of wafers, wet etching of contact openings was replaced with plasma etching and thickness of PECVD oxide was increased to 300nm so that during peroxide etching the buried molybdenum metal is not attacked. Another solution tried is using molybdenum covered with 50 nm titanium nitride as the buried actuation electrode. Using titanium nitride would protect the topside buried molybdenum during peroxide etching. The parameters of the wafer fabricated are given in table 5.6.

Table 5.6: Fabrication procedure 3: parameters of wafers fabricated

Wafer	Buried electrode	Thermal Oxide	Thickness of electrode used	PECVD Oxide	Gap size
10	Molybdenum + Titanium nitride	90nm	100nm + 50nm	300nm	100nm
11	Molybdenum	90nm	100nm	300nm	100nm

The fabrication procedure used to fabricate wafers 10 and 11 is similar to the fabrication procedure 2. Plasma etching was used to etch the contact openings using reactive ion etcher which has been shown in figure 5.5. There are two electrodes. The top electrode is grounded and the bottom electrode is negatively charged. The RF generator creates an alternating field

between the electrodes which creates a plasma of the gases inside the chamber. The ionized species are accelerated towards the bottom electrode where they etch away the film.

For the wafer 10, some white particles were seen all over the wafer (see figure 5.11a), after using reactive ion etcher to etch away the unmasked oxide on the wafer. These particles stayed on the device even after remaining thermal oxide was etched away in BHF. It is unknown what these particles are. They could have been a result of some reaction of titanium nitride, molybdenum and fluorine gas, since the reactive ion etcher uses fluorine gas.

As can be seen from figure 5.11 and 5.12, the graphene membrane was not suspended in both these cases even after using mo50 etching recipe and thin thermal oxide. Also, the oxide on top of the metal in both cases is not uniform. It either reacted with molybdenum at high temperature or some other chemical reaction during the fabrication procedure led to this non uniformity of oxide on the metal. Whatever maybe the case, these results clearly indicate that using molybdenum as the buried electrode is not a good option from both device and suspension of graphene membrane point of view. Hence, the next subsections look into other metal/semimetal electrodes.

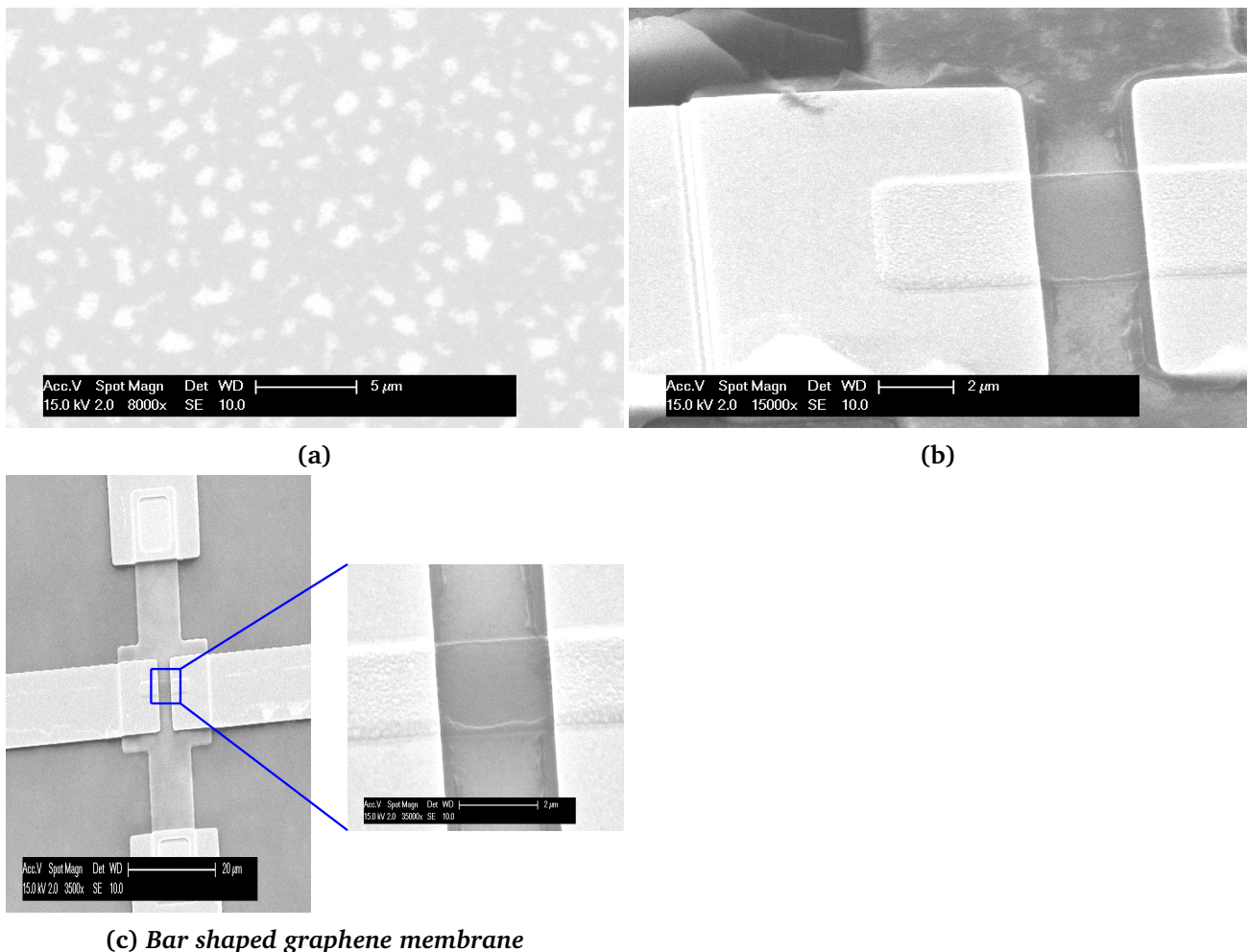


Figure 5.11: SEM images of collapsed graphene membranes on molybdenum + titanium nitride electrodes

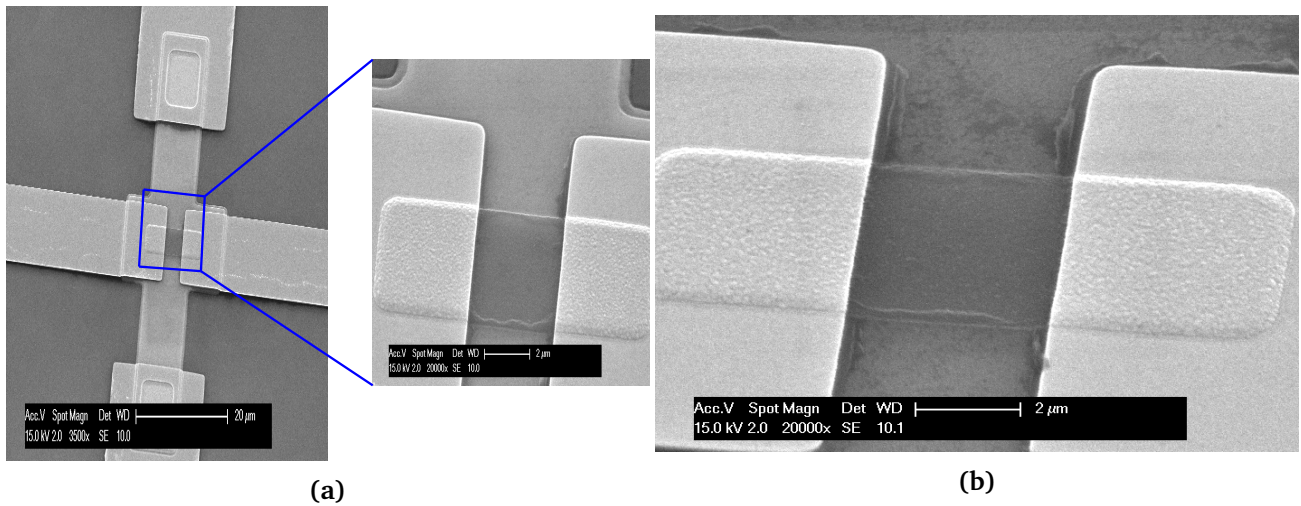


Figure 5.12: SEM images of collapsed graphene membranes on metal molybdenum electrodes

## 5.2 Fabrication of suspended graphene membranes with different types of electrodes

As seen in the previous section, using a buried molybdenum electrode the device had many issues. Hence, other options for the actuation electrode were explored. One of the important criteria to be considered while choosing the material which could be used as electrode is its melting temperature. Since during graphene growth, we go to high temperature such as 950 ° Celsius, the melting temperature of the conductor should be considerably higher than 950 ° Celsius. Another factor considered is the availability of the material in our laboratory. The melting temperature of the different metal/semi metal available in our laboratory which could be used as the buried electrode are given in table 5.7. The different metals used as actuation electrode along with their thicknesses are given in table 5.8. The flowchart for the fabrication of graphene resonators with actuation electrode polysilicon and niobium is included in appendix .1.

Table 5.7: Melting temperature of different metals/semi-metals

Buried electrode	Melting temperature (° celsius)
Polysilicon	1409.85
Niobium	2469.00
Titanium	1668.00
Titanium nitride	2930.00

Table 5.8: Wafers fabricated with different types of buried metal electrodes

Buried electrode	Thermal Oxide	Thickness of electrode used	PECVD Oxide	Gap size
Doped Polysilicon	90 nm	99 nm	100 nm	200 nm
Niobium	90 nm	100 nm	100 nm	100 nm
Titanium nitride + Titanium	90 nm	100 nm + 10 nm	100 nm	100 nm

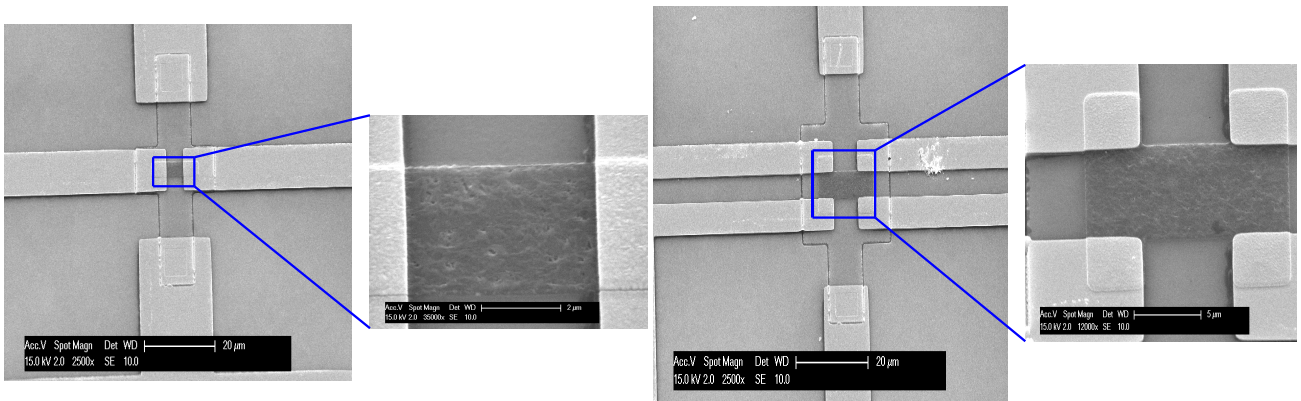
### 5.2.1 Polysilicon

Polysilicon is ultra pure form of silicon. It is polycrystalline in nature that is it is composed of many small crystals. It is deposited using LPCVD (low pressure chemical vapour deposition) furnace. The reaction that takes place is given in equation 5.13, which occurs at 500-800 ° C [119].



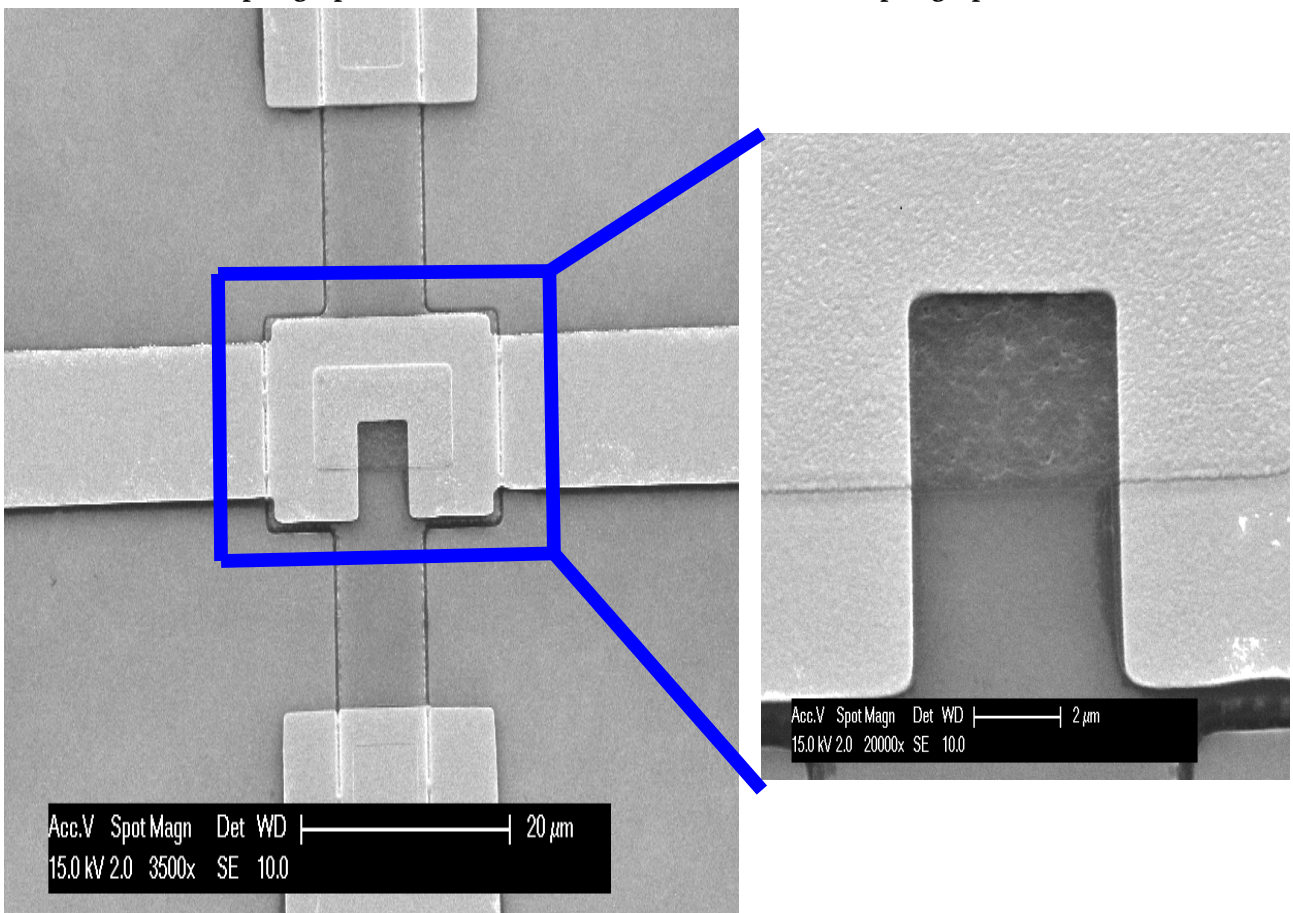
Polysilicon is then doped by boron atoms. This is done in order to improve the contact resistance and lower the sheet resistance of polysilicon. Route 1 of figure 5.4 is adopted and polysilicon is directly patterned and etched. Polysilicon can be cleaned in HNO<sub>3</sub> after etching and so any photoresist residues will be removed from the polysilicon surface during cleaning. So, the adhesion between polysilicon and the PECVD TEOS oxide is good. Hence, oxide is not used as a hard mask to pattern polysilicon. Another critical step is the opening of the contacts. As seen in the previous case of molybdenum, this step caused undercut which led to breaking of oxide. However, since polysilicon does not react with BHF and moreover the adhesion of PECVD TEOS oxide on polysilicon is good, wet etching with BHF does not create any issues such as undercut or breaking away of the oxide. The choice of 200nm catalyst molybdenum for polysilicon was not made because of any specific reason. It was chosen arbitrarily.

The sem images of the fabricated graphene samples with polysilicon electrode are shown in figure 5.13. The 3D AFM image is shown in figure 5.14.



(a) Bar shaped graphene membrane

(b) H shaped graphene membrane



(c) Three sided graphene membrane

Figure 5.13: SEM images of suspended graphene membranes on polysilicon electrodes



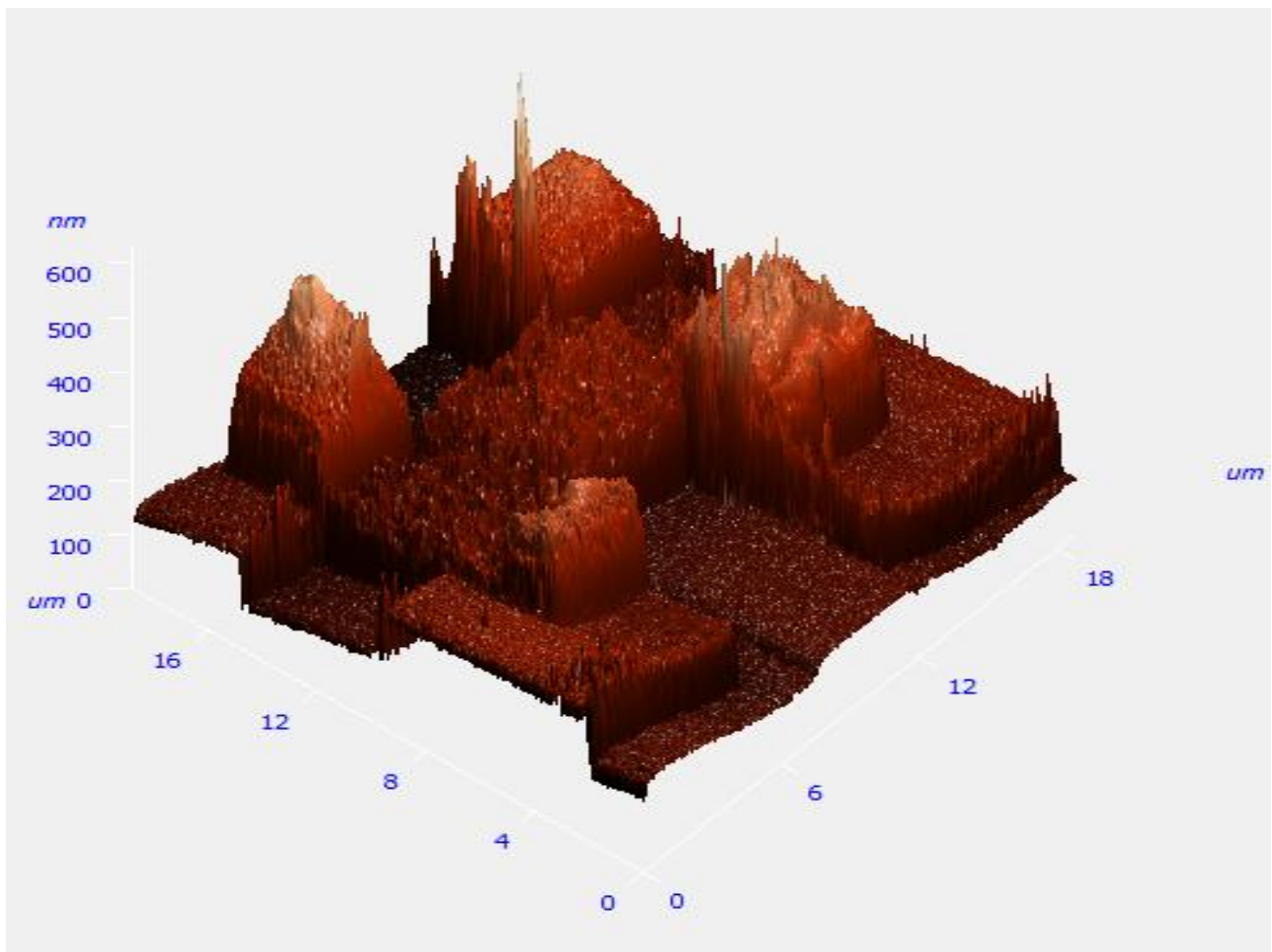


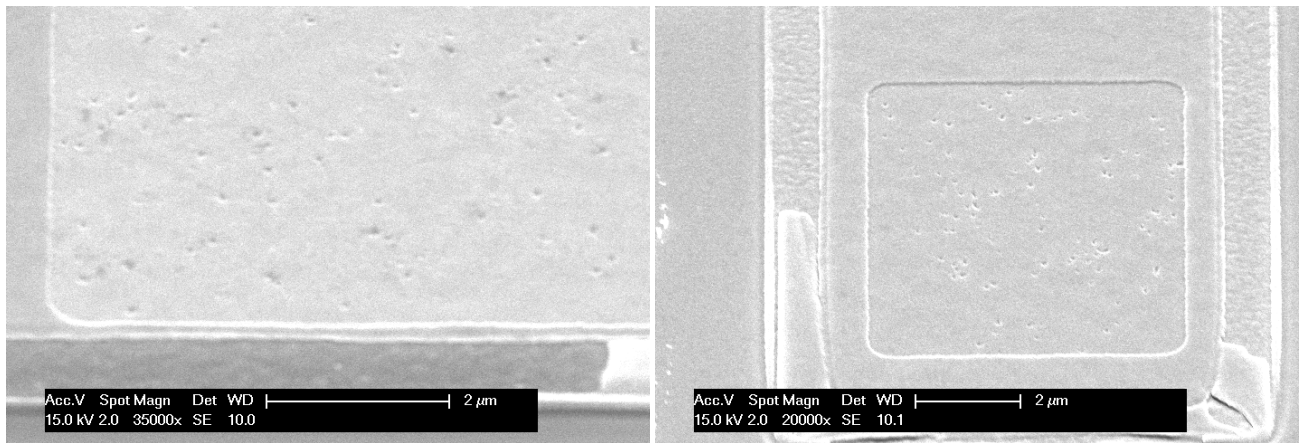
Figure 5.14: 3D AFM image of graphene membrane suspended on polysilicon electrode

### 5.2.2 Niobium and titanium nitride + titanium

The other two electrodes that were tried as the actuation electrode are niobium and titanium nitride. Both of these electrodes were deposited using DC magnetron sputtering process. Also, both these metals can be cleaned in  $\text{HNO}_3$  after photoresist removal and so the adhesion between oxide and the metal should not be a problem. So, no oxide hard mask was required to pattern them. Wet etching was used to open contact openings for both these metals as BHF does not react with either of them.

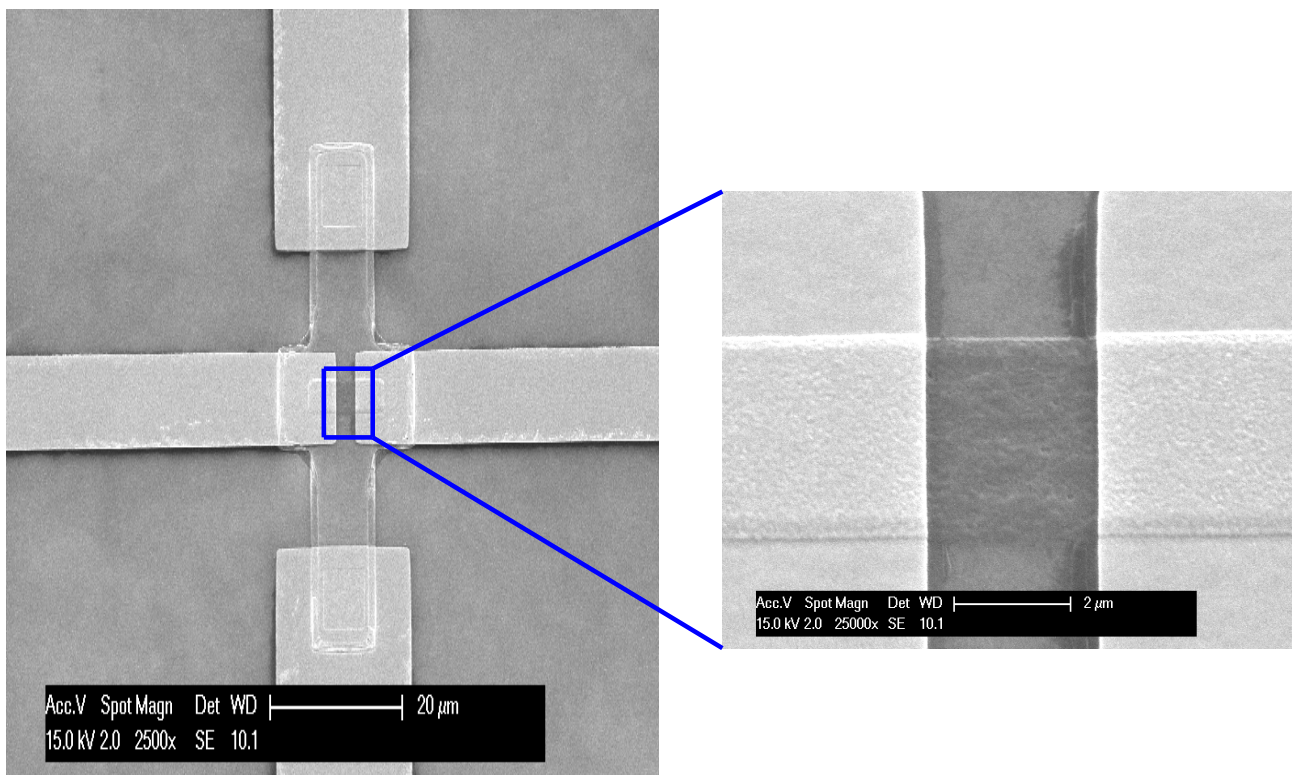
Figure 5.15a and 5.15b show SEM images of the contact opening to the niobium electrode before and after gold deposition. These images show porous structure. These porous structures indicate that niobium might have reacted with oxide to form a different compound. It is suspected that BHF forms pores on this oxide during etching [120].

As can be seen from figures 5.15c, 5.16, 5.17 and 5.18, graphene membrane is suspended on niobium electrode but not on titanium nitride electrode even though both have the devices went through the same fabrication procedure and have similar parameters. This shows that choice of metal is very crucial in fabricating the graphene electrostatic devices.



(a) Contact opening before gold deposition

(b) Contact opening after gold deposition



(c) Bar shaped graphene membrane

Figure 5.15: SEM image of graphene membrane on niobium electrode

5.2. FABRICATION OF SUSPENDED GRAPHENE MEMBRANES WITH DIFFERENT TYPES OF ELECTRODES

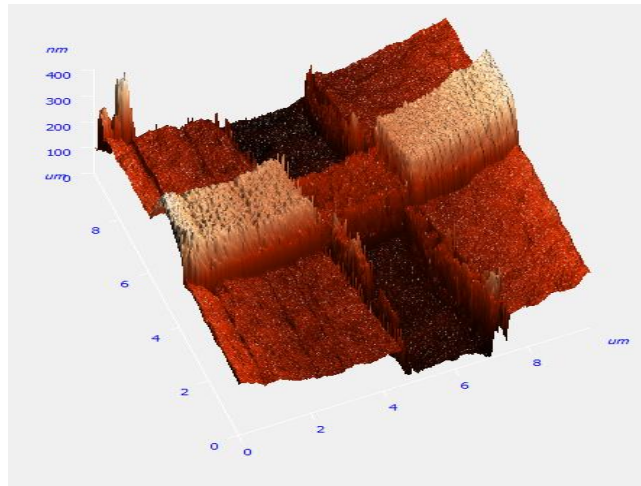
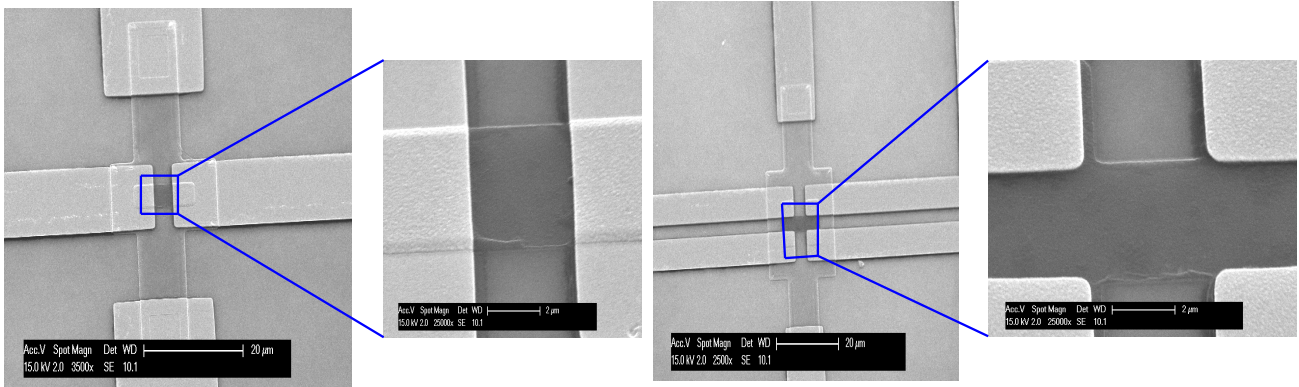


Figure 5.16: 3D AFM image of graphene membrane on niobium electrode



(a) Bar shaped membrane

(b) H shaped membrane

Figure 5.17: SEM images of collapsed graphene membranes on Titanium nitride + Titanium electrode

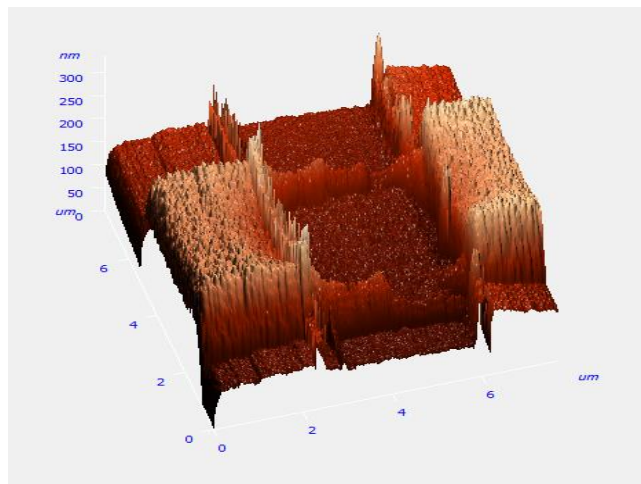


Figure 5.18: 3D AFM image of graphene membrane on TiN + Ti electrode

### 5.3 Summary

This chapter presented the various attempts made to fabricate suspended graphene membrane on a buried electrode. The various failed attempts made to incorporate molybdenum as the buried actuation electrode pointed towards using other metal electrodes. Finally, graphene membrane is suspended on polysilicon and niobium electrodes. More results will be presented in chapter 7 to find out if the graphene membrane is fully suspended or not. The fact that graphene membrane is suspended on some metals and not on others points towards the changing stress that could be responsible for the collapse of the membranes.

Next chapter presents the characterization and the various measurements performed on these fabricated graphene samples.

# Chapter 6

## Measurements

### 6.1 Dynamical characterization

In order to know whether the graphene samples fabricated in chapter 4 and 5, can be used as a resonator and subsequently as a sensor, there is a need to characterize the dynamical properties of the graphene membrane and measure its resonant frequency. A quick way to characterize the resonant frequency of graphene membranes with high throughput is by using laser interferometry setup. In the past, this setup has been used time and again to measure the resonant frequency of the graphene membranes [8, 121]. Such a system is available to us and the resonant frequency measurements of the graphene samples using this setup has been described in this subsection.

#### 6.1.1 Resonant frequency measurements using laser interferometry setup

The schematic representation of the optical setup used to perform these measurements is shown in the figure 6.1. The sample is mounted in a vacuum chamber which has a stage that can be moved in x, y and z direction. Changing the x and y direction, moves the sample left/right or top/bottom respectively and the z direction changes the focus of the sample. The blue laser (405nm diode laser), gets reflected by dichroic mirror and hits the graphene sample. This is used to actuate the graphene membrane by optical adsorption and thermomechanical force [25]. The red laser (632 nm He-Ne laser) is used to detect the mechanical motion of the graphene membrane. A polarized beam splitter allows the incoming light from the red laser to transmit which becomes circularly polarized after passing the quarter wave plate. The dichroic mirror allows this red light, to pass through it. The red laser light hits the graphene membrane and the back plate silicon and gets reflected by both, which causes interference between the two reflected lights. This interference of light is reflected by the polarized beam splitter to the photodiode. The vector network analyzer shows the frequency spectrum of the resonating sample by detecting the red laser and modulating the intensity of blue laser [122, 123].

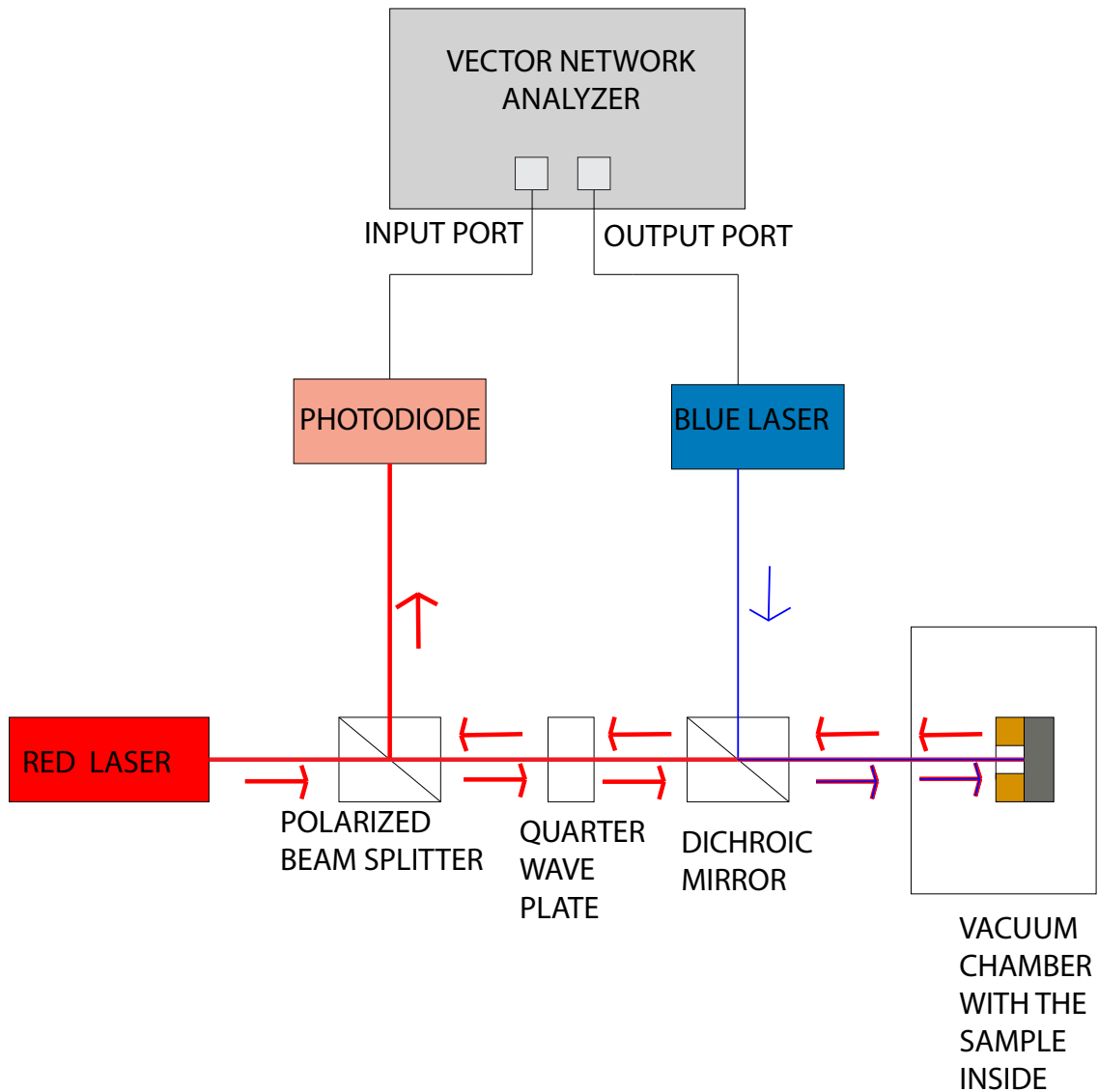
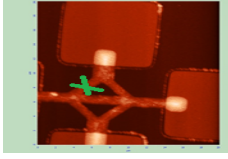
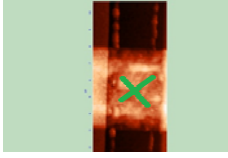
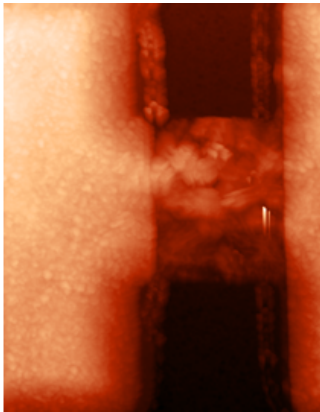


Figure 6.1: *Laser interferometry setup*

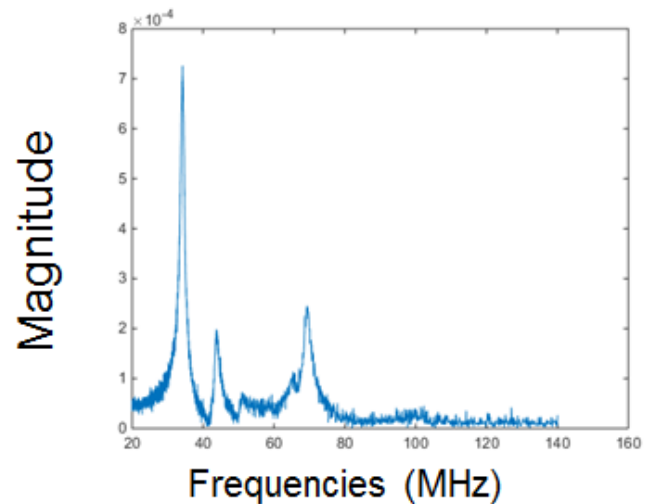
For the 200nm gap size suspended graphene membrane, resonant frequency measurements are shown in table 6.1. Also, various coupled frequencies were observed for some of the structures. One of these has been shown in figure 6.2. The fact that all our graphene resonator structures have a suspended gold part along with suspended graphene membranes could be responsible for getting these coupled frequencies.

**Table 6.1: Resonant frequencies observed for 200nm gap size graphene resonators. The cross is where the resonant frequency is observed**

Structure	Size ( $\mu\text{m}$ )	Resonant frequency (MHz)
	$3.5 \times 1$ bar	83
	$4 \times 4$ bar shaped	99



(a)  $4 \times 4$  Hbar structure



(b) Coupled resonant frequencies observed

**Figure 6.2: Resonant frequency measurements using optical setup**

No measurement results were obtained for any of the 100nm gap size graphene membrane sample using the optical setup. This could be because only parts of the membrane were suspended or due to alignment laser issues. It could also be due to less power being delivered from the blue laser which is not enough for the membrane to heat up and actuate.

One of the major difficulties faced during this measurement was to perform the experiment by keeping the red and the blue laser on the same spot. This way, it became difficult to say which part of the device (suspended gold or suspended graphene) is responsible for giving the fundamental frequency. This problem has been addressed in the next subsection.

### 6.1.2 Gold resonance

All the devices fabricated in this work, have a suspended gold part also along with the suspended graphene membrane. This is because there is some part of gold that grows on molybdenum and when this molybdenum is released at the end of the fabrication, gold is suspended for that part. Hence, the devices fabricated are coupled devices with both, parts of gold and graphene suspended. So, the resonant frequencies obtained from the laser

interferometry setup could be due to suspended gold , suspended graphene membrane or both. In order to understand, which part of device (graphene, gold or graphene-gold ) is giving the fundamental frequency, the fundamental frequencies were recorded for three sets of contact resistance structures. Figure 6.3 shows the design of the Rc structures used and explains the different parts of the device. These structures were used because the length of the graphene membrane ( $L_g$ ), width of the graphene membrane ( $W_g$ ) and width of the suspended gold part ( $W_s$ ) remains constant for each set of ( $L_g \times W_g$ ) Rc structures with only the length of the suspended part of gold ( $L_s$ ) increasing in that set of Rc structures. Hence, by using these structures it becomes easy to analyze if the graphene membrane is moving or gold.

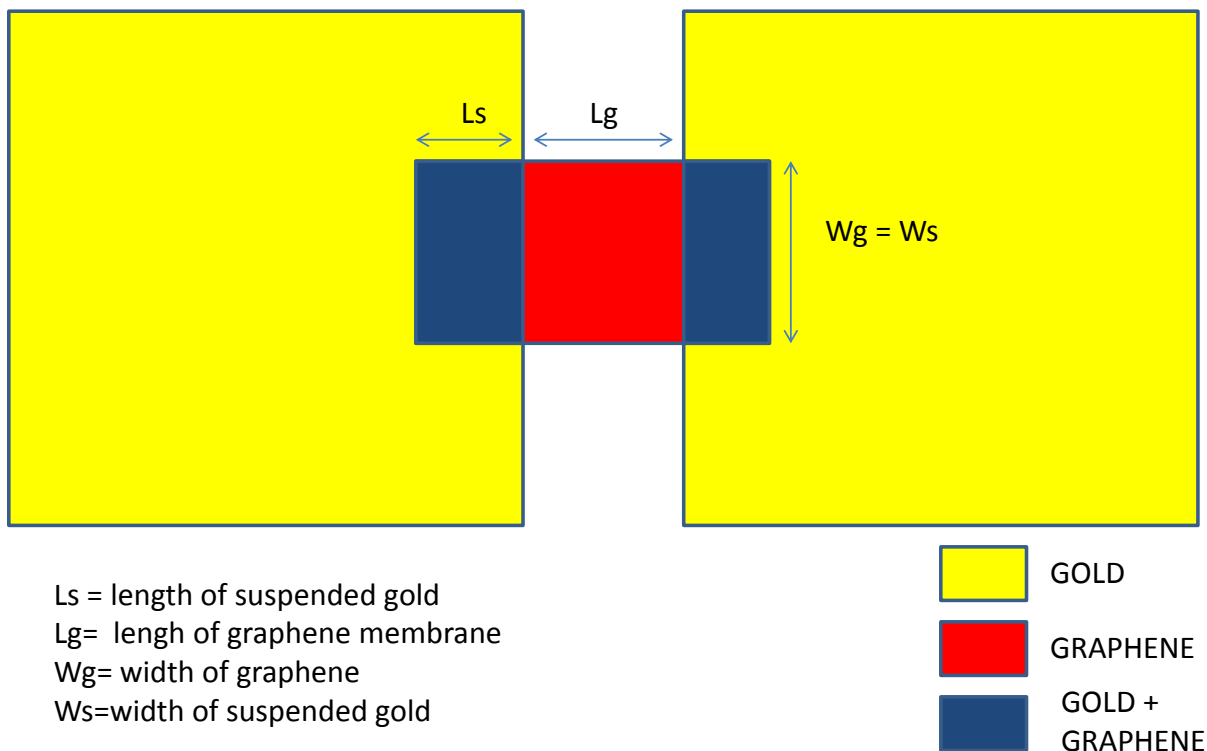


**Figure 6.3: Rc structure used for analyzing gold resonances**

The fundamental frequencies obtained for  $6 \times 4$  ,  $4 \times 4$  and  $5 \times 3$  Rc structures by using the interferometry setup is given in the table 6.2, 6.3 and 6.4 respectively. As can be seen from table 6.2 and table 6.3 , except for the first reading for length  $2 \mu m$ , the fundamental frequencies obtained from the interferometry setup are similar for  $6 \times 4$  Rc structure and  $4 \times 4$  Rc structure. It indicates that the fundamental frequencies obtained are not due to graphene motion since the length of the graphene membrane is different in both these devices which should be giving different resonant frequencies. These resonances could be due to to gold contact moving since the length ( $L_s$ ) and width ( $W_s$ ) of the gold contact remains same for both the set of devices,  $6 \times 4$  Rc structure and  $4 \times 4$  Rc structure .To confirm this, a comsol simulations were used. A plate model is used to do simulations on suspended part of gold. The frequencies obtained the suspended part of gold for all the three structures,  $6 \times 4$  ,  $4 \times 4$  and  $5 \times 3$  Rc structures are noted down in the tables 6.2, 6.3 and 6.4 respectively. The



comsol simulation results are shown in figure 6.4. It can be seen clearly that the obtained frequencies from the interferometry setup are similar to ones obtained by comsol simulations for all the three set of Rc structures. This proves that fundamental frequencies obtained are due to the suspended gold moving and not graphene. In [73], it has been reported that the fundamental frequencies of the beam, which depend on pressure due to squeeze film effect, are graphene modes. However, since the fabrication procedure used in this work is similar to [73] and the structure fabricated in [73] also has a gold-graphene interface, the reported graphene modes should be due to suspended gold moving and not graphene.

**Table 6.2: Frequency analysis for the  $6 \times 4$  Rc structure**

<b>Suspended Gold length <math>L_s</math> (<math>\mu\text{m}</math>)</b>	<b>Frequency from interferometry setup (MHz)</b>	<b>Frequency simulated in COMSOL (MHz) , <math>W_s = 4 \mu\text{m}</math></b>
2	38.50	34.76
4	33.66	27.60
6	31.14	26.62
8	28.20	26.29
10	30.30	26.09
12	29.18	25.86
14	26.24	25.71
16	28.20	25.55
18	27.36	25.30
20	29.60	25.19

**Table 6.3: Frequency analysis for the  $4 \times 4$  Rc structure**

<b>Suspended Gold length <math>L_s</math> (<math>\mu\text{m}</math>)</b>	<b>Frequency from interferometry setup (MHz)</b>	<b>Frequency simulated in COMSOL (MHz) , <math>W_s = 4 \mu\text{m}</math></b>
2	50.32	34.76
4	32.82	27.60
6	30.72	26.62
8	28.90	26.29
10	26.94	26.09
12	26.80	25.86
14	27.22	25.71
16	24.28	25.55
18	26.94	25.30
20	29.18	25.19

Table 6.4: Frequency analysis for the  $5 \times 3$  Rc structure

Suspended Gold length $L_s$ ( $\mu\text{m}$ )	Frequency from interferometry setup (MHz)	Frequency simulated in COMSOL (MHz) , $W_s = 3 \mu\text{m}$
2	51.72	52.48
4	49.70	46.80
6	56.20	45.92
8	46.68	45.40
10	42.20	45.06
12	43.60	44.63
14	39.96	44.04
16	42.06	43.86
18	42.76	43.21
20	40.80	43.12

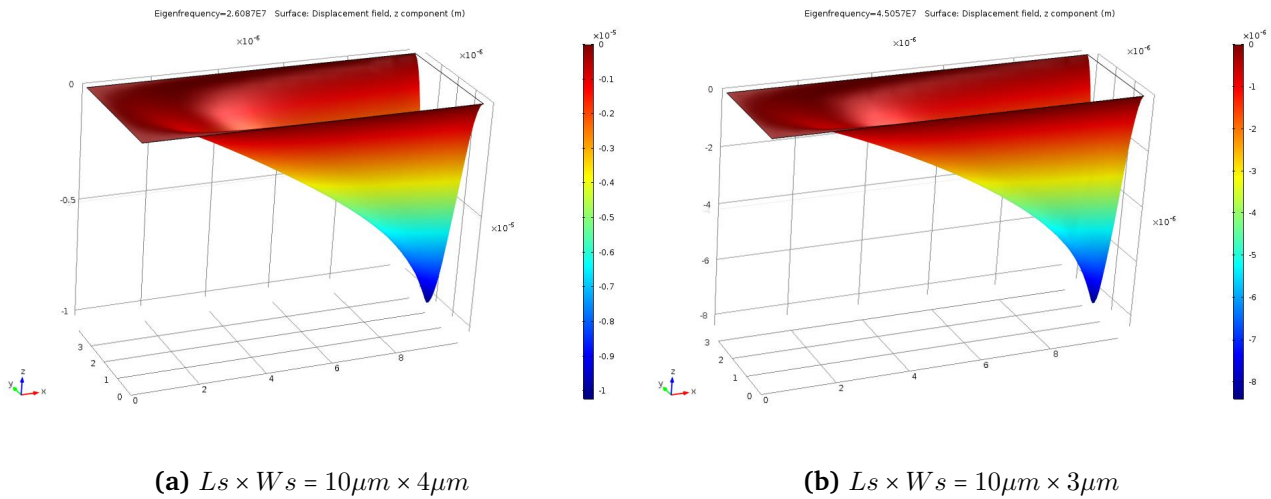


Figure 6.4: COMSOL frequency simulation of suspended gold part in Rc structures

The above experiment clearly shows that the fundamental frequency obtained using the laser setup is because of the gold moving. It is very difficult to observe the resonant frequency of graphene using the blue laser actuation. In the past [15] has also shown the presence of these gold resonances in their graphene devices. Chen et al. in [15] says that the resonant frequency of graphene is much more tunable with external tension than gold since graphene is tension dominated whereas gold is much thicker and bending rigidity dominant. Since the stiffness of graphene is much more tunable than gold, we can determine whether the resonant frequency is coming from graphene or gold by applying large deflections or force. This idea is useful in separating the gold and the graphene frequencies. In order to apply large out of plane deflections to the graphene membrane, we use an electrostatic force that requires an electrostatic gate. This experiment has been described in the next subsection.

### 6.1.3 Electrostatic actuation

For this experiment, setup shown in figure 6.5 has been used. The thermal actuation by blue laser is replaced with an electrostatic actuation and the red laser is used to detect the

mechanical motion of the resonating graphene membrane. Graphene membrane is grounded and a DC + AC voltage is given to the back gate which in this case is silicon, to see the deflection in the graphene membrane due to electrostatic force. The AC voltage is much smaller than the DC voltage. Due to the voltage difference, electric field will develop between the graphene membrane and the back plate and an electrostatic force will act which will deflect the graphene membrane. Since the graphene membrane is grounded, the electrostatic force developed between the membrane and the back gate will always be attractive irrespective of the voltage applied on the back gate. The AC voltage is kept constant and the frequency is observed by sweeping the DC voltage.

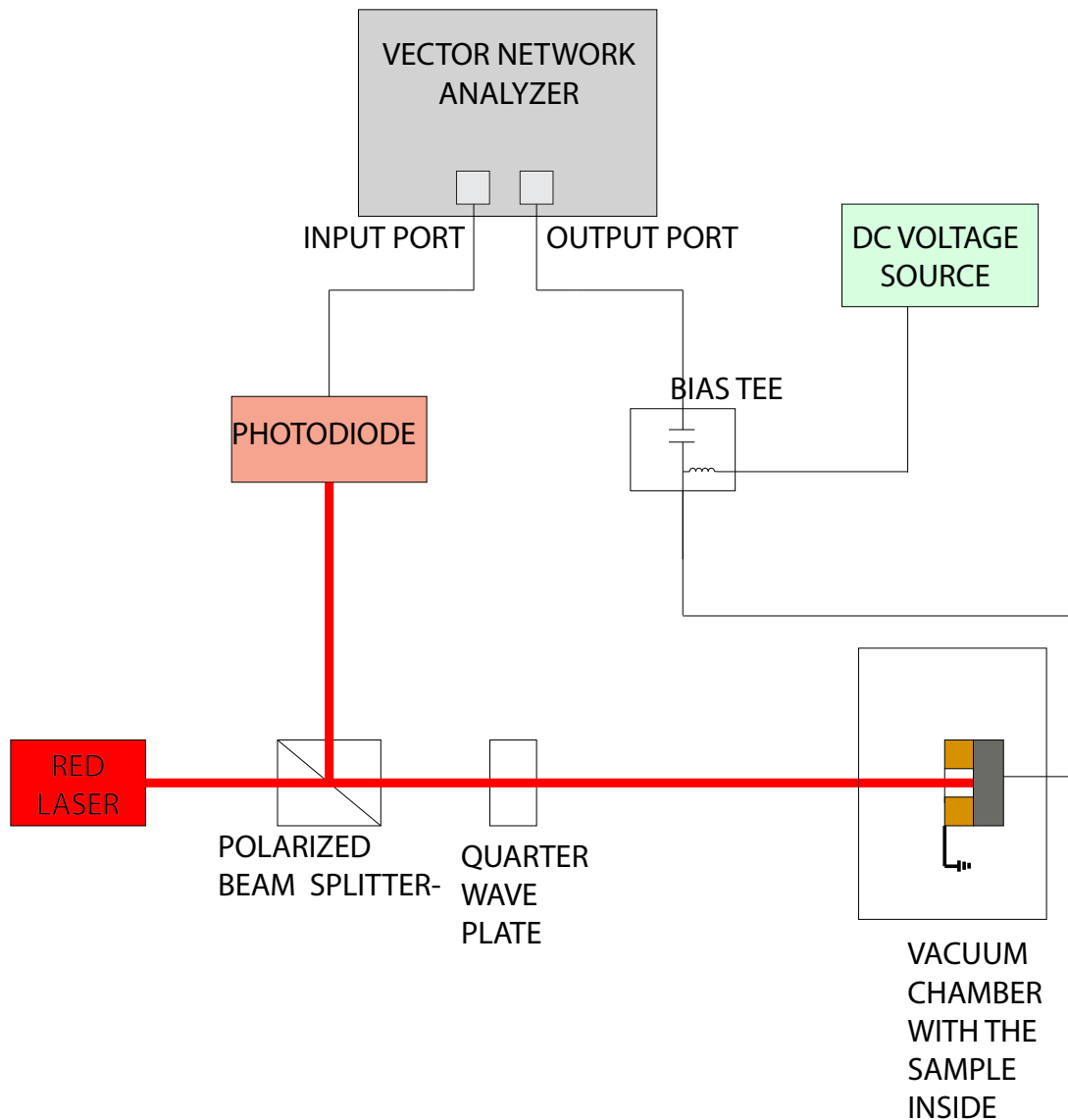
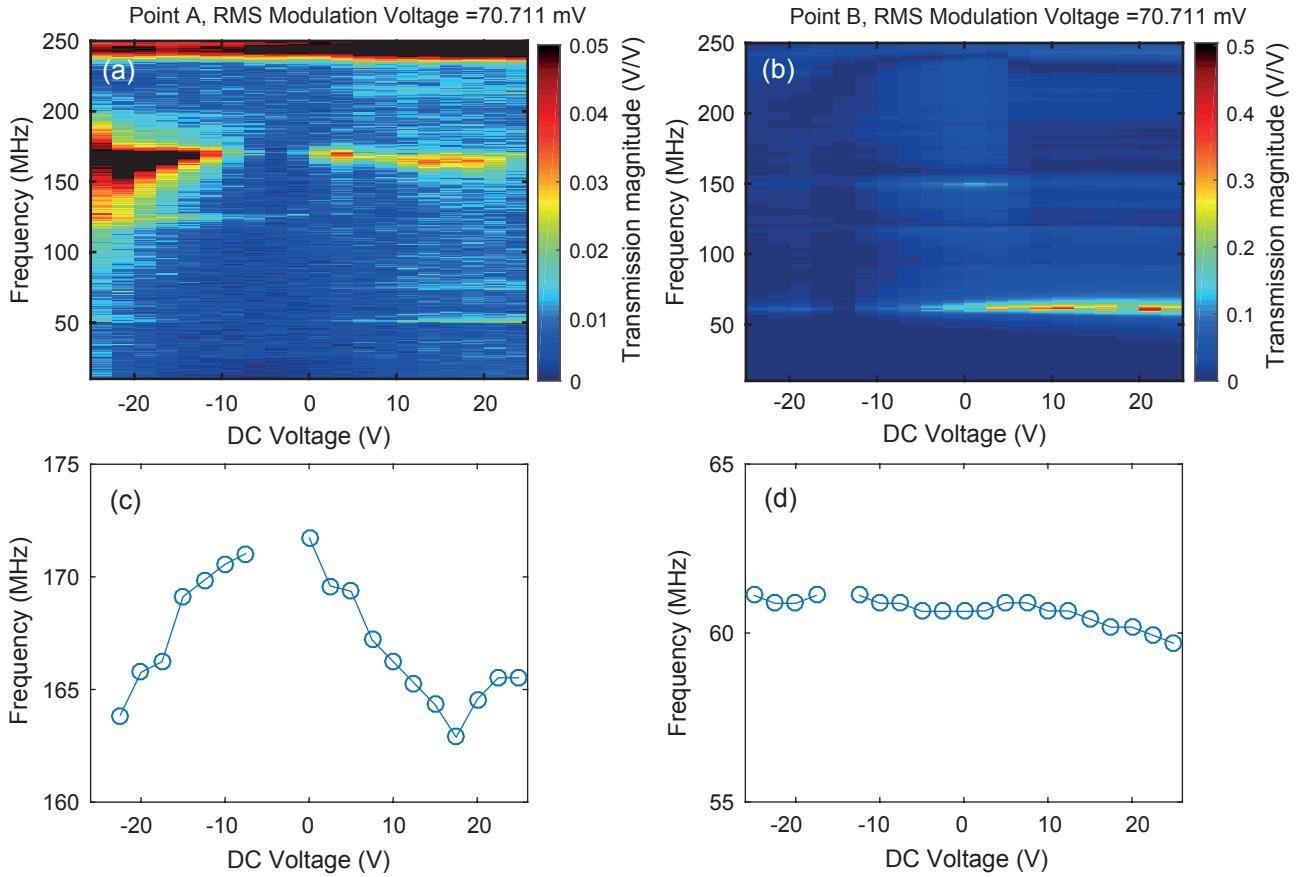


Figure 6.5: Setup used for electrostatic tuning experiment

By changing the x, y and z directions of the stage, we were getting completely different mechanical responses. The higher frequency peak was tuning a lot more than the low frequency peak. The high frequency peak could be that of graphene.

This is because frequency of the graphene membrane is much more tunable with the

electrostatic force than that of the gold. Gold (100 nm) is thicker than graphene (8 nm) which makes gold bending rigidity dominant and so its frequency does not change easily with external force. This is shown in 6.6 where the DC electrostatic tuning of graphene (point A) is much more than the DC electrostatic tuning of gold (point B) at the same modulating AC voltage. Gold resonant frequency is observed at around 60 MHz and the graphene resonant frequency is observed at around 170 MHz for  $5 \times 3$  Rc structure . Figure 6.7 shows the transmission voltage obtained from the VNA vs frequencies for  $5 \times 3$  Rc structure .



**Figure 6.6:** DC electrostatic tuning for (a) graphene  $5 \times 3$  Rc structure (b) gold ( $L_s = 16 \mu\text{m}$ ) (c) shift in the frequency with DC voltage for graphene (d) shift in the resonant frequency with DC voltage for gold

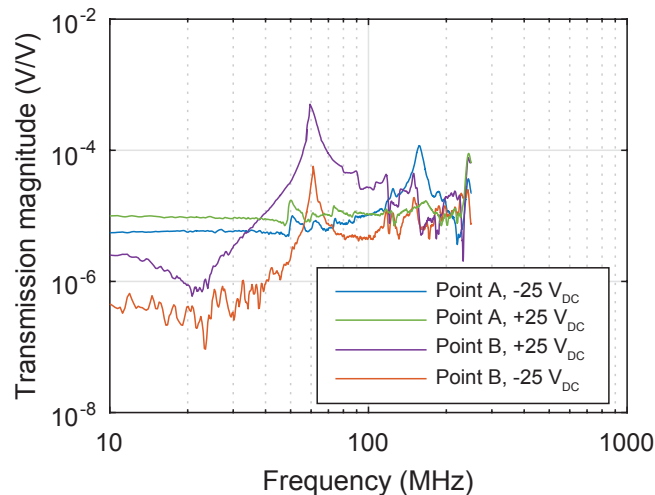


**Figure 6.7:** Transmission magnitude vs frequency for  $5 \times 3$  Rc structure

However, as graphene is supposed to be having a high built-in tension, spring hardening would be a stronger proof of graphene moving. In order to be sure that the high frequency peak is that of graphene, we drive the system with a large actuation force to measure the non-linear dynamic response. The concept of non-linearity in graphene membranes has been discussed in chapter 2.

#### 6.1.4 Non linearity in graphene membranes

This experiment is done on the RC structures using the same setup shown in figure 6.5 where the electrostatic actuation is used to actuate the resonator and the red laser is used to detect the mechanical motion of the resonator. However, in this case, the DC voltage, given to the back gate, is kept constant and the AC modulating voltage is increased. At very high driving voltages the motional amplitude of the resonator becomes non-linear and so a change in resonant frequency is observed. There are two forces that contribute to this non-linearity. One is the pulling of the resonator towards the substrate due to the electrostatic actuation. This force reduces the spring constant, thereby, reducing the frequency of resonator. It is called as capacitive softening. The other is the tension in the resonator that will increase the frequency of the graphene resonator by increasing its stiffness. This is called as hardening. The bending rigidity is proportional to  $thickness^3$  for a material. Since graphene is around 8nm thick and gold is 100nm thick, gold has much more bending rigidity than graphene. Graphene, on the other hand is tension dominated. This means that it will take a larger electrostatic force to change the frequency of gold as compared to graphene. It can be observed in figure 6.8, where the electrostatic force softening for graphene happens at a lower drive voltage (0.1452 mV) as compared to gold (0.2461 mV). Also, the shift in frequency due to softening is much more for graphene as compared to gold. As can be seen in figure 6.8(a), graphene shows capacitive softening (decrease in frequency) and hardening due to tension (increase in tension). On the other hand, as can be seen in figure 6.8 (b) gold shows only capacitive softening. This is due to the fact that graphene has much more tension than gold. Along with shifting of the peaks due to softening and hardening, broadening of the peaks is also visible in the figure 6.8.

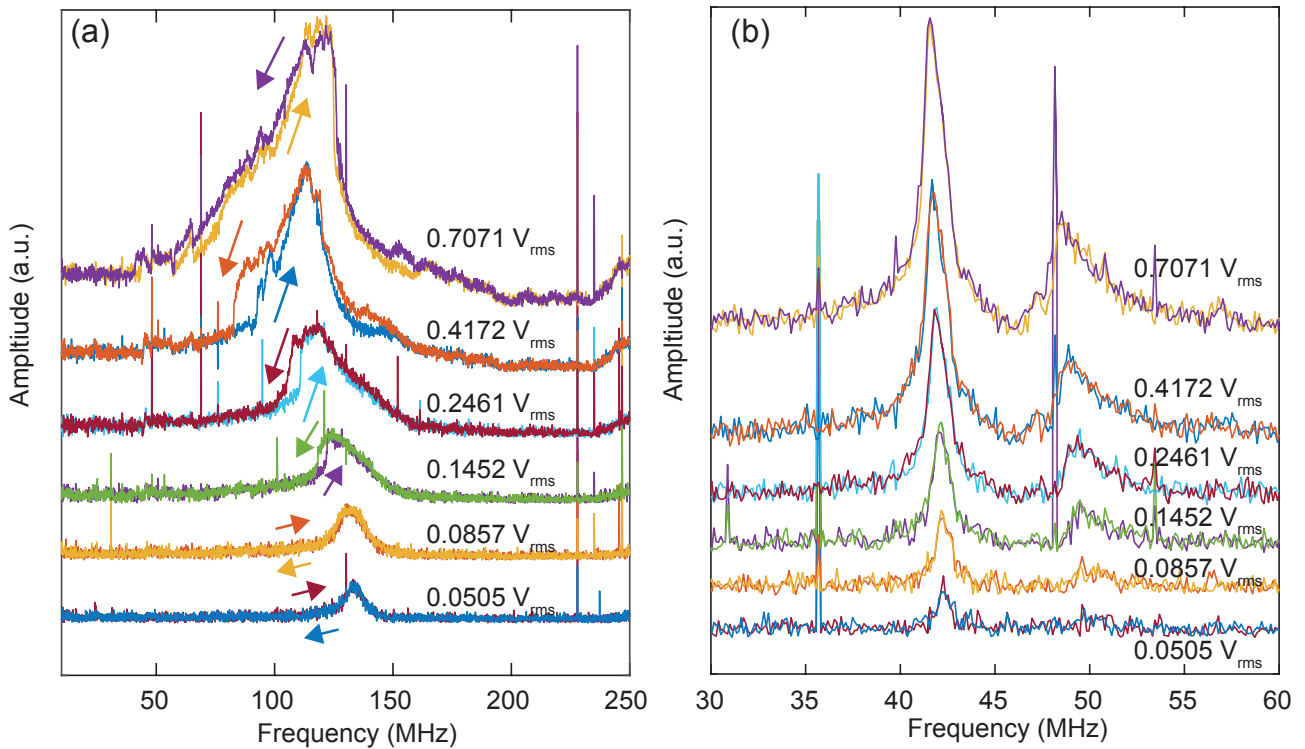


**Figure 6.8: Non linearity experiment (a) graphene membrane (b) gold**

Non linearity is performed on another Rc structure and the two points on which the measurements are taken have been shown in figure 6.9. The results for both the points have been shown in figure 6.10. At point A, the amplitude of oscillation becomes highly non linear at high driving voltages. At these voltages, the amplitude becomes asymmetric and hysteresis is observed. An increase in resonant frequency is observed due to the tension in the membrane. Point B shows small capacitive softening and no hysteresis. Point A is most likely the frequency of the graphene membrane because of the high non linearity and tension observed as compared to point B, which is suspended gold. The edges play a very important role in determining the frequency of the suspended graphene membrane and in our case the graphene motion is observed at the edges of the membrane. However, it is intriguing to find a gold mode (Point B) on the graphene membrane.

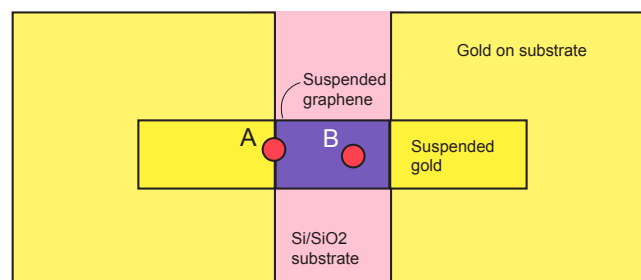


**Figure 6.9: Schematic representation of the Rc structure for non linearity experiment**

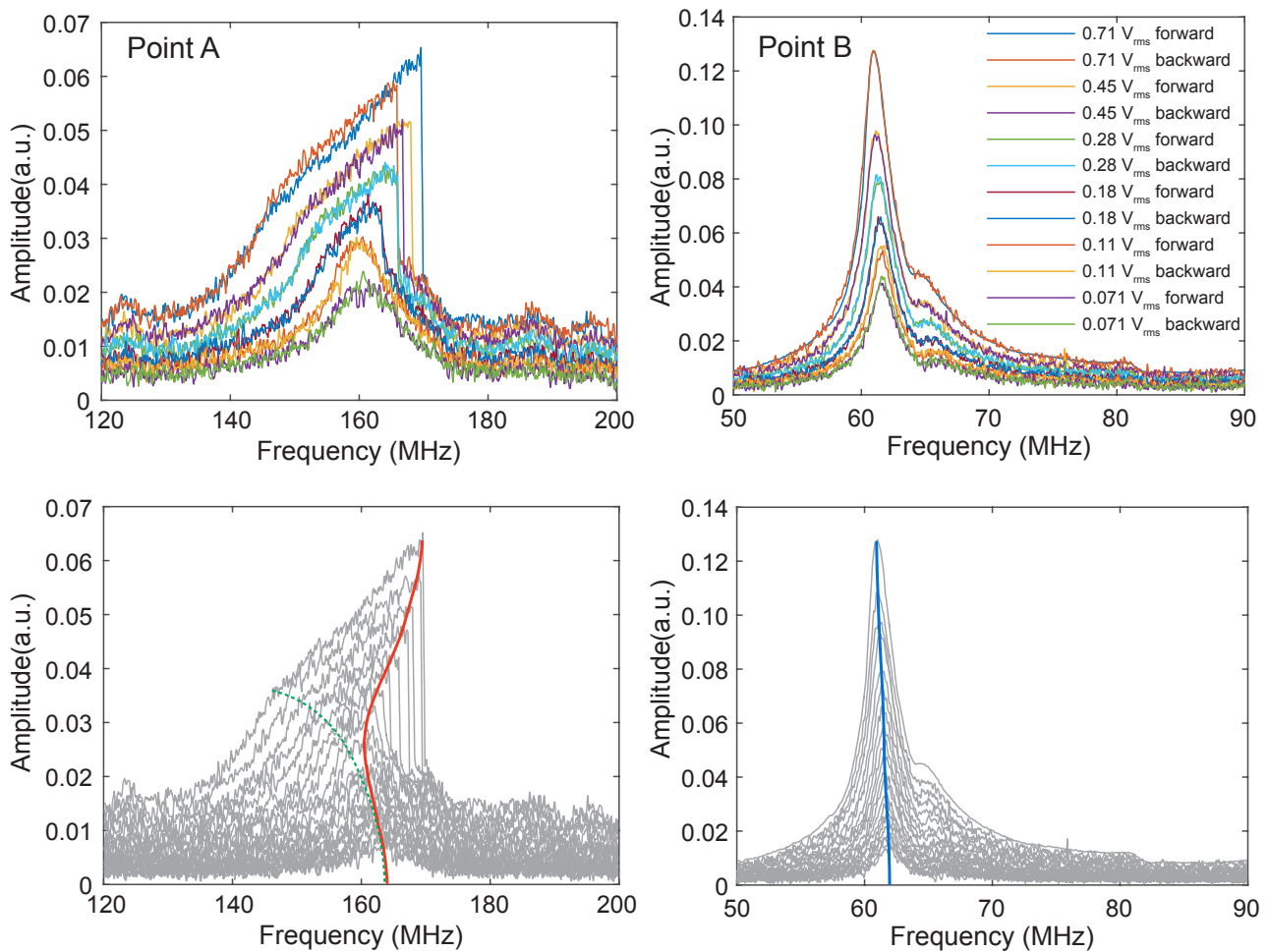


**Figure 6.10: Non linearity experiment results for Point A and Point B. Bottom left: shift in resonant frequency for point A. Bottom right: shift in resonant frequency for point B**

We see a clear spring-hardening in the high frequency peak, that is not there for the low-frequency peak, this is a stronger proof of the high frequency peak being that of graphene.

### 6.1.5 Optical measurements on graphene samples with localized electrode

In chapter 5, we have shown the fabrication procedure of suspended graphene resonators on niobium and polysilicon electrode. Having a localized electrode reduces the parasitic capacitances in the device. The DC tuning and non linearity experiments were performed on the graphene membranes with polysilicon electrode. Figure 6.11 shows the position of laser for point A and point B. As can be seen from figure 6.12, the frequency at point A tunes much more than the frequency observed at point B. This indicates that the higher resonant frequency being observed at around 160 MHz could that be of graphene.

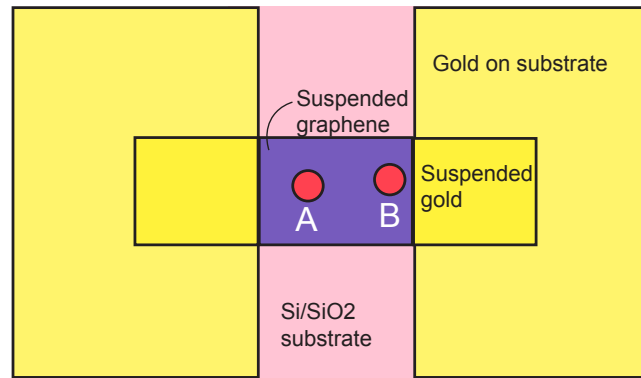


Figure 6.11: Schematic representation of the laser positions on the Rc structure of the polysilicon die

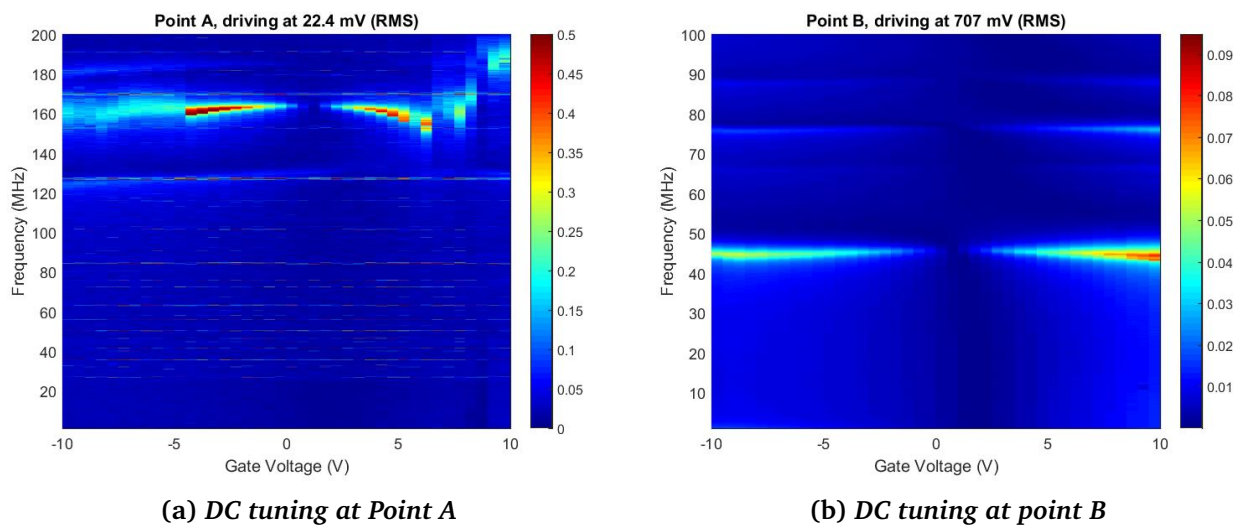


Figure 6.12: DC tuning of graphene resonator with polysilicon electrode

The results of the non linearity experiments for point A and B have been shown in figures 6.13 and 6.14 respectively. At point a, the motional amplitude becomes highly nonlinear for high actuation voltages unlike at point B. This spring hardening indicates towards the high frequency peak being that of graphene.



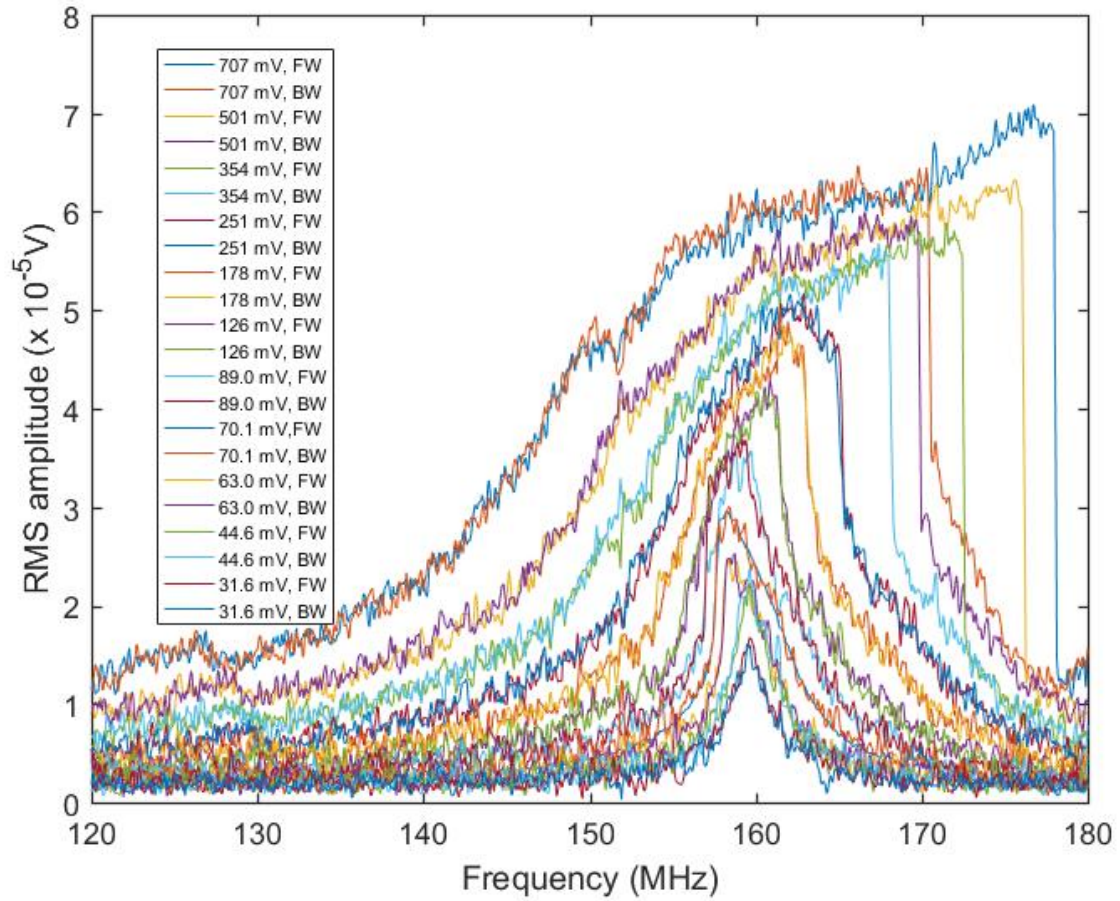


Figure 6.13: Non linearity at point A

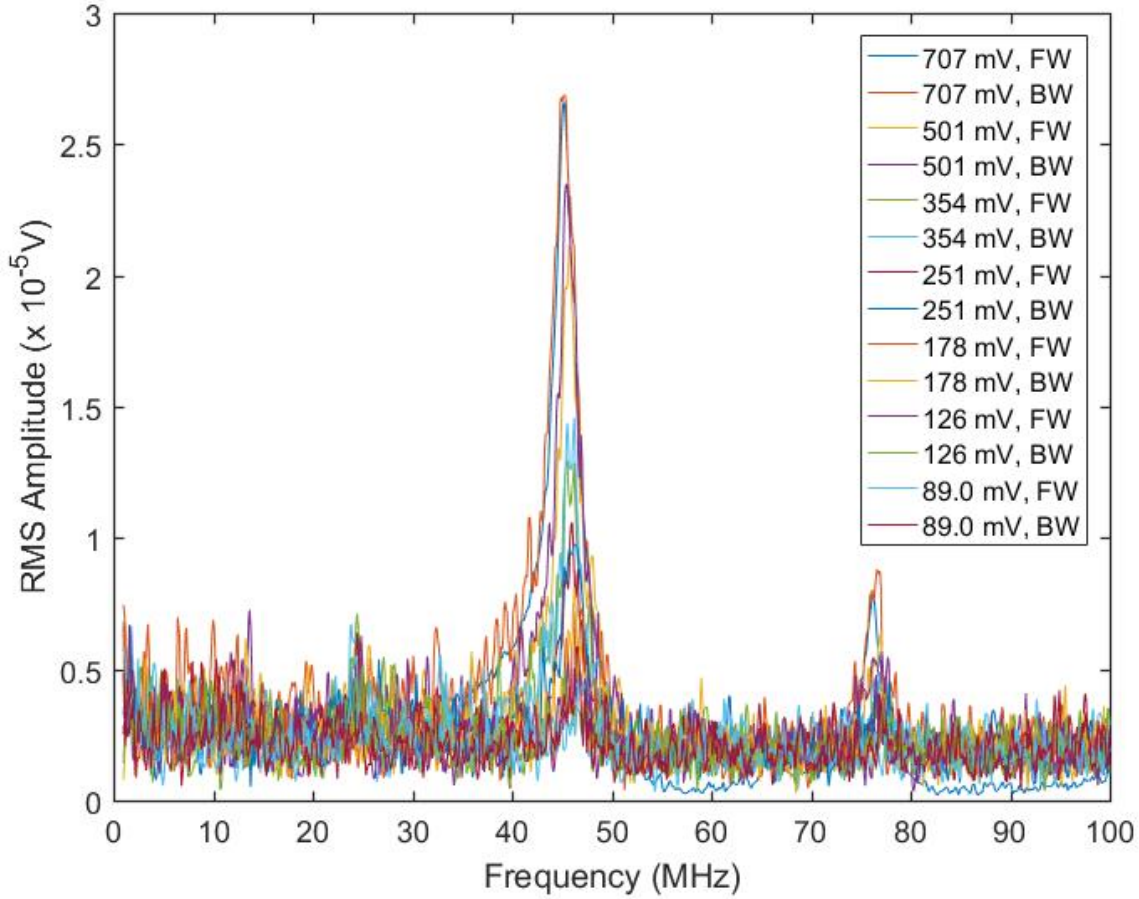


Figure 6.14: *Non linearity at point B*

### 6.1.6 Discussion

We know from the above experiments that the fundamental mode being detected is that of gold. Since graphene is much more tunable to external tension than gold, performing DC tuning and non linearity experiments is the correct approach towards finding the graphene frequency. However, in order to analyze the results obtained, let us analyze with the help of a model.

A simplified model for a gate tuning can be given by equation 6.1 [7]. This is the model for deflection in the graphene membrane due to static force. Here  $k$  is the stiffness of the graphene membrane,  $E$  is the Young's modulus of graphene,  $W$  is the width of the graphene,  $L$  is the length of the graphene,  $\epsilon$  is the initial built in strain in the graphene membrane,  $z$  is the midpoint displacement of the graphene membrane,  $C$  is the capacitance and  $V$  is the voltage applied to the capacitor. The first term is the resonant frequency of the graphene membrane when the applied gate voltage to it is 0. The second term is spring hardening and the third term reflects the spring softening effect.

$$k = \frac{16EW\epsilon}{3L} + \frac{256EWz^2}{3L^3} - \frac{C''V^2}{2} \quad (6.1)$$

When the graphene membrane has a high initial built in strain, with increasing gate voltage, the last term dominates causing decrease in the stiffness of the membrane. Decrease in stiffness leads to decrease in resonant frequency. This is the capacitive softening effect. When the initial built in strain in the graphene membrane is small, the additional tension induced in the membrane due to high displacement dominates, thereby increasing the tension

in the membrane. This increases the stiffness in the membrane and so the frequency increases. This is the spring hardening effect. For intermediate strain the resonant frequency first decreases then increases.

For our case, we observe the capacitive softening effect in the DC tuning experiment. For the non linearity experiment, we observe first capacitive softening and then spring hardening effect. We have discussed that graphene has high built in tension due to process, see chapter 2. We expect our fabricated few layer graphene membranes to be in tension. If that is the case spring hardening should be observed for large deflections in the graphene membranes. Since we get different results from the two experiments, it is difficult to say if the detected mode is that of graphene.

Another issue is that unlike single layer graphene membranes, we have few layer graphene membranes of around 8 nm thickness. In our case we cannot ignore the bending rigidity of the graphene membrane and so even the bending rigidity has to be taken into account along with the tension for the calculation of resonant frequency of graphene membrane in our case. We have observed wrinkles and corrugations in our suspended graphene membrane (See chapter 4). These wrinkles and corrugations could be increasing the bending rigidity of the graphene membranes. So our resonator is a much more complex system. In order to find out the resonant frequency of the graphene motion in our resonators, more research needs to be done.

## 6.2 Electrical measurements

This section presents the electrical measurements performed on the graphene samples.

### 6.2.1 I-V measurements

The first set of electrical measurements were done to extract the contact resistance of graphene. The aim of the experiments is to study the influence of parameters such as size of the graphene membrane, gap size and contact area between gold and graphene on the contact resistance of graphene.

#### 6.2.1.1 Methodology and circuit

The measurements are performed using four point probe method in which current is forced to two terminals and voltage is sensed through the other two terminals. We use a method similar to the one given in [124] to extract the contact resistances of graphene membrane.

The structures used for measuring the contact resistance is given in figure 6.15. The total resistance is obtained by adding the contact resistances and resistance due to graphene membrane as shown in equation 6.2. After putting the value for resistance of graphene in equation 6.2, we get equation 6.3. In equation 6.3,  $l_g$  is the length of the graphene membrane and  $w_g$  is the width of the graphene membrane. On rearranging the terms in equation 6.3, equation 6.4 is obtained. Equation 6.4 can be plotted as a straight line with  $y = R_{\text{total}} \times w_g$ ,  $x = l_g$ ,  $m = \rho$  and  $c = R_c \times w_g$ . For a fixed width of graphene, the length of graphene is plotted against the  $R_{\text{total}} \times w_g$ . The slope of this line gives  $R_c \times w_g$ . By plugging in the values of  $w_g$  (in our case  $4 \mu\text{m}$ ), value of  $R_c$  are obtained.

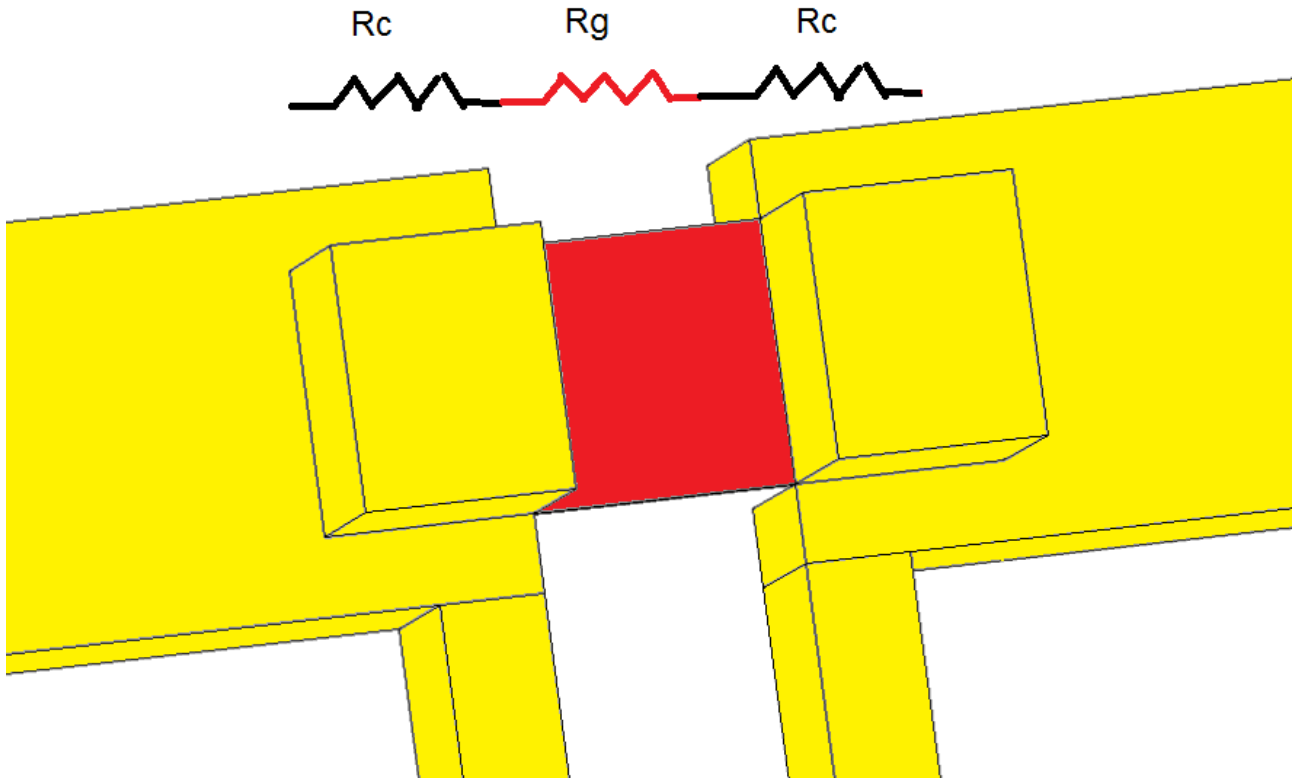


Figure 6.15: Schematic 3D representation of the  $R_c$  structure contact resistance experiment

$$R_{\text{total}} = R_c + R_g \quad (6.2)$$

$$R_{\text{total}} = R_c + \frac{\rho l_g}{w_g} \quad (6.3)$$

$$R_{\text{total}} \times w_g = \rho l_g + R_c \times w_g \quad (6.4)$$

### 6.2.1.2 Results and discussion

Tables 6.5, 6.6, 6.7 and 6.8 give the resistance and contact resistance measurement results for the 100 nm and 200 nm gap size of graphene respectively.

Table 6.5: Resistance( $k\Omega$ ) measurement results for 100nm gap size garphene membranes

$L_g \times W_g (\mu m^2)$	$L_c$									
	2 $\mu m$	4 $\mu m$	6 $\mu m$	8 $\mu m$	10 $\mu m$	12 $\mu m$	14 $\mu m$	16 $\mu m$	18 $\mu m$	20 $\mu m$
10 $\times$ 4	open	4.43	5.06	2.97	2.78	2.21	1.98	open	open	2.36
8 $\times$ 4	4.39	6.91	4.80	2.70	2.54	2.11	2.36	2.04	1.99	1.96
6 $\times$ 4	2.62	1.95	2.88	1.86	1.78	1.89	1.83	2.25	1.79	1.80
4 $\times$ 4	2.43	1.76	1.34	4.36	1.63	open	1.50	1.40	0.89	1.80
2 $\times$ 2	open	open	open	open	open	open	open	open	short	1.52
5 $\times$ 3	3.93	2.20	2.25	2.42	2.03	1.58	1.68	1.93	2.14	2.24

**Table 6.6: Contact Resistance measurement results for 100nm gap size garphene membranes, width of graphene=4  $\mu m$**

$L_c$	$R_C W (k\Omega\mu m)$	$R_C (k\Omega)$
2 $\mu m$	0.41	0.10
4 $\mu m$	-1.55	-0.39
6 $\mu m$	-2.12	-0.53
8 $\mu m$	8.28	2.07
10 $\mu m$	1.42	0.71
12 $\mu m$	2.86	0.71
14 $\mu m$	2.46	0.61
16 $\mu m$	1.87	0.47
18 $\mu m$	-0.19	-0.05
20 $\mu m$	2.67	0.67

**Table 6.7: Resistance ( $k\Omega$ ) measurement results for 200nm gap size garphene membranes**

$L_g \times W_g (\mu m^2)$	$L_c$									
	2 $\mu m$	4 $\mu m$	6 $\mu m$	8 $\mu m$	10 $\mu m$	12 $\mu m$	14 $\mu m$	16 $\mu m$	18 $\mu m$	20 $\mu m$
10 $\times$ 4	13.60	16.80	13.70	open	10.50	10.30	11.60	10.10	9.26	10.70
8 $\times$ 4	19.8	13.30	13.20	52.80	9.06	10.30	9.05	9.04	9.74	10.10
6 $\times$ 4	open	10.80	15.3	14.7	8.93	8.94	8.75	8.23	7.90	7.00
4 $\times$ 4	7.42	9.94	7.18	9.94	5.63	4.77	8.42	6.20	7.52	6.81
2 $\times$ 2	4.69	5.44	11.7	12.4	7.76	5.33	6.90	7.51	5.21	7.94
5 $\times$ 3	9.07	9.50	7.18	9.94	5.63	9.66	8.42	10.80	7.52	9.65

**Table 6.8: Contact Resistance measurement results for 200nm gap size garphene membranes, width of graphene=4  $\mu m$**

$L_c$	$R_C W (k\Omega\mu m)$	$R_C (k\Omega)$
2 $\mu m$	7.75	1.94
4 $\mu m$	9.26	2.32
6 $\mu m$	12.47	3.12
8 $\mu m$	-76.95	-19.24
10 $\mu m$	6.74	1.68
12 $\mu m$	4.59	1.15
14 $\mu m$	12.02	3.00
16 $\mu m$	8.03	2.01
18 $\mu m$	12.27	3.07
20 $\mu m$	6.97	1.74

On increasing the contact area between graphene and gold, the total resistance of the device decreased. However, when the contact area was too large, measurements show a slight increase in total resistance i.e. an increase in total resistance is seen from 18 to 20  $\mu m$  contact area. However, a lot of the values obtained in the 200 nm sample are deviating from this trend. On keeping the gold graphene contact area constant and increasing the length of the graphene membrane, the total resistance increases. The yield is found to be 78.3 % for 100 nm gap size graphene membrane and 96.67 % for the 200 nm gap size graphene membrane. Hence, the 200 nm sample gives a higher yield.

We do not observe any clear trend in the contact resistance values obtained. The negative resistances obtained could be due to wrong measurements.

We are getting higher resistance values for 200 nm gap size graphene membrane than the 100 nm gap size graphene membrane. An explanation for this can be given using the relation between mobility and strain given in [125]. The Fermi velocity will decrease with increase in strain [125]. The mobility will decrease with decrease in the Fermi velocity [125]. The resistance will increase with the decrease in mobility. This means with the increase in strain, the resistance increases. We expect the 200 nm gap size graphene membrane to be more compressively strained than the 100 nm gap size graphene membrane (See the next chapter 7). If the 200 nm gap size of graphene membrane is more compressively strained, then the relation between the strain and resistance could be an explanation for the increase in resistance values seen for 200 nm gap size of graphene membrane.

### 6.2.2 Resistance measurements

Resistance measurements were also performed on the graphene samples with polysilicon and niobium electrodes. Results are given in table 6.9.

**Table 6.9: Resistance measurement results for polysilicon and niobium die**

	graphene	gate	between graphene and gate
Niobium	11.65 ( $\Omega$ )	16.54 ( $\Omega$ )	0.65 ( $\Omega$ )
polysilicon	4.06 (k $\Omega$ )	5.31 (k $\Omega$ )	44.95 (k $\Omega$ )

From the resistance measurement results in the previous section, we know that the resistance of graphene cannot be as low as obtained in the case of graphene membrane on niobium electrode. This means that current is not passing through the graphene but the electrode. Also, a very low resistance value is obtained between the graphene and niobium electrode, indicating that the oxide in between is no longer acting as an effective insulator. It is possible that due to the high growth temperatures during graphene growth, the oxide reacts with niobium and forms a type of niobium oxide that is a conductor. Another possibility is that niobium starts diffusing through the oxide at high temperature. The resistance between the polysilicon electrode and graphene is in k $\Omega$ , which indicates that the capacitor is leaking. Improvements need to be made in the fabrication flow of these devices so that they can work as effective capacitors.

## 6.3 Summary

This chapter presented the measurements performed on the graphene samples. From the optical measurements, it became clear that it is very difficult to detect the resonant frequency due to graphene in our resonators. One of the reasons of not getting the results we expect could be due to our graphene membranes being partially suspended. For this we need to reflect more on the process of suspension of graphene membrane. In order to analyze the process of suspension of graphene membranes, a cause analysis has been done which has been presented in the next chapter.

# Chapter 7

## Analysis of cause of collapse of graphene membranes

In this chapter, the cause of collapse of the graphene membranes is investigated. There are three main reasons to do this analysis. One is that it will shed light on the process of formation of suspended graphene membranes. Second is that it will help to optimize the parameters related to suspending graphene membranes on different substrates. Third it will address the problem of suspending graphene membranes on the smallest gap sizes possible i.e. it will help in the miniaturization of the gap sizes.

### 7.1 Cause Analysis

As discussed in the chapter 4, the graphene membranes were found to be collapsed after release. In order to find out the cause of collapse of these graphene membranes, the process parameters used to fabricate these wafers and the fabrication process parameters used in [73] were compared. The differences between both these process parameters have been tabulated in table 7.1.

The mentioned differences in table 7.1 could affect the suspension of the membranes in following ways. Different oxide thickness could have a different residual stress which could also affect the suspension. Since oxide is a thermal insulator, there can be a temperature gradient in the device during the high temperature graphene growth process, the etching of molybdenum or the deposition of metal molybdenum.

As far as the etching recipe is concerned, different types of gases and parameters are used for different etching recipes. This could influence the sidewall etching of molybdenum which could affect the graphene growth at the sidewalls and in turn its suspension.

The resist thickness and different exposure energy values could affect the sidewall of molybdenum . Keeping molybdenum at the edges ring of the wafer leads to stress in the wafer [73]. This could shift the alignment marker position which could cause misalignment between the molybdenum and the gold layer. Furthermore, the stress could affect the stress in the graphene layer. In our case, we remove molybdenum from the edges of the wafer, in order to reduce stress. Whether this difference could affect the suspension of the membrane needs to be inspected. Graphene growth recipe is a crucial step in the suspension of the membrane. Since the deposition time and temperature is different for both the graphene growth recipes mentioned in table 7.1 , it could affect the thickness of graphene membrane and its morphology. The last difference in which TiN (titanium nitride) is deposited on the backside of the wafer, could cause some stress in the wafer. Stress in the device could play a very important role in the suspension of the membrane.

Table 7.1: Differences in fabrication processes parameters of suspended graphene membranes

	Differences	Fabrication process parameters used in [73]	Fabrication process parameters used in this work
1	Oxide thickness and recipe	90 nm (dry oxidation)	1000 nm (wet oxidation)
2	Mo etching technique	Mo_50	Mo_test2
3	Resist thickness and exposure energy	1.4 $\mu\text{m}$ and 140 $\text{mJ}/\text{cm}^2$	2.1 $\mu\text{m}$ and 240 $\text{mJ}/\text{cm}^2$
4	Mo removal at the edges of the wafer	No	Yes
5	Graphene growth recipe	5 min( 950 ° Celsius )	40 min ( 915 ° Celsius )
6	Gold mask and TiN deposition on backside of wafer	Manual coating and development, No TiN deposition	Automatic coating and development using EVG120, TiN deposition

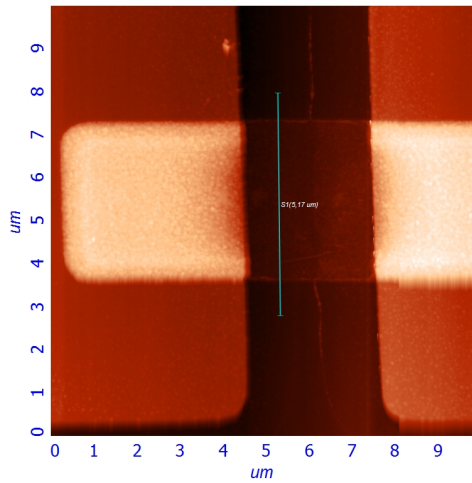
For complete investigation, six wafers were fabricated using the same fabrication process flow used in [73] with only one parameter changing in each of them. These changing parameters are from the fabrication process flow used in this work. For example, wafer 1 was fabricated using the same process parameters used in [73] except for the oxide thickness. Instead of 90 nm dry oxide, a 900 nm of wet oxide was grown on this wafer. Similarly, one parameter was changed in all the other five wafers as given in table 7.2. For this analysis, graphene resonators with 100 nm gap size were fabricated on all the six wafers. 100 nm gap size was chosen, to analyze the miniaturization aspect as it is expected that realizing a thin gap is more difficult than a thick gap.

Table 7.2: Analysis of cause of collapse of membranes

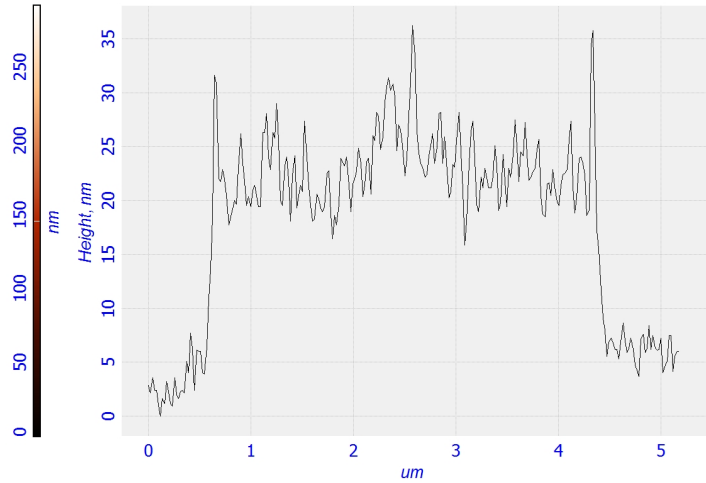
Wafer	Changed parameter	Value	Suspended
1	Oxide Thickness	900 nm	×
2	Mo etching technique	Mo_test2	×
3	Resist thickness and exposure energy	2.1 $\mu\text{m}$ and 240 $\text{mJ}/\text{cm}^2$	✓
4	Mo removal at the edges of the wafer	Yes	✓
5	Graphene growth recipe	40 min	✓
6	Coating and development using wafertrack EVG120 (TiN deposition at the backside)	Automatic	✓



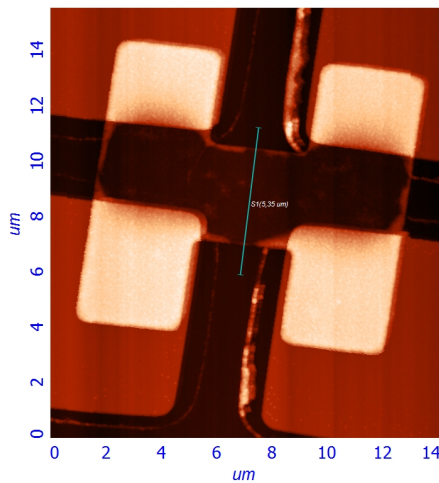
The AFM and SEM images ( See figure 7.1) of the samples clearly show that graphene membranes in wafer 1 and 2 are totally flat and lying on the oxide. The differences in height of 20 to 30 nm observed for these samples in the AFM images are due to the differences in the oxide thicknesses as described in chapter 4 section 4.1. On the other hand, graphene membranes of the other four wafers (See figures 7.2 and 7.3) showed rough crumpled like structure with a height difference of around 150 nm above the oxide. These differences can shed light on process or mechanism of suspension



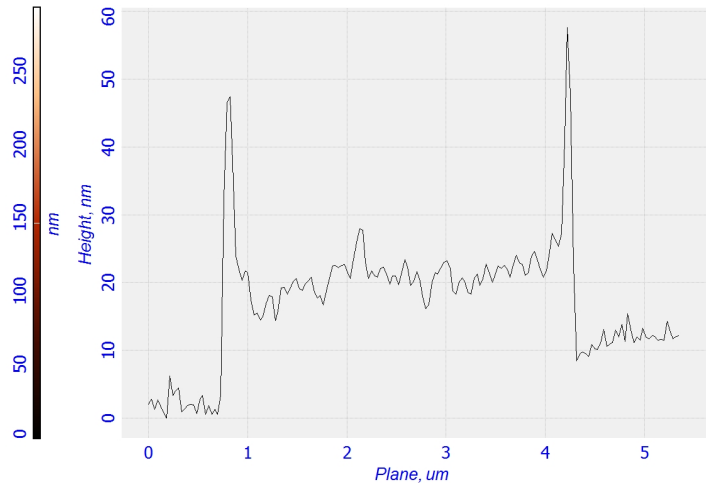
(a) Wafer 1



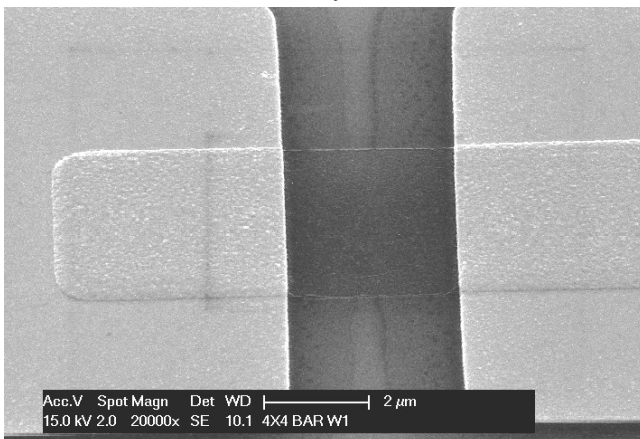
(b) Cross section across wafer 1 membrane



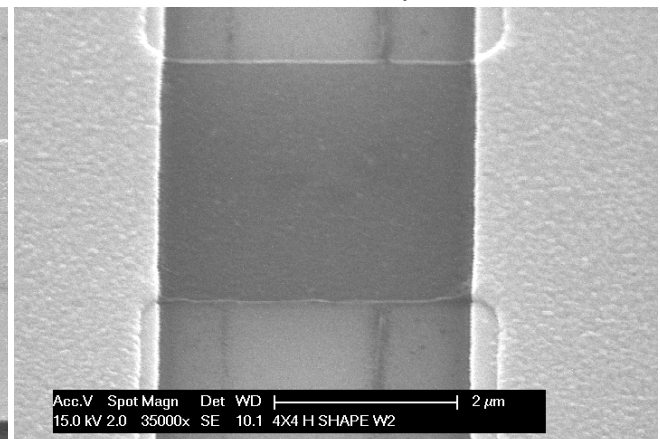
(c) Wafer 2



(d) Cross section across wafer 2 membrane

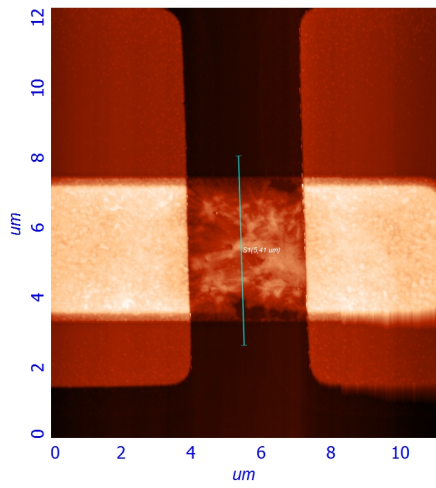


(e) Wafer 1

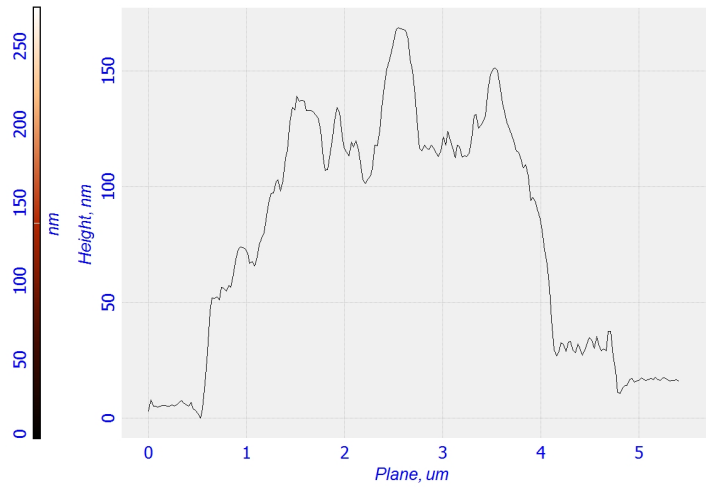


(f) Wafer 2

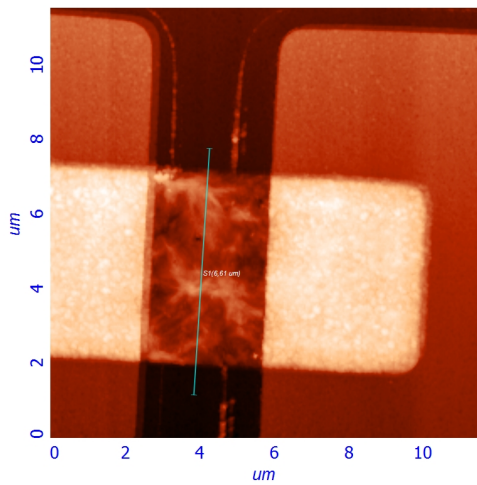
Figure 7.1: AFM and SEM images of cause analysis wafer 1 and wafer 2



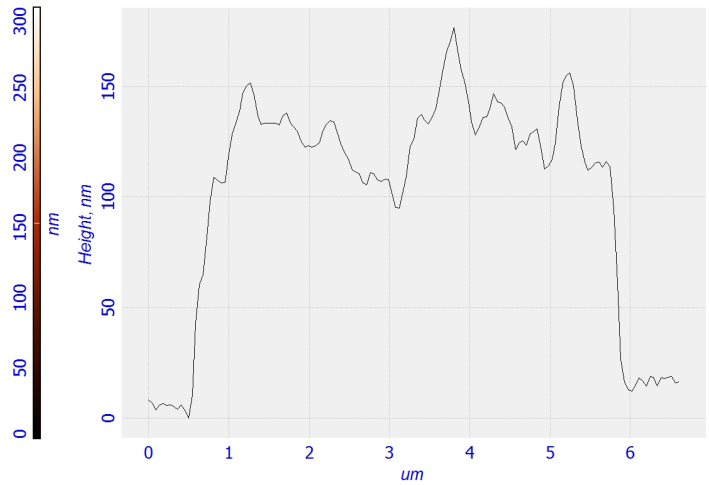
(a) Wafer 3



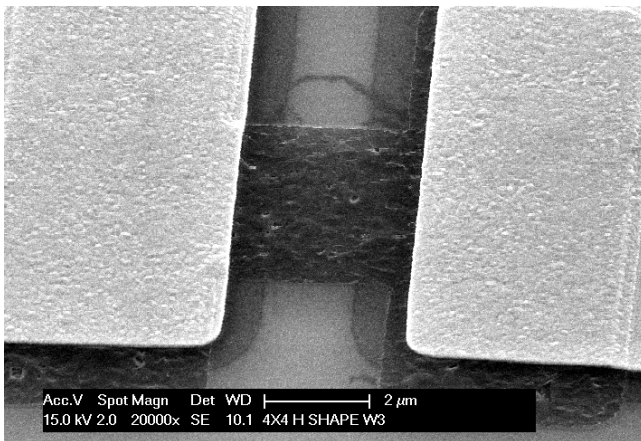
(b) Cross section across wafer 3 membrane



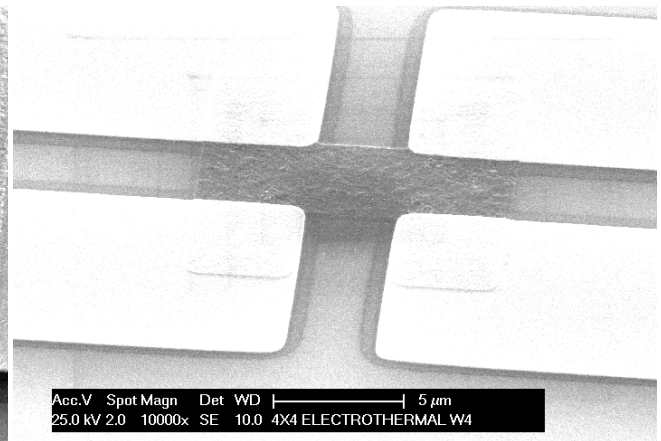
(c) Wafer 4



(d) Cross section across wafer wafer 4 membrane



(e) Wafer 3



(f) Wafer 4

Figure 7.2: AFM and SEM images of cause analysis wafer 3 and wafer 5

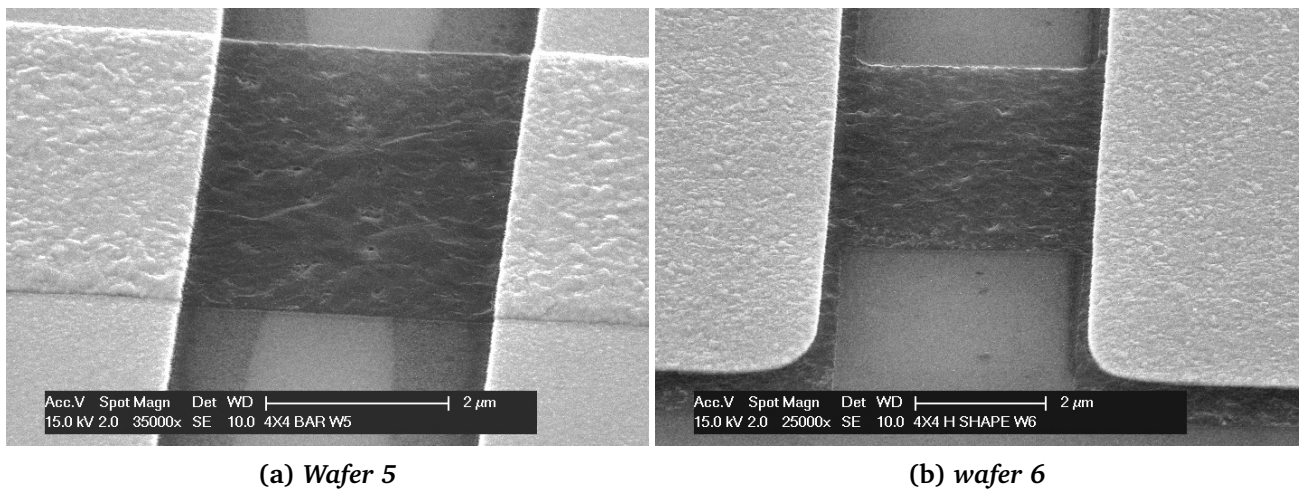


Figure 7.3: SEM images of cause analysis wafer 5 and wafer 6

Another wafer was prepared with repeated TiN deposition at the backside. Around 500 to 600nm of TiN was deposited at the backside of this wafer. The graphene membranes in this wafer were also suspended showing that even such a thick layer of TiN at the backside of the wafer does not affect the suspension of the membrane. Since all the parameters in the fabrication process of the 6 wafers were the same except one changing parameter in each of them, it became clear that that oxide thickness of 1000 nm wet oxide and molybdenum etching recipe Motest2 were responsible for the collapse of the graphene membranes in the earlier fabricated batch. Before going into a detailed analysis on each of these two causes, some important observations have been described in the next section.

## 7.2 Important Observations

The dies of all the six wafers fabricated for cause analysis, were investigated before release of the graphene membranes i.e. before the molybdenum was etched with peroxide. Interestingly, they also showed some peculiar differences. As can be seen from figure 7.4, on observing these samples under the microscope, some black dot type structures were observed for all the wafers except wafer 1 and wafer 2. Even SEM images of the samples before release (figure 7.5) show no roughening and patches in graphene membrane for wafer 1 and wafer 2 unlike other wafers.

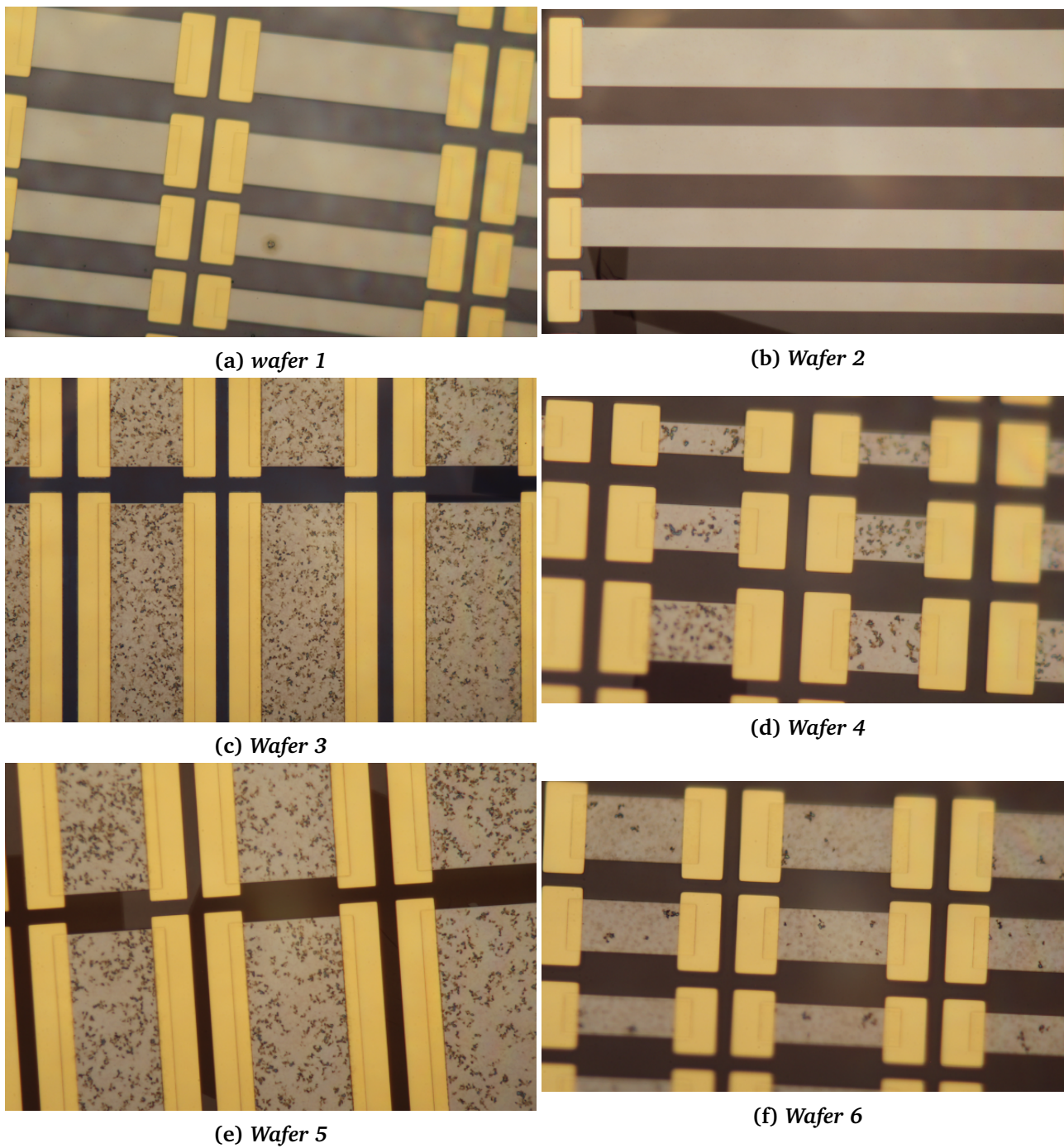


Figure 7.4: Microscope images of cause analysis wafers before release

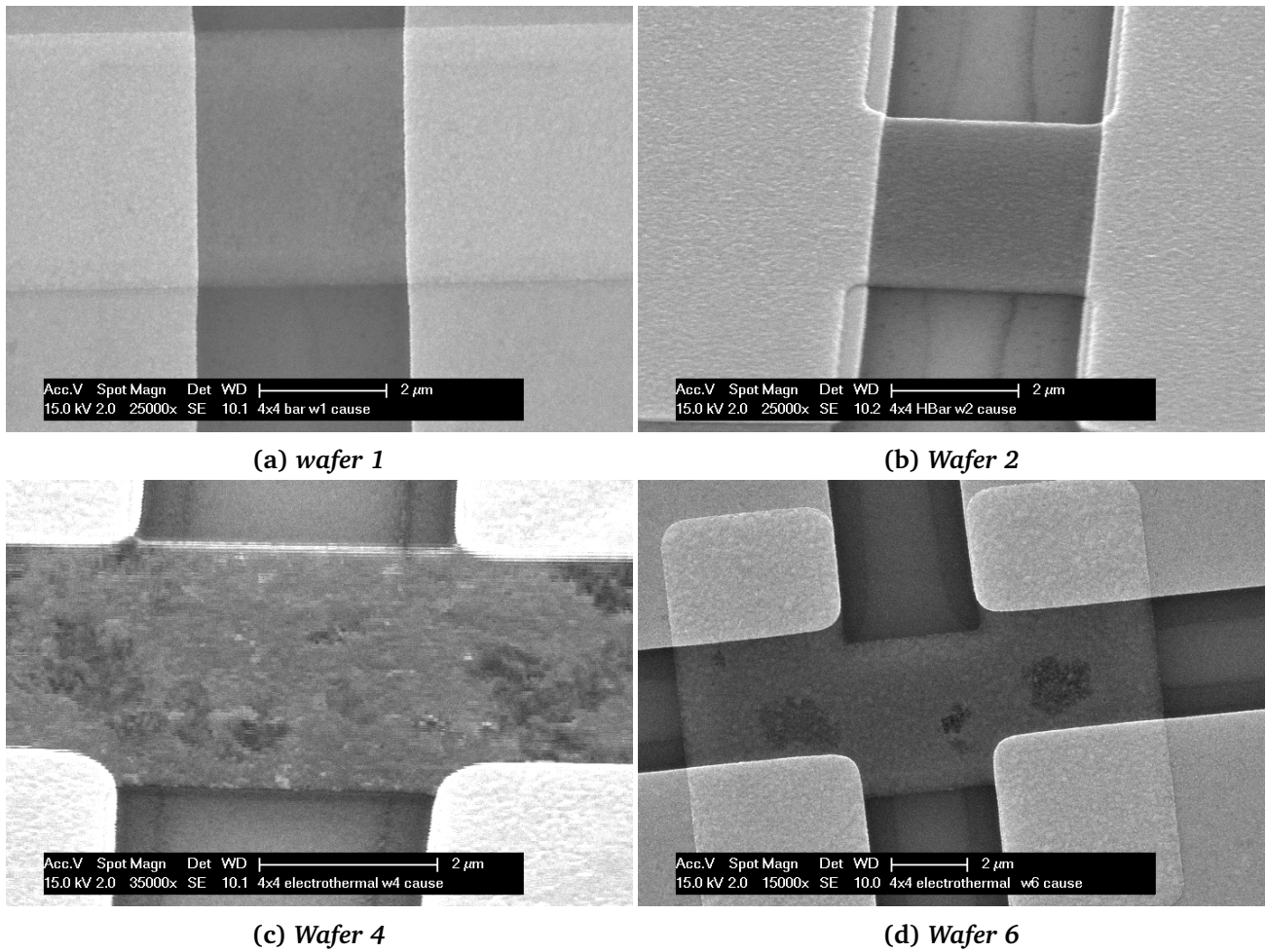
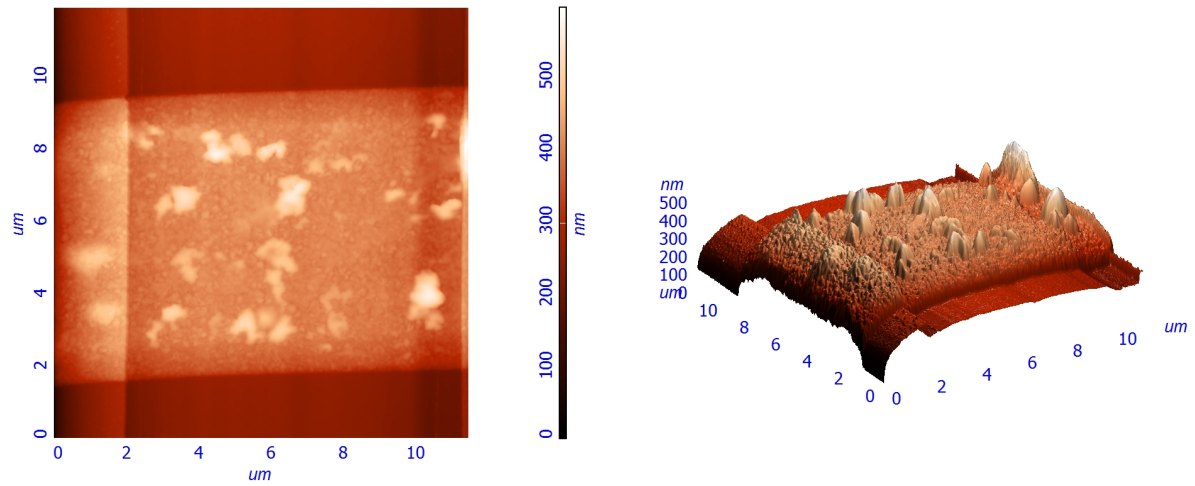


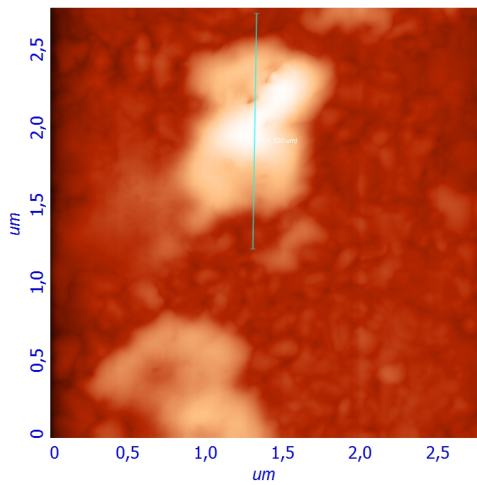
Figure 7.5: SEM images of cause analysis wafers before release

For greater clarity, AFM was performed on the samples before release. The AFM images show balloon like structures deforming from graphene membrane. For wafer 4 (see figure 7.6), in which molybdenum ring was removed from the edge of the wafer, bubble like structures of much greater heights were found. As shown in image 7.7, for wafer 5, these balloon or bubble like structures were of around 90nm height. Interestingly, no such structure were observed for wafer 2 (See figure 7.8). These differences lead us to believe that suspension of a device can be investigated even before etching of the molybdenum and the release steps. When EDX measurements were performed, we observed significant higher oxygen content in the graphene bubble area than the the other area of the graphene membrane. To investigate the relation between these huge graphene bubbles on the samples before release and the suspension of the graphene membrane, first some past research work on the observation of these graphene bubbles was done and will be presented in the next section.

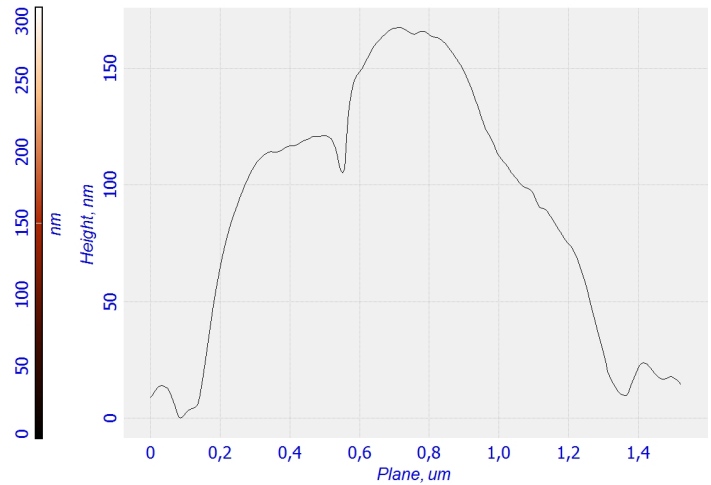


(a) Wafer 4 : Bar structure

(b) Wafer 4 : 3D Structure

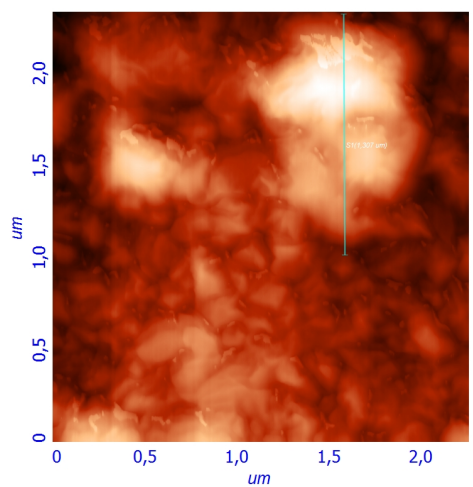


(c) Graphene bubble

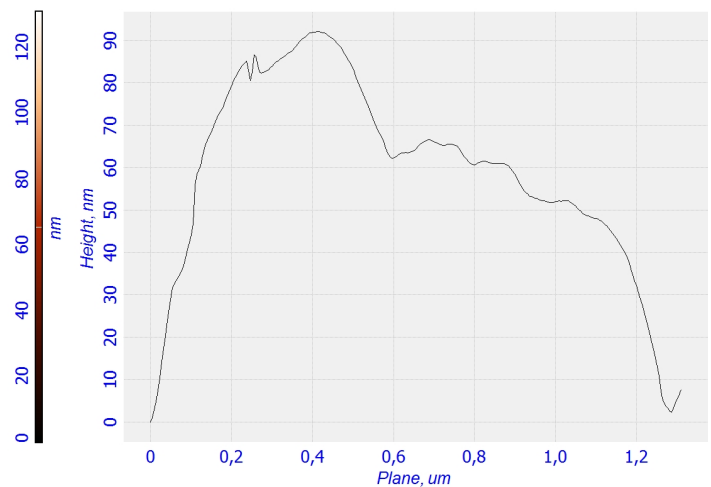


(d) Cross section across the bubble

Figure 7.6: AFM image analysis on wafer 4 before release



(a) Wafer 5 : Bubble



(b) Wafer 5 : Cross section

Figure 7.7: AFM image analysis on wafer 5 before release

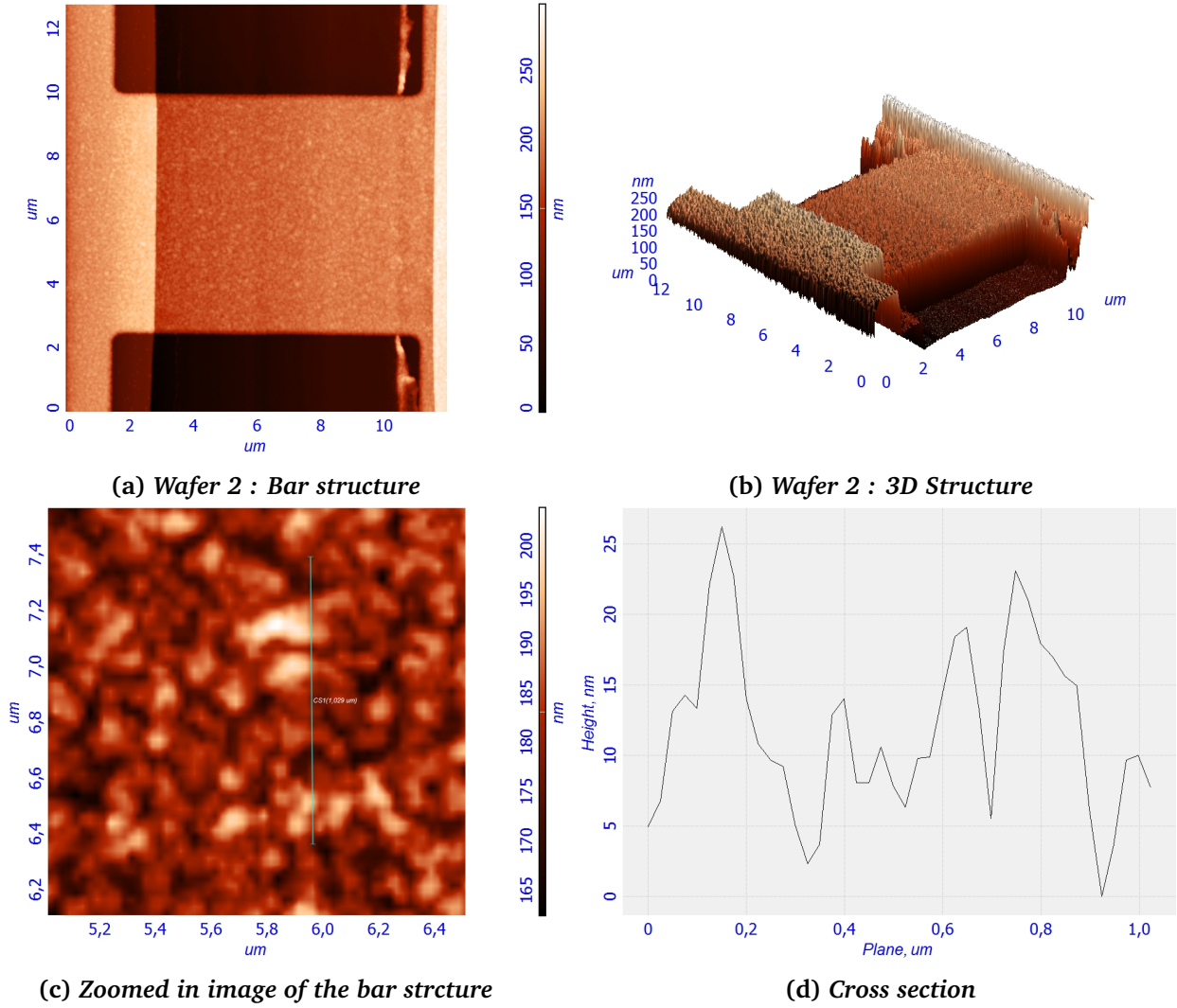


Figure 7.8: AFM image analysis on wafer 2 before release

## 7.3 Graphene Bubbles

When graphene is placed on a flat surface like graphite and  $\text{MoS}_2$ , large number of bubbles appear in the exfoliated graphene [126]. These structure reach equilibrium when annealed. The observed bubbles are of different shapes such as circular, pyramidal and triangular [126]. According to E Khestanov et al. this happens due to the contaminant (hydrocarbons, water etc.) trapped inbetween the graphene layer and the underneath substrate. In order to make the area contamination free, graphene membrane squeezes out the contaminant (adsorbed water or hydrocarbons) and uplifts the graphene into bubble like shape. The figure 7.9 shows the schematic of a graphene bubble [126].

Equation 7.1 shows relation between the Van der Waals energy ( $E_v$ ) and the adhesion energy ( $\gamma$ ). In equation (7.2)  $\gamma_{gs}$  is the adhesion energy between graphene and the substrate,  $\gamma_{gb}$  is the adhesion energy between graphene and substance inside the bubble and  $\gamma_{bs}$  is the adhesion energy between the substance in the bubble and the substrate. Competition between Van der Waals energy and the elastic energy determines the value of  $\frac{h_{\max}}{R}$ , called as the aspect ratio of bubble . This aspect ratio is independent of the properties of the substance captured within and depends on the strain in the graphene membrane [126].

$$E_v = \pi\gamma R^2 \quad (7.1)$$

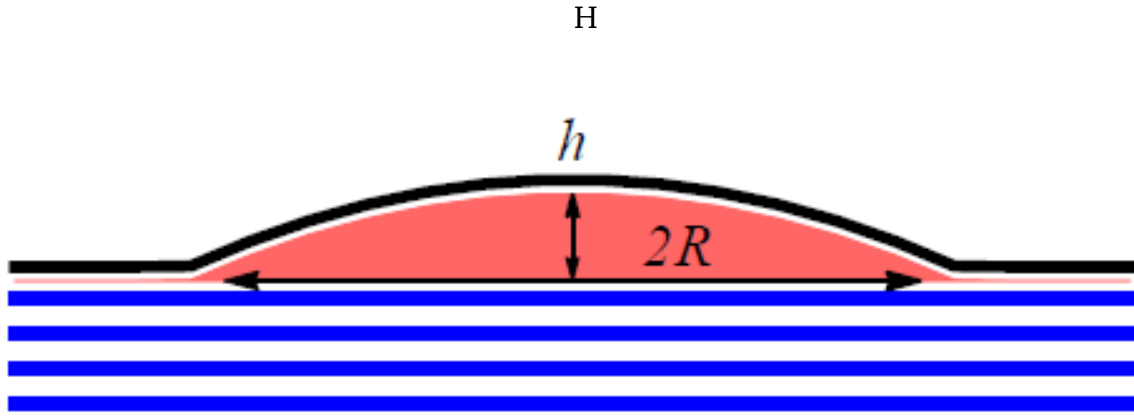


Figure 7.9: Schematic of graphene bubble [126]

$$\gamma = \gamma_{gs} - \gamma_{gb} - \gamma_{bs} \quad (7.2)$$

E. Khestanova et al. in their research have shown that in the presence of tensile strain these graphene bubbles become shorter. On the other hand, in the presence of compressive strain, the aspect ratio of these graphene bubbles i.e.  $\frac{h_{\max}}{R}$  becomes bigger.

Research in the past has shown the presence of graphene bubbles on silicon dioxide when it is attacked by HF/H<sub>2</sub>O or by bombardment of energy protons [127]. It has been shown that these graphene bubbles formation in both cases is due to gases (released from silicon dioxide) trapped underneath the graphene sheet [127]. The work done to expand the gas inside the bubble is equal to the work done to detach a part of the graphene from silicon dioxide substrate in the form of a bubble. On equating the forces between these two pressures, the pressure inside the graphene bubble can be calculated using equation 7.3. Here,  $p$  is the pressure inside the bubble,  $\sigma$  is the Van der Waals energy interaction between graphene and silicon dioxide per unit area,  $\phi$  is the slope of the graphene sheet at the edge of the bubble,

$$p = \frac{2\sigma}{a \sin \phi} \quad (7.3)$$

In equation 7.4,  $a$  is the radius of the bubble and  $h$  is the height of the bubble.

$$\sin \phi = \frac{2ah}{a^2 + h^2} \quad (7.4)$$

This relation shows that smaller bubbles have higher pressure. When smaller bubble is connected to a larger bubble, gas will flow from the smaller bubble to larger graphene bubble. This phenomenon, according to Stolyarova et al., occurs during annealing of the graphene sample and leads to coalescence of graphene bubbles. For the above given relations the graphene sheet and the substrate surface is considered to be flat which is not true in our case. Corrugations or roughness of the substrate on which graphene is growing facilitates in the formation of graphene bubbles [127]. These graphene bubbles have been observed to grow in the depression regions of the substrate surface.

Another important observation is the release of SiF<sub>4</sub> and H<sub>2</sub>O, when silicon dioxide is attacked by HF and water. According to Stolyarova et al., these gaseous products get filled inside the graphene bubbles after etching of the complete oxide layer. These bubbles are formed due to high pressure of the gas which gets stabilized due to the Van der Waals interaction between graphene and the oxide.



In order to investigate the bubble like structures observed on our samples and whether or not they have any relation with suspension of the devices, stress measurements were performed. These measurements have been described in the next section.

## 7.4 Stress measurements

Broadly, the stresses in thin films can be classified as extrinsic and intrinsic stresses. The extrinsic stress is stress that is induced in a thin film due to external factors such as thermal mismatch between the substrate and the thin film. If the thermal expansion coefficient of the substrate is different from the thermal expansion coefficient of the thin film and the thin film is deposited at high temperature on the substrate and then cooled to room temperature, then stress and strain will develop in thin film. Extrinsic stresses are generally uniform and so the measurement will give the average stress in the thin film.

Thermal stress develops in thin films due to difference in thermal expansion coefficient between the the membrane and the substrate. If the film initially shrinks in comparison to the substrate, tensile stress develop in the film and compressive stress in the substrate. For the structure to be in equilibrium, the force and the bending moments at the cross section of the device should vanish [128]. Hence, the thin film bends the substrate structure upwards to counteract the uncompensated bending moments [128]. Similarly thin films with compressive stress will bend the substrate downwards. These two cases have been schematically represented in 7.10.

The intrinsic stress occurs due to internal factors such as deposition conditions, doping, impurities etc. This stress is not uniform through the depth of the film and so a stress gradient occurs between the top and bottom of the thin film.

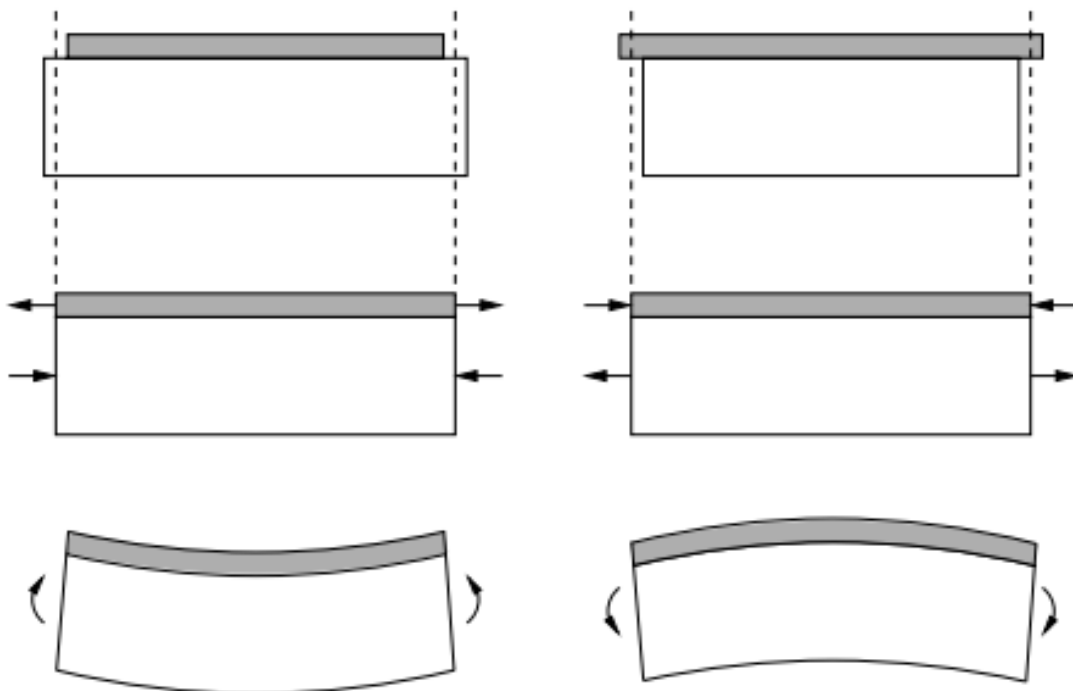


Figure 7.10: *Tensile and compressive stress due to mismatch in thermal expansion coefficients*[128]

Thin films on a thick substrate have residual stress because of which they expand or contract and bend the substrate. In order to measure this residual stress, the method used

is stoney's equation: Using stoney's equation the residual stress in a membrane can be calculated by measuring the bending in the curvature due to expansion/contraction of the thin film on the substrate. However, this calculated stress is the average stress in the thin film. That means that this stress would be present in the centre of the thin film.

The stoney's formula is given by the equation 7.5 . Here,  $\sigma_f$  is the stress in the film,  $d_s$  is the thickness of the substrate,  $d_f$  is thickness of the film,  $R_{pre}$  is the radius of curvature measured before the deposition of the film and  $R_{post}$  is the radius of curvature after the deposition of the film.

$$\sigma_f = \frac{E_s d_s^2}{6(1 - \nu_s)} \frac{1}{d_f} \left( \frac{1}{R_{post}} - \frac{1}{R_{pre}} \right) \quad (7.5)$$

This equation can also be applied to a stack of thin layers on top of the substrate as far as the total thickness of these thin films is much less than the thickness of the substrate. As the bending moments of each of the thin film can be added together, the residual stress of each layer contributes to the partial bending of the substrate.

The stress measurements in our case were performed using stress machine which uses laser scanner to measure the radius of curvature before the depositions of the film and after the deposition of the film. Table 7.3 shows the stress measurements for molybdenum. Molybdenum used in our case has a very large tensile stress. Table 7.4 gives stress measurements of wafers with no oxide on the backside of the wafer. The stress measurement values given in the table are the stress values in the combined layer and not individual layers. For example stress of -87 MPa is the average stress in the entire heterostructure containing graphene, molybdenum and oxide. It can be seen that all the oxides initially have compressive stress. Some of these values are similar to the ones obtained [129]. After molybdenum deposition, which has a high tensile stress in our case, they all become more tensile. After graphene growth the average stress in the stack of thin films becomes more tensile.

**Table 7.3: Stress measurements for molybdenum**

Metal	Thickness(nm)	Stress(MPa)
Molybdenum	100	1093
Molybdenum	200	1264

However, we realized that these measurements are not close to our original scenario since the collapsing membranes (see chapter 4) had oxide on both sides of the wafer. Hence, we performed the measurements again. This time we took the initial reference measurement with the wafer with oxide on both sides of the wafer. The results have been presented in table 7.5. It can be seen that unlike the previous measurements, this time both the wafers become less tensile during graphene growth. This shows that the oxide at the backside of the wafer makes the average stress in the wafer more compressive after graphene growth. After molybdenum removal, the average stress becomes much more compressive for dry oxide wafers than wet oxide wafers. This proves that graphene membrane on wafer 6 is much more compressively strained than on wafer 7.

Table 7.4: Stress measurements with backside oxide etched

Wafer	Oxide	Thickness of oxide (nm)	After Oxide deposition (MPa)	After 100nm Molybdenum deposition (MPa)	After Graphene (8nm) growth (MPa)
1	Dry Oxide	306	-530	-105	-87
2	Wet Oxide	987	-290	-157	-40
3	PECVD Oxide	106	-150	397	445
4	Dry Oxide	89	-361	416	521
5	Wet Oxide	115	-271	283	412

Table 7.5: Stress measurements of wafers with oxide on both sides of wafer

Wafer	Oxide	After 100nm Molybdenum deposition (MPa)	After Graphene (8nm) growth (MPa)	After Molybdenum removal (MPa)
6	Dry Oxide(92nm)	1319	892	-1759
7	Wet Oxide(1006nm)	1281	966	-688

## 7.5 Possible explanations for collapsing graphene membranes

From the discussions in the previous sections, the following hypothesis can be formed regarding the collapse of the graphene membranes.

### 7.5.1 Oxide thickness

- Hypothesis 1 Graphene bubbles theory + stress results

From the stress measurements, one of the most probable explanation of collapse of graphene membrane seems to be due the stress or elastic energy in the membrane. As discussed in section 7.3, graphene bubbles become larger for compressive strain and smaller for tensile strain. It can be seen from the stress measurements table 7.5 that after catalyst molybdenum removal, wafer with 90nm dry oxide becomes much more compressive than wafer with wet oxide. Since, graphene is in much more compressive strain when on dry oxide as compared to wet oxide, one possible explanation is that the bubbles become larger for dry oxide but not for wet oxide.

The presence of graphene bubbles on dry oxide wafers before release and not on wet oxide wafers also supports the bubble theory. These graphene bubbles, observed on molybdenum are expected to facilitate in the the formation of more bubbles when molybdenum is removed. This could be understood using the graphene bubble model shown in figure 7.9. A larger bubble implies less Van der Waals energy between graphene and the substrate, as compared to when graphene is lying on the substrate. When this molybdenum is removed during peroxide etching, the adhesion energy is not enough to pull the graphene membrane towards it due to these bubbles formation that have decreased the adhesion energy.

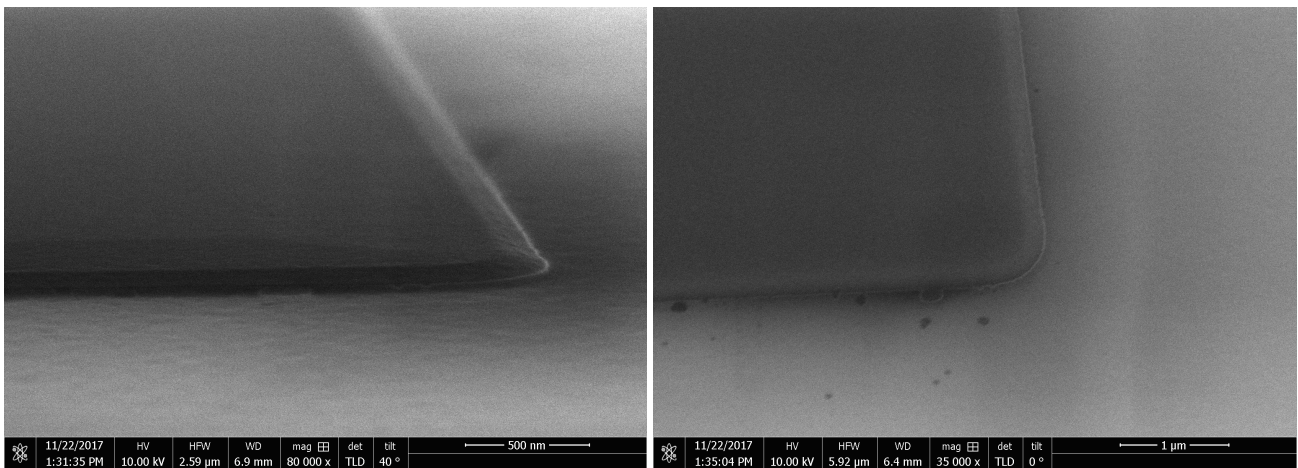
- Hypothesis 2 Conceptual analysis using residual stress in oxide

After molybdenum removal, the stress in the wafer is mainly due to oxide. For our case, the graphene membranes were fabricated on wafers with oxide on both sides. Hence, to get close to the real situation, it is important to include the stress due to oxide at the backside of the wafer also. If a wafer is grown with similar layer thickness on both sides of wafer, ideally the average stress in the wafer due to both layers should be zero. However, that is not what we observe for dry oxidation. We tested three wafers of similar thicknesses before and after oxide growth. For 1000 nm wet oxides, the stress in all the three wafers tested comes out to be very low (around 2MPa). However for 90 nm dry oxidation wafers, all the three wafers show compressive stress ranging from -33 MPa to -431MPa. This means that wafers with dry oxide are compressive whereas the average stress in wafers with wet oxide is almost zero. This again substantiates hypothesis 1 (compressive strain and bubble theory).

## 7.5.2 Molybdenum etching recipe

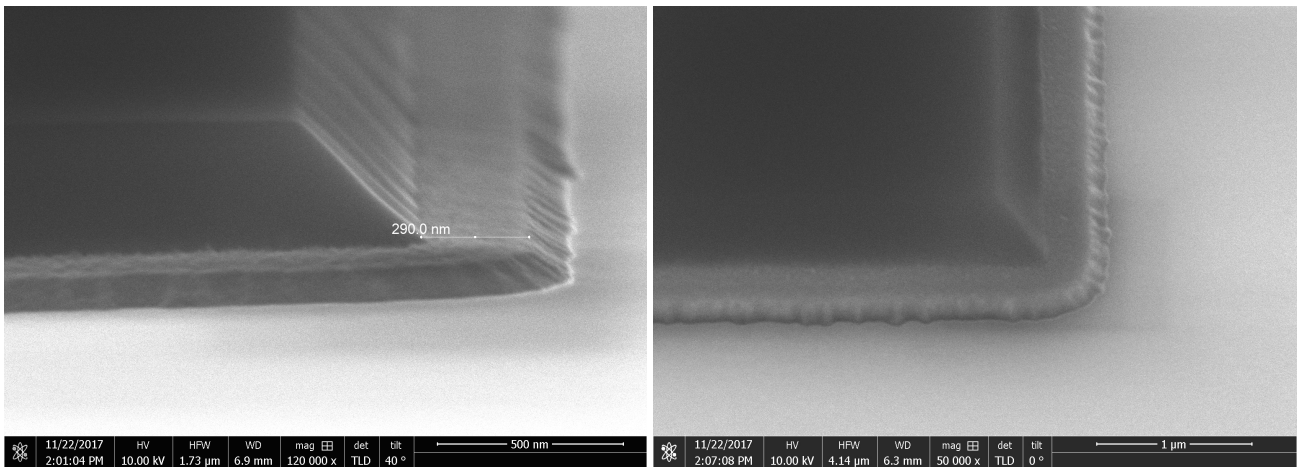
In order to understand this cause, the differences between both the etching recipes was investigated. The Mo50 recipe uses HBr and chlorine whereas the Motest2 recipe uses chlorine and oxygen.

- Hypothesis 1 The Sidewalls



(a) Mo50 recipe

(b) Mo50 recipe



(c) Motest2 recipe

(d) Motest2 recipe

Figure 7.11: SEM images of patterned and etched molybdenum

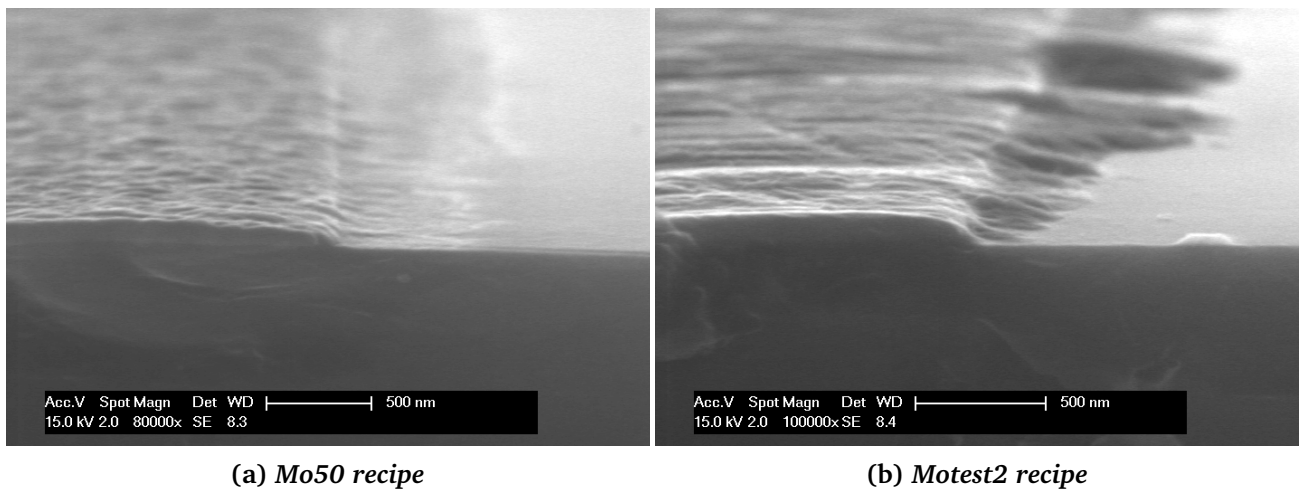


Figure 7.12: SEM images after graphene growth

As can be seen from the image 7.11 , using the Motest2 recipe , there is no photoresist remaining at the edges of the molybdenum after patterning and etching of the unmasked molybdenum. This is possibly due to oxygen present in Motest2 recipe attacking the photoresist. Since at the edges, the photoresist is attacked both laterally and from top side, it is removed from the edges of all the structure using Motest2 recipe. The implication of this could be that at the edges molybdenum has been oxidized due to the presence of oxygen. This also means that graphene grown at the edges would not be similar to the graphene grown on the remaining part of the structure which can be seen from the image 7.12. Graphene layer seems to be stretched and forming bubbles at the edges of the wafer. The sidewall morphology of molybdenum and the strange growth of graphene at the sidewalls for structures using Motest2 etching recipe are responsible for its collapse.

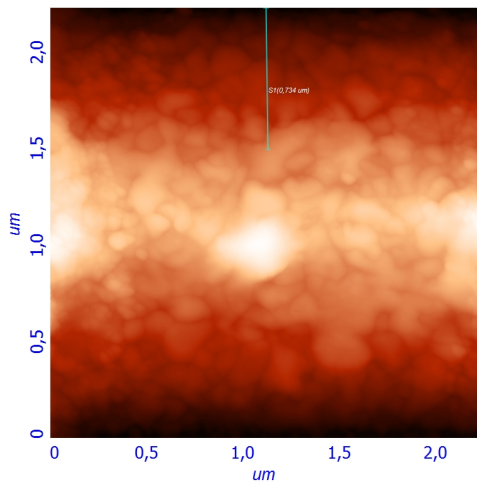
- Hypothesis 2 Graphene bubbles

No graphene bubbles were observed on wafer using Motest2 recipe before release (See figure 7.8). Because there are no bubbles present to reduce the adhesion energy between the graphene film and silicon dioxide after molybdenum removal, the membrane collapses after release.

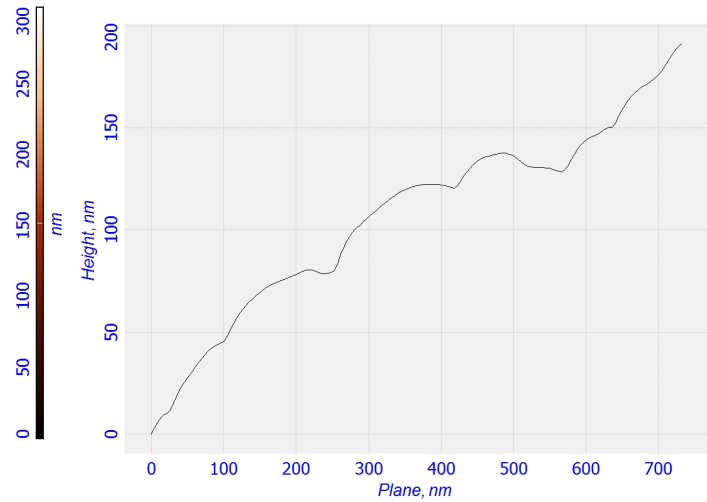
## 7.6 Analysis

We have seen from the stress measurements that 200 nm molybdenum has more tensile stress than 100 nm molybdenum. When graphene is grown on 200 nm molybdenum and after molybdenum is removed, we expect it to be more compressively strained than the 100 nm gap size. This is because a larger tensile stress removal from the the device should make it more compressively strained as compared to removal of a lower tensile stress.

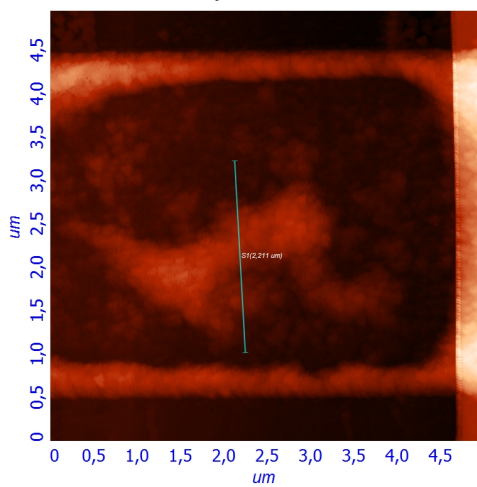
Another interesting observation from the images (See figures 7.13 (a) and (b)) is that graphene grows dome like on compressively strained molybdenum i.e. graphene membrane that is likely to be suspended is in compressive strain in both vertical and horizontal directions.



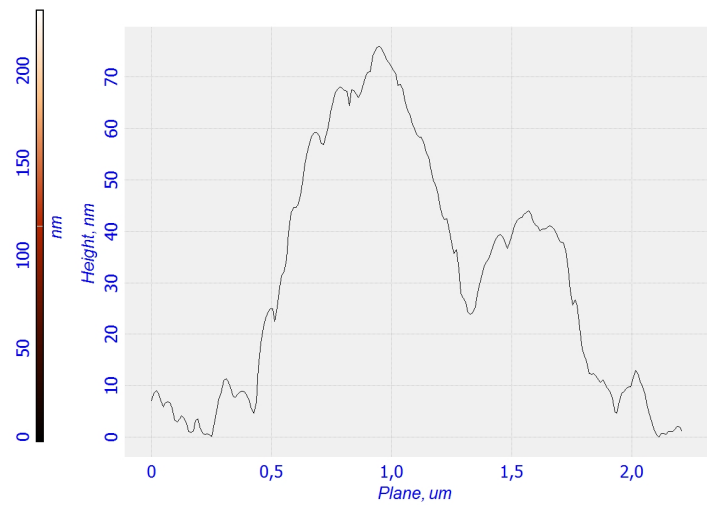
(a) Domelike structure in 200 nm graphene sample before release



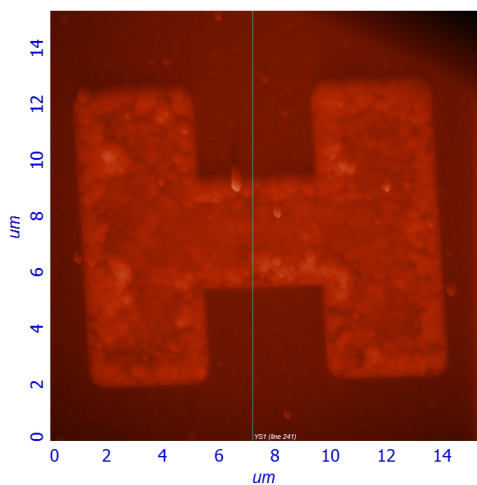
(b) Crosssection of 200 nm sample



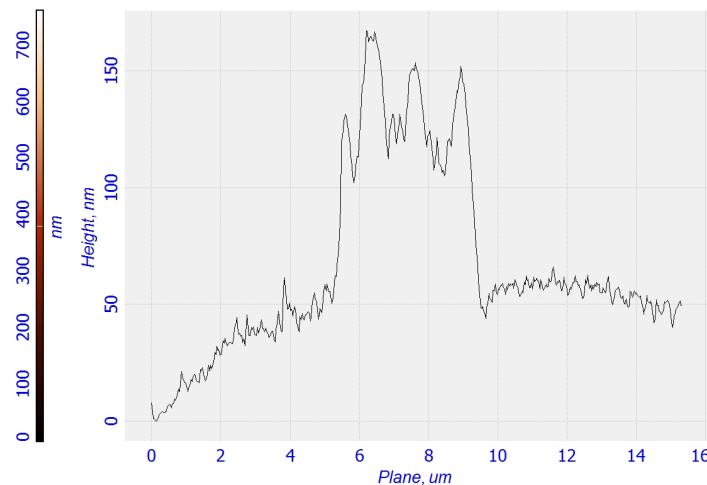
(c) Structure on wet oxide with backside oxide etched



(d) Crosssection across bubble



(e) Sample without gold anchors



(f) Cross section across line

Figure 7.13: AFM image analysis

We know from the previous results that graphene membranes on die with 1000 nm of oxide on both sides of wafer were not suspended. To test the influence of the backside oxide, we took another die from the same wafer on which steps till gold deposition were completed. Then we removed oxide from the backside of the wafer using BHF and performed the release steps. Interestingly, this time we found bubble like structures appearing in the centre of the

graphene membrane (See figures 7.13 (c) and (d)). This indicates two important points. The oxide on the backside of 1000 nm wet oxide wafer should be etched before graphene growth itself, to see if the graphene membrane is completely suspended or not. Secondly, we know from stress measurements that on removal of oxide from backside of wafer, the stress in the wafer becomes more compressive. So, compressive stress is facilitating in the suspension process.

A die with 200 nm gap size was released without gold contacts. Its cross sectional profile looks similar to the suspended graphene membranes with gold contacts (See figures 7.13 (e) and (f)). This shows that gold contacts are not necessary to suspend graphene membranes. Since the graphene membrane cannot be floating by itself in air, it is either touching the substrate at edges and/or more places. This indicates that it is not completely suspended. We expect our other graphene samples to be suspending by the same mechanism indicating that most of our graphene membranes are partially suspended.

## 7.7 Cause analysis: types of oxide

We know that if around 1000 nm of wet oxide is used in the process then the membranes collapse but if 90nm dry oxide is used then they are suspended. However, some questions still need to be answered. What is the maximum and minimum thickness of oxide that could be used to suspend the graphene membranes? Along with thickness does the difference in recipes between wet and dry oxidation also impact the suspension of graphene membranes?

In order to analyse these aspects, another batch of wafers was fabricated to find out if the membranes were suspended or not. For the first batch of wafers, 300 nm and 112 nm of wet oxide wafer were found to be collapsed. In the second batch of wafers 90 nm dry oxide was kept for reference along with PECVD oxide and wet oxide wafers. This time all the wafers were found to be suspended. This difference in results for the same thickness of wet oxide is intriguing.

**Table 7.6: Types of oxide: Cause analysis: first batch**

Wafer	Oxide	Thickness of oxide (nm)	Partially Suspended
8	Dry Oxide	300	×
9	Wet Oxide	112	×

**Table 7.7: Types of oxide: Cause analysis: second batch**

Wafer	Oxide	Thickness of oxide (nm)	Partially Suspended
10	Dry Oxide	87	✓
11	Wet Oxide	109	✓
12	PECVD Oxide	100	✓

## 7.8 Case study

We know from the stress measurements that molybdenum has a very high tensile stress and so is not a very good option to be used as the buried metal since it will make the stress in the wafer more tensile. Tensile stress leads to tensile strain in the graphene membrane which does not facilitate graphene bubbles to form. Such type of analysis becomes more complex for the actuator model as more number of layers are involved in it. In order to analyze why graphene membrane suspends on some metals and not on others, stress measurements were performed on the other conductors that were used as buried electrodes. These stress measurements are presented in table 7.8. For polysilicon, the stress result is for 99 nm of polysilicon deposited on both sides of the wafer.

**Table 7.8: Stress measurements for buried metals**

Buried Metal	Thickness(nm)	Stress(MPa)
Neobium	100	-329
Titanium + Titanium Nitride	10 + 100	-353
Molybdenum + titanium nitride	100 + 50	840
Polysilicon	99	16

As can be seen from table 7.8, unlike molybdenum, niobium and titanium nitride + titanium, have compressive stress. The values are comparable. Since, all the parameters used for graphene resonator with niobium electrode and graphene resonator with titanium nitride + titanium are similar, graphene membrane's suspension on only one of these metals is intriguing. To analyze this aspect, stress measurements were performed for both these metals. The results of these stress measurements are given in table 7.9. The initial reference measurements were done with 90 nm dry oxide on both sides of wafer. Clear differences are seen between wafer 13 and wafer 14 till molybdenum deposition i.e. TiN is tensile whereas Nb is compressive. However, not much difference in the stress values have been found between the two wafers after graphene growth and removal of molybdenum. The possible cause of collapse of membrane in this case needs further research.

**Table 7.9: Stress measurements : case study**

Wafer	Metal	After metal deposition	After 100nm PECVD Oxide deposition (MPa)	After 100nm molybdenum deposition (MPa)	After Graphene growth (8nm) (MPa)	After etching of molybdenum (MPa)
13	TiN + Ti (110nm)	-249	211	585	724.92	473
14	Nb (100nm)	-269	-777	-73	668	414



## 7.9 Summary

From cause analysis we know that a thick wet oxide of 1000 nm and the Motest 2 recipe using chlorine-oxygen chemistry to etch molybdenum are responsible for causing the graphene membranes to collapse.

Bubble like structures were observed on only graphene samples which were going to be suspended after release. On doing EDX measurements, we found that these bubble structures have significant more oxygen content than the other areas of graphene membranes. The stress measurements show wafer with dry oxide to be much more compressively strained than wafer with 1000 nm wet oxide after molybdenum removal. According to us, compressive strain is facilitating the bubbles to become bigger, thereby reducing the adhesion energy between the graphene membrane and the substrate and helping it to suspend.

For the Motest2 etched wafers, it was found that oxygen attacked the edges of photoresist from all sides of the structure, leaving a thin strip of molybdenum at the edges without photoresist. It was found that after graphene growth this strip of molybdenum influenced graphene growth causing graphene to grow much longer at the edges and forming big bubbles at the edges.

That wafer with 1000 nm of wet oxide which had shown collapsed membranes in the past, was released with the backside oxide etched. We observed some part of the central graphene membrane forming bubble like structures. There is a possibility of gas (released from oxide during etching of molybdenum) being trapped under it since it is sealed from all sides.

Structures with 200 nm gap size were released without gold anchors. Their AFM cross sectional profile looked similar to the ones with gold anchors. They also showed roughening. This shows that gold contacts are not necessary to suspend graphene membranes. Since the graphene membrane cannot be floating by itself in air, it is either touching the substrate at edges and/or more places. This indicates that it is not completely suspended. We expect our other graphene samples to be suspending by the same mechanism indicating that most of our graphene membranes are partially suspended.

The deposited molybdenum in our case has a very high tensile stress and so it is not useful as a buried metal because it will make the average stress in the the stack of thin films more tensile. We know from our previous measurements that compressive stress facilitates in suspending graphene membranes. However, its usage as a catalyst should not be a problem as it is removed after graphene growth thereby making the average stress in the thin layer stack much less tensile or more compressive depending on the stack of layers. No clear conclusion could be drawn regarding why graphene membranes on niobium are likely suspended but completely collapsed on TiN + Ti .

# Chapter 8

## Conclusion

The first goal of the project was to study the effect of size and shape of the graphene membrane on its suspension. To investigate this aspect, we fabricated graphene membranes of various shapes and sizes using wafer scale transfer free approach where the gap size is defined by the thickness of the molybdenum. We found that more number of graphene membranes with 200 nm gap size were suspended than 100 nm gap size graphene membranes. Also, larger areas of graphene membranes with the 200 nm gap size were suspended as compared to graphene membrane with 100 nm gap size. We did not observe any effect of the geometry of the membrane on its suspension. Finally, we also found that suspended graphene membranes was more crumpled and corrugated as compared to collapsed graphene membranes.

The second goal of the project was to fabricate suspended graphene membranes on an actuation electrode. It was found that the graphene membranes were partially suspended on p doped polysilicon and niobium electrodes and fully collapsed on molybdenum, titanium nitride + molybdenum or titanium nitride + titanium electrodes. On investigating the stress of these layers, it was found that p type doped polysilicon used had a very low stress and the molybdenum deposited in our case has a very high tensile stress. Stresses in niobium and titanium nitride + titanium electrode were found to be almost comparable. Some arguments have been given as to why graphene suspended on niobium electrode but not on titanium nitride + titanium electrode in chapter 7 but the exact reason for suspension is not known as of now and should be further investigated.

In order to investigate the dynamical properties of suspended graphene membranes, measurements using laser interferometry setup were performed in chapter 6. From the experiments and Comsol simulations, we found that the fundamental mode being detected was of the suspended gold and not the graphene. DC tuning and non linearity experiments indicated the presence of a graphene mode however since spring hardening of the suspected graphene frequency was only observed in non linearity experiment and graphene membrane was only partially suspended, more research needs to be done to show the presence of a resonant frequency due to graphene motion.

Besides measurements on the mechanical resonance, electrical resistance measurements were performed. We found that the 200 nm gap size graphene membranes have a higher contact resistances than the 100 nm gap size membranes. The resistance between the graphene membrane and the niobium electrode came out to be  $0.65 \Omega$  showing that it acted like a resistor. The resistance between the graphene membrane and the polysilicon electrode was found to be  $44.95 \text{ k}\Omega$ , indicating that the capacitor was very leaky. Improvements need to be made in the fabrication process of these actuators.

The next goal was to investigate how the process parameters influence the suspension of the graphene membrane. On changing one parameter in each wafer, we found that the

graphene on the wafer with 1000 nm wet oxide and the wafer which used chlorine-oxygen gases to etch molybdenum (Motest2 recipe) was collapsed. This indicates that the thickness of oxide and the etching recipe are responsible for the collapse of the graphene membranes. This led us to conclude that the process of suspension of the graphene membrane is sensitive to process parameters such as the oxide thickness and etching recipe.

On further investigating the collapse of membrane, we found the presence of bubble like structures on graphene samples which formed suspended membranes after release. Such structures were not found for collapsed graphene membrane samples before the release. After performing EDX analysis of the graphene membrane, we found significantly more oxygen content in the bubble area than the rest of the graphene area. The exact composition of these bubbles and the cause of their formation is unknown as for now. Some hypothesis related to these bubbles formation has been presented in chapter 7. According to us, the appearance of graphene bubbles could be facilitating the process of suspension or indicating that graphene membrane would be eventually suspended. However, whether a clear relation exists between appearance of the graphene bubbles on samples before release and its suspension, needs further investigation.

Beside the bubble we found that the stress value after removal of molybdenum from 90 nm dry oxide wafer is much more compressive than 1000 nm wet oxide wafer. This led us to conclude that the suspended graphene membranes are more compressively strained than the collapsed membranes. It was found that a graphene membrane of 200 nm gap size without gold contacts is also partially suspended. This shows that support from gold anchors is not necessary for the suspension of graphene membrane.

Most of our graphene membranes are only partially suspended. Suspension of the complete membrane is crucial for fabricating graphene based resonators. More research needs to be done in order to completely understand the process of suspension of the graphene membrane. This can then help define process flows and optimize process parameters to fully suspend graphene membranes in large areas which can eventually be used as resonators and sensors.

## Future Work

1. We already measured stress in the thin films using wafer curvature measurements. Another way of measuring stress could be by using structures. During my thesis work, I had tried to measure the stress in structure of dry oxide but the stress gradient in the beams was so high that they formed a ring instead. So, I would like to suggest this for future work. If we use structures instead of full layer to analyze stress, we could observe, we could observe the stress induced in it due to heating or cooling. We would also have better idea of strain gradient then.
2. The observed bubbles in the this work definitely need to be analyzed more. Infact the suspension of the graphene membrane needs to be further investigated. Various tests can be performed for this. For example after release, the oxide can be etched from underneath the wafers and then EDX measurement can be used to analyze the graphene membrane. This way we would know how silicon dioxide is affecting the suspension of the membrane. Also an EDX done on the graphene membrane without etching the oxide after release could solve various issues.
3. In order to get rid of the red laser of the optical setup, I would suggest doing transconductance measurements on the graphene samples [10].

# Bibliography

- [1] Harold G Craighead. Nanoelectromechanical systems. *Science*, 290(5496):1532–1535, 2000.
- [2] KL Ekinici and ML Roukes. Nanoelectromechanical systems. *Review of scientific instruments*, 76(6):061101, 2005.
- [3] Wen-Ming Zhang, Kai-Ming Hu, Zhi-Ke Peng, and Guang Meng. Tunable micro-and nanomechanical resonators. *Sensors*, 15(10):26478–26566, 2015.
- [4] YT Yang, Carlo Callegari, XL Feng, KL Ekinici, and ML Roukes. Zeptogram-scale nanomechanical mass sensing. *Nano letters*, 6(4):583–586, 2006.
- [5] HJ Mamin and D Rugar. Sub-attoNewton force detection at millikelvin temperatures. *Applied Physics Letters*, 79(20):3358–3360, 2001.
- [6] MD LaHaye, Olivier Buu, Benedetta Camarota, and KC Schwab. Approaching the quantum limit of a nanomechanical resonator. *Science*, 304(5667):74–77, 2004.
- [7] Changyao Chen and James Hone. Graphene nanoelectromechanical systems. *Proceedings of the IEEE*, 101(7):1766–1779, 2013.
- [8] J Scott Bunch, Arend M Van Der Zande, Scott S Verbridge, Ian W Frank, David M Tanenbaum, Jeevak M Parpia, Harold G Craighead, and Paul L McEuen. Electromechanical resonators from graphene sheets. *Science*, 315(5811):490–493, 2007.
- [9] J Scott Bunch, Scott S Verbridge, Jonathan S Alden, Arend M Van Der Zande, Jeevak M Parpia, Harold G Craighead, and Paul L McEuen. Impermeable atomic membranes from graphene sheets. *Nano letters*, 8(8):2458–2462, 2008.
- [10] Yuehang Xu, Changyao Chen, Vikram V Deshpande, Frank A DiRenno, Alexander Gondarenko, David B Heinz, Shuaimin Liu, Philip Kim, and James Hone. Radio frequency electrical transduction of graphene mechanical resonators. *Applied Physics Letters*, 97(24):243111, 2010.
- [11] Jeremy T Robinson, Maxim Zalalutdinov, Jeffrey W Baldwin, Eric S Snow, Zhongqing Wei, Paul Sheehan, and Brian H Houston. Wafer-scale reduced graphene oxide films for nanomechanical devices. *Nano Letters*, 8(10):3441–3445, 2008.
- [12] Arend M van der Zande, Robert A Barton, Jonathan S Alden, Carlos S Ruiz-Vargas, William S Whitney, Phi HQ Pham, Jiwoong Park, Jeevak M Parpia, Harold G Craighead, and Paul L McEuen. Large-scale arrays of single-layer graphene resonators. *Nano letters*, 10(12):4869–4873, 2010.

- [13] Daniel Garcia-Sanchez, Arend M van der Zande, A San Paulo, Benjamin Lassagne, Paul L McEuen, and Adrian Bachtold. Imaging mechanical vibrations in suspended graphene sheets. *Nano letters*, 8(5):1399–1403, 2008.
- [14] Shriram Shivaraman, Robert A Barton, Xun Yu, Jonathan Alden, Lihong Herman, MVS Chandrashekar, Jiwoong Park, Paul L McEuen, Jeevak M Parpia, Harold G Craighead, et al. Free-standing epitaxial graphene. *Nano letters*, 9(9):3100–3105, 2009.
- [15] Changyao Chen, Sami Rosenblatt, Kirill I Bolotin, William Kalb, Philip Kim, Ioannis Kymissis, Horst L Stormer, Tony F Heinz, and James Hone. Performance of monolayer graphene nanomechanical resonators with electrical readout. *Nature nanotechnology*, 4(12):861–867, 2009.
- [16] A Rao, C Sood, K Subrahmanyam, and A Govindaraj. Graphene: the new two-dimensional nanomaterial. *Angewandte Chemie International Edition*, 48(42):7752–7777, 2009.
- [17] F Schedin, AK Geim, SV Morozov, EW Hill, P Blake, MI Katsnelson, and KS Novoselov. Detection of individual gas molecules adsorbed on graphene. *Nature materials*, 6(9):652–655, 2007.
- [18] Nihar Mohanty and Vikas Berry. Graphene-based single-bacterium resolution biodevice and dna transistor: interfacing graphene derivatives with nanoscale and microscale biocomponents. *Nano letters*, 8(12):4469–4476, 2008.
- [19] Inanc Meric, Melinda Y Han, Andrea F Young, Barbaros Ozyilmaz, Philip Kim, and Kenneth L Shepard. Current saturation in zero-bandgap, top-gated graphene field-effect transistors. *Nature nanotechnology*, 3(11):654–659, 2008.
- [20] Anderson D Smith, Sam Vaziri, Anna Delin, M Ostling, and Max C Lemme. Strain engineering in suspended graphene devices for pressure sensor applications. In *Ultimate Integration on Silicon (ULIS), 2012 13th International Conference on*, pages 21–24. IEEE, 2012.
- [21] Changgu Lee, Xiaoding Wei, Jeffrey W Kysar, and James Hone. Measurement of the elastic properties and intrinsic strength of monolayer graphene. *science*, 321(5887):385–388, 2008.
- [22] Gwan-Hyoung Lee, Ryan C Cooper, Sung Joo An, Sunwoo Lee, Arend van der Zande, Nicholas Petrone, Alexandra G Hammerberg, Changgu Lee, Bryan Crawford, Warren Oliver, et al. High-strength chemical-vapor-deposited graphene and grain boundaries. *Science*, 340(6136):1073–1076, 2013.
- [23] H Zhao, K Min, and NR Aluru. Size and chirality dependent elastic properties of graphene nanoribbons under uniaxial tension. *Nano letters*, 9(8):3012–3015, 2009.
- [24] Robert A Barton, Jeevak Parpia, and Harold G Craighead. Fabrication and performance of graphene nanoelectromechanical systems. *Journal of Vacuum Science & Technology B, Nanotechnology and Microelectronics: Materials, Processing, Measurement, and Phenomena*, 29(5):050801, 2011.
- [25] Robin J Dolleman, Dejan Davidovikj, Santiago J Cartamil-Bueno, Herre SJ van der Zant, and Peter G Steeneken. Graphene squeeze-film pressure sensors. *Nano letters*, 16(1):568–571, 2015.

- [26] Henk W Ch Postma. Rapid sequencing of individual dna molecules in graphene nanogaps. *Nano letters*, 10(2):420–425, 2010.
- [27] Grégory F Schneider, Stefan W Kowalczyk, Victor E Calado, Grégory Pandraud, Henny W Zandbergen, Lieven MK Vandersypen, and Cees Dekker. Dna translocation through graphene nanopores. *Nano letters*, 10(8):3163–3167, 2010.
- [28] Kaveh M Milaninia, Marc A Baldo, Alfonso Reina, and Jing Kong. All graphene electromechanical switch fabricated by chemical vapor deposition. *Applied Physics Letters*, 95(18):183105, 2009.
- [29] Brian Thomas Kelly. *Physics of graphite*. 1981.
- [30] Maria E Suggs. Graphene resonators analysis and film transfer. *Sandia Report, SAND2012-4433, Unlimited Release*, 2012.
- [31] Kostya S Novoselov, Andre K Geim, Sergei V Morozov, D Jiang, Y\_ Zhang, Sergey V Dubonos, Irina V Grigorieva, and Alexandr A Firsov. Electric field effect in atomically thin carbon films. *science*, 306(5696):666–669, 2004.
- [32] Kirill I Bolotin, KJ Sikes, Zd Jiang, M Klima, G Fudenberg, J Hone, Ph Kim, and HL Stormer. Ultrahigh electron mobility in suspended graphene. *Solid State Communications*, 146(9):351–355, 2008.
- [33] SV Morozov, KS Novoselov, MI Katsnelson, F Schedin, DC Elias, John A Jaszczak, and AK Geim. Giant intrinsic carrier mobilities in graphene and its bilayer. *Physical review letters*, 100(1):016602, 2008.
- [34] Cristina Gómez-Navarro, Marko Burghard, and Klaus Kern. Elastic properties of chemically derived single graphene sheets. *Nano letters*, 8(7):2045–2049, 2008.
- [35] Hikari Tomori, Akinobu Kanda, Hidenori Goto, Youiti Ootuka, Kazuhito Tsukagoshi, Satoshi Moriyama, Eiichiro Watanabe, and Daiju Tsuya. Introducing nonuniform strain to graphene using dielectric nanopillars. *Applied physics express*, 4(7):075102, 2011.
- [36] Alexander L Kitt, Zenan Qi, Sebastian Remi, Harold S Park, Anna K Swan, and Bennett B Goldberg. How graphene slides: measurement and theory of strain-dependent frictional forces between graphene and sio<sub>2</sub>. *Nano letters*, 13(6):2605–2610, 2013.
- [37] Alexander L Kitt, Vitor M Pereira, Anna K Swan, and Bennett B Goldberg. Lattice-corrected strain-induced vector potentials in graphene. *Physical Review B*, 85(11):115432, 2012.
- [38] Andre K Geim and Konstantin S Novoselov. The rise of graphene. *Nature materials*, 6(3):183–191, 2007.
- [39] Qiugu Wang, Wei Hong, and Liang Dong. Graphene “microdrums” on a freestanding perforated thin membrane for high sensitivity mems pressure sensors. *Nanoscale*, 8(14):7663–7671, 2016.
- [40] Anderson D Smith, Sam Vaziri, Frank Niklaus, Andreas C Fischer, Mikael Sterner, Anna Delin, Mikael Östling, and Max C Lemme. Pressure sensors based on suspended graphene membranes. *Solid-State Electronics*, 88:89–94, 2013.

- [41] He Tian, Yi Shu, Xue-Feng Wang, Mohammad Ali Mohammad, Zhi Bie, Qian-Yi Xie, Cheng Li, Wen-Tian Mi, Yi Yang, and Tian-Ling Ren. A graphene-based resistive pressure sensor with record-high sensitivity in a wide pressure range. *Scientific reports*, 5, 2015.
- [42] Yu-Min Chen, Shih-Ming He, Chi-Hsien Huang, Cheng-Chun Huang, Wen-Pin Shih, Chun-Lin Chu, Jing Kong, Ju Li, and Ching-Yuan Su. Ultra-large suspended graphene as a highly elastic membrane for capacitive pressure sensors. *Nanoscale*, 8(6):3555–3564, 2016.
- [43] Jun Ma, Wei Jin, Hoi Lut Ho, and Ji Yan Dai. High-sensitivity fiber-tip pressure sensor with graphene diaphragm. *Optics letters*, 37(13):2493–2495, 2012.
- [44] Hyeun Joong Yoon, Jin Ho Yang, Zhixian Zhou, Sang Sik Yang, Mark Ming-Cheng Cheng, et al. Carbon dioxide gas sensor using a graphene sheet. *Sensors and Actuators B: Chemical*, 157(1):310–313, 2011.
- [45] Wenjing Yuan and Gaoquan Shi. Graphene-based gas sensors. *Journal of Materials Chemistry A*, 1(35):10078–10091, 2013.
- [46] Hiram Conley, Nickolay V Lavrik, Dhiraj Prasai, and Kirill I Bolotin. Graphene bimetallic-like cantilevers: probing graphene/substrate interactions. *Nano letters*, 11(11):4748–4752, 2011.
- [47] R Rasuli, MM Ahadian, et al. Mechanical properties of graphene cantilever from atomic force microscopy and density functional theory. *Nanotechnology*, 21(18):185503, 2010.
- [48] Alfonso Reina, Xiaoting Jia, John Ho, Daniel Nezich, Hyungbin Son, Vladimir Bulovic, Mildred S Dresselhaus, and Jing Kong. Large area, few-layer graphene films on arbitrary substrates by chemical vapor deposition. *Nano letters*, 9(1):30–35, 2008.
- [49] Nan Liu, Lei Fu, Boya Dai, Kai Yan, Xun Liu, Ruiqi Zhao, Yanfeng Zhang, and Zhongfan Liu. Universal segregation growth approach to wafer-size graphene from non-noble metals. *Nano letters*, 11(1):297–303, 2010.
- [50] Qingkai Yu, Jie Lian, Sujitra Siriponglert, Hao Li, Yong P Chen, and Shin-Shem Pei. Graphene segregated on ni surfaces and transferred to insulators. *Applied Physics Letters*, 93(11):113103, 2008.
- [51] Seunghyun Lee, Kyunghoon Lee, and Zhaohui Zhong. Wafer scale homogeneous bilayer graphene films by chemical vapor deposition. *Nano letters*, 10(11):4702–4707, 2010.
- [52] Xuesong Li, Weiwei Cai, Jinho An, Seyoung Kim, Junghyo Nah, Dongxing Yang, Richard Piner, Aruna Velamakanni, Inhwa Jung, Emanuel Tutuc, et al. Large-area synthesis of high-quality and uniform graphene films on copper foils. *Science*, 324(5932):1312–1314, 2009.
- [53] Xuesong Li, Weiwei Cai, Luigi Colombo, and Rodney S Ruoff. Evolution of graphene growth on ni and cu by carbon isotope labeling. *Nano letters*, 9(12):4268–4272, 2009.
- [54] Gregory W Cushing, Viktor Johaneck, Jason K Navin, and Ian Harrison. Graphene growth on pt (111) by ethylene chemical vapor deposition at surface temperatures near 1000 k. *The Journal of Physical Chemistry C*, 119(9):4759–4768, 2015.



- [55] Xiaohong An, Fangze Liu, Yung Joon Jung, and Swastik Kar. Large-area synthesis of graphene on palladium and their raman spectroscopy. *The Journal of Physical Chemistry C*, 116(31):16412–16420, 2012.
- [56] Hiroki Ago, Yoshito Ito, Noriaki Mizuta, Kazuma Yoshida, Baoshan Hu, Carlo M Orofeo, Masaharu Tsuji, Ken-ichi Ikeda, and Seigi Mizuno. Epitaxial chemical vapor deposition growth of single-layer graphene over cobalt film crystallized on sapphire. *Acs Nano*, 4(12):7407–7414, 2010.
- [57] Samira Naghdi, Kyong Yop Rhee, Man Tae Kim, Babak Jaleh, and Soo Jin Park. Atmospheric chemical vapor deposition of graphene on molybdenum foil at different growth temperatures. *Carbon letters*, 18(1):37–42, 2016.
- [58] Yuanwen Wu, Guanghui Yu, Haomin Wang, Bin Wang, Zhiying Chen, Yanhui Zhang, Xiaoping Shi, Xiaoming Xie, Zhi Jin, and Xinyu Liu. Synthesis of large-area graphene on molybdenum foils by chemical vapor deposition. *Carbon*, 50(14):5226–5231, 2012.
- [59] KAI Yan, LEI Fu, Hailin Peng, and Zhongfan Liu. Designed cvd growth of graphene via process engineering. *Accounts of chemical research*, 46(10):2263–2274, 2013.
- [60] NC Bartelt and KF McCarty. Graphene growth on metal surfaces. *MRS bulletin*, 37(12):1158–1165, 2012.
- [61] Cecilia Mattevi, Hokwon Kim, and Manish Chhowalla. A review of chemical vapour deposition of graphene on copper. *Journal of Materials Chemistry*, 21(10):3324–3334, 2011.
- [62] GA López and EJ Mittemeijer. The solubility of c in solid cu. *Scripta Materialia*, 51(1):1–5, 2004.
- [63] Yelena Grachova, Sten Vollebregt, Andrea Leonardo Lacaita, and Pasqualina M Sarro. High quality wafer-scale cvd graphene on molybdenum thin film for sensing application. *Procedia Engineering*, 87:1501–1504, 2014.
- [64] Kerstin Schneider, Annika Bräuer, Monika Fleischer, and Dieter P Kern. Graphite/graphene grown on molybdenum via cvd. In *Nanotechnology (IEEE-NANO), 2015 IEEE 15th International Conference on*, pages 481–484. IEEE, 2015.
- [65] S Vollebregt, B Alfano, F Ricciardella, AJM Giesbers, Y Grachova, HW van Zeijl, T Polichetti, and PM Sarro. A transfer-free wafer-scale cvd graphene fabrication process for mems/nems sensors. In *Micro Electro Mechanical Systems (MEMS), 2016 IEEE 29th International Conference on*, pages 17–20. IEEE, 2016.
- [66] IW Frank, David M Tanenbaum, AM Van der Zande, and Paul L McEuen. Mechanical properties of suspended graphene sheets. *Journal of Vacuum Science & Technology B: Microelectronics and Nanometer Structures Processing, Measurement, and Phenomena*, 25(6):2558–2561, 2007.
- [67] Xu Du, Ivan Skachko, Anthony Barker, and Eva Y Andrei. Approaching ballistic transport in suspended graphene. *Nature nanotechnology*, 3(8):491–495, 2008.
- [68] Benjamín Alemán, William Regan, Shaul Aloni, Virginia Altoe, Nasim Alem, Cag˘lar Girit, Baisong Geng, Lorenzo Maserati, Michael Crommie, Feng Wang, et al. Transfer-free batch fabrication of large-area suspended graphene membranes. *ACS nano*, 4(8):4762–4768, 2010.

- [69] Vibhor Singh, Shamashis Sengupta, Hari S Solanki, Rohan Dhall, Adrien Allain, Sajal Dhara, Prita Pant, and Mandar M Deshmukh. Probing thermal expansion of graphene and modal dispersion at low-temperature using graphene nanoelectromechanical systems resonators. *Nanotechnology*, 21(16):165204, 2010.
- [70] CL Wong, M Annamalai, ZQ Wang, and M Palaniapan. Characterization of nanomechanical graphene drum structures. *Journal of Micromechanics and Microengineering*, 20(11):115029, 2010.
- [71] Haidong Wang, Xing Zhang, and Hiroshi Takamatsu. Ultraclean suspended monolayer graphene achieved by in situ current annealing. *Nanotechnology*, 28(4):045706, 2016.
- [72] Elizabeth Ledwosinska, Abdeladim Guermoune, Mohamed Siaj, and Thomas Szkopek. Fabrication and characterization of suspended graphene membranes for miniature golay cells. In *SPIE OPTO*, pages 86240U–86240U. International Society for Optics and Photonics, 2013.
- [73] S Vollebregt, RJ Dolleman, HSJ van der Zant, PG Steeneken, and PM Sarro. Suspended graphene beams with tunable gap for squeeze-film pressure sensing. In *Solid-State Sensors, Actuators and Microsystems (TRANSDUCERS), 2017 19th International Conference on*, pages 770–773. IEEE, 2017.
- [74] Silvan Schmid, Luis Guillermo Villanueva, and Michael Lee Roukes. *Fundamentals of nanomechanical resonators*. Number EPFL-BOOK-220923. Springer, 2016.
- [75] Enrico Mastropaolo, Graham S Wood, Isaac Gual, Philippa Parmiter, and Rebecca Cheung. Electrothermally actuated silicon carbide tunable mems resonators. *Journal of Microelectromechanical Systems*, 21(4):811–821, 2012.
- [76] Enrico Mastropaolo, Rebecca Cheung, Anne Henry, and Erik Janzén. Electrothermal actuation of silicon carbide ring resonators. *Journal of Vacuum Science & Technology B: Microelectronics and Nanometer Structures Processing, Measurement, and Phenomena*, 27(6):3109–3114, 2009.
- [77] DH Young, SP Timoshenko, and W Weaver. *Vibration problems in engineering*. Wiley, 1974.
- [78] Shengwei Jiang, Shuai Shi, and Xuefang Wang. Nanomechanics and vibration analysis of graphene sheets via a 2d plate model. *Journal of Physics D: Applied Physics*, 47(4):045104, 2013.
- [79] Annalisa Fasolino, JH Los, and Mikhail I Katsnelson. Intrinsic ripples in graphene. *arXiv preprint arXiv:0704.1793*, 2007.
- [80] Menno Poot and Herre SJ van der Zant. Nanomechanical properties of few-layer graphene membranes. *Applied Physics Letters*, 92(6):063111, 2008.
- [81] Niklas Lindahl, Daniel Midtvedt, Johannes Svensson, Oleg A Nerushev, Niclas Lindvall, Andreas Isacson, and Eleanor EB Campbell. Determination of the bending rigidity of graphene via electrostatic actuation of buckled membranes. *Nano letters*, 12(7):3526–3531, 2012.
- [82] Wenzhong Bao, Feng Miao, Zhen Chen, Hang Zhang, Wanyoung Jang, Chris Dames, and Chun Ning Lau. Controlled ripple texturing of suspended graphene and ultrathin graphite membranes. *Nature nanotechnology*, 4(9):562–566, 2009.

- [83] Duhee Yoon, Young-Woo Son, and Hyeonsik Cheong. Negative thermal expansion coefficient of graphene measured by raman spectroscopy. *Nano letters*, 11(8):3227–3231, 2011.
- [84] Nicolas Mounet and Nicola Marzari. First-principles determination of the structural, vibrational and thermodynamic properties of diamond, graphite, and derivatives. *Physical Review B*, 71(20):205214, 2005.
- [85] KV Zakharchenko, MI Katsnelson, and Annalisa Fasolino. Finite temperature lattice properties of graphene beyond the quasiharmonic approximation. *Physical review letters*, 102(4):046808, 2009.
- [86] KV Zakharchenko, JH Los, Mikhail I Katsnelson, and Annalisa Fasolino. Atomistic simulations of structural and thermodynamic properties of bilayer graphene. *Physical Review B*, 81(23):235439, 2010.
- [87] PL De Andres, F Guinea, and MI Katsnelson. Bending modes, anharmonic effects, and thermal expansion coefficient in single-layer and multilayer graphene. *Physical Review B*, 86(14):144103, 2012.
- [88] Wei Gao and Rui Huang. Thermomechanics of monolayer graphene: Rippling, thermal expansion and elasticity. *Journal of the Mechanics and Physics of Solids*, 66:42–58, 2014.
- [89] Jin-Wu Jiang, Bing-Shen Wang, Jian-Sheng Wang, and Harold S Park. A review on the flexural mode of graphene: lattice dynamics, thermal conduction, thermal expansion, elasticity and nanomechanical resonance. *Journal of Physics: Condensed Matter*, 27(8):083001, 2015.
- [90] Stav Zaitsev, Oleg Shtempluck, Eyal Buks, and Oded Gottlieb. Nonlinear damping in a micromechanical oscillator. *Nonlinear Dynamics*, 67(1):859–883, 2012.
- [91] Valentin Afraimovich, Albert CJ Luo, and Xilin Fu. *Nonlinear dynamics and complexity*. Springer, 2014.
- [92] Xuefeng Song, Mika Oksanen, Mika A Sillanpaa, HG Craighead, JM Parpia, and Pertti J Hakonen. Stamp transferred suspended graphene mechanical resonators for radio frequency electrical readout. *Nano letters*, 12(1):198–202, 2011.
- [93] A Eichler, Joel Moser, J Chaste, M Zdrojek, I Wilson-Rae, and Adrian Bachtold. Nonlinear damping in mechanical resonators made from carbon nanotubes and graphene. *Nature nanotechnology*, 6(6):339–342, 2011.
- [94] Ron Lifshitz and MC Cross. Nonlinear dynamics of nanomechanical and micromechanical resonators. *Review of nonlinear dynamics and complexity*, 1:1–52, 2008.
- [95] Ramon Costa Castelló, AM Shkel, and A Fargas Marquès. Modelling the electrostatic actuation of mems: state of the art 2005. 2005.
- [96] Xue Ming Henry Huang, Christian A Zorman, Mehran Mehregany, and Michael L Roukes. Nanoelectromechanical systems: Nanodevice motion at microwave frequencies. *Nature*, 421(6922):496–496, 2003.

- [97] Ram Gopal Sharma. *Superconductivity: Basics and applications to magnets*, volume 214. Springer, 2015.
- [98] Wang Suocheng, Hao Yongping, and Liu Shuangjie. The design and analysis of a mems electrothermal actuator. *Journal of Semiconductors*, 36(4):044012, 2015.
- [99] Minhang Bao and Heng Yang. Squeeze film air damping in mems. *Sensors and Actuators A: Physical*, 136(1):3–27, 2007.
- [100] Stephen D Senturia. *Microsystem design*. Springer Science & Business Media, 2007.
- [101] Ashok Kumar Pandey. *Analysis of squeeze film damping in microdevices*. PhD thesis, G17927, 2012.
- [102] HH Richardson and S YAMANAIVII. A study of fluid squeeze-film damping. *Journal of Basic Engineering*, pages 451–456, 1966.
- [103] JJ Blech. On isothermal squeeze films. *Journal of lubrication technology*, 105(4):615–620, 1983.
- [104] Joachim N Burghartz and Behzad Rejaei. On the design of rf spiral inductors on silicon. *IEEE transactions on electron devices*, 50(3):718–729, 2003.
- [105] Plasma de delaquage et de traitement de surface (tepla 300). <https://www.laas.fr/public/sites/www.laas.fr.public/files/general/service-team/pdf/Tepla.pdf>, 2017 (accessed October 24, 2017).
- [106] Lecture 23: Oxidation. <http://nptel.ac.in/courses/113106062/Lec23.pdf>, 2017 (accessed October 24, 2017).
- [107] What is dc sputtering? <http://www.semicore.com/news/94-what-is-dc-sputtering>, 2017 (accessed October 26, 2017).
- [108] Spin coating and development : Evg 120. <http://www.laas.fr/files/pistes.ENG.pdf>, 2017 (accessed October 26, 2017).
- [109] Inductive coupled plasma etching (aviza technology omega201). <https://www.laas.fr/public/sites/www.laas.fr.public/files/general/service-team/pdf/aviza-GaAs.pdf>, 2017 (accessed October 25, 2017).
- [110] Inc XACTIX. Isotropic etching with xenon difluoride. <https://wcam.engr.wisc.edu/Public/Reference/PlasmaEtch/XACTIX%20XeF2%20Presentation.pdf>, 2017 (accessed October 24, 2017).
- [111] DR Nelson and L Peliti. Fluctuations in membranes with crystalline and hexatic order. *Journal de Physique*, 48(7):1085–1092, 1987.
- [112] Jannik C Meyer, Andre K Geim, Mikhail I Katsnelson, Konstantin S Novoselov, Tim J Booth, and Siegmund Roth. The structure of suspended graphene sheets. *Nature*, 446(7131):60–63, 2007.
- [113] P Blake, EW Hill, AH Castro Neto, KS Novoselov, D Jiang, R Yang, TJ Booth, and AK Geim. Making graphene visible. *Applied Physics Letters*, 91(6):063124, 2007.

- [114] M Raposo, Q Ferreira, and PA Ribeiro. A guide for atomic force microscopy analysis of soft-condensed matter. *Modern research and educational topics in microscopy*, 1:758–769, 2007.
- [115] Pecvd reactor. <http://www.laas.fr/files/reactPECVD.eng.pdf>, 2017 (accessed November 16, 2017).
- [116] <http://nptel.ac.in/courses/103106075/Courses/Lecture15.html>, 2017 (accessed November 17, 2017).
- [117] John H Scofield, A Duda, D Albin, BL Ballard, and PK Predecki. Sputtered molybdenum bilayer back contact for copper indium diselenide-based polycrystalline thin-film solar cells. *Thin solid films*, 260(1):26–31, 1995.
- [118] Majid Khan and Mohammad Islam. Deposition and characterization of molybdenum thin films using dc-plasma magnetron sputtering. *Semiconductors*, 47(12):1610–1615, 2013.
- [119] David Vernon Morgan and Kenneth Board. *An introduction to semiconductor microtechnology*. John Wiley & Sons, 1990.
- [120] Jinsub Choi, Jae Hoon Lim, Sang Cheon Lee, Jeong Ho Chang, Kyung Ja Kim, and Min Ae Cho. Porous niobium oxide films prepared by anodization in hf/h<sub>3</sub>po<sub>4</sub>. *Electrochimica acta*, 51(25):5502–5507, 2006.
- [121] Dejan Davidovikj, Jesse J Slim, Santiago J Cartamil-Bueno, Herre SJ van der Zant, Peter G Steeneken, and Warner J Venstra. Visualizing the motion of graphene nanodrums. *Nano letters*, 16(4):2768–2773, 2016.
- [122] Andres Castellanos-Gomez, Ronald van Leeuwen, Michele Buscema, Herre SJ van der Zant, Gary A Steele, and Warner J Venstra. Single-layer mos<sub>2</sub> mechanical resonators. *Advanced Materials*, 25(46):6719–6723, 2013.
- [123] Santiago J Cartamil-Bueno, Peter G Steeneken, Frans D Tichelaar, Efren Navarro-Moratalla, Warner J Venstra, Ronald van Leeuwen, Eugenio Coronado, Herre SJ van der Zant, Gary A Steele, and Andres Castellanos-Gomez. High-quality-factor tantalum oxide nanomechanical resonators by laser oxidation of tase<sub>2</sub>. *Nano Research*, 8(9):2842–2849, 2015.
- [124] Ryo Nouchi, Tatsuya Saito, and Katsumi Tanigaki. Observation of negative contact resistances in graphene field-effect transistors. *Journal of Applied Physics*, 111(8):084314, 2012.
- [125] Anderson D Smith, Frank Niklaus, Alan Paussa, Stephan Schroder, Andreas C Fischer, Mikael Sterner, Stefan Wagner, Sam Vaziri, Fredrik Forsberg, David Esseni, et al. Piezoresistive properties of suspended graphene membranes under uniaxial and biaxial strain in nanoelectromechanical pressure sensors. *ACS nano*, 10(11):9879–9886, 2016.
- [126] E Khestanova, F Guinea, L Fumagalli, AK Geim, and IV Grigorieva. Graphene bubbles on a substrate: universal shape and van der waals pressure. *arXiv preprint arXiv:1604.00086*, 2016.

- [127] E Stolyarova, D Stolyarov, Kirill Bolotin, S Ryu, L Liu, KT Rim, M Klima, M Hybertsen, I Pogorelsky, I Pavlishin, et al. Observation of graphene bubbles and effective mass transport under graphene films. *Nano letters*, 9(1):332–337, 2008.
- [128] Jean Laconte, Denis Flandre, and J P Raskin. Thin dielectric films stress extraction. *Micromachined Thin-Film Sensors for SOI-CMOS Co-Integration*, pages 47–103, 2006.
- [129] H Kahn, N Jing, M Huh, and AH Heuer. Growth stresses and viscosity of thermal oxides on silicon and polysilicon. *Journal of materials research*, 21(1):209–214, 2006.

# List of Figures

1.1	Transduction mechanism in a nanoresonator. Adapted from [2]	3
1.2	Graphene : parent of all graphitic forms Taken from [38]	4
1.3	a) Typical growth mechanism of films other than graphene. b) Underlayer mechanism of graphene growth on metals. Taken from [60]	5
1.4	CVD of graphene on substrates via two different routes	6
1.5	Actuation and detection of a graphene resonator. Adapted from [73]	8
2.1	Different types of mechanical resonators	10
2.2	Deflection of rectangular, square and circular shaped graphene sheets vs number of layers of graphene sheets. Taken from [78]	12
2.3	Plot of resonant frequency vs temperature for DC gate voltage of 15V. The arrows indicate the external strain in suspended membranes. Taken from [69]	12
2.4	Duffing nonlinear behaviour of doubly clamped graphene resonator, positive nonlinear spring constant and negative(inset) nonlinear spring constant. Taken from [92]	13
2.5	Magnetic actuation of a doubly clamped resonator. Taken from [3]	15
2.6	Electrostatic actuator model with a mechanical force	16
2.7	Strain in bimetal structure due to difference in thermal expansion of coefficients of the two different materials. Taken from [98]	16
2.8	Diagram of squeeze film flow. A) Downward normal motion B) Upward normal motion. Taken from [101]	18
3.1	3D representation of the graphene resonators along with their mask designs. Red: Suspended graphene membrane. Yellow: Gold metal	20
3.2	Cross sectional view of a graphene resonator	21
3.3	Other graphene resonators. Red: Suspended graphene Yellow: Gold metal	21
3.4	Mask design and 3D schematic representation of the graphene electrostatic capacitor. The gold bond pads on the contact opening have not been shown in the 3D schematic model	22
3.5	Complete mask design of an electrostatically actuated graphene resonator with gold bond pads. Blue: actuation electrode, Red: graphene membrane, Black: contact openings, Yellow: gold metal	23
3.6	Cross sectional view (Horizontal cross section of the figure 3.5) of an electrostatically actuated graphene resonator. Red coloured capacitances are the stray capacitances	24
3.7	Other structures which can be used as electrostatic actuators	25
3.8	The mask design of a magnetically actuated rectangular graphene membrane. Yellow: gold, Red: graphene, Blue: buried metal	26
3.9	Mask design for Wheatstone bridge configuration. Yellow: gold, Red: graphene, Blue: buried metal	26
3.10	Mask design of a gold graphene resonator. Yellow: Gold metal Red: Graphene, Blue: Buried metal molybdenum	28

3.11	Equivalent mechanical diagram of the goldgraphene resonator . . . . .	28
4.1	Fabrication process flow for suspended graphnene membranes . . . . .	31
4.2	TEPLA: the photoresist stripper. Taken from [105] . . . . .	32
4.3	DC magnetron sputtering of molybdenum. Adapted from [107] . . . . .	34
4.4	Automatic coater and developer: EVG 120. Taken from [108] . . . . .	34
4.5	EF exposure on the dies of the wafer . . . . .	35
4.6	Line width structures . . . . .	36
4.7	E-F measurement results for 2.1 $\mu\text{m}$ line . . . . .	36
4.8	Inductive Coupled Plasma Etching. Taken from [109] . . . . .	37
4.9	Blackmagic machine used to grow graphene . . . . .	38
4.10	Steps undertaken for the release of the membrane . . . . .	39
4.11	Suspended graphene membrane for pirani sensor application . . . . .	40
4.12	Xactix Equipment. Taken from [110] . . . . .	40
4.13	SEM images of the device etched in Xactix . . . . .	41
4.14	SEM images of the collapsed graphene membranes . . . . .	42
4.15	SEM images of the suspended graphene membranes . . . . .	42
4.16	Structure of suspended garphene membrane. Red square denotes the crests and the green square denotes the trough . . . . .	43
4.17	Microscope images of different types of graphene membranes . . . . .	44
4.18	Dark field images taken on different samples of graphene membrane . . . . .	45
4.19	SEM and AFM Images of 200 nm gap size samples . . . . .	46
5.1	Fabrication Process flow of electrostatically actuated graphene resonator (vertical cross section of figure 3.5 in chapter 3) . . . . .	52
5.2	PECVD reactor chamber. Taken from [115] . . . . .	53
5.3	Microscope images of the electrostatic devices fabricated using fabrication procedure 1 . . . . .	54
5.4	Two routes to pattern burried molybdenum . . . . .	55
5.5	Schematic representation of a reactive ion etcher. [116] . . . . .	56
5.6	SEM and microscope images of wafer 5 . . . . .	58
5.7	Microscope images of the devices fabricated : fabrication procedure 2 . . . . .	59
5.8	SEM images of the devices fabricated : fabrication procedure 2 . . . . .	59
5.9	Wafer 1 . . . . .	60
5.10	AFM images of the devices fabricated on wafer 6 . . . . .	60
5.11	SEM images of collapsed graphene membranes on molybdenum + titanium nitride electrodes . . . . .	61
5.12	SEM images of collapsed graphene membranes on metal molybdenum electrodes . . . . .	62
5.13	SEM images of suspended graphene membranes on polysilicon electrodes . . . . .	64
5.14	3D AFM image of graphene membrane suspended on polysilicon electrode . . . . .	65
5.15	SEM image of graphene membrane on niobium electrode . . . . .	66
5.16	3D AFM image of graphene membrane on niobium electrode . . . . .	67
5.17	SEM images of collapsed graphene membranes on Titanium nitide + Titanium electrode . . . . .	67
5.18	3D AFM image of graphene membrane on TiN + Ti electrode . . . . .	67
6.1	Laser interferometry setup . . . . .	70
6.2	Resonant frequency measurements using optical setup . . . . .	71
6.3	Rc structure used for analyzing gold resonances . . . . .	72
6.4	COMSOL frequency simulation of suspended gold part in Rc structures . . . . .	74
6.5	Setup used for electrostatic tuning experiment . . . . .	75



6.6	DC electrostatic tuning for (a) graphene $5 \times 3$ Rc structure (b) gold ( $L_s = 16 \mu\text{m}$ ) (c) shift in the frequency with DC voltage for graphene (d) shift in the resonant frequency with DC voltage for gold . . . . .	76
6.7	Transmission magnitude vs frequency for $5 \times 3$ Rc structure . . . . .	76
6.8	Non linearity experiment (a) graphrene membrane (b) gold . . . . .	78
6.9	Schematic represenattion of the Rc structure for non linearity experiment . . . . .	78
6.10	Non linearity experiment results for Point A and Point B. Bottom left: shift in resonant frequency for point A. Bottom right: shift in resoannt frequency for pont B . . . . .	79
6.11	Schematic representation of the laser positions on the Rc structure of the polysilicon die . . . . .	80
6.12	DC tuning of graphene resonator with polysilicon electrode . . . . .	80
6.13	Non linearity at point A . . . . .	81
6.14	Non linearity at point B . . . . .	82
6.15	Schematic 3D represenattion of the Rc structure contact resistance experiment . . . . .	84
7.1	AFM and SEM images of cause analysis wafer 1 and wafer 2 . . . . .	89
7.2	AFM and SEM images of cause analysis wafer 3 and wafer 5 . . . . .	90
7.3	SEM images of cause analysis wafer 5 and wafer 6 . . . . .	91
7.4	Microscope images of cause analysis wafers before release . . . . .	92
7.5	SEM images of cause analysis wafers before release . . . . .	93
7.6	AFM image analysis on wafer 4 before release . . . . .	94
7.7	AFM image analysis on wafer 5 before release . . . . .	94
7.8	AFM image analysis on wafer 2 before release . . . . .	95
7.9	Schematic of graphene bubble [126] . . . . .	96
7.10	Tensile and compressive stress due to mismatch in thermal expansion coefficients[128] . . . . .	97
7.11	SEM images of patterned and etched molybdenum . . . . .	100
7.12	SEM images after graphene growth . . . . .	101
7.13	AFM image analysis . . . . .	102

# List of Tables

1.1	List of graphene resonators fabricated in the past. Taken from [3, 7]	2
2.1	Comparison of different actuation methods. Taken from [3, 95]	17
4.1	Silicon Dioxide: Thickness and Uses. Taken from [106]	33
4.2	Molybdenum 100 nm recipe	33
4.3	Optimized exposure energy and focus values for different thickness values of photoresist	36
4.4	Fabrication Results (First Batch)	41
4.5	Fabrication Results (Second Batch)	42
4.6	AFM images of collapsed graphene samples	47
4.7	AFM images of 200 nm gap size graphene samples	48
4.8	AFM images of 100 nm gap size graphene samples	49
5.1	Fabrication procedure 1 parameters and results	54
5.2	Recipes:PECVD and PECVD Oxide	56
5.3	DC Power and Argon Pressure values for wafers fabricated at different times	57
5.4	Wafer 5 Parameters	57
5.5	Fabrication Procedure 2 Parameters	58
5.6	Fabrication procedure 3: parameters of wafers fabricated	60
5.7	Melting temperature of different metals/semi-metals	62
5.8	Wafers fabricated with different types of buried metal electrodes	63
6.1	Resonant frequencies observed for 200nm gap size graphene resonators. The cross is where the resonant frequency is observed	71
6.2	Frequency analysis for the 6 ×4 Rc structure	73
6.3	Frequency analysis for the 4 ×4 Rc structure	73
6.4	Frequency analysis for the 5 ×3 Rc structure	74
6.5	Resistance( $k\Omega$ ) measurement results for 100nm gap size graphene membranes	84
6.6	Contact Resistance measurement results for 100nm gap size graphene membranes, width of graphene= $4 \mu m$	85
6.7	Resistance ( $k\Omega$ ) measurement results for 200nm gap size graphene membranes	85
6.8	Contact Resistance measurement results for 200nm gap size graphene membranes, width of graphene= $4 \mu m$	85
6.9	Resistance measurement results for polysilicon and niobium die	86
7.1	Differences in fabrication processes parameters of suspended graphene membranes	88
7.2	Analysis of cause of collapse of membranes	88
7.3	Stress measurements for molybdenum	98
7.4	Stress measurements with backside oxide etched	99
7.5	Stress measurements of wafers with oxide on both sides of wafer	99
7.6	Types of oxide: Cause analysis:first batch	103

7.7 Types of oxide: Cause analysis:secind batch . . . . . 103

7.8 Stress measurements for buried metals . . . . . 104

7.9 Stress measurements : case study . . . . . 104

**.1 APPENDIX A**

# **Suspended Graphene membranes with Buried metal**

## **Flow chart**

**Version**

**August 2017**

**Sten Vollebregt, Manvika Singh**

**EC2125**

**Process engineer: Manvika Singh**

**Start: AUGUST 2017**

**Contamination: Yes**

**Labs: CR100, CR10000, SAL, MEMS, (Kavli)**

**EKL(Else Kooi Laboratory)  
DELFT UNIVERSITY OF TECHNOLOGY**

Address : Feldmannweg 17, 2628 CT Delft, The  
P.O. Box: 5053, 2600 GB Delft, The Netherlands  
Phone : +31 - (0)15 - 2783868  
Fax : +31 - (0)15 - 2622163  
Website : <http://ekl.tudelft.nl/EKL/Home.php>

### Detailed information about possible contamination:

#### Place/Clean Rooms used in process:

- Write the sequence of used labs from start to finish.
- Which (Non-standard) materials or process steps
- What kind of process or machine was used?
- The other materials that wafers contain that are also processed on this machine

Lab/Clean room	(Non-standard) material/ process steps	Process/Machine/	Other materials used in machine
CR100	non	non	non
CR10000	Yes, graphene	BlackMagic	Cu, Pt, Ni
SAL		Mo wet etching	
CR100		Litho on PAS5500/80	
MEMS	Yes, Cr/Au	Baltzers	Cr, Au, Ti, Pt

#### If other labs are used:

Write the steps number: Possible contamination issues/materials.

None

If there are non-standard processing steps in a standard process: Write down the steps number, the material and machine that is used.

Step number	Material	Machine/Tool
30	Graphene	Sigma

One litho step has to be performed after the graphene growth on the waferstepper. For this manual coating and development on contaminated chucks will be used. During exposure the special contaminated wafer carrier will be used.

## **STARTING MATERIAL**

Use 15 **single side polished process wafers**, with the following specifications:

Type:	p-type
Orientation:	1-0-0, 0 deg off orientation
Resistivity:	2-5 $\Omega\text{cm}$
Thickness:	525 $\pm$ 15 $\mu\text{m}$
Diameter:	100.0 $\pm$ 0.2 mm

Wafers taken out of an already opened box must be cleaned before processing, according to the standard procedure.  
Wafers taken out of an unopened wafer box do not have to be cleaned before processing.

And use 2 double-sided polished high-resistance process wafers

Type:	p-type
Orientation:	1-0-0, 0 deg off orientation
Resistivity:	1000-10000 $\Omega\text{cm}$
Thickness:	500 $\pm$ 15 $\mu\text{m}$
Diameter:	100.0 $\pm$ 0.2 mm

## EC2125

### 1. COATING AND BAKING

Use the EVG 120 wafertrack to coat the wafers with resist, and follow the instructions specified for this equipment. The process consists of a treatment with HMDS (hexamethyldisilazane) vapor with nitrogen as a carrier gas, spin coating with Shipley SPR3012 positive photoresist, and a soft bake at 95degC for 90 seconds. Always check the temperature of the hotplate and the relative humidity ( $48 \pm 2$  %) in the room first.

Use coating **Co – Zero Layer** (resist thickness: 1.400  $\mu\text{m}$ ).

### 2. ALIGNMENT AND EXPOSURE

Processing will be performed on the ASM PAS 5500/80 automatic waferstepper.

Follow the operating instructions from the manual when using this machine.

Use **COMURK mask** the correct litho job:

Litho/10-10-comurk0.0

And the correct exposure energy (120  $\text{mJ}/\text{cm}^2$ ).

### 3. DEVELOPMENT

Use the EVG 120 wafertrack to develop the wafers, and follow the instructions specified for this equipment. The process consists of a post-exposure bake at 115 degC for 90 seconds, followed by a development step using Shipley MF322 developer (single puddle process), and a hard bake at 100 degC for 90 seconds. Always check the temperature of the hotplates first.

Use development **program Dev - SP**

### 4. INSPECTION: LINEWIDTH

Visually inspect the wafers through a microscope, and check the linewidth. No resist residues are allowed.

### 5. NUMBER WAFERS

Number the wafers using the glass scribe.

### 6. PLASMA ETCHING OF ALIGNMENT MARKS

Use the Trikon Omega 201 plasma etcher.

Follow the operating instructions from the manual when using this machine.

The process conditions of the etch program may not be changed !

Use sequence **URK\_NPD** and set the platen temperature to **20 °C** to etch 1200 Å deep ASM URK's into the silicon.

### 7. CLEANING PROCEDURE: TEPLA + HNO<sub>3</sub> 100% and 65%

Plasma strip	Use the Tepla plasma system to remove the photoresist in an oxygen plasma. Follow the instructions specified for the Tepla stripper, and use the quartz carrier. Use program 1
Cleaning	10 minutes in fuming nitric acid (Merck: HNO <sub>3</sub> 100% selectipur) at ambient temperature. Use wet bench "HNO <sub>3</sub> (100%)" and the carrier with the red dot.
QDR	Rinse in the Quick Dump Rinser with the standard program until the resistivity is 5 M $\Omega$ .
Cleaning	10 minutes in concentrated nitric acid (Merck: HNO <sub>3</sub> 65% selectipur) at 110 °C. Use wet bench "HNO <sub>3</sub> (65%)" and the carrier with the red dot.
QDR	Rinse in the Quick Dump Rinser with the standard program until the resistivity is 5 M $\Omega$ .
Drying	Use the Semitool "rinsers/dryer" with the standard program, and the white carrier with a red dot.



## 8. OXIDATION

Furnace no: C2

Target thickness: 90 nm

Program name: dryoxide 1hr 7min 30s

PROCESS	TEMPERATURE (in oC)	GASES & FLOWS (in liter/min)	TIME (in minutes)	REMARKS
boat in	800	nitrogen: 3.0 oxygen: 0.3	5	
stabilize	800	nitrogen: 3.0 oxygen: 0.3	10	
heat up	+10 oC/min	nitrogen: 3.0 oxygen: 0.3	30	
stabilize	1100	nitrogen: 3.0 oxygen: 0.3	10	
oxidation	1100	hydrogen: 2.25 oxygen: 3.85	135	
cool down	-5 oC/min	nitrogen: 3.0	100	wait for operator
boat out	600	nitrogen: 3.0	5	

**NOTE: The total process time can be slightly reduced in the "cool down" step: the "boat out" step can be started after ± 60 minutes, when the actual temperature of the furnace will be about 800 oC.**

## 9. MEASUREMENT: OXIDE THICKNESS

Use the Leitz MPV-SP measurement system to measure the oxide thickness:

Program: Th. SiO2 on Si, >50nm auto5pts

Oxide thickness: 90 nm

## 10. Metall deposition @ Class 100, W2-W4

For wafer 2 use recipe Nb\_100nm (at 50C or 450C, input from Juan needed)

## 11. Poly-Si deposition @ Class 100, W1

Use recipe LPOLYNEW

## 12. BORON IMPLANTATION, W1

Ion B<sup>+</sup>  
Energy 10.0 keV  
Dose 1.0 x 10<sup>15</sup> (1.0E15) ions/cm<sup>2</sup>  
Remarks The angle of implant is standard 7 deg.  
The flat side of the wafer must be turned 22 deg north east.

## 13. CLEANING PROCEDURE, W1

Plasma strip Use the Tepla plasma system to remove the photoresist residues from the implanter in an oxygen plasma.  
Follow the instructions specified for the Tepla stripper, and use the quartz carrier.  
Use program 1: 1000 watts power  
Cleaning Use wetbench "HNO<sub>3</sub> (100%) for metals" and the carrier with the red/yellow dot.  
10 minutes in fuming nitric acid (Merck: HNO<sub>3</sub> (100%), selectipur; ambient temperature).  
QDR Rinse in the Quick Dump Rinser with the standard program until the resistivity is 5 MΩ.  
Drying Use the Avenger "Rinser/dryer" with the standard program. Always use the carrier for metals (black dot)

#### 14. COATING AND BAKING, ALL WAFERS

Use the EVG 120 wafertrack to coat the wafers with resist, and follow the instructions specified for this equipment. The process consists of a treatment with HMDS (hexamethyldisilazane) vapor with nitrogen as a carrier gas, spin coating with Shipley SPR3012 positive photoresist, and a soft bake at 95degC for 90 seconds. Always check the temperature of the hotplate and the relative humidity ( $48 \pm 2 \%$ ) in the room first.

Use coating Co – **3012 – 2,1  $\mu\text{m}$**  (resist thickness: 2.100  $\mu\text{m}$ ).

#### 15. ALIGNMENT AND EXPOSURE, ALL WAFERS

Processing will be performed on the ASM PAS 5500/80 automatic waferstepper.

Follow the operating instructions from the manual when using this machine.

Use **EC2125 mask**, layer MetalMo (layer 1)

Energy = 340  $\text{mJ}/\text{cm}^2$  focus = -1

Also expose the edge: g10a1-edge(full), layer ID =2, and the exposure energy  $E = T \text{ mJ}/\text{cm}^2$ . The reason for this is that Mo at the edge will result in more sliplines during graphene growth, which will give exposure problems .

#### 16. DEVELOPMENT, ALL WAFERS

Use the EVG 120 wafertrack to develop the wafers, and follow the instructions specified for this equipment. The process consists of a post-exposure bake at 115 degC for 90 seconds, followed by a development step using Shipley MF322 developer (single puddle process), and a hard bake at 100 degC for 90 seconds. Always check the temperature of the hotplates first.

Use development **program Dev - SP**

#### 17. INSPECTION: LINEWIDTH, ALL WAFERS

Visually inspect the wafers through a microscope, and check the linewidth. No resist residues are allowed. Use program StdOxide (8-10 nm/s) and change time to  $t=15 \text{ s}$ .

#### 18. PLASMA ETCHING OF Metal or Si

Use the Trikon Omega 201 plasma etcher.  
Follow the operating instructions from the manual when using this machine.  
The process conditions of the etch program may not be changed !

Use sequence **see below** and set the platen temperature to **25 °C**. Check the time is set for 100 nm.

**Perform a test on one wafer first and check for etching residues and SiO<sub>2</sub> over-etch**

**For wafer 1 Use LEON\_1, etch rate should be ~ 320 nm/min, so ~ 20-25 sec**

**For wafer 2 Use aloxetc for 12 sec**

#### 19. Remove photoresist using TEPLA, all wafers

##### Recipe 1

#### 20. CLEANING PROCEDURE, W1,

Cleaning	Use wetbench "HNO <sub>3</sub> (100%) for metals" and the carrier with the red/yellow dot. 10 minutes in fuming nitric acid (Merck: HNO <sub>3</sub> (100%), selectipur; ambient temperature).
QDR	Rinse in the Quick Dump Rinser with the standard program until the resistivity is 5 M $\Omega$ .
Drying	Use the Avenger "Rinser/dryer" with the standard program. Always use the carrier for metals (black dot)

## 21. CLEANING PROCEDURE, W2

Resist stripping      In Aceton bath in etching line for 1 min  
Cleaning              Use wetbench "HNO<sub>3</sub> (100%) for metals" and the carrier with the red/yellow dot.  
                            **Max. 3 minutes** in fuming nitric acid (Merck: HNO<sub>3</sub> (100%), selectipur; ambient temperature).  
QDR                    Rinse in the Quick Dump Rinser with the standard program until the resistivity is 5 MΩ.  
Drying      Use the Avenger "Rinser/dryer" with the standard program. Always use the carrier for metals (black dot)

## 22. DEPOSITION PECVD OXIDE

Use the Novellus PECVD reactor to deposit 200/300nm thick TEOS based silicon oxide  
Follow the operating instructions from the manual when using this machine.

Use **xxnmSTDTEOS. Temp. 350 °C, check deposition time!**

100 nm  
Time: 3.3 sec

## 23. Catalyst deposition @ Class 100

Use the TRIKON SIGMA sputter coater for the deposition of the catalyst metal Mo layer on the process wafers.  
Follow the operating instructions from the manual when using this machine.

Wy-y: Mo: 100 nm, recipe Mo\_100nm\_50C for wafer 2,  
                            Mo\_200\_50C for wafer1

Visual inspection: the metal layer must look shiny.

## 24. COATING AND BAKING

Processing will be performed on the EVG 120 wafertrack automatically:  
This includes a HMDS (hexa methyl disilazane) treatment with nitrogen carrier gas , the coating with  
AZ NLOF2020 resist (spin velocity 5600 rpm ; spin time 30 s) , and prebaking for 1,5 minute at 95 °C.  
Follow the instructions specified for this equipment, and always check the temperature of the hotplate first.

Use Coating Program "Co-3012-2,1um" (resist thickness: 2.100 μm at 48% RV).

## 25. ALIGNMENT AND EXPOSURE

Processing will be performed on the ASM PAS 5500/80 automatic waferstepper.  
Follow the operating instructions from the manual when using this machine.

Use EC2125 graphene mask (image 2)

Energy: 240, Focus-1

Also expose the edge: g10a1-edge(full), layer ID =2, and the exposure energy  $E = \text{TBD mJ/cm}^2$ . The reason for this is that Mo at the edge will result in more sliplines during graphene growth, which will give exposure problems .

## 26. DEVELOPMENT

Use the EVG 120 wafertrack to develop the wafers, and follow the instructions specified for this equipment.  
The process consists of a post-exposure bake at 115 degC for 90 seconds, followed by a development step using Shipley MF322 developer (single puddle process), and a hard bake at 100 degC for 90 seconds.  
Always check the temperature of the hotplates first.

Use development program Dev – SP

## 27. PLASMA ETCHING OF MOLYBDENUM

Use the Trikon Omega 201 plasma etcher.  
Follow the operating instructions from the manual when using this machine.  
The process conditions of the etch program may not be changed !

Use sequence **MO\_50NM** and set the platen temperature to **25 °C**.  
For wafer 4 min 30 s  
For Wafer 4 : 2min 20 s

**Perform a test on one wafer first and check for Mo etching residues and SiO<sub>2</sub> over-etch.**

#### **28. RESIST STRIPPING IN NMP @ SAL + Rinse**

As Mo cannot be cleaned using HNO<sub>3</sub> (it etches) the resist will be stripped using NMP at 70 °C for 8 min. Use a q-tip to remove residues. Rinse in DI water for 5 min. Dry using dryer in SAL

#### **29. Graphene growth @ Class 10000**

Use the AIXTRON BlackMagic Pro to grow CNTs using LPCVD at 915°C. Use recipe: Mo\_NEW\_915C\_40min

**Use graphene reactor interior (Cu contaminated)!**

**USE WHITE BLISTER WITH Cu WRITTEN ON IT**

#### **30. Titanium Nitride deposition @ BACKSIDE**

Use the TRIKON SIGMA sputter coater for the deposition of the capping metal TiN layer on the backside of the process wafers.

Follow the operating instructions from the manual when using this machine.

Recipe TiN\_100nm\_50C

**Use a dedicated carrier wafer!**

**USE GREEN BLISTER**

#### **31. COATING AND BAKING**

Processing will be performed on the EVG 120 wafertrack automatically:

This includes a HMDS (hexa methyl disilazane) treatment with nitrogen carrier gas , the coating with SPR3012 resist (spin velocity 5600 rpm ; spin time 30 s) , and prebaking for 1,5 minute at 95 °C.

Follow the instructions specified for this equipment, and always check the temperature of the hotplate first.

Use Coating Program “Co-3012-1,4um” (resist thickness: 1.400 µm at 48% RV).

#### **32. EXPOSURE**

Processing will be performed on the ASM PAS 5500/80 automatic waferstepper.

Follow the operating instructions from the manual when using this machine.

Use **mask EC2125 CO1 (image 3)**, energy = 140 mJ/cm<sup>2</sup>

#### **33. DEVELOPMENT**

Use the EVG 120 wafertrack to develop the wafers, and follow the instructions specified for this equipment.

The process consists of a post-exposure bake at 115 degC for 90 seconds, followed by a development step using Shipley MF322 developer (single puddle process), and a hard bake at 100 degC for 90 seconds.

Always check the temperature of the hotplates first.

Use development program Dev – SP

#### **34. WET ETCHING OF CO**

Use BHF(1:7) in SAL to etch (35 s) through the PECVD oxide.

### 35. RESIST STRIPPING IN NMP @ SAL

As Mo cannot be cleaned using HNO<sub>3</sub> (it etches) the resist will be stripped using NMP at 70 °C for 8 min. Use a q-tip to remove residues.

### 36. COATING AND BAKING

Processing will be performed on the EVG 120 wafertrack automatically:

This includes a HMDS (hexa methyl disilazane) treatment with nitrogen carrier gas, the coating with AZ NLOF2020 resist (spin velocity 5600 rpm ; spin time 30 s), and prebaking for 1,5 minute at 95 °C. Follow the instructions specified for this equipment, and always check the temperature of the hotplate first.

Use Coating Program “Co-2020-3 μm” (resist thickness: 3.000 μm at 48% RV).

### 37. EXPOSURE

Processing will be performed on the ASM PAS 5500/80 automatic waferstepper. Follow the operating instructions from the manual when using this machine.

Use **mask EC2125 MetalAu (image 4)**, energy = 55 mJ/cm<sup>2</sup>

### 38. DEVELOPMENT

Use the EVG 120 wafertrack to develop the wafers, and follow the instructions specified for this equipment. The process consists of a post-exposure bake at 115 degC for 90 seconds, followed by a development step using Shipley MF322 developer (single puddle process), and a hard bake at 100 degC for 90 seconds. Always check the temperature of the hotplates first.

Dev-X Link Bake Only

Use development program Dev – Lift-Off

### 39. Cr and Au EVOPORATION @ MEMS (by Sten)

Use the Baltzers Cr/Au evaporator to deposited 10 nm Cr and 100 nm Au. For W1 perform a 4 min HF-dip etch in 0.55% HF just before loading to remove the native-oxide.

**USE WHITE BLISTER WITH Cu and Au WRITTEN ON IT**

### 40. Mo removal @ Kavli

Etch the Mo by using H<sub>2</sub>O<sub>2</sub> for 5 min

### 41. CPD @ Kavli

Put the samples directly from DI water in IPA, leave them for 10 min. Next, transfer to VLSI grade IPA and leave for another 5 min. Load the dies into the Leica CPD machine and use Program 1 (slow).

Wafer Number	Thermal Oxide	Buried Metal	PECVD Oxide	Catalyst Molybdenum
1	90nm	Polysilicon (99nm)	100nm	200nm
2	90nm	Nb(100nm)	100nm	100nm